

Electromagnetic methods for imaging subsurface injections

by

Lindsey J. Heagy

B.Sc. Geophysics, University of Alberta, 2012

A THESIS SUBMITTED IN PARTIAL FULFILLMENT
OF THE REQUIREMENTS FOR THE DEGREE OF

Doctor of Philosophy

in

THE FACULTY OF SCIENCE
(Earth, Ocean and Atmospheric Sciences)

The University of British Columbia
(Vancouver)

June 2018

© Lindsey J. Heagy, 2018

Abstract

A thesis.

Revision: August 18, 2018

Preface

Chapter 2 presents an approach for constructing a physical property model of a fractured volume of rock. Mike Wilt, Jiuping Chen, Nestor Cuevas at Schlumberger. An earlier version of this work was presented at three conferences Heagy and Oldenburg (2013); Heagy et al. (2014a); Wilt et al. (2014) and included a patent Wilt et al. (2015).

Chapter 3 was submitted to Computers and Geosciences and is currently under review. The submitted manuscript is available on the ArXiv . Preliminary versions of this work were presented at two conferences Heagy et al. (2015, 2017b)

Appendix C was published in Computers and Geosciences (Heagy et al., 2017a)

Table of Contents

Abstract	ii
Preface	iii
Table of Contents	iv
List of Tables	ix
List of Figures	x
Acknowledgments	xxxii
Dedication	xxxiii
1 Introduction	1
1.1 Hydraulic Fracturing	2
1.2 Electromagnetic geophysics	5
1.2.1 Forward simulation	5
1.3 Geophysical inversions	5
1.4 Steel-cased boreholes	7
1.5 Thesis outline	7

1.6	A note on reproducibility	7
2	A physical property model for a fractured volume of rock	8
2.0.1	Proppant selection	9
2.0.2	Numerical Modelling	10
2.0.3	Chapter overview	12
2.1	Homogenization workflow using effective medium theory	12
2.1.1	Summary of self-consistent effective medium theory	15
2.1.2	Step 1: Effective conductivity of a proppant-fluid mixture	18
2.1.3	Step 2: Effective conductivity of fractured volume of rock	22
2.1.4	Summary	29
2.2	Feasibility of EM for detecting fractures	29
2.3	Conclusion	35
3	Modelling electromagnetics on cylindrical meshes with applications to steel-cased wells	38
3.1	Introduction	38
3.2	Numerical tools	44
3.2.1	Discretization	46
3.2.2	Validation	51
3.3	Numerical Examples	54
3.3.1	DC Resistivity Part 1: Electric fields, currents and charges in a long well	54
3.3.2	DC Resistivity Part 2: Finite Length Wells	57
3.3.3	Time Domain Electromagnetics	60

3.3.4	Frequency Domain Electromagnetics Part 1: Comparison with scale model results	63
3.3.5	Frequency Domain Electromagnetics Part 2: Conductivity and permeability in the inductive response of a well	71
3.4	Summary and Outlook	76
4	Direct current resistivity with steel-cased wells	80
4.1	Introduction	80
4.2	Governing equations and numerical modelling	83
4.3	DC resistivity for casing integrity	84
4.3.1	Basic experiment	85
4.3.2	Survey design considerations	90
4.3.3	Factors influencing detectability	93
4.3.4	Summary	103
4.4	Survey design for exciting targets at depth	105
4.4.1	Source location	106
4.4.2	Target properties	109
4.5	Coarse-scale approximations of the well	124
4.5.1	Replacing a hollow-cased well with a solid cylinder	126
4.5.2	Cartesian grid	132
4.6	Conclusion	135
5	Electromagnetics with steel cased wells	138
6	An inversion approach for subsurface injections	139
6.1	Introduction	139
6.2	Geophysical Inversions	142

6.2.1	Choosing an inversion model	146
6.3	Inversions with steel-cased wells	152
6.3.1	Standard Tikhonov inversion	154
7	Conclusions and Future Work	159
Bibliography		160
A Concentric spheres in a uniform electrostatic field		179
A.1	Setup	179
A.2	Solving for the Potential	181
A.2.1	Solving for the coefficients	182
A.2.2	Sanity Checks	194
A.3	Effective Conductivity Expression	200
B Self consistent effective medium theory derivatives		203
C A framework for simulation and inversion in electromagnetics		206
C.1	Introduction	206
C.2	Background	210
C.2.1	Governing Equations	213
C.3	Motivation	215
C.4	Simulation Framework	216
C.4.1	Model and Physical Properties	222
C.4.2	Physics	223
C.4.3	Sources	228
C.4.4	Fields	230
C.4.5	Receivers	231

C.4.6	Summary	231
C.5	Examples	232
C.5.1	Cylindrically Symmetric Inversions	233
C.5.2	Bookpurnong Field Example	236
C.5.3	Steel-Cased Well: Sensitivity Analysis for a Parametric Model	242
C.6	Conclusion	254

List of Tables

Table 4.1	Integrated secondary charge over a target adjacent to the casing, as shown in Figure 4.14.	114
Table 4.2	Integrated secondary charge over a target that is not electrically connected to the casing, as shown in Figure 4.17.	120
Table C.1	Comparison of the maximum amplitude of the sensitivity with respect to each model parameter, and the approximate perturbation in that parameter required to produce a 10^{-9} V/m change in the measured data. The conversion from a perturbation in log-conductivity to conductivity is given by equation C.26. The perturbation in conductivity is also provided in terms of a percentage of the true model conductivity.	256

List of Figures

Figure 1.1 Conventional reservoirs contain oil and gas that have migrated upwards under pressure until they are trapped by a cap rock (left), while non-conventional tight or shale oil and gas reservoirs contain hydrocarbons that are trapped in low permeability formations (right).	3
Figure 1.2 Overview of a geophysical inversion workflow. Adapted from Cockett et al. (2015).	6
Figure 2.1 Constructing a physical property model for a fractured volume of rock using effective medium theory. The electrical conductivity of the proppant fluid mixture is given by σ_2 , the conductivity of the background reservoir rock by σ_1 . Using effective medium theory, the coarse-scale anisotropic conductivity, Σ^* describing the fractured volume of rock is computed.	14
Figure 2.2 Effective conductivity of a proppant-fluid mixure for five different proppant conductivities, each indicated in the legend. The conductivity of the fluid is 3 S/m, similar to the conductivity of sea-water.	19

Figure 2.3	Impact of the conductivity of the fluid on the effective conductivity of a proppant-fluid mixture. Panel (a) shows the effective conductivity for mixtures with a 10^3 S/m proppant and panel (b) shows the effective conductivity for mixtures with a 10^4 S/m proppant. The conductivity of the fluid is indicated by the legend.	20
Figure 2.4	Effective conductivity of a 3-phase proppant-fluid mixture consisting of resistive proppant (10^{-6} S/m), conductive proppant (10^5 S/m) and saline fluid (3 S/m). The legend indicates the percentage of conductive proppant in the proppant mixture and the x-axis is the volume fraction of proppant in the proppant-fluid mixture.	21
Figure 2.5	Effective conductivity of a 3-phase proppant-fluid mixture consisting of resistive proppant (10^{-6} S/m), conductive proppant (10^5 S/m) and saline fluid (3 S/m). The proppant mixture contains 25% conductive proppant and 75% resistive proppant. The legend indicates the aspect ratio of the elongated conductive proppant filler (prolate spheroids).	23
Figure 2.6	Oblate spheroid with normal along the x -axis. The y and z semi-axes are equal, and aspect ratio is $\alpha = b/a < 1$	24

- Figure 2.7 Effective, anisotropic conductivity for a fractured rock with spheroidal cracks whose normal is oriented along the y -axis for five different aspect ratios, indicated by the legend. The black dashed lines show the upper and lower Wiener Bounds, which are identical the volume-weighted arithmetic and harmonic averages of the conductivity of the rock (0.1 S/m) and proppant-fluid mixture (2500 S/m). The black dash-dot lines are the anisotropic Hashin-Shtrikman upper and lower bounds computed using an aspect ratio of 10^{-5} in equation 2.12. Panel (a) shows the full range $0 \leq \varphi \leq 1$, and panel (b) zooms in to $0 \leq \varphi \leq 0.005$. Note that in (b), any curve that deviates from the lower bound is the $\sigma_{x,z}$ component; all σ_x values lie on the lower bound for the concentration range shown. 27
- Figure 2.8 Effective, isotropic conductivity for a fractured rock with randomly oriented spheroidal cracks for five different aspect ratios, indicated by the legend. The black dashed lines show the upper and lower Wiener Bounds, which are identical the volume-weighted arithmetic and harmonic averages of the conductivity of the rock (0.1 S/m) and proppant-fluid mixture (2500 S/m).The black dash-dot lines are the isotropic Hashin-Shtrikman upper and lower bounds. The semi-transparent dotted lines show $\sigma_{x,z}$ from Figure 2.7 Panel (a) shows the full range $0 \leq \varphi \leq 1$, and panel (b) zooms in to $0 \leq \varphi \leq 0.01$. . 28

Figure 2.9 Setup for the crosswell electromagnetic simulation. Ten fractures, each with 3mm thickness and 50m radius are spaced over a 10m interval along the injection well. The dipole transmitter is positioned inside of the injection well and oriented along the x-axis. Receivers are located in an offset well and measure the real and imaginary parts of the x-component of the magnetic field.	32
Figure 2.10 Simulated secondary magnetic field data for: (a) the anisotropic fracture model and (b) the isotropic fracture model, in a crosswell survey conducted at 100Hz. The top row shows the real component and the bottom row shows the imaginary component of the measured magnetic flux (nT). In all plots, the x-axis shows the transmitter location relative to the center of the fracture, the y-axis shows the receiver location, and the color indicates the secondary magnetic flux with respect to a 0.1 S/m whole-space. Values beneath the noise floor of 10^{-4} nT have been masked and display as white. To display the signal as a percentage of the primary, we have included a semi-transparent overlay between 0% and 5%; low percentage values plot as darker greys.	34
Figure 2.11 Simulated secondary magnetic field data for: (a) the anisotropic fracture model and (b) the isotropic fracture model, in a crosswell survey conducted at 200Hz. The top row shows the real component and the bottom row shows the imaginary component of the measured magnetic flux (nT), similar to Figure 2.10	36

Figure 3.1	Anatomy of a finite volume cell in a (a) cartesian, rectangular mesh, (b) cylindrically symmetric mesh, and (c) a three dimensional cylindrical mesh.	46
Figure 3.2	Construction of a 3D cylindrical mesh from a cartesian mesh.	50
Figure 3.3	Depth slice (left) and cross section (right) through the 3D cylindrical mesh used for the comparison with Commer et al. (2015). The source and receivers are positioned along the $\theta = 90^\circ$ line. The mesh extends 3600m radially and 3300m vertically to ensure that the fields have sufficiently decayed before reaching the boundaries.	53
Figure 3.4	Time domain EM response comparison with (Commer et al., 2015). Each of the different line colors is associated with a different location; offsets are with respect to the location of the well.	54
Figure 3.5	(a) Total charge density, (b) secondary charge density, (c) electric field, and (d) current density in a section of the pipe near the source at $z=-500\text{m}$	57
Figure 3.6	(a) Current along a well for 5 different wellbore lengths. The x-axis is depth normalized by the length of the well. The black dashed line shows the short-well approximation (equation 45 in Kaufman and Wightman (1993)) for a 200m long well. The black dash-dot line shows the long-well approximation (equation 53 in Kaufman and Wightman (1993)) for a 4000m well. (b) Charge per unit length along the well for 5 different wellbore lengths.	60

Figure 3.7 Current density for a time domain experiment where one electrode is connected to the top of the casing and a return electrode is on the surface, 1000m away. Six different times are shown, corresponding to each of the six rows; the times are indicated in the plots in panel (d). Panel (a) shows a zoomed-in cross section of the current density in the immediate vicinity of the steel cased well. Panel (b) shows a cross section through the half-space along the same line as the source-wire. Panels (c) and (d) show depth-slices of the currents at 54m and 801m depth.	64
Figure 3.8 Field strength ratio (FSR), the ratio of the measured vertical magnetic field with the free space magnetic field, as a function of frequency for two different receiver locations. In (a), the receiver is in the same plane as the source, in (b), the receiver is 1.49m offset from the source.	67
Figure 3.9 Magnetic flux density at 0.1Hz in the region of the pipe near the plane of the source for (a) the “infinite” pipe, where the source is located at -4.5m and the pipe extends from 0m to -9m, (b) a “semi-infinite” pipe, where the source is located at 0m and the pipe extends to -9m. In (c), we zoom in to the top 5cm of the “semi-infinite” pipe, and (d) shows the 5cm at the top-end of the “infinite” pipe.	69
Figure 3.10 Field strength ratio, FSR, for a receiver positioned 3cm beneath the plane of the source. For comparison, we have plotted the FSR for the permeable pipe when the source and receiver lie in the same plane ($L=0.00m$) with the semi-transparent orange lines. Note that the infinite-pipe solutions for $L=0.03m$ and $L=0.00m$ overlap.	70

Figure 3.11 Normalized secondary field, NSF, as a function of frequency for two wells. The NSF is the ratio of the secondary vertical magnetic field with the primary magnetic field at the receiver location ($z=-500m$); the primary is defined as the whole-space primary.	73
Figure 3.12 Secondary magnetic flux density (with respect to a whole-space primary) at five different frequencies for a conductive pipe (top row) and for a conductive, permeable pipe (bottom row).	74
Figure 3.13 Normalized secondary field (NSF) through time. In the time-domain, we compute the NSF by taking the difference between the total magnetic flux at the receiver and the whole-space response and then taking the ratio with the whole-space magnetic flux prior to shutting off the transmitter.	75
Figure 3.14 Secondary magnetic flux density for a conductive well (top row) and a conductive, permeable well (bottom row) through time. The source waveform is a step-off waveform.	76
Figure 4.1 Cross section showing: (a) electrical conductivity, (b) current density, (c) charge density, and (d) electric field for a top-casing DC resistivity experiment over (top) an intact 1000m long well and (bottom) a 1000m long well with a 10m flaw at 500m depth.	87
Figure 4.2 (a) Charge along the length of the intact well (black), a 500m well (“short”, grey dash-dot), and a well with a 10m flaw at 500m depth (blue), in a top-casing DC resistivity experiment. (b) Secondary electric field due on the surface of the earth due to the flaw in the casing. The primary is defined as the electric field due to the 1000m long intact well. The return electrode is 2000m away from the well.	88

Figure 4.5 Radial electric field as the depth of the flaw along a 1km long well is varied. The positive electrode is connected to the top of the casing, the negative electrode is positioned 500m away and data are measured along a line 90° from the source electrodes. In (a), we show the total electric field for four flawed wells, each with a 10m flaw at the depth indicated on the legend. The black line shows the radial electric field due to an intact well; we define this as the primary. In (b), the secondary radial electric field is plotted and in (c), we show the secondary radial electric field as a percentage of the primary. . . 95

Figure 4.6 Radial electric field as the conductivity of the background is varied for a 1km well with a 10m flaw at 500m depth. The positive electrode is connected to the top of the casing, the negative electrode is positioned 500m away and data are measured along a line 90° from the source electrodes. In (a), we show the total electric field for five different background conductivities, each indicated on the legend. The solid lines indicate the response of the flawed well and the dashed lines indicate the response of the intact well (the primary). In (b), the secondary radial electric field is plotted and in (c), we show the secondary radial electric field as a percentage of the primary. . . 97

Figure 4.7	Radial electric field as the conductivity of a 50m thick layer positioned at 400m depth is varied. The positive electrode is connected to the top of the casing, the negative electrode is positioned 500m away and data are measured along a line 90° from the source electrodes. In (a), we show the total electric field five different layer conductivities. The black line shows the scenario where the layer has the same conductivity as the background. The dashed-lines indicate the intact well and the solid lines indicate the flawed well. In (b), the secondary radial electric field is plotted (with respect to an intact well primary) and in (c), we show the secondary radial electric field as a percentage of the primary.	98
Figure 4.8	Cross section showing: (a) electrical conductivity, (b) current density, (c) charge density, and (d) electric field for a top-casing DC resistivity experiment over models with a conductive layer (top two rows) and a model with a resistive layer (bottom two rows). In all, the layer extends from 400m to 450m depth. The plots in the second and fourth rows show the model, currents, charges and electric fields for a well with a 10m flaw at 500m depth.	100
Figure 4.9	(a) Charge along the length of wells with three different conductivities (each indicated by a different color in the legend). The intact wells are denoted with dashed lines and the flawed wells are denoted with solid lines. (b) Secondary charge along the flawed and short wells. The primary is defined as the electric field due to the 1000m long intact well. The return electrode is 2000m away from the well.	101

Figure 4.10 Radial electric field as the conductivity of the casing is varied for a 1km well with a 10m flaw at 500m depth. The positive electrode is connected to the top of the casing, the negative electrode is positioned 500m away and data are measured along a line 90° from the source electrodes. In (a), we show the total electric field for three different casing conductivities, each indicated on the legend. The solid lines indicate the response of the flawed well and the dashed lines indicate the response of the intact well (the primary). In (b), the secondary radial electric field is plotted and in (c), we show the secondary radial electric field as a percentage of the primary. . . . 102

Figure 4.11 Radial electric field as the vertical extent of the flaw is varied. The positive electrode is connected to the top of the casing, the negative electrode is positioned 500m away and data are measured along a line 90° from the source electrodes. In (a), we show the total electric field four different flaw extents. The black line shows the response of the intact well. The dashed-lines indicate the partially flawed wells (50% of the circumference is compromised) and the solid lines flawed wells in which the entire circumference of the well has been compromised. In (b), the secondary radial electric field is plotted (with respect to an intact well primary) and in (c), we show the secondary radial electric field as a percentage of the primary. . . 104

Figure 4.12 Electrode locations to be compared. The top casing electrode (blue), centered electrode (green, 500m depth), and downhole electrode (red, 500m depth) are connected to the casing. The surface electrode (orange) is offset from the well by 0.1m. The remaining electrodes are positioned along the axis of the casing. Panel (a) shows the entire length of the casing, while (b) zooms in to the bottom of the casing to show the separation between the electrodes beneath the casing.	107
Figure 4.13 Total current density along a vertical line offset (a) 25m, (b) 50m and (c) 100m from the axis of the casing, which extends from the surface (0m) to 1000m depth. The electrode locations correspond to those shown in Figure 4.12. For reference, a simulation with an electrode 20m below the casing when there is no casing present is shown in black.	110
Figure 4.14 Cross section showing: (a) electrical conductivity, (b) current density, (c) charge density, and (d) electric field for a DC resistivity experiment with a conductive target (top) and a resistive target (bottom). The positive electrode is positioned in the casing at the 912.5m depth. The casing is shown by the black line that extends to 1km depth in panel (a).	112

Figure 4.15 Cross section showing: (a) electrical conductivity, (b) current density, (c) charge density, and (d) electric field for a DC resistivity experiment with a conductive target (top) and a resistive target (bottom). The positive electrode is positioned at 912.5m depth. No casing is included in this simulation. Note that the colorbars for the charge density (c) and electric field (d) are different than those used in Figure 4.14. For the resistive target, the colorbar is saturated, the charge density over the resistive target is on the order of 10^{-13} C/m^3 . 113

Figure 4.17 Cross section showing: (a) electrical conductivity, (b) current density, (c) charge density, and (d) electric field for a DC resistivity experiment with a conductive target (top) and a resistive target (bottom) which is not in contact with the well. The positive electrode is positioned in the casing at the 912.5m depth. The casing is shown by the black line that extends to 1km depth in panel (a). 118

Figure 4.18 Radial electric field at the surface as the conductivity of a cylindrical target, which is not contact with the well, is varied. The target has a radius of 25m and extends in depth from 900m to 925m. The return electrode is on the surface, 500m from the well and data are measured along a line perpendicular to the source. The panels on the left show (a) the total electric field, (b) the secondary electric field with respect to a primary that does not include the target, and (c) the secondary electric field as a percentage of the primary for a survey in which the positive electrode is positioned downhole at 912.5m depth. The panels on the right similarly show (d) the total electric field, (e) the secondary electric field, and (f) the secondary electric field as a percentage of the primary for a top-casing experiment. The data shown in Figure 4.16, for the target in contact with the well, are plotted in the dashed, semi-transparent lines for reference. 119

Figure 4.19 Depth slice showing the primary electric field due to a downhole electrode and a return electrode located on the surface at $x=-500\text{m}$, $y=0\text{m}$. The red line indicates the azimuth of the source. We examine the 3 different target azimuths shown by the white outlines. The solid line indicates the target inline with the source, the dashed is 90° from the source line, and the dotted line is 180° from the source line.

Figure 4.20 Integrated anomalous current density (excitation), as defined in equation 4.6, for a $50\text{m} \times 50\text{m} \times 25\text{m}$ target at 900m depth in a DC experiment with the positive electrode (a) downhole at 912.5m depth, and (b) a top-casing electrode. The return electrode is positioned on the surface 500m from the well. Each line color indicates a different target-conductivity. The different line styles correspond to different target azimuths relative to the plane of the source electrodes and correspond to those shown in Figure 4.19. The solid line indicates a target inline with the source, the dashed is 90° from the source, and the dotted line is 180° from the source. Offset is calculated from the center of the well to the edge of the target closest to the well. . . . 123

Figure 4.22 Currents (top row) and charges (bottom row) along the length of a hollow steel-cased well (solid lines), solid cylinder with conductivity equal to that of the steel-cased well (dashed-lines), and a solid cylinder with a conductivity such that the product of the conductivity and the cross sectional area of the cylinder is equal to that of the hollow-pipe (dotted lines). Each of the line-colors corresponds to a different casing length, as indicated in the legend. In (a), we show the vertical current in the casing, (b) shows the difference from the true, hollow-cased well in the vertical current within the casing, and (c) shows that difference as a percentage of the true currents. In (d), we show the charge per unit length along the casing, (e) shows the difference from the true, hollow-cased well and (f) shows that differences as a percentage of the true charge distribution. The x-axis on all plots is depth normalized by the length of the casing. . . .

Figure 4.23 Radial electric field measured at the surface for a model of a hollow steel-cased well (solid lines), a solid cylinder with conductivity equal to that of the steel-cased well (dashed-lines), and a solid cylinder with a conductivity such that the product of the conductivity and the cross sectional area of the cylinder is equal to that of the hollow-pipe (dotted lines). Each of the line-colors corresponds to a different casing length, as indicated in the legend. In (a), we show the total radial electric field, (b) shows the difference in electric field from that due to the true, hollow-cased well, and (c) shows that difference as a percentage of the true electric fields. The x-axis on all plots is distance from the well normalized by the length of the casing. . . . 129

Figure 4.24 Three realizations of a 2km long casing in a layered background, where the conductivity of the layers is assigned randomly. Each layer is 50m thick, and the mean conductivity of the background is 0.1 S/m. The color of the title corresponds to the plots of the currents and charges in Figure 4.25 130

Figure 4.25 (a) Total vertical current through the casing for the three layered-earth models shown in Figure 4.24. The solid lines indicate the response of the true, hollow steel cased-well and the dotted lines indicate the response of a solid cylinder having the same cross-sectional conductance as the hollow well. (b) Difference between the currents along the casing in the solid well approximation and the true, hollow well. (c) Charge per unit length for each of the models. (d) Difference in charge per unit length between the true model of the casing and the approximation which preserves cross-sectional conductance. 131

Figure 6.2	(a) Synthetic data for the down-hole casing experiment for the background, prior to the fracture (solid lines), and after the fracture (dots), (b) secondary electric field (fracture - background), and (c) secondary electric field as a percentage of the primary (background). The color of the lines or dots indicates the depth of the source.	155
Figure 6.3	(a) Observed and predicted radial electric field data, (b) difference between the observed and predicted data (V/m), (c) difference between the observed and predicted data as a percentage of the observed data, and (d) conductivity model recovered in the inversion. The colors in (a), (b), and (c) indicate the source location as shown in Figure 6.2. The white outline in (d) outlines the true geometry of the fracture zone and the grey line shows the location of the well-bore. The data are fit to a global χ -factor < 0.1	156
Figure 6.4	Tikhonov inversion result, similar to that shown in 6.3 that fits the data to a global χ -factor < 0.05	157
Figure 6.5	Tikhonov inversion result, similar to that shown in 6.4 that uses $\alpha_x = 100$	158
Figure A.1	Problem setup. Concentric spheres in a uniform electric field.	180
Figure C.1	Inversion approach using the SIMPEG framework. Adapted from Cockett et al. (2015)	211
Figure C.2	Forward simulation framework.	217
Figure C.3	Location of variables in the finite volume implementation for both a unit cell in (a) cartesian and (b) cylindrical coordinates (after Heagy et al. (2015))	218

Figure C.4	(a) Contributions of each module to the sensitivity. (b) process for computing $\mathbf{J}\mathbf{v}$ and (c) $\mathbf{J}^\top \mathbf{v}$; stars indicate where the source derivatives are incorporated.	220
Figure C.5	Mapping an inversion model, a 1D layered, log conductivity model defined below the surface, to electrical conductivity defined in the full simulation domain.	223
Figure C.6	Diagram showing the entire setup and organization of (a) the frequency domain simulation; (b) the time domain simulation; and (c) the common inversion framework used for each example. The muted text shows the programmatic inputs to each class instance. . .	234
Figure C.7	(a) True and recovered models for the FDEM and TDEM inversions; predicted and observed data for (b) the FDEM example, and (c) the TDEM example. In (b) the magnetic field data are in the negative z-direction.	237
Figure C.8	400 Hz In-phase RESOLVE data at (left) and High Moment SkyTEM data at 156μ s. The white dot at (462100m, 6196500m) on both images is the location of the stations chosen to demonstrate the 1D inversions in frequency and time.	238
Figure C.9	(a) Models recovered from from the 1D inversion of RESOLVE (back) and SkyTEM (blue) data at the location (462100m, 6196500m). (b) Observed (lines) and predicted (points) frequency domain data. (c) Observed and predicted time domain data. (d) Source waveform used in for the SkyTEM inversion, the x-axis is time (μ s) on a linear scale.	241

Figure C.10 (a) Conductivity model 9.9m below the surface from a stitched 1D inversion of RESOLVE data. (b) Real component of the observed RESOLVE data at 400Hz. (c) Real component of the predicted data at 400Hz.	242
Figure C.11 Setup of parametric models and calculation of the sensitivity for a primary secondary approach of simulating 3D geology and steel casing.	244
Figure C.12 Cross sectional slice of primary (casing + background) real current density. The colorbar is logarithmically scaled and shows the amplitude of the real current density.	248
Figure C.13 Depth slice at z=-950m showing the source current density for the secondary problem.	248
Figure C.14 Simulated real electric field data as measured at the surface using a primary secondary approach for casing and a conductive target (outlined in white). The upper panels show the total E_x (a) and E_y (b); the lower panels show the secondary (due to the conductive block) E_x (c) and E_y (d). Note that the colorbars showing the secondary electric fields are not on the same scale. The limits of the colorbars have been set so that the zero-crossing is always shown in the same color.	249
Figure C.15 Sensitivity of surface real E_x (left) and E_y (right) data with respect to the physical properties, $((V/m)/(\log(\sigma)))$	251
Figure C.16 Sensitivity of surface real E_x (left) and E_y (right) data with respect to the layer geometry, $((V/m)/m)$	252

Acknowledgments

People, Funding.

Dedication

Family.

Chapter 1

Introduction

As conventional, easily accessible, hydrocarbon resources are being depleted, there is an increase in the use of secondary and enhanced recovery techniques, for example using water or CO₂ to re-pressurize a reservoir, accompanied by an increase in the exploration and development of unconventional resources such as shale gas formations.

The combination of horizontal drilling and hydraulic fracturing are key technologies for extracting hydrocarbons from shale and low permeability, “tight” reservoirs. As a byproduct of fracturing, wastewater, if not recycled, must be disposed of. In many cases this is achieved by injecting the wastewater into the subsurface through an injection well. Similarly, with recognition of the hazard that carbon-dioxide poses as a contributor to global warming, efforts are being made to capture and store CO₂ in the subsurface. In each of these scenarios, there are both environmental and economic motivations for characterizing the distribution of injected materials.

To focus the research questions addressed in this thesis, we take the application of hydraulic fracturing as the primary motivating application, keeping in mind that the connections and similarities with other subsurface injections.

1.1 Hydraulic Fracturing

Hydraulic fracturing is used to extract hydrocarbons from tight (low-permeability) and shale formations where oil and gas will not easily flow. In such settings, hydraulic fracturing is used to create pathways for the hydrocarbons to flow (Figure 1.1). The process of inducing a fracture involves sealing off a section of the well and pumping fluid into that section under high pressure until the rock fails and cracks open up in the direction of the minimum principal stress. Typically, once the rock has fractured, sand or ceramic particles, referred to as proppant, are pumped into the formation to keep the newly created pathways open. Many of the wells drilled in the past two decades are horizontal wells, and typically 15 to 30 fracture stages (in some cases up to 60) are performed along the length of the well (Maxwell, 2014). The extent of the fractures, and distribution of proppant and fluid within these fractures, are key factors that determine the available pathways for oil or gas to flow to the well, and thus, the resulting production of the resource (Brannon and Starks, 2008; Cipolla et al., 2009). Therefore, in order to assess: how effectively the fracture treatment has stimulated the reservoir, how efficiently resources, such as water, have been used to create the fracture, and to understand the environmental and economic impacts of the fracture itself; we need a method to delineate the extent of the proppant and fluid within the reservoir.

Despite recent advances, there are still many unknowns in the fracturing process; chief among them is the extent and distribution of proppant and fluid within the reservoir. Microseismic is used to detect acoustic events generated as the fracture propagates through the reservoir. It can provide information about fracture geometry (Cipolla et al., 2009; Warpinski, 1996; Maxwell et al., 2002), but not all fractures generate a measurable seismic response (Cipolla and Wright, 2002; Barree et al., 2002), and a microseismic response contains no information about the proppant or fluid distribution within the

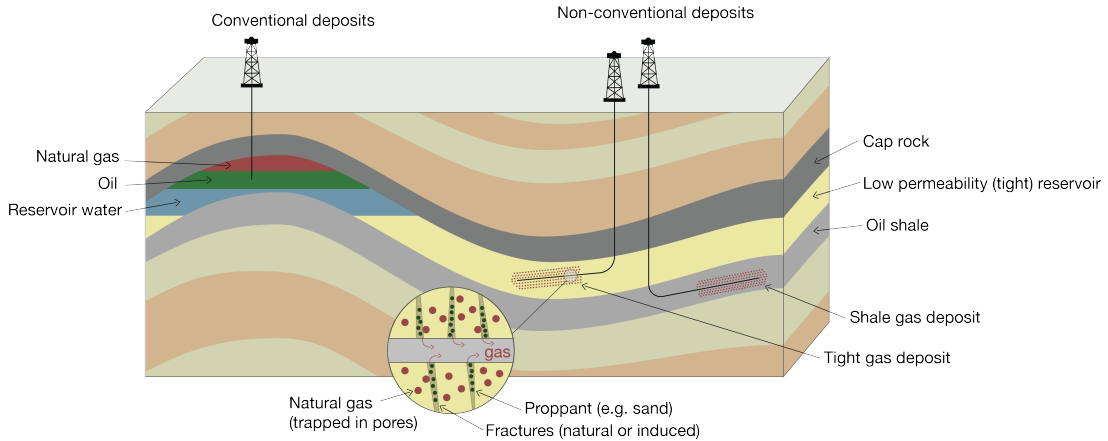


Figure 1.1: Conventional reservoirs contain oil and gas that have migrated upwards under pressure until they are trapped by a cap rock (left), while non-conventional tight or shale oil and gas reservoirs contain hydrocarbons that are trapped in low permeability formations (right).

reservoir (Warpinski, 1996; Barree et al., 2002). Tiltmeters are used to characterize the deformation of the rock due to the presence of a fracture or a change in the stress distribution (Wright et al., 1998), but they are incapable of providing direct information about the proppant or fluid distributions (Cipolla and Wright, 2002; Warpinski, 1996). Tracers and well logs are used to characterize the fracture geometry and fluid distribution, but their depth of investigation is limited to within a few meters of the wellbore (Cipolla and Wright, 2002). To delineate the extent of the proppant within the reservoir, we need a method that is both sensitive to the presence of the injected materials and can be implemented on the reservoir scale (Cipolla and Wright, 2002; Warpinski, 1996; Barree et al., 2002; Cipolla et al., 2009).

To accomplish this task, we propose to use electromagnetic (EM) geophysical techniques. For EM to be a viable method for imaging the distribution of proppant and fluid within a fractured volume of rock, we require that: (1) the fractured volume of rock

have physical properties which are distinct from the background, host rock, (2) the survey must be sensitive to this contrast, and (3) once the data have been collected, they must be interpreted or inverted in a meaningful manner. We also note that this is a time-lapse problem; that is, by inducing a fracture, the physical properties of the reservoir have been altered. In order to characterize such a change, we must view the imaging problem as a time-lapse one, and collect data to provide us with a before and an after data-view of the reservoir.

Variations in subsurface electrical conductivity have been used as a diagnostic physical property in sedimentary settings for characterizing geologic formations, and the properties and distribution of fluids within those formations. Hydrocarbons are much more resistive than saline formation fluids. In enhanced oil recovery projects, fluids are injected into the formation, which may be less resistive than the hydrocarbons they replace. These contrasts have been the target of cross-well, surface-to-borehole and borehole-to-surface electromagnetic (EM) methods for reservoir monitoring and characterization applications (cf. Bevc and Morrison (1991); Wilt et al. (1995); Marsala et al. (2008, 2011, 2014)).

In the case of hydraulic fracturing, the physical properties of the fractured volume of the reservoir depend upon the properties of the injected fluid and proppant particles. Saline water may be used, as is often the case when recycled water is used, and electrically conductive proppant may be manufactured and injected (Cannan et al., 2014; Vengosh et al., 2014; King, 2010). One or both of these may be used to create a physical property contrast between the host reservoir rock and the fractured volume of the reservoir. This contrast is what we aim to excite using an electromagnetic (EM) survey.

1.2 Electromagnetic geophysics

Electromagnetics is governed by Maxwell's equations,

$$\begin{aligned}\nabla \times \vec{e} + \frac{\partial \vec{b}}{\partial t} &= 0 \\ \nabla \times \vec{h} - \frac{\partial \vec{d}}{\partial t} &= \vec{j}\end{aligned}\tag{1.1}$$

where \vec{e} is the electric field (V/m), \vec{b} is the magnetic flux density (T), \vec{h} is the magnetic field (A/m), \vec{d} is the electric displacement (C/m²), \vec{j} is the current density (A/m²)

1.2.1 Forward simulation

1.3 Geophysical inversions

Once data have been collected, an inverse problem can be formulated. The goal of the inversion is to extract information about the subsurface from the data. Formulating, implementing and solving the inverse problem can be viewed as a workflow consisting of inputs, implementation, and evaluation, as shown in Figure ???. The inputs are composed of the data, the governing equations, and prior knowledge or assumptions about the setting. In the case of the fracturing problem, this may include well-log resistivity measurements which provide information about the background, knowledge of where the fracture was initiated, and the volumes of proppant and fluid pumped to create the fracture. The implementation consists of two broad categories: the forward simulation and the inversion. The forward simulation is the means by which we solve the governing equations given a model, and the inversion components evaluate and update this model. We are considering a gradient based approach, which updates the model through

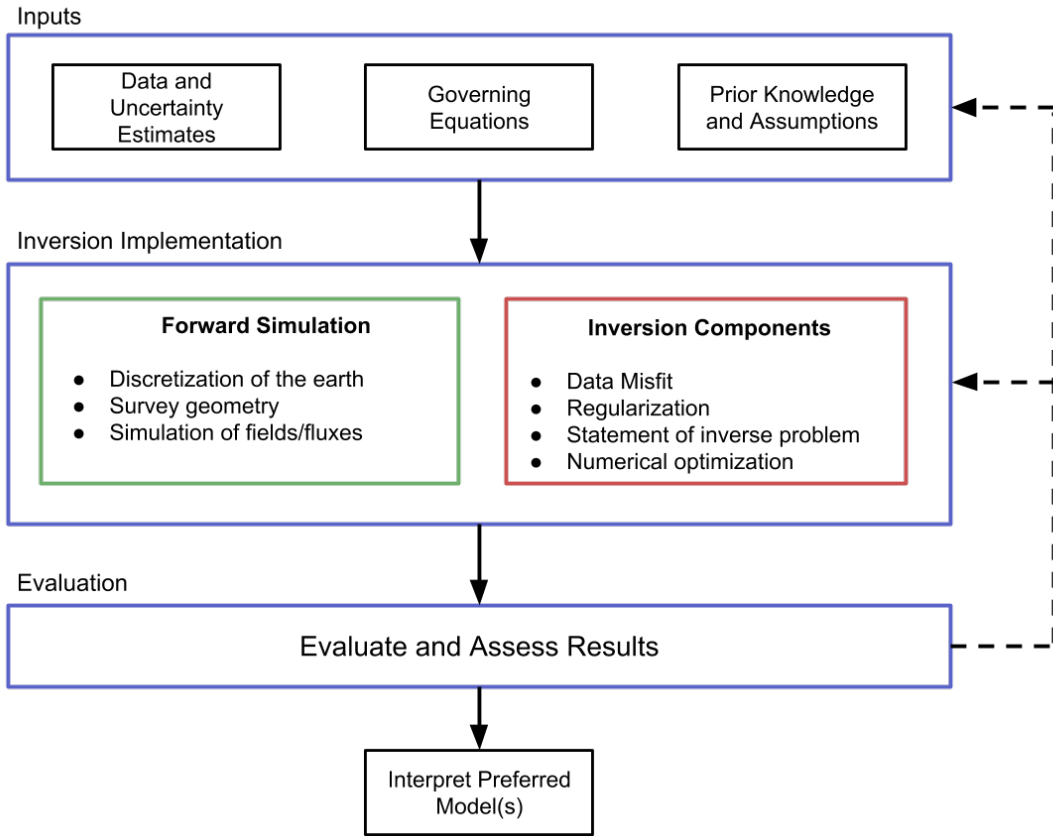


Figure 1.2: Overview of a geophysical inversion workflow. Adapted from Cockett et al. (2015).

an optimization routine. The output of this implementation is a model, which, prior to interpretation, must be evaluated. This requires considering, and often re-assessing, the choices and assumptions made in both the input and implementation stages (c.f. Oldenburg and Li (2005b); Haber (2014a); Cockett et al. (2015)).

1.4 Steel-cased boreholes

1.5 Thesis outline

1.6 A note on reproducibility

Chapter 2

A physical property model for a fractured volume of rock

For electromagnetic methods to be sensitive to a propped, fractured volume of rock, the fractured volume of rock must have physical properties which are distinct from the background, host rock. For EM methods, this means the electrical conductivity, magnetic permeability, or dielectric permittivity of the fractured rock must be distinct. Dielectric permittivity only plays a significant role when the frequency of the source is sufficiently high, in the hundreds of kilohertz to megahertz range, as is used in ground penetrating radar. Over the length-scales we need to consider for imaging fractures, 100s to 1000s of meters, attenuation of the EM signals due to skin depth effects make GPR impractical. Thus, we will work at lower frequencies, in the quasi-static regime of Maxwell's equations, and concern ourselves only with magnetic permeability and electrical conductivity. The materials traditionally used as proppant, typically sand and ceramics, tend to have similar physical properties to the reservoir that they are being pumped into, making it difficult to detect them on the scale of the reservoir. However, if

the proppant were made electrically conductive or magnetically permeable, for instance by coating it with graphite or including magnetite particles, it may create a sufficient physical property contrast that can be imaged using EM.

2.0.1 Proppant selection

To make the proppant electromagnetically distinct from the host rock, either the magnetic permeability or the electrical conductivity of the proppant could be targeted. Zawadzki and Bogacki (2016) provides an overview of possible magnetic proppants and highlights some practical considerations for the choice of material. For any proppant or additive, the constraints include: the mechanical strength of the particles must be able to withstand the pressure of the closing fracture without crushing and clogging the fracture pathways; the material shouldnt be toxic or reactive; and the price-point should be reasonable since high volumes are needed. Zawadzki and Bogacki (2016) also provide a general classification of material types that could be considered: feedstock material, materials that are mixed with conventional proppant or replace conventional proppant, could include magnetite or steel particles. Both have a significant magnetic permeability, however, magnetite crushes easily, and although steel has significant mechanical strength, it is challenging to manufacture particles that are small enough (typically $< 2\text{mm}$ in diameter). They also consider ferrofluids, which contain microscopic ferromagnetic particles in suspension, and magnetic nanoparticles. Both are sufficiently small and remain in suspension so clogging is less of a concern. However, the cost of either material is quite significant and steps must be taken to reduce the environmental hazard posed. This is particularly important for nanoparticles as they tend to be much more reactive than particles of the same material but larger in size (Zawadzki and Bogacki, 2016). Continuing advances in nanotechnology has prompted some authors, e.g.

(Rahmani et al., 2014), to pursue analysis of the use of magnetic markers for mapping hydraulic fractures using electromagnetic techniques.

Magnetic permeability of common materials tends to vary over an order of magnitude Telford et al. (1990a), while electrical conductivity of common materials can vary over > 8 orders of magnitude. Comparatively, there are many more materials that are electrically conductive than there are with a significant magnetic permeability. Materials such as coke breeze, a hardened graphite coating applied to conventional proppants, have been considered by numerous authors, as have a range of manufactured electrically conductive proppants (Pardo and Torres-Verdin, 2013; Hoversten et al., 2015; Weiss et al., 2015; Labrecque et al., 2016; Hu et al., 2018). For these reasons, we focus on electrically conductive proppants and treat the fractured region of the reservoir as an electrically conductive geophysical target.

2.0.2 Numerical Modelling

Numerical modelling is a critical component for assessing the feasibility of detecting a fractured volume of rock with an electromagnetic survey. To run a simulation, we need to discretize the modelling domain and represent the electrical conductivity of the earth on the simulation mesh. It is important to consider the large range of scales at play when considering fractures. The proppant which fills the fractures is micro-to-millimeters in diameter. The fractures are millimeters thick and we are aiming to characterize a region of the reservoir which extends hundreds of meters from the injection point at the well, tens to hundreds of meters in height, and tens of meters along the length of the well-bore. Furthermore, the numerical simulation domain must extend far enough to satisfy boundary conditions (typically that the fields have sufficiently decayed). This problem is exacerbated when one considers an inversion, where many forward simula-

tions must be performed. We cannot expect a method to be capable of imaging both such a substantial volume of the subsurface while also having the resolution on the scale of the proppant particles. Thus, we require a characterization of the bulk impact of the conductive proppant within a fractured volume of rock. How we construct such a bulk physical property model depends on the geometry and complexity of the induced fractures, for instance, different approaches should be considered if the fracture is a simple planar fracture versus a complex fracture network, as depicted in Figure ?? (c.f. Cipolla et al. (2008b)).

To overcome these challenges, there are several approaches that may be taken; the appropriate choice will depend upon both the fracture complexity and the purpose of the simulation. If the fine-scale geometry of the fractures is defined, for example in a feasibility study built from a synthetic fracture model, then numerical upscaling (Durlofsky, 2003; Caudillo-Mata et al., 2014; Caudillo-mata et al., 2016) or multiscale techniques (Haber, 2014b) can be employed. In general, though, the fine-scale fracture geometry is not known; only a handful of studies have “ground-truthed” the geometry of an induced fracture by mining the fractured region (Cipolla et al., 2008a). Furthermore, in an inversion, we cannot expect to resolve individual fractures, rather, we aim to characterize the bulk impact due to electrically conductive fractures in a conductive medium. To estimate a bulk conductivity, effective medium theory is one approach that can be taken (c.f. Torquato (2002); Milton (2002); Berryman and Hoversten (2013)). These methods assume that the composite material is composed of a collection of randomly distributed spheres or ellipsoids (which may be preferentially aligned). The estimated conductivity depends upon the conductivity of each of the materials, their shape, and volume in the composite material. Looking forward to the inverse problem, these methods have the added benefit that they provide a conduit for incorporating a-priori information such as

expected primary-fracture orientation, and volumes of proppant and fluid.

In this work, we adopt an effective medium theory approach. We take into account the conductivity of the host rock, the fracturing fluid and the proppant. The main simplifying assumption we employ is on the geometry of the fractures: we assume that they are composed of a collection of ellipsoidal cracks which may be preferentially or randomly aligned.

2.0.3 Chapter overview

The purpose of this chapter is twofold: (1) we develop a workflow for estimating the physical properties of a fractured volume of rock containing proppant and fluid that have distinct electromagnetic properties from the host and (2) we assess if, using a commercially available electromagnetic survey, we can detect the anomaly introduced by the fracture in the data. All of the computations shown in this chapter are open-source and available as Jupyter notebooks at: <https://github.com/simpeg-research/heagy-2018-fracture-physprops>.

2.1 Homogenization workflow using effective medium theory

In this approach, we treat the fractures as being composed of a collection of preferentially (or randomly) oriented ellipsoidal cracks and based on the density of cracks within a given volume of rock, construct an anisotropic description of the coarse-scale conductivity.

Effective medium approximations range from applying simple harmonic or arithmetic averaging of conductivity values, for example when constructing a representative voxel conductivity model from well-log measurements, to more involved analytic or

empirical relationships such as Archies law (Archie, 1942), which is commonly applied for estimating the conductivity of a fluid-filled rock. Although discovered empirically, the simplest version of Archies law is one example of a differential effective medium approximation which can be derived analytically. It assumes a background matrix, and uses an incremental approach to constructing a homogenized conductivity (c.f. Torquato (2002); Milton (2002)). However, for describing a fractured volume of rock, differential effective medium approximations are not appropriate as they assume that the rock-matrix is always connected (Torquato, 2002); in the composite material we are considering, a single computational voxel may be intersected by a fracture, meaning the rock matrix is not connected. The Maxwell-approximation (Maxwell, 1873) is yet another effective-medium approximation. It again makes a distinction between the background and the included phases, and assumes no interaction between inclusions.

We opt to consider self-consistent effective medium theory (SCEMT, also sometimes referred to as the Coherent Potential Approximation, CPS, or Bruggeman mixing). This is an effective medium approach which makes no distinction between background and included phases (e.g. see Torquato (2002)). Berryman and Hoversten (2013) similarly suggest using self-consistent effective medium theory for fractured rocks where the fractures are filled with fluid.

Milton (1985) demonstrated the physical realizability of SCEMT; he showed that SCEMT is asymptotically the exact solution for the effective conductivity for fractal-like composites that are self-similar at many scales. Physical realizability means that the estimates given by SCEMT will always be within the Hashin-Shtrikman bounds; at a minimum, this provides confidence that the conductivity estimates it provides are physically within a reasonable realm.

We construct the physical property model for a fractured volume of rock in two

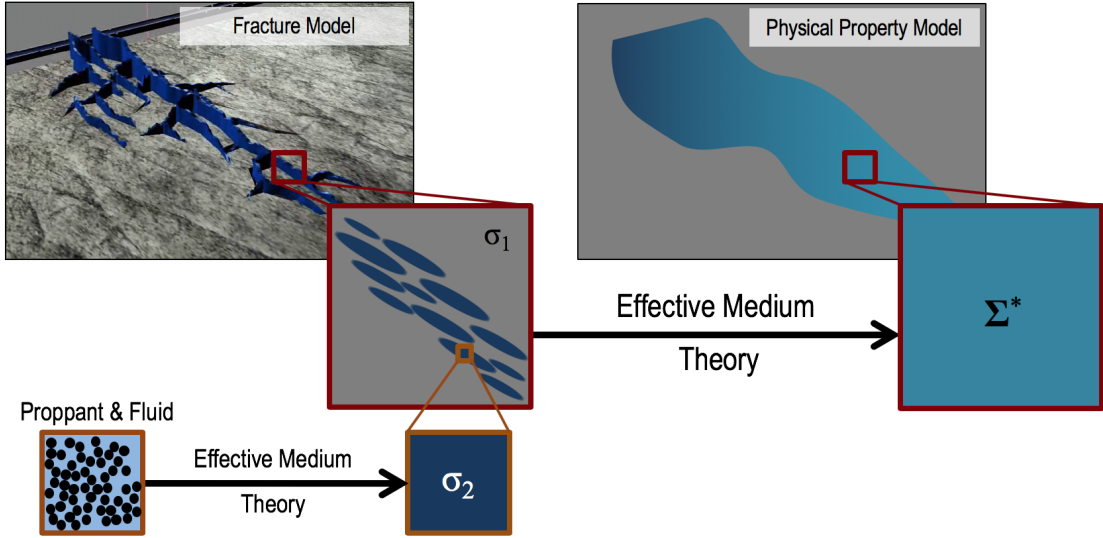


Figure 2.1: Constructing a physical property model for a fractured volume of rock using effective medium theory. The electrical conductivity of the proppant fluid mixture is given by σ_2 , the conductivity of the background reservoir rock by σ_1 . Using effective medium theory, the coarse-scale anisotropic conductivity, Σ^* describing the fractured volume of rock is computed.

steps, as shown in Figure 2.1. Given the conductivity of the fluid and proppant particles, we estimate the effective conductivity, σ_2 , of a mixture of proppant and fluid. Next, we treat the fracture as consisting of a collection of ellipsoidal cracks filled with the proppant-fluid mixture. The ellipsoidal cracks may be preferentially aligned in a single or multiple directions or they may be randomly oriented. In both cases, we use the self-consistent effective medium theory, originally due to Bruggeman (1935) and further developed by Landauer (1952, 1978). In the following sections, we develop the theory and demonstrate its application for computing the effective conductivity of a proppant-fluid mixture as well as a fractured volume of rock.

2.1.1 Summary of self-consistent effective medium theory

Chapter 18 of Torquato (2002) provides an overview of effective medium theory approaches, and the discussion presented in this section follows their presentation. Here, we discuss self-consistent effective medium theory. Berryman and Hoversten (2013) present a similar overview, introducing several simplifying assumptions tailored for estimating the effective conductivity of a naturally fractured rock where the fractures are a relatively small concentration with respect to the host rock. Here, we work with the general formulation with the aim of being suitable for calculating both the effective conductivity of a proppant-fluid mixture as well as arbitrarily oriented fractures, each at potentially high concentrations.

Each material, or phase, in the composite is assumed to be made up of spherical or ellipsoidal particles with a known aspect ratio. Starting from the solution for a sphere or an ellipsoid in a uniform electric field, the effective conductivity of a heterogeneous medium is chosen to be the conductivity for which the average perturbation to the electric field – the difference between the electric field in the homogenized medium and the true conductivity model – is zero. That is,

$$\sum_{j=1}^N \varphi_j (\Sigma^* - \sigma_j \mathbf{I}) \mathbf{R}^{(j,*)} = 0 \quad (2.1)$$

where N is the number of different phases of materials, φ_j is the volume fraction of the j -th phase, and σ_j is the electrical conductivity of the j -th phase. Σ^* is the 3×3 effective conductivity tensor, and \mathbf{I} is the 3×3 identity matrix. The matrix $\mathbf{R}^{(j,*)}$ is the electric field concentration tensor, and depends both on the shape of the inclusions (ie. proppant particles or cracks composing a fracture) and conductivity of the j -th phase, as well as the effective conductivity Σ^* .

For spherical particles, the electric field concentration tensor $\mathbf{R}^{(j,*)}$ reduces to a scalar, namely,

$$\mathbf{R}^{(j,*)} = \left[\mathbf{I} + \frac{1}{3} \Sigma^{*-1} (\sigma_j \mathbf{I} - \Sigma^*) \right]^{-1} \quad (2.2)$$

The resultant effective conductivity expression in 2.1 then reduces to a scalar equation.

If instead ellipsoidal inclusions are considered, the electric field concentration tensor is given by

$$\mathbf{R}^{(j,*)} = \left[\mathbf{I} + \mathbf{A} \Sigma^{*-1} (\sigma_j \mathbf{I} - \Sigma^*) \right]^{-1} \quad (2.3)$$

Where \mathbf{A} is the de-polarization tensor. For simplicity, we will assume that we are working with spheroids, either oblate (pancake-like) or prolate (needle-like) spheroids which have two semi-axes that are equal. The general solution for spheroids with three distinct semi-axes is presented in chapter 17 of Torquato (2002) and additionally discussed in Berryman and Hoversten (2013). For a spheroid with semi-axes $a_1 = a_2 = a$ and $a_3 = b$ that is aligned so that a_3 lies along the z-axis, the depolarization tensor is given by

$$\mathbf{A} = \begin{bmatrix} Q & & \\ & Q & \\ & & 1 - 2Q \end{bmatrix} \quad (2.4)$$

For prolate spheroids, with aspect ratio $\alpha = b/a > 1$, Q is given by

$$Q = \frac{1}{2} \left(1 + \frac{1}{\alpha^2 - 1} \left[1 - \frac{1}{2\chi_b} \ln \left(\frac{1 + \chi_b}{1 - \chi_b} \right) \right] \right) \quad (2.5)$$

and for oblate spheroids ($\alpha = b/a < 1$),

$$Q = \frac{1}{2} \left(1 + \frac{1}{\alpha^2 - 1} \left[1 - \frac{1}{\chi_a} \tan^{-1}(\chi_a) \right] \right) \quad (2.6)$$

with

$$\chi_a^2 = -\chi_b^2 = \frac{1}{\alpha^2} - 1 \quad (2.7)$$

For preferentially aligned spheroids, the matrix \mathbf{A} can be rotated as to align with the spheroidal axis using standard coordinate rotations. If the spheroids are randomly oriented, then we replace $\mathbf{R}^{(j,*)}$ with $1/3\text{trace}(\mathbf{R}^{(j,*)})$ in equation 2.1, and the effective conductivity expression reduces to a scalar equation. Note, that for spherical inclusions, $Q = 1/3$ and thus \mathbf{A} reduces to a scalar equal to $1/3$, showing that 2.3 is consistent with 2.2.

To solve for the effective conductivity, which is an implicit expression for Σ^* , we rearrange equation 2.1 to

$$\Sigma^* \sum_{j=0}^N \varphi_j \mathbf{R}^{(j,*)} = \sum_{j=0}^N \varphi_j \sigma_j \mathbf{R}^{(j,*)} \quad (2.8)$$

and solve

$$\Sigma^* = \sum_{j=0}^N \varphi_j \sigma_j \mathbf{R}^{(j,*)} \left(\sum_{j=0}^N \varphi_j \mathbf{R}^{(j,*)} \right)^{-1} \quad (2.9)$$

using fixed-point iteration as $\mathbf{R}^{(j,*)}$ depends on Σ^* . Note that the matrix inverse in 2.9 is a 3×3 matrix inverse and thus is cheap to explicitly compute. The fixed point iteration is performed until the recovered effective conductivity converges within a predefined tolerance.¹ In the following sections, we use this formulation to estimate the effective

¹Berryman and Hoversten (2013) similarly use a fixed-point iteration to solve for the effective conductivity, however in their formulation, they isolate Σ^* by pulling out the first term in the summation in 2.1, leading to an update of the form

$$\Sigma^* = \sigma_0 \mathbf{I} - \frac{1}{\varphi_0} \mathbf{R}^{(0,*)}^{-1} \sum_{j=1}^N \varphi_j (\Sigma^* - \sigma_j \mathbf{I}) \mathbf{R}^{(j,*)}$$

This is equivalent to equation 10 in Berryman and Hoversten (2013) with the simplifications that $\mathbf{R}^{(j,*)}$ is replaced by $\mathbf{R}^{(j,0)}$ under the assumption that the fractures compose a small volume fraction of the fractured rock. In practice, this approach is suitable for low concentrations of included phases, but can

conductivity of a range of proppant-fluid mixtures as well as for a fractured volume of rock.

2.1.2 Step 1: Effective conductivity of a proppant-fluid mixture

In general, an induced fracture will be filled with two types or phases of material: proppant and fluid. Often this mixture is referred to as a slurry. There are two principal types of mixtures we will consider, one where all of the proppant is conductive, and the second when there is a conductive filler added to a conventional proppant.

We start by considering the case of a proppant with uniform conductivity, for instance if a conductive proppant, or coated proppant were used. We assume the conductivity of the proppant particles is known; Appendix A includes a derivation for an effective conductivity of two concentric spheres for the scenario where the conductivity of a proppant particle and its coating are known independently.

For spherical proppant particles, the tensor-values in equation 2.1 reduces to a scalar-valued equation, and the resulting effective conductivity is isotropic. In Figure 2.2, we show the effective conductivity found using equations 2.1 and 2.2 for a proppant-fluid mixture as the concentration of proppant in the mixture (φ) is varied. The conductivity of the fluid is 3 S/m (similar to that of sea-water), and the proppant conductivity is varied logarithmically from 10 S/m to 10^5 S/m. For example, coke-breeze, a graphite based material has conductivities ~ 3000 S/m, and other authors have considered the use of contrast agents that reach conductivities of 10^5 S/m Weiss et al. (2015) and 10^6 S/m Pardo and Torres-Verdin (2013), which are similar to the conductivity of steel.

When the volume fraction of proppant is less than 1/3, the conductivity of the fluid

cause instability in the algorithm at higher concentrations (it is possible for updates to be negative, and therefore unphysical); the authors noted challenges with algorithm convergence when the concentration of inclusions exceeded 0.2.

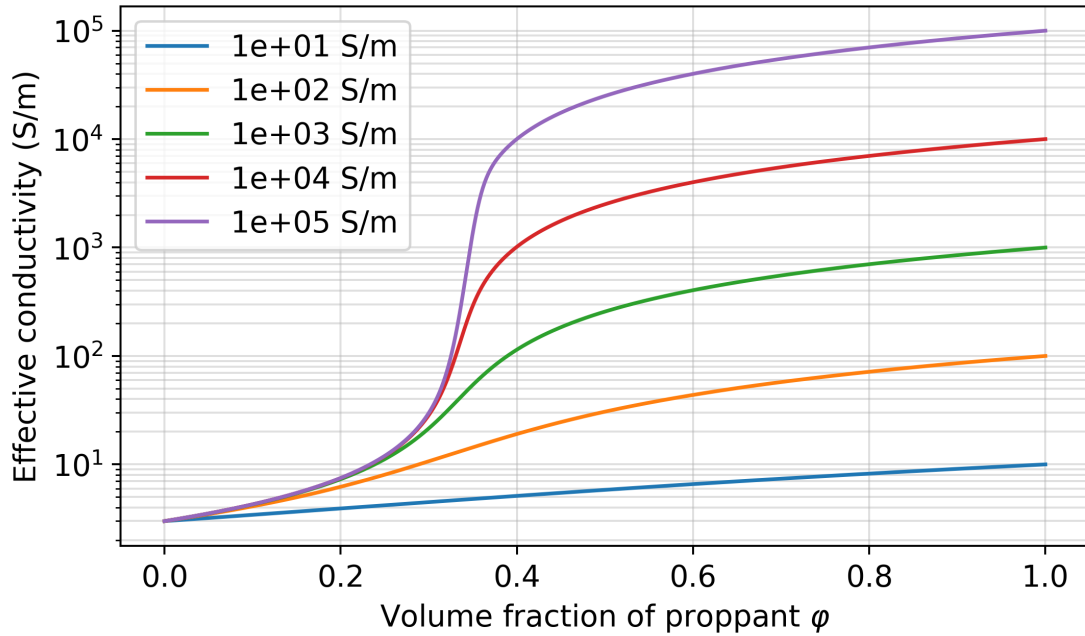


Figure 2.2: Effective conductivity of a proppant-fluid mixture for five different proppant conductivities, each indicated in the legend. The conductivity of the fluid is 3 S/m, similar to the conductivity of sea-water.

is the dominant control on the resulting effective conductivity. Above a volume fraction of 1/3, the conductivity of the proppant is the primary contributor to the effective conductivity. The threshold between these behaviors is the *percolation threshold*. Below it, the concentration of conductive material is low enough that it is quite likely disconnected, above 1/3, the concentration is high enough to start forming connected, electrically conductive pathways, causing a large jump in the effective conductivity of the system. Although proppant typically composes 10% to 20% of the injected slurry, some of the injected fluid leaks off into the surrounding geologic formation leaving proppant concentration that can be 50% in the fractures Novotny (1977); Hoversten et al. (2015).

The conductivity of the fluid also changes the resultant effective conductivity of the mixture. In Figure 2.3, we compare the effective conductivity for a mixture of con-

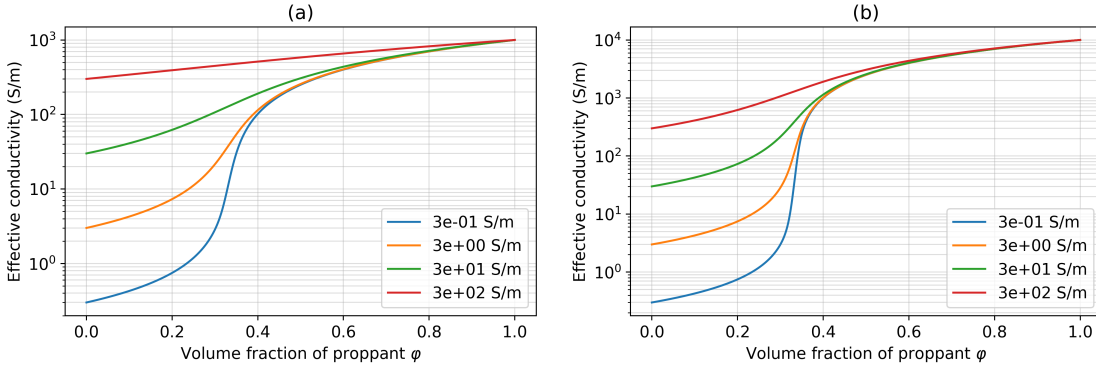


Figure 2.3: Impact of the conductivity of the fluid on the effective conductivity of a proppant-fluid mixture. Panel (a) shows the effective conductivity for mixtures with a 10^3 S/m proppant and panel (b) shows the effective conductivity for mixtures with a 10^4 S/m proppant. The conductivity of the fluid is indicated by the legend.

ductive proppant (panel (a): 10^3 S/m, panel (b): 10^4 S/m) and four different fluid conductivities, ranging from 0.3 S/m to 300 S/m, as indicated in the legend. Although the conductivity of the fluid makes a significant difference at low proppant concentrations, above the percolation threshold of 33%, the curves start to converge, particularly when the contrast between the conductivity of the proppant and the fluid exceeds 3 orders of magnitude. Thus, if the proppant can be made sufficiently conductive, its conductivity will be the controlling factor on the effective conductivity of the slurry that remains in the fractures.

The previous examples considered a 2-phase mixture in which all of the proppant was electrically conductive, however, depending on the setting and the cost to manufacture conductive proppant, it may be mixed in with conventional, resistive proppant. To examine this, we consider a proppant-fluid mixture composed of three materials, fluid (3 S/m), conventional, resistive proppant (10^{-6} S/m) and conductive proppant (10^5 S/m). The effective conductivities of proppant-fluid mixtures for five different proppant

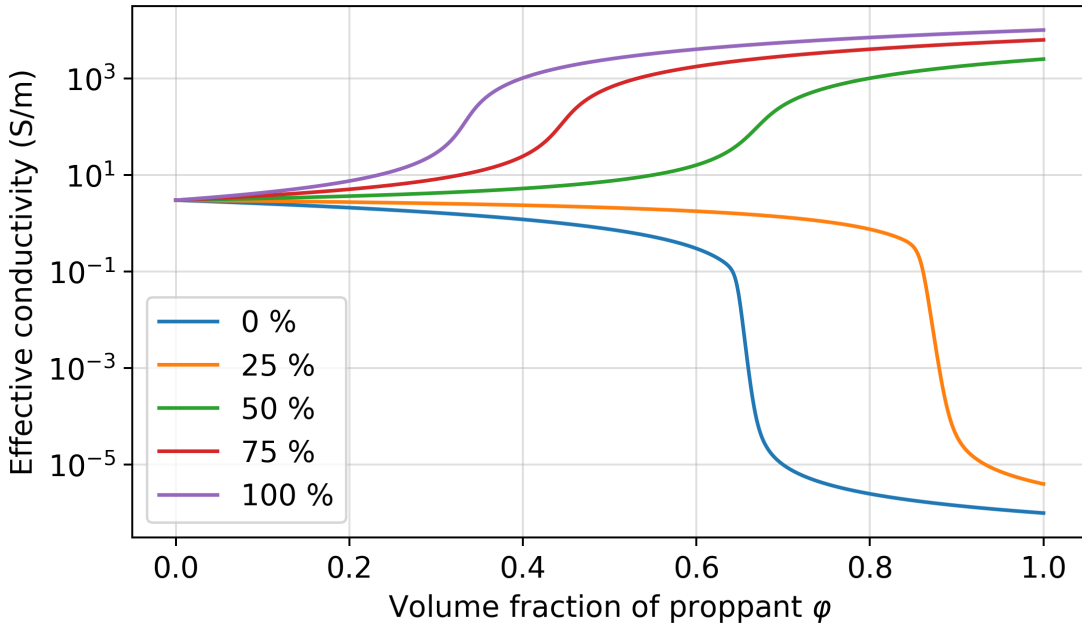


Figure 2.4: Effective conductivity of a 3-phase proppant-fluid mixture consisting of resistive proppant (10^{-6} S/m), conductive proppant (10^5 S/m) and saline fluid (3 S/m). The legend indicates the percentage of conductive proppant in the proppant mixture and the x-axis is the volume fraction of proppant in the proppant-fluid mixture.

blends, where the relative concentration of the conductive proppant is varied from 0% to 100% of the proppant phase, are shown in Figure 2.4. Again, we see the impacts of the percolation threshold; when the conductive proppant composes less than 1/3 of the proppant pack, the effective conductivity is dominated by the resistive proppant. When the conductive proppant composes more than 1/3 of the proppant pack, we see that with increasing proppant concentration, the effective conductivity of the mixture is dominated by the conductive proppant. However, the percolation threshold for each of these mixtures is different. This is because it is the volume-fraction of the conductive proppant in the three-phase mixture, not the ratio of proppant to fluid, that determines when connected, electrically conductive pathways may be formed.

Another factor influencing the effective conductivity of a mixture is the shape of the materials. For the previous examples, the proppant was assumed to be composed of spherical particles. If elongated, conductive particles were included, we expect that connected, conductive pathways would form at lower concentrations. For instance, consider a 3 phase proppant mixture consisting of fluid (3 S/m), resistive, spherical proppant (10^{-6} S/m), and elongated, electrically conductive proppant (10^5 S/m). Assume that the ratio of conductive to resistive proppant is 0.25 (below the percolation threshold for spherical particles). If the elongated particles (prolate spheroids) are randomly oriented, then the resulting effective conductivity is isotropic, meaning it is independent of the directions of the inducing field and resulting current. The conductivity predicted by effective medium theory for mixtures with five different aspect ratios is shown in figure 2.5. The aspect ratio of the conductive particles influences the concentration at which we observe percolation. The more elongated the particles, the lower the concentration at which percolation occurs.

In summary, there are several approaches that can be taken to create an electrically conductive proppant-fluid mixture. Spherical proppant particles which are themselves electrically conductive or coated with a conductive material can comprise the entire proppant pack. If conductive proppant is mixed with a conventional, resistive sand or ceramic particles, then at least 1/3 of the proppant mixture needs to be comprised of electrically conductive particles to create a conductive mixture. This ratio can be reduced if elongated particles, such as metallic strips, are used in the proppant mixture.

2.1.3 Step 2: Effective conductivity of fractured volume of rock

The next step is to estimate the effective conductivity of a fractured volume of rock. We again employ self-consistent effective medium theory as described in section 2.1.1

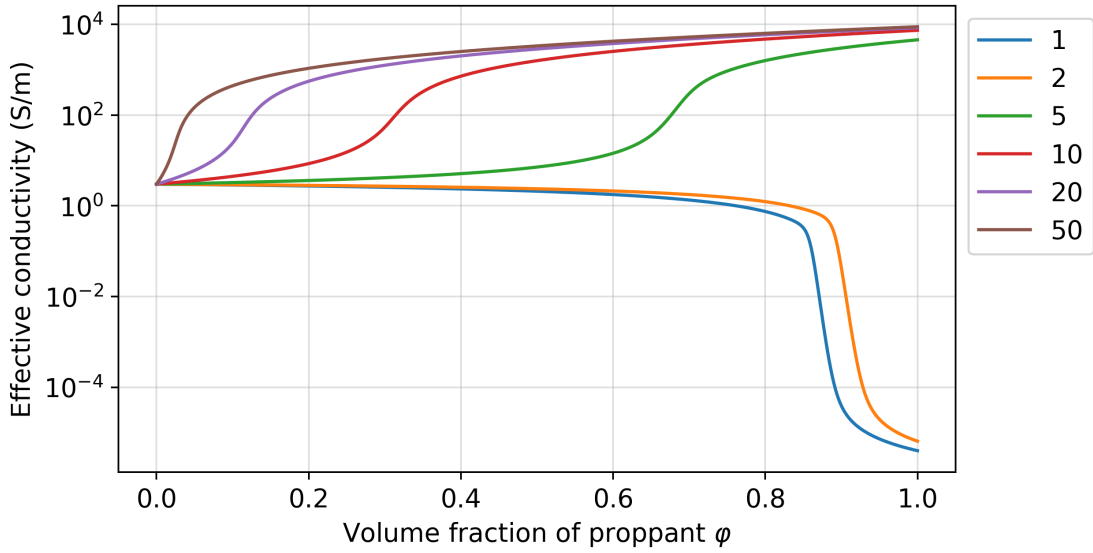


Figure 2.5: Effective conductivity of a 3-phase proppant-fluid mixture consisting of resistive proppant (10^{-6} S/m), conductive proppant (10^5 S/m) and saline fluid (3 S/m). The proppant mixture contains 25% conductive proppant and 75% resistive proppant. The legend indicates the aspect ratio of the elongated conductive proppant filler (prolate spheroids).

and consider the induced fractures to be composed of spheroidal cracks. Based on the analysis in the previous section, we consider a proppant-fluid mixture that has a conductivity of 2500 S/m. This could be achieved with spherical proppant particles having a conductivity of 10^4 S/m in a 50/50 mixture with water of 3 S/m (see Figure 2.2). Similar conductivities could be achieved with elongated particles mixed with conventional proppant as shown in Figure 2.5. Lab measurements conducted by Zhang et al. (2016) showed that a proppant-fluid mixture composed of petroleum coke particles and seawater which fills the pore-spaces reached a conductivity of ~ 1000 S/m at 37.6% porosity. With further increase in confining pressure (thus reducing porosity and increasing the concentration of proppant), the observed conductivities range from 3000 – 5000 S/m. These results provide further confidence that conductivities > 1000 S/m for the mixture

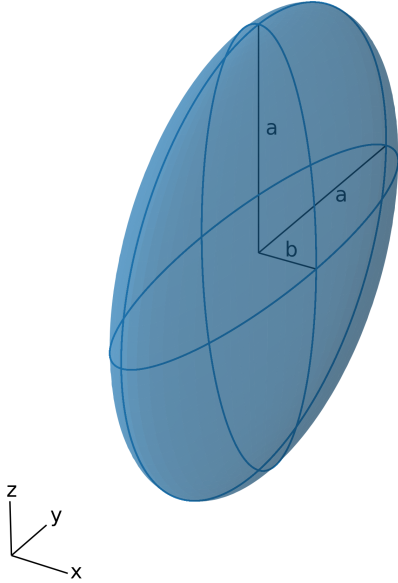


Figure 2.6: Oblate spheroid with normal along the x -axis. The y and z semi-axes are equal, and aspect ratio is $\alpha = b/a < 1$.

filling the hydraulic fractures are attainable.

For the following example, we will assume that the conductivity of the host-rock is 0.1 S/m. There are two scenarios we will consider, in the first, we assume the cracks are preferentially aligned, with the thin dimension of the oblate spheroid oriented along the x -axis, as shown in Figure 2.6. In this case, the recovered effective conductivity will be anisotropic, described by a diagonal matrix with entries $\sigma_y = \sigma_z \geq \sigma_x$:

$$\Sigma^* = \begin{bmatrix} \sigma_x & & \\ & \sigma_y & \\ & & \sigma_z \end{bmatrix} \quad (2.10)$$

Note that arbitrary, non-axes aligned, orientations can be considered; all that is required is that the depolarization tensor described in 2.4 is rotated to the desired orientation.

To estimate the effective conductivity of a fractured volume of rock, we must also specify the aspect ratio of the cracks. In estimating this, assume a fractal-like approximation, where the aspect ratio of the fracture is representative of the aspect ratio of the cracks that compose it. For example, if the fracture extends 50m laterally and has a width on the order of millimeters, then the aspect ratio is on the order of 10^{-5} . In Figure 2.7, we have plotted the diagonal elements of the effective conductivity for five different aspect ratios, indicated in the legend, as a function of the volume fraction of conductive fractures in the rock volume sampled. Panel (a) shows the full range from $0 \leq \varphi \leq 1$ and panel (b) zooms in to lower concentrations ($0 \leq \varphi \leq 0.01$) which are more representative of a fractured rock volume, on the scale that we will consider for numerical modelling (e.g. if 10 fractures, each with 3mm width intersect a $10\text{m} \times 10\text{m} \times 10\text{m}$ cell, then $\varphi = 0.003$). In each of the plots, we have also included the upper and lower Wiener bounds (see equation 21.14 in Torquato (2002); originally attributed to Wiener (1912)):

$$\begin{aligned}\sigma_{\text{W}}^+ &= \sum_{j=0}^N \varphi_j \sigma_j \\ \sigma_{\text{W}}^- &= \left(\sum_{j=0}^N \frac{\varphi_j}{\sigma_j} \right)^{-1}\end{aligned}\tag{2.11}$$

in the black dashed lines; these can be understood as similar to parallel and series circuit approximations to the conductivity. In the black dash-dot lines are the upper and lower Hashin-Shtrikman bounds for 2-phase anisotropic media in the black dash-dot (see equations 21.25 and 21.26 in Torquato (2002), which is the anisotropic generalization of the

isotropic bounds derived by Hashin and Shtrikman (1962)):

$$\begin{aligned}\sigma_{\text{HS}}^+ &= \sigma_W^+ \mathbf{I} + (\sigma_1 - \sigma_0)^2 \tilde{\mathbf{A}} \cdot \left[\sigma_1 \mathbf{I} + \frac{\sigma_1 - \sigma_0}{\varphi_0} \tilde{\mathbf{A}} \right]^{-1} \\ \sigma_{\text{HS}}^- &= \sigma_W^+ \mathbf{I} + (\sigma_1 - \sigma_0)^2 \tilde{\mathbf{A}} \cdot \left[\sigma_0 \mathbf{I} + \frac{\sigma_0 - \sigma_1}{\varphi_1} \tilde{\mathbf{A}} \right]^{-1}\end{aligned}\quad (2.12)$$

For $\sigma_1 \geq \sigma_0$ and

$$\tilde{\mathbf{A}} = -\varphi_0 \varphi_1 \mathbf{A}_1 \quad (2.13)$$

where \mathbf{A}_1 is the depolarization tensor for the ellipsoidal cracks given by equation 2.4. For the bounds shown in the plot, the smallest aspect ratio, 10^{-5} was used to calculate the depolarization tensor. For the very significant aspect ratios used here, the Hashin-Shtrikman bounds are nearly identical to the Wiener bounds. Each component of the recovered effective conductivity should fall within these bounds.

For aspect ratios less than 10^{-3} , we see very little distinction between the estimate of $\sigma_{y,z}$ and σ_x ; the difference between the recovered effective conductivities for the aspect ratios of 10^{-4} and 10^{-5} is less than 1% for all values of φ . This indicates that for sufficiently thin cracks, the exact aspect ratio is not critical for estimating a representative conductivity of the fractured rock.

At the concentrations we expect to be observing in a hydraulic fracturing scenario (Figure 2.7b), we see that the effective conductivity along the normal of the fractures coincides with the lower bounds and remains nearly identical to the conductivity of the host rock for all aspect ratios shown, as may be expected. For the components of the conductivity along the cracks ($\sigma_{y,z}$), the effective conductivity mimics the behavior of the upper bounds. These components of the conductivity are similar to the behavior expected from a parallel-circuit approximation.

For settings where planar fractures are expected, an single orientation of the inclu-

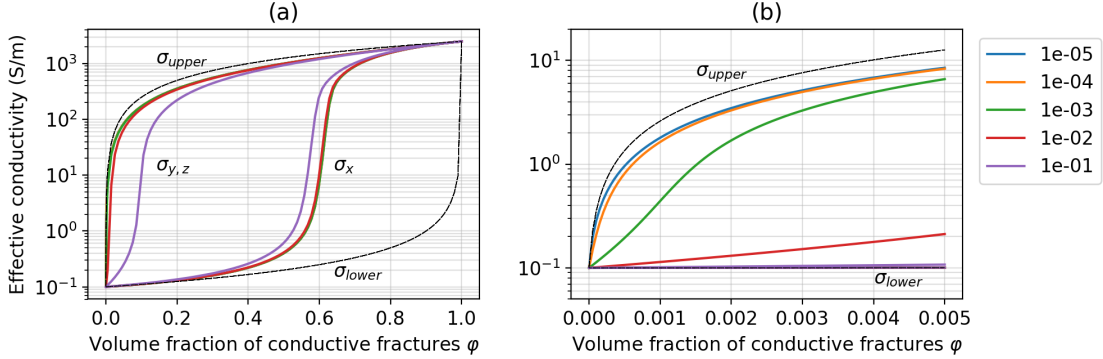


Figure 2.7: Effective, anisotropic conductivity for a fractured rock with spheroidal cracks whose normal is oriented along the y-axis for five different aspect ratios, indicated by the legend. The black dashed lines show the upper and lower Wiener Bounds, which are identical the volume-weighted arithmetic and harmonic averages of the conductivity of the rock (0.1 S/m) and proppant-fluid mixture (2500 S/m). The black dash-dot lines are the anisotropic Hashin-Shtrikman upper and lower bounds computed using an aspect ratio of 10^{-5} in equation 2.12. Panel (a) shows the full range $0 \leq \varphi \leq 1$, and panel (b) zooms in to $0 \leq \varphi \leq 0.005$. Note that in (b), any curve that deviates from the lower bound is the $\sigma_{x,z}$ component; all σ_x values lie on the lower bound for the concentration range shown.

sions produces similar behavior to what would be expected if we performed simple series-and-parallel circuit approximations to the components perpendicular to and along the fracture. However, if more complex fracture networks are expected, it may be more appropriate to assume the cracks are randomly oriented. In this case, an isotropic conductivity describes the fractured volume of rock. Using the same aspect ratios shown in Figure 2.7 above, we compute the isotropic effective conductivity as a function volume fraction of fractures in Figure 2.8. For reference, the conductivity along the fractures, $\sigma_{y,z}$ from Figure 2.7, is plotted in semi-transparent lines. As in the previous Figure, panel (a) shows the full range from $0 \leq \varphi \leq 1$ and panel (b) zooms in to lower concentrations: $0 \leq \varphi \leq 0.01$.

Again, we see that for aspect ratios smaller than 10^{-3} there is little difference be-

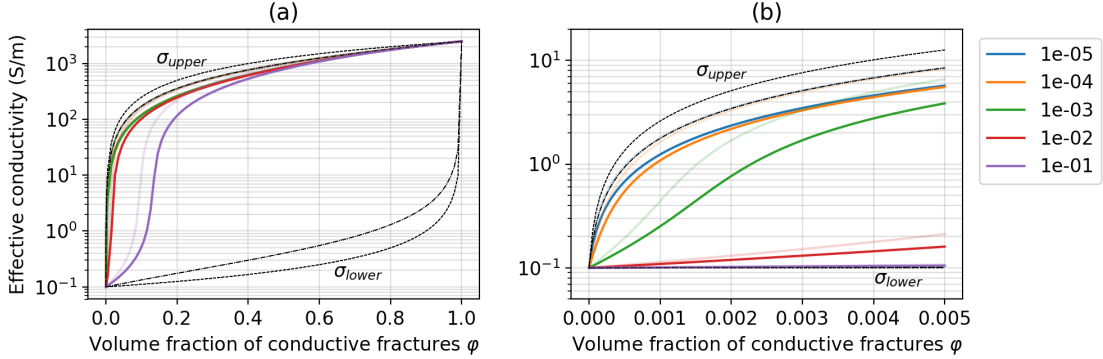


Figure 2.8: Effective, isotropic conductivity for a fractured rock with randomly oriented spheroidal cracks for five different aspect ratios, indicated by the legend. The black dashed lines show the upper and lower Wiener Bounds, which are identical the volume-weighted arithmetic and harmonic averages of the conductivity of the rock (0.1 S/m) and proppant-fluid mixture (2500 S/m). The black dash-dot lines are the isotropic Hashin-Shtrikman upper and lower bounds. The semi-transparent dotted lines show $\sigma_{x,z}$ from Figure 2.7. Panel (a) shows the full range $0 \leq \varphi \leq 1$, and panel (b) zooms in to $0 \leq \varphi \leq 0.01$.

tween the estimated effective conductivity of the fractured rock volume. The estimate of the effective conductivity largely follows the behavior of the upper bounds, while the magnitude of the effective conductivity is slightly reduced as compared to the component of the conductivity along the fractures in the anisotropic case. If we consider a $10m \times 10m \times 10m$ computational cell with fractures having an aspect ratio of 10^{-5} and composing 0.3% of the total volume (e.g. 10 fractures, each with 3mm width), we obtain $\sigma_x = \sigma_z = 5.2$ S/m, $\sigma_y = 0.1$ S/m for the case where the cracks are preferentially aligned while for the case where the cracks are randomly oriented, we obtain $\sigma^* = 3.5$ S/m.

Due to the large contrast between the conductive fractures and the host rock, the conductivity of the background has marginal effect on $\sigma_{x,z}$ in the anisotropic example or on σ^* . If we consider the example with $\varphi = 0.003$, as before, and instead use a

background conductivity of 0.01 S/m, the effective anisotropic conductivity is $\sigma_x = \sigma_z = 5.1$ S/m, $\sigma_y = 0.01$ S/m and for the isotropic case $\sigma^* = 3.4$ S/m. However, if the background is made more conductive and the contrast between the conductive fractures and the host reduced, we do see some impact. Setting the background to 1 S/m for this same example, we obtain $\sigma_x = \sigma_z = 6.4$ S/m, $\sigma_y = 1$ S/m for the anisotropic case and $\sigma^* = 4.7$ S/m for the isotropic case.

2.1.4 Summary

To construct an approximate conductivity model of a fractured volume of rock, we use a two step process: first, we estimate the effective conductivity of a mixture of proppant and fluid that fills the fractures and second, we estimate the effective conductivity of a fractured volume of rock.

In the section that follows, we will compare numerical simulations of a crosswell electromagnetic survey for both anisotropic and isotropic conductivity models of a fractured volume of rock, representing planar and complex fracture networks, respectively.

2.2 Feasibility of EM for detecting fractures

With the capability to estimate a physical property model of a fractured volume of rock, we now examine the feasibility of detecting a conductive, fractured region of a reservoir with an electromagnetic survey. The purpose of this section is to demonstrate detectability for a simple model of a fracture with existing electromagnetic imaging techniques. The survey we consider is a frequency-domain crosswell electromagnetic survey. In a crosswell EM survey a transmitter coil, which produces a time-varying magnetic field at a single frequency is positioned inside of one well. Time-varying magnetic fields induce time-varying currents in the earth whose distribution and magnitude depends upon the

conductivity of the earth. These currents in turn generate secondary magnetic fields. In a second well, an array of receiver induction coils, which measure the time rate-of-change of the magnetic field (db/dt , in units of volts), are positioned. The measured voltages can be converted to magnetic field values. To conduct a survey, the position of the receivers is fixed and the transmitter is moved at a fixed rate along the borehole (typically 3-5 meters per minute). The receivers are repositioned, and the process repeated (Wilt et al., 1995). Both the transmitter and receivers are oriented along the axis of the borehole; for vertical wells, this means the transmitter is a vertical magnetic dipole, and the receivers measure the z-component of the magnetic field. Since its development, crosswell surveys have been used for a range of reservoir imaging problems for enhanced oil recovery including monitoring steam injections (Wilt et al., 1997) and water floods (Wilt et al., 2012), including a survey conducted in a pair of horizontal wells (Marsala et al., 2015; Marsala* et al., 2015). In this section, we consider a crosswell survey and examine the feasibility of detecting signal due to a fractured volume of rock.

The setup we consider is shown in Figure 2.9; a crosswell EM survey conducted in a pair of horizontal wells that are spaced 500m apart, as shown in Figure 2.9. The transmitter is oriented along the x-axis and positioned in the same well as where the fracture stimulation was performed; the receivers are in the offset well and measure the real and imaginary parts of the x-component of the magnetic field. In the numerical modelling, we assume that the wells are sufficiently deep so that the background can be treated as a whole-space. We do not consider steel-cased boreholes in this example and instead assume that the boreholes are open-holes or cased with fibreglass casing as in Wilt et al. (2012). The additional complications due to steel cased wells will be discussed in the following three chapters.

Most hydraulic fracture operations involve injecting $\sim 800\text{m}^3$ to 4000 m^3 (5000 to

25000 bbls) of proppant-fluid slurry into the reservoir rock, with the proppant comprising 10% to 20% of this mixture (Hoversten et al., 2015). In this example, we consider a fracture that is on the lower-end, with an 800m^3 slurry comprised of 15% proppant by volume. A significant portion of the fluid typically leaks off into the surrounding formation (Novotny, 1977), so we will assume that the final mixture filling the cracks contains 50% fluid and 50% proppant. This gives a total fracture volume of 240 m^3 . To distribute this volume, we assume that 10 fractures, each with 3mm width are positioned within a 10m interval along the well. Conserving volume and assuming circular fractures gives us a 50 m radius for each of the 10 fractures; we work with circular fractures as the resultant model is cylindrically symmetric, which significantly reduces the computational cost of the simulation.

For the physical properties, we treat the background as a whole-space with a conductivity of 0.1 S/m. Within the fractures, we use a two-phase proppant-fluid mixture, where all of the proppant is assumed to be spherical particles as in Figure 2.2. We use a proppant conductivity of 10^4 S/m and a fluid conductivity of 3 S/m; in a 50-50 mixture, the effective conductivity computed using SCEMT, is 2500 S/m. To estimate the effective conductivity of the fractured volume of rock, we consider two scenarios: (1) the fractures are preferentially aligned and we estimate an anisotropic effective conductivity as in Figure 2.7; and (2) the fractures are sufficiently complex that we can approximate them as a collection of randomly oriented cracks, as in Figure 2.8. We estimate a single conductivity for the 10m wide cylinder with 50m radius that encloses the fractures. Within this region, the fractures comprise 0.3% of the total volume. To estimate the aspect ratio, we assume that the shape of the large fracture, with 3mm width and 50m radius (100m diameter) is representative of the shape of the cracks that comprise it, thus the aspect ratio is 3×10^{-5} . The estimated effective conductivity for the anisotropic case

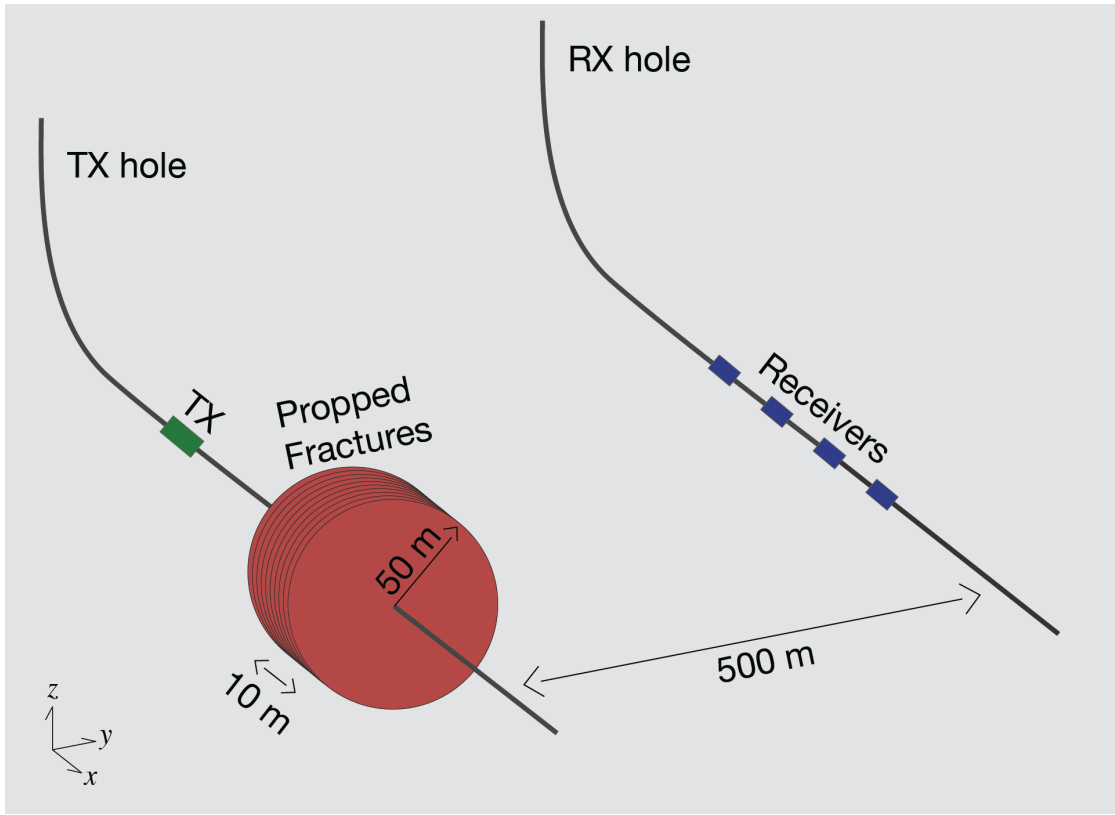


Figure 2.9: Setup for the crosswell electromagnetic simulation. Ten fractures, each with 3mm thickness and 50m radius are spaced over a 10m interval along the injection well. The dipole transmitter is positioned inside of the injection well and oriented along the x-axis. Receivers are located in an offset well and measure the real and imaginary parts of the x-component of the magnetic field.

is $\sigma_y = \sigma_z = 5$ S/m parallel to the fractures and $\sigma_x = 0.1$ S/m perpendicular to the fractures. For the second scenario, with randomly oriented cracks, the estimated isotropic conductivity is 3 S/m.

In terms of survey parameters, the dipole-moment of the transmitter is 5000 Am² and we use a transmitter frequency of 100Hz, consistent with values stated in Wilt et al. (1995); Wilt (2003). For a signal to be detectable, we require that: (a) the secondary signal, that is, the difference between the data measured with and without the fractures

present, be above the noise floor of the receivers, and (b) that the secondary signal comprises a significant percentage of the primary (model without the fractures). Marsala* et al. (2015) demonstrated noise levels of 0.5×10^{-5} nT and 0.5% repeatability between data profiles for a cross-well survey conducted between two open-hole horizontal wells, citing that “this was the lowest noise ever recorded with a crosswell EM system.” Using this as an upper-bound on our expectations, we adopt a more conservative noise level of 1×10^{-4} nT and select a percent-threshold of 5%. Thus, we consider signal above 1×10^{-4} nT and comprising $> 5\%$ of the primary as detectable.

Figure 2.10 shows the simulated secondary magnetic field data computed for (a) the anisotropic model and (b) the isotropic model at 100 Hz. The top row shows the real component and the bottom row shows the imaginary component. The x-axis shows the transmitter location relative to the center of the fracture, the y-axis shows the receiver location, and the color indicates the secondary magnetic field with respect to a 0.1 S/m whole-space. Regions of the plot which are colored, and are not covered by the semi-transparent overlay, indicate signal which is both above the noise floor and comprises a significant percentage of the primary.

As might be expected, when the transmitter and receiver are centered with the fracture, the secondary signal reaches its maximum amplitude in both the real and imaginary components. The anisotropic model produces stronger signals; the geometry of the survey is perfectly coupled to the radial components of the conductivity (σ_y and σ_z) as the resultant currents and electric fields are purely azimuthal in orientation. An isotropic simulation using $\sigma = 5$ S/m produces identical results to the anisotropic model for this survey geometry. Interestingly, the region over which data is measurable differs between the real and imaginary components. The real component is measurable over a larger range of transmitter positions, while the imaginary component is measurable

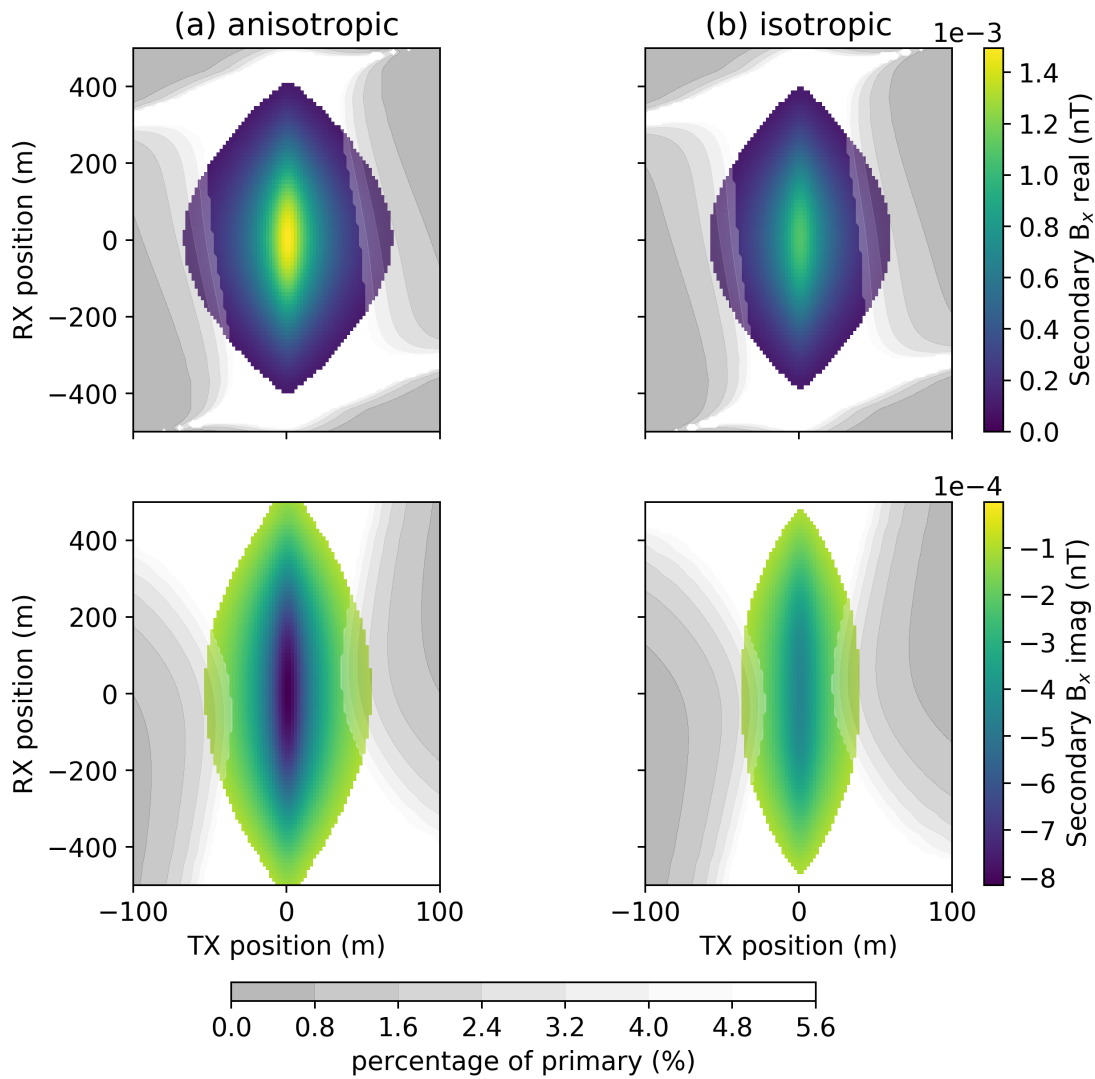


Figure 2.10: Simulated secondary magnetic field data for: (a) the anisotropic fracture model and (b) the isotropic fracture model, in a crosswell survey conducted at 100Hz. The top row shows the real component and the bottom row shows the imaginary component of the measured magnetic flux (nT). In all plots, the x-axis shows the transmitter location relative to the center of the fracture, the y-axis shows the receiver location, and the color indicates the secondary magnetic flux with respect to a 0.1 S/m whole-space. Values beneath the noise floor of 10^{-4} nT have been masked and display as white. To display the signal as a percentage of the primary, we have included a semi-transparent overlay between 0% and 5%; low percentage values plot as darker greys.

over a larger range of receiver locations. The partition of EM energy into the real and imaginary components is a function of the conductivity of the medium as well as the frequency. For example, if we increase the frequency to 200 Hz, the amplitude of the imaginary component is larger than the real, and it is measurable over a larger set of source-receiver combinations, as shown in Figure 2.11.

For the simple setup shown here, there are a significant number of data that can be collected in a cross-well survey which are sensitive to both the anisotropic and isotropic fracture models. In both the 100 Hz and 200 Hz surveys, the extent over which either or both of the real and imaginary components of the data are above the noise floor and comprise a significant percentage of the primary field spanned 100m for the transmitter location and > 800m for the receiver locations. These results provide confidence that EM is a potentially diagnostic tool for characterizing the propped region of a reservoir. Naturally, the success, or not, of EM in a given setting will depend upon the background conductivity, volume and conductivity of the proppant and fluid, as well as noise conditions in the field. Thus, forward modelling tailored to the setting is required to assess feasibility.

2.3 Conclusion

The large range of scales involved in describing a propped, fractured volume of rock as a geophysical target for an electromagnetic survey poses a challenge for performing numerical simulations. We approached this problem by using effective medium theory to estimate the electrical conductivity of a fracture volume of rock in two steps. First, we estimated the conductivity of a slurry containing proppant and fluid. We demonstrated several approaches for creating an electrically conductive slurry, including using conductive particles (or particles coated with a conductive material) as the proppant or

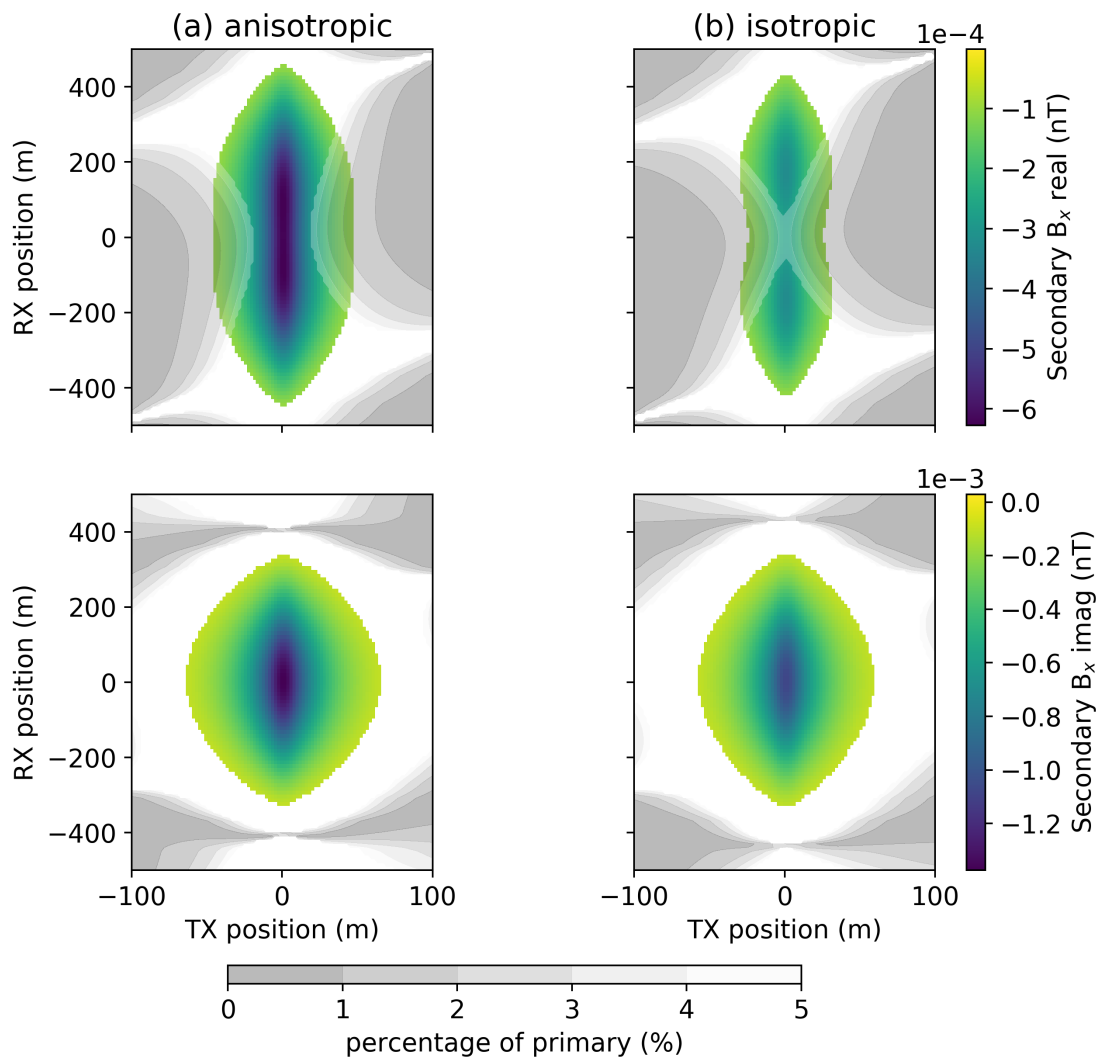


Figure 2.11: Simulated secondary magnetic field data for: (a) the anisotropic fracture model and (b) the isotropic fracture model, in a crosswell survey conducted at 200Hz. The top row shows the real component and the bottom row shows the imaginary component of the measured magnetic flux (nT), similar to Figure 2.10

including conductive particles, which might be elongated to enhance the conductivity at lower concentrations. General agreement with the values published in the laboratory experiment by Zhang et al. (2016) gives confidence that the estimates produced using effective medium theory are representative of the conductivities that can be achieved; a more rigorous comparison would require control on the conductivity of each of the constituents. In the second step, we estimated the effective conductivity of a fractured volume of rock by assuming that the fracture is composed of a collection of ellipsoidal cracks. These cracks may be preferentially oriented, if simple planar fractures are expected, or randomly oriented if a more complex fracture network is anticipated.

Using this approach, we developed isotropic and anisotropic electrical conductivity models considering proppant and fluid volumes that are representative of current hydraulic fracture operations and simulated a crosswell EM survey. In this example, the fractured volume was detectable if we assume noise estimates that have demonstrated to be achievable in horizontal wells for a waterflood monitoring experiment. This provides evidence that EM has the potential to be a suitable method for characterizing the propped region of a hydraulically fractured reservoir.

The examples examined here neglect the effects of steel-cased well on EM signals. In the vast majority of settings where hydraulic fracturing is conducted, the wells are cased with steel, and therefore, this complication needs to be addressed. For induction problems, the concern is attenuation of the electromagnetic signals, as eddy currents may be induced in the steel cased well. However, there is increasing interest in using the steel casing as an “extended electrode” to help deliver current to depth. In the following chapters, we develop a strategy for including steel cased wells in the EM numerical simulations and examine their influence on EM signals.

Chapter 3

Modelling electromagnetics on cylindrical meshes with applications to steel-cased wells

3.1 Introduction

A number of geophysical electromagnetic (EM) problems lend themselves to cylindrical geometries. Airborne EM problems over a 1D layered earth or borehole-logging applications fall into this category; in these cases cylindrical modelling, which removes a degree of freedom in the azimuthal component, can be advantageous as it reduces the computation load. This is useful when running an inversion where many forward modellings are required, and it is also valuable when exploring and building up an understanding of the behaviour of electromagnetic fields and fluxes in a variety of settings, such as the canonical model of an airborne EM sounding over a sphere, as it reduces feedback time between asking a question and visualizing results (e.g. Oldenburg et al.

(2017)).

Beyond these simple settings, there are also a range of scenarios where the footprint of the survey is primarily cylindrical, but 2D or 3D variations in the physical property model may be present. For example if we consider a single sounding in an Airborne EM survey, the primary electric fields are rotational and the magnetic fields are poloidal, but the physical property model may have lateral variations or compact targets. More flexibility is required from the discretization to capture these features. In this case, a 3D cylindrical geometry, which incorporates azimuthal discretization may be advantageous. It allows finer discretization near the source where we have the most sensitivity and the fields are changing rapidly. Far from the source, the discretization is coarser, but it still conforms to the primary behaviour of the EM fields and fluxes and captures the rotational electric fields and poloidal magnetic flux.

In other cases, the most significant physical property variations may conform to a cylindrical geometry, for example in settings where vertical metallic well-casings are present, or in the emerging topic of using geophysics to “look ahead” of a tunnel boring machine. In particular, understanding the behavior of electromagnetic fields and fluxes in the presence of steel-cased wells is of interest across a range of applications, from characterizing lithologic units with well-logs (Kaufman, 1990; Kaufman and Wightman, 1993; Augustin et al., 1989), to identifying marine hydrocarbon targets (Kong et al., 2009; Swidinsky et al., 2013; Tietze et al., 2015), to mapping changes in a reservoir induced by hydraulic fracturing or carbon capture and storage (Pardo and Torres-Verdin, 2013; Börner et al., 2015; Um et al., 2015; Weiss et al., 2016; Hoversten et al., 2017; Zhang et al., 2018). Carbon steel, a material commonly used for borehole casings, is highly electrically conductive ($10^6 – 10^7$ S/m) and has a significant magnetic permeability ($\geq 100 \mu_0$) (Wu and Habashy, 1994); it therefore can have a significant

influence on electromagnetic signals. The large contrasts in physical properties between the casing and the geologic features of interest, along with the large range of scales that need to be considered to model both the millimeter-thick casing walls while also capturing geologic features, provide interesting challenges and context for electromagnetics in cylindrical geometries. As such, we will use EM simulations of conductive, permeable boreholes as motivation throughout this paper.

In much of the early literature, the casing was viewed as a nuisance which distorts the EM signals of interest. Distortion of surface direct current (DC) resistivity and induced polarization (IP) data, primarily in hydrocarbon settings, was examined in (Wait, 1983; Holladay and West, 1984; Johnston et al., 1987) and later extended to grounded source EM and IP in (Wait and Williams, 1985; Williams and Wait, 1985; Johnston et al., 1992). Also in hydrocarbon applications, well-logging in the presence of steel cased boreholes is motivation for examining the behavior of electromagnetic fields and fluxes in the vicinity of casing. Initial work focussed on DC resistivity with (Kaufman, 1990; Schenkel and Morrison, 1990; Kaufman and Wightman, 1993; Schenkel and Morrison, 1994), and inductive source frequency domain experiments with (Augustin et al., 1989). Kaufman (1990) derives an analytical solution for the electric field at DC in an experiment where an electrode is positioned along the axis of an infinite-length well. The mathematical solutions presented shows how, and under what conditions, horizontal currents leak into the formation outside the well. Moreover, Kaufman (1990) showed, based upon asymptotic analysis, which fields to measure inside the well so that information about the formation resistivity could be obtained. This analysis is extended to include finite-length wells in Kaufman and Wightman (1993). Schenkel and Morrison (1994) show the importance of considering the length of the casing in borehole resistivity measurements, and demonstrate the feasibility of cross-well DC resistivity. They

also show that the presence of a steel casing can improve sensitivity to a target adjacent to the well. In frequency domain EM, Augustin et al. (1989) consider a loop-loop experiment, where a large loop is positioned on the surface of the earth and a magnetic field receiver is within the borehole. Magnetic permeability is included in the analysis and a “casing correction”, effectively a filter due to the casing on inductive-source data, is introduced. This work was built upon for considering cross-well frequency domain EM experiments (Uchida et al., 1991; Wilt et al., 1996).

For larger scale geophysical surveys, steel cased wells have been used as “extended electrodes.” Rocroi and Koulikov (1985) used a pair of well casings as current electrodes for reservoir characterization in hydrocarbon applications. In near-surface settings (Ramirez et al., 1996; Rucker et al., 2010; Rucker, 2012) considered the use of monitoring wells as current and potential electrodes for a DC experiment aimed at imaging nuclear waste beneath a leaking storage tank. Similarly, ? considers the use of groundwater wells for monitoring a saltwater intrusion and investigates numerical strategies for simulating casings as long electrodes. Imaging hydraulic fractures has been a motivator for a number of studies at DC or EM, among them Weiss et al. (2016); Hoversten et al. (2017). Some of these have suggested the use of casings that include resistive gaps so that currents may be injected in a segment of the well and potentials measured across the other gaps along the well (Nekut, 1995; Zhang et al., 2018). There has also been a rise in interest in modelling casings for casing integrity applications where the aim of the DC or EM survey is to diagnose if a well is flawed or intact based on data collected on the surface (Wilt et al., 2018).

As computing resources increased, our ability to forward-simulate more complex scenarios has improved. However, the large physical property contrasts and disparate length scales introduced when a steel cased well is included in a model still present

computational challenges. Even the DC problem, which is relatively computationally light, has posed challenges; those are exacerbated when solving the full Maxwell equations in the frequency (FDEM) or time domain (TDEM) and can become crippling for an inversion. For models where the source and borehole are axisymmetric, cylindrical symmetry may be exploited to reduce the dimensionality, and thus the number of unknowns, in the problem (e.g. Pardo and Torres-Verdin (2013); Heagy et al. (2015)).

To reduce computational load in a 3D simulation, a number of authors have employed simplifying assumptions. Several authors replaced the steel-cased well with a solid borehole, either with the same conductivity as the hollow-cased well (e.g. Um et al. (2015); Puzyrev et al. (2017)) or preserving the cross sectional conductance (e.g. Swidinsky et al. (2013); Kohnke et al. (2017)), so that a coarser discretization may be used; ? similarly replaces the borehole with a coarser conductivity structure and adopts an OcTree discretization locally refine the mesh around the casing. Yang and Oldenburg (2016) uses a circuit model and introduces circuit components to account for the steel cased well in a 3D DC resistivity experiment. Another approach has been to replace the well with an “equivalent source”, for example, a collection of representative dipoles, inspired from Cuevas (2014b), or with linear charge distributions for a DC problem (Weiss et al., 2016). For the frequency domain electromagnetic problem, a method of moments approach, which replaces the casing with a series of current dipoles, has been taken in Kohnke et al. (2017).

For 3D survey geometries, only a handful of forward simulations which accurately discretize the casing have been demonstrated, and they have been achieved at significant computational cost. Recent examples, including Commer et al. (2015); Um et al. (2015); Puzyrev et al. (2017), perform time and frequency domain simulations with finely-discretized boreholes; they required the equivalent of days of compute-time for a

single forward simulation to complete. While these codes will undoubtedly see improvements in efficiency, what we present here is an alternative approach to the discretization which capitalizes on the cylindrical geometry of a borehole.

We introduce an approach and associated open-source software implementation for simulating Maxwell's equations over conductive, permeable models on 2D and 3D cylindrical meshes. The software is written in Python (?) and is included as an extension to the SimPEG ecosystem (Cockett et al., 2015; Heagy et al., 2017a). Within the context of current research connected to steel-cased wells, our aim with the development and distribution of this software is two-fold: (1) to facilitate the exploration of the physics of EM in these large-contrast settings, and (2) to provide a simulation tool that can be used for testing other EM codes. The large physical property contrasts in both conductivity and permeability means the physics is complicated and often non-intuitive; as such, we prioritize the ability of the researcher to access and visualize fields, fluxes, and charges in the simulation domain. This is particularly useful when the software is used in conjunction with Jupyter notebooks which facilitate exploration of numerical results (Perez et al., 2015). As the mesh conforms to the geometry of a vertical borehole, a fine discretization can be used in its vicinity without resulting in a onerous computation. This provides the opportunity to build an understanding of the physics of EM in settings with vertical boreholes prior to moving to settings with deviated and horizontal wells. We demonstrate the software with examples at DC, in the frequency domain, and in the time domain. Source-code for all examples is provided as Jupyter notebooks at <https://github.com/simpeg-research/heagy-2018-emcyl> (Heagy, 2018); they are licensed under the permissive MIT license with the hope of reducing the effort necessary by a researcher to compare to or build upon this work.

Our paper is organized in the following manner. In section 3.2, we introduce the

governing equations, Maxwell's equations, and describe their discretization in cylindrical coordinates. We then compare our numerical implementation to the finite element and finite difference results shown in (Commer et al., 2015) as well as a finite volume OcTree simulation described in (Haber et al., 2007). Section 3.3 contains numerical examples of the DC, frequency domain EM, and time domain EM implementations. The two DC resistivity examples (sections 3.3.1 and 3.3.2) are built upon the foundational work in (Kaufman, 1990; Kaufman and Wightman, 1993) which use asymptotic analysis to draw conclusions about the behavior of the electric fields, currents, and charges for a well where an electrode has been positioned along its axis. The next example, in section 3.3.3, is motivated by the interest in using a steel-cased well as an “extended electrode” in a time domain EM experiment. We perform a “top-casing” experiment, with one electrode connected to the top of the well and examine the currents in the surrounding geologic formation through time. Our final two examples, in sections 3.3.4 and 3.3.5, consider a frequency domain experiment inspired by (Augustin et al., 1989). These examples demonstrate the impact of magnetic permeability on the character of the magnetic flux within the vicinity of the borehole and discusses the resulting magnetic field measurements made within a borehole.

3.2 Numerical tools

The governing equations under consideration are Maxwell's equations. Here we provide a brief overview and recommend Ward and Hohmann (1988) for more detail. Under the quasi-static approximation, Maxwell's equations are given by:

$$\begin{aligned} \nabla \times \vec{e} + \frac{\partial \vec{b}}{\partial t} &= 0 \\ \nabla \times \vec{h} - \vec{j} &= \vec{s}_e \end{aligned} \tag{3.1}$$

where \vec{e} is the electric field, \vec{b} is the magnetic flux density, \vec{h} is the magnetic field, \vec{j} is the current density and \vec{s}_e is the source current density. Maxwell's equations can also be formulated in the frequency domain, using the $e^{i\omega t}$ Fourier Transform convention, they are

$$\begin{aligned}\nabla \times \vec{E} + i\omega \vec{B} &= 0 \\ \nabla \times \vec{H} - \vec{J} &= \vec{s}_e\end{aligned}\tag{3.2}$$

The fields and fluxes are related through the physical properties: electrical conductivity (σ , or its inverse, resistivity ρ) and magnetic permeability (μ), as described by the constitutive relations

$$\begin{aligned}\vec{J} &= \sigma \vec{E} \\ \vec{B} &= \mu \vec{H}\end{aligned}\tag{3.3}$$

At the zero-frequency limit, we also consider the DC resistivity experiment, described by

$$\begin{aligned}\nabla \cdot \vec{j} &= I(\delta(\vec{r} - \vec{r}_{s^+}) - \delta(\vec{r} - \vec{r}_{s^-})) \\ \vec{e} &= -\nabla \phi\end{aligned}\tag{3.4}$$

where I is the magnitude of the source current density, \vec{r}_{s^+} and \vec{r}_{s^-} are the locations of the current electrodes, and ϕ is the scalar electric potential.

Of our numerical tools, we require the ability to simulate large electrical conductivity contrasts, include magnetic permeability, and solve Maxwell's equations at DC, in frequency and in time in a computationally tractable manner. Finite volume methods are advantageous for modelling large physical property contrasts as they are conserva-

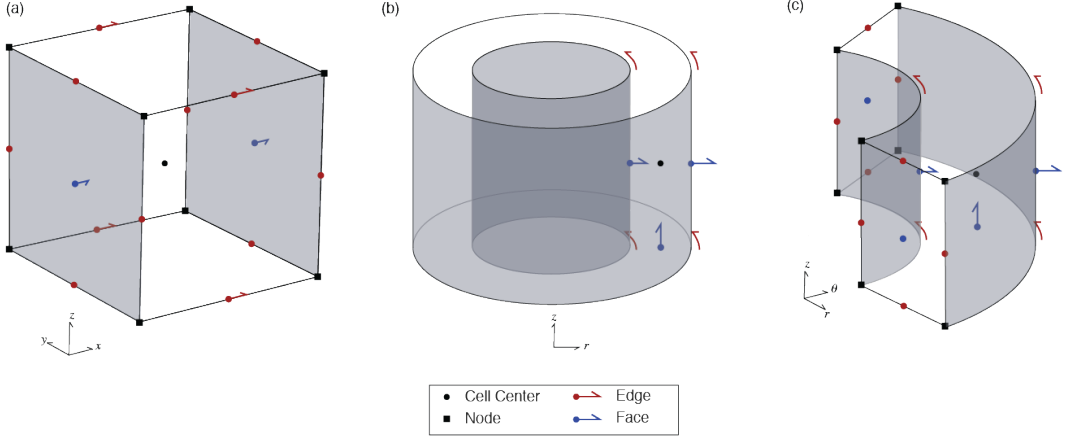


Figure 3.1: Anatomy of a finite volume cell in a (a) cartesian, rectangular mesh, (b) cylindrically symmetric mesh, and (c) a three dimensional cylindrical mesh.

tive and the operators “mimic” properties of the continuous operators, that is, the edge curl operator is in the null space of the face divergence operator, and the nodal gradient operator is in the null space of the edge curl operator (Hyman and Shashkov, 1999). As such, they are common practice for many electromagnetic simulations (e.g. Horesh and Haber (2011); Haber (2014b); Jahandari and Farquharson (2014) and references within), and will be our method of choice.

3.2.1 Discretization

To represent a set of partial differential equations on the mesh, we use a staggered-grid approach (Yee, 1966) and discretize fields on edges, fluxes on faces, and physical properties at cell centers, as shown in Figure 3.1. Scalar potentials can be discretized at cell centers or nodes. We consider both cylindrically symmetric meshes and fully 3D cylindrical meshes; the anatomy of a finite volume cell for these scenarios is shown in Figure 3.1 (b) and (c).

To discretize Maxwell's equations in the time domain (equation 3.1) or in the frequency domain (equation 3.2), we invoke the constitutive relations to formulate our system in terms of a single field and a single flux. This gives a system in either the electric field and magnetic flux (E-B formulation), or the magnetic field and the current density (H-J formulation). For example, in the frequency domain, the E-B formulation is

$$\begin{aligned} \mathbf{Ce} + i\omega \mathbf{b} &= \mathbf{0} \\ \mathbf{C}^\top \mathbf{M}_{\mu^{-1}}^f \mathbf{b} - \mathbf{M}_\sigma^e \mathbf{e} &= \mathbf{s}_e \end{aligned} \tag{3.5}$$

and the H-J formulation is

$$\begin{aligned} \mathbf{C}^\top \mathbf{M}_\rho^f \mathbf{j} + i\omega \mathbf{M}_\mu^e \mathbf{h} &= \mathbf{0} \\ \mathbf{Ch} - \mathbf{j} &= \mathbf{s}_e \end{aligned} \tag{3.6}$$

where $\mathbf{e}, \mathbf{b}, \mathbf{h}, \mathbf{j}$ are vectors of the discrete EM fields and fluxes; \mathbf{s}_m and \mathbf{s}_e are the discrete magnetic and electric source terms, respectively; \mathbf{C} is the edge curl operator, and the matrices $\mathbf{M}_{\text{prop}}^{e,f}$ are the edge / face inner product matrices. In particular, variable electrical conductivity and variable magnetic permeability are captured in the discretization. The time domain equations are discretized in the same manner as is discussed in (Heagy et al., 2017a); for time-stepping, a first-order backward Euler approach is used. Although the midpoint method, which is second-order accurate, could be considered, it is susceptible to oscillations in the solution, which reduce the order of accuracy, unless a sufficiently small time-step is used (Haber et al., 2004; Haber, 2014b).

At the zero-frequency limit, each formulation has a complementary discretization for the DC equations, for the E-B formulation the discretization leads to a nodal dis-

cretization of the electric potential ϕ , giving

$$\begin{aligned} -\mathbf{G}^\top \mathbf{M}_\sigma^e \mathbf{e} &= \mathbf{q} \\ \mathbf{e} &= -\mathbf{G}\phi \end{aligned} \tag{3.7}$$

where \mathbf{G} is the nodal gradient operator, and \mathbf{q} is the source term, defined on nodes. Note that the nodal gradient takes the discrete derivative of nodal variables, and thus the output is on edges. The H-J formulation leads naturally to a cell centered discretization of the electric potential

$$\begin{aligned} \mathbf{V}\mathbf{D}\mathbf{j} &= \mathbf{q} \\ \mathbf{M}_\rho^f \mathbf{j} &= \mathbf{D}^\top \mathbf{V}\phi \end{aligned} \tag{3.8}$$

Where \mathbf{D} is the face divergence operator, \mathbf{V} is a diagonal matrix of the cell volumes, \mathbf{q} is the source term, which is defined at cell centers as is ϕ . Here, the face divergence takes the discrete derivative from faces to cell centers, thus its transpose takes a variable from cell centers to faces. For a tutorial on the finite volume discretization of the DC equations, see (Cockett et al., 2016b).

For the EM simulations, natural boundary conditions are employed; in the E-B formulation, this means $\vec{B} \times \vec{n} = 0|_{\partial\Omega}$, and in the H-J formulation, we use $\vec{J} \times \vec{n} = 0|_{\partial\Omega}$. Within the DC simulations, there is flexibility on the choice of boundary conditions employed. In the simplest scenario, for the nodal discretization, we use Neumann boundary conditions, $\sigma \vec{E} \cdot \vec{n} = 0|_{\partial\Omega}$, and for the cell centered discretization, we use Dirichlet boundary conditions $\phi = 0|_{\partial\Omega}$.

When employing a cylindrical mesh, the distinction between where the electric and magnetic contributions are discretized in each formulation has important implica-

tions. If we consider the cylindrically symmetric mesh (Figure 3.1b) and a magnetic dipole source positioned along the axis of symmetry (sometimes referred to as the TE mode), we must use the E-B formulation of Maxwell's equation to simulate the resulting toroidal magnetic flux and rotational electric fields. If instead, a vertical current dipole is positioned along the axis of symmetry (also referred to as the TM mode), then the H-J formulation of Maxwell's equations must be used in order to simulate toroidal currents and rotational magnetic fields. The advantage of a fully 3D cylindrical mesh provides additional degrees of freedom, with the discretization in the azimuthal direction, allowing us to simulate more complex responses. However, in order to avoid the need for very fine discretization in the azimuthal direction, we should select the most natural formulation of Maxwell's equations given the source geometry being considered. For a vertical steel cased well and a grounded source, we expect the majority of the currents to flow vertically and radially, thus the more natural discretization to employ is the H-J formulation of Maxwell's equations.

Haber (2014b) provides derivations and discussion of the differential operators and inner product matrices; though they are described for a cartesian coordinate system and a rectangular grid, the extension to a three dimensional cylindrical mesh is straightforward. Effectively, a cartesian mesh is wrapped so that the x components become r components, and y components become θ components, as shown in Figure 3.2.

The additional complications that are introduced are: (1) the periodic boundary condition introduced on boundary faces and edges in the azimuthal direction, (2) the removal of radial faces and azimuthal edges along the axis of symmetry, and (3) the elimination of the degrees of freedom of the nodes and edges at the boundary and as well as the nodes and vertical edges along the axis of symmetry. The implementation of the 3D cylindrical mesh is provided as a part of the `discretize` package

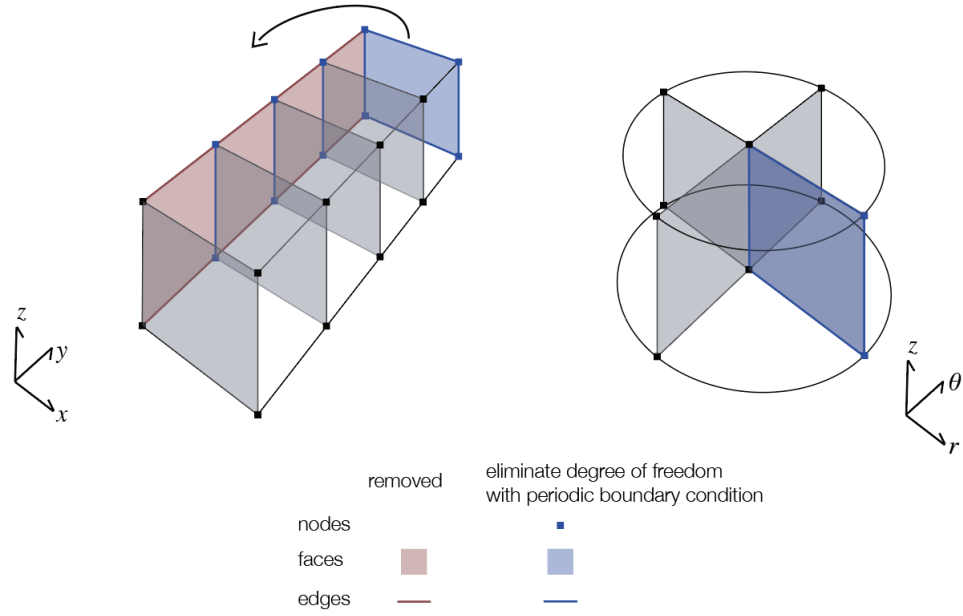


Figure 3.2: Construction of a 3D cylindrical mesh from a cartesian mesh.

(<http://discretize.simpeg.xyz>), which is an open-source python package that contains finite volume operators and utilities for a variety of mesh-types. All differential operators are tested for second order convergence and for preservation of mimetic properties (as described in Haber (2014b)). `discretize` is developed in a modular, object-oriented manner and interfaces to all of the SimPEG forward modelling and inversion routines, thus, once the differential operators have been implemented, they can be readily used to perform forward simulations (Cockett et al., 2015; Heagy et al., 2017a). One of the benefits of SimPEG for forward simulations is that values of the fields and fluxes are readily computed and visualized, which enables researchers to examine the physics as well as to simulate data. Development within the SimPEG ecosystem follows best practices for modern, opens-source software, including: peer review of code changes and additions, versioning, automated testing, documentation, and issue tracking.

3.2.2 Validation

Testing for the DC, TDEM, and FDEM implementations includes comparison with analytic solutions for a dipole in a whole-space. These examples are included as supplementary examples with the distributed notebooks. We have also compared the cylindrically symmetric implementation at low frequency with a DC simulations from a Resistor Network solution developed in MATLAB with (Figure 3 in Yang and Oldenburg (2016)).

Here, we include a comparison with the time domain electromagnetic simulation shown in Figures 13 and 14 of Commer et al. (2015). A 200m long well, with a conductivity of 10^6 S/m, outer diameter of 135 mm, and casing thickness of 12 mm is embedded in a 0.0333 S/m background. For the material inside the casing, we use a conductivity equal to that of the background. The conductivity of the air is set to 3×10^{-4} S/m and the permeability of the casing is ignored ($\mu = \mu_0$). A 10 m long inline electric dipole source is positioned on the surface, 50 m radially from the well. The radial electric field is sampled at 5 m, 10 m, 100 m, 200 m and 300 m along a line 180° from the source.

Two simulations are included in Commer et al. (2015): a finite element (FE) and a finite difference (FD) solution. Both simulation meshes capture the thickness of the casing with a single cell or single tetrahedral element. The finite element solution mesh consisted of over 8 million tetrahedral elements and the simulation completed in 63 hours on a single core of an Intel Xeon X5550 processor (2.67 GHz). For the finite difference solution, a conservative time-stepping was used ($\Delta t = 3 \times 10^{-10}$ s), resulting in a total of >120 million time steps. This simulation took 23.2 hours using 512 cores on an Intel Xeon architecture (2.33 GHz).

Additionally, include a comparison with the 3D UBC finite volume OcTree time domain code (Haber et al., 2007). The OcTree mesh allows for adaptive refinement of the mesh around sources, receivers, and conductivity structures within the domain, thus

reducing the number of unknowns in the domain as compared to a tensor mesh. The mesh in the UBC simulation included 5 011 924 cells, with the finest cells being equal to the width of the casing; 154 time steps were taken and 10 different step-lengths were used (requiring 10 different matrix factorizations). This simulation took 57 minutes to run on a single Intel Xeon X5660 processor (2.80GHz).

For the 3D cylindrical simulation, we use a mesh that has 4 cells radially across the width of the casing, 2.5m vertical discretization, and azimuthal refinement near the source and receivers (along the $\theta = 90^\circ$ line), as shown in Figure 3.3. The mesh has a total of 309 120 cells. For the time discretization, the smallest time-step we use is 10^{-6} s; the time-mesh is coarsened at later times. We used a moderately conservative time-stepping scheme with 187 time-steps total. Seven different step-lengths were employed, requiring seven matrix factorizations. To solve the system matrix, the direct solver PARDISO was used (Petra et al., 2014; Cosmin et al., 2016). The simulation took 14 minutes to run on a single Intel Xeon X5660 processor (2.80GHz).

In Figure 3.4, we show the absolute value of the radial electric field sampled at five stations; each of the different line colors is associated with a different location, and offsets are with respect to the location of the well. Solutions were interpolated to the same offset using nearest neighbor interpolation. The 3D cylindrical simulation (SimPEG) is plotted with a solid line and overlaps with the UBC solution (dash-dot line) for all times shown. The finite element (FE) solution from Commer et al. (2015) is shown with the dashed lines, and the finite difference (FD) solution is plotted with dotted lines. The 3D cylindrical (SimPEG) and UBC solutions are overall in good agreement with the solutions from Commer et al. (2015). There is a difference in amplitude and position of the zero-crossing (the v-shape visible in the blue and orange curves) between the Commer solutions and the SimPEG / UBC solutions at the shortest two offsets in the early

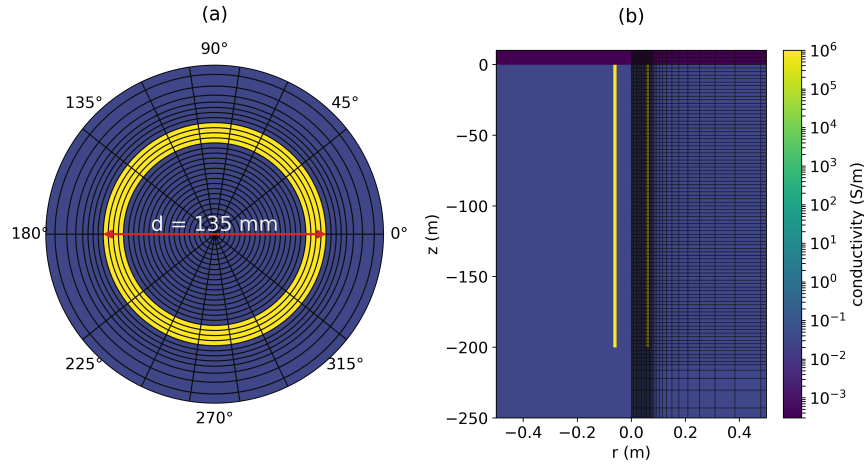


Figure 3.3: Depth slice (left) and cross section (right) through the 3D cylindrical mesh used for the comparison with Commer et al. (2015). The source and receivers are positioned along the $\theta = 90^\circ$ line. The mesh extends 3600m radially and 3300m vertically to ensure that the fields have sufficiently decayed before reaching the boundaries.

times. At such short offsets from a highly conductive target, details of the simulation and discretization, such as the construction of the physical property matrices in each of the various approaches become significant; this likely accounts for the discrepancies but a detailed code-comparison is beyond the scope of this paper. Our aim with this comparison is to provide evidence that our numerical simulation is performing as expected; the overall agreement with Commers and UBCs results provides confidence that it is.

This example demonstrates agreement between the 3D cylindrical solution and solutions obtained with independently developed codes. Importantly, it also shows how, by using a cylindrical discretization which conforms to the conductivity structure of interest, the size of the mesh and resultant cost of the computation can be greatly reduced. This is true even with relatively conservative spatial and temporal discretizations. Minimizing computation time was not a main focus in the development of the software and there are still opportunities for improving efficiency. As an open-source project, contrib-

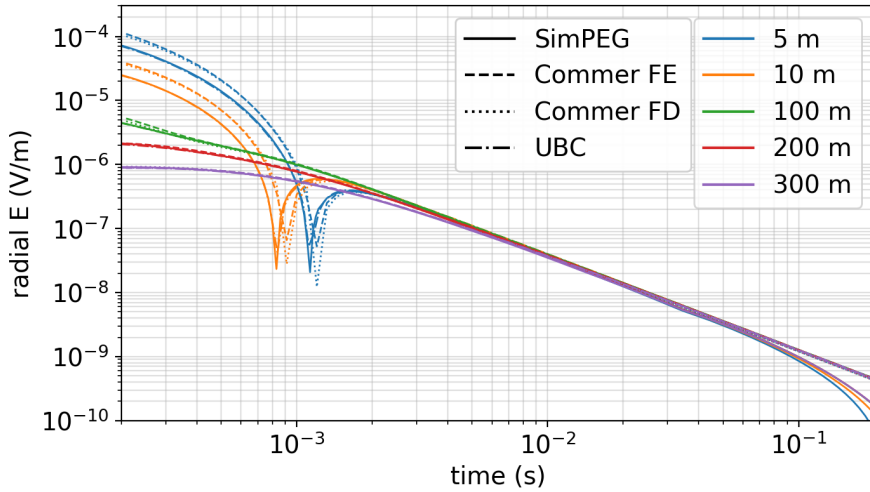


Figure 3.4: Time domain EM response comparison with (Commer et al., 2015). Each of the different line colors is associated with a different location; offsets are with respect to the location of the well.

butions from the wider community are encouraged.

3.3 Numerical Examples

We demonstrate the implementation through examples using the DC, time domain EM and frequency domain EM codes. To focus discussion, each of the examples explores an aspect of the physical behavior of electromagnetic fields and fluxes in the presence of a steel-cased well.

3.3.1 DC Resistivity Part 1: Electric fields, currents and charges in a long well

In his two seminal papers on the topic, Kaufman uses transmission line theory to draw conclusions about the behaviour of the electric field when an electrode is positioned inside of an infinite casing. In this first example, we will revisit some of the physical insights discussed in (Kaufman, 1990; Kaufman and Wightman, 1993) that followed

from an analytical derivation and compare those to our numerical results. In the second example, we look at the distribution of current and charges as the length of the well is varied and compare those to the analytical results discussed in (Kaufman and Wightman, 1993)

We start by considering a 1km long well (10^6 S/m) in a whole space (10^{-2} S/m), with the conductivity of the material inside the borehole equal to that of the whole space. For modelling, we will use a cylindrically symmetric mesh. The positive electrode is positioned on the borehole axis in the mid-point of a 1km long well; a distant return electrode is positioned 1km away at the same depth.

Kaufman discusses the behavior of the electric field by dividing the response into three zones: a near zone, an intermediate zone and a far zone (Kaufman, 1990; Kaufman and Wightman, 1993). In the near zone, the electric field has both radial and vertical components, negative charges are present on the inside of the casing, and positive charges are present on the outside of the casing. The near zone is quite localized and typically, its vertical extent is no more than ~ 10 borehole radii away from the electrode. To examine these features in our numerical simulation, we have plotted in Figure 3.5: (a) the total charge, (b) secondary charges, (c) electric field, and (d) current density in a portion of the model near the source. The behaviours expected by Kaufman are consistent with our numerical results.

Discussion

Within the near-zone, the total charge is dominated by the large positive charge at the current electrode location and negative charges that exist along the casing wall where current is moving from a resistive region inside the borehole into a conductor. The extent of the negative charges along the inner casing wall is more evident when we look at the

secondary charge, which is obtained by subtracting the charge that would be observed in a uniform half-space from the total charge (Figure 3.5b). Inside the casing, we can see the transition from near-zone behavior to intermediate zone behavior approximately 0.5 m above and below the source; that is equal to 10 borehole radii from the source location, which agrees with Kaufman's conclusion.

In the intermediate zone, Kaufman discusses a number of interesting aspects with respect to the behavior of the electric fields and currents which we can compare with the observed behavior in Figure 3.5. Among them, he shows that the electric field within the borehole and casing is directed along the vertical axis; as a result no charges accumulate on the inner casing wall. Charges do, however, accumulate on the outer surface of the casing; these generate radially-directed electric fields and currents, often referred to as leakage currents, within the formation. At each depth slice through the casing and borehole, the electric field is uniform, however, due to the high conductivity of the casing, most of the current flows within the casing. The vertical extent of the intermediate zone depends on the resistivity contrast between the casing and the surrounding formation and extends beyond several hundred meters before transitioning to the far zone, where the influence of the casing disappears (Kaufman, 1990).

The radially directed fields from the casing, and the length of the intermediate zone, have practical implications in the context of well-logging because they delineate the region in which measurements can be made to acquire information about the formation resistivity outside the well. Within the intermediate zone, fields behave like those due to a transmission line (Kaufman, 1990), and multiple authors have adopted modelling strategies that approximate the well and surrounding medium as a transmission line (Kong et al., 2009; Aldridge et al., 2015). We will extend this analysis in the next example and discuss how the length of the well impacts the behavior of the charges,

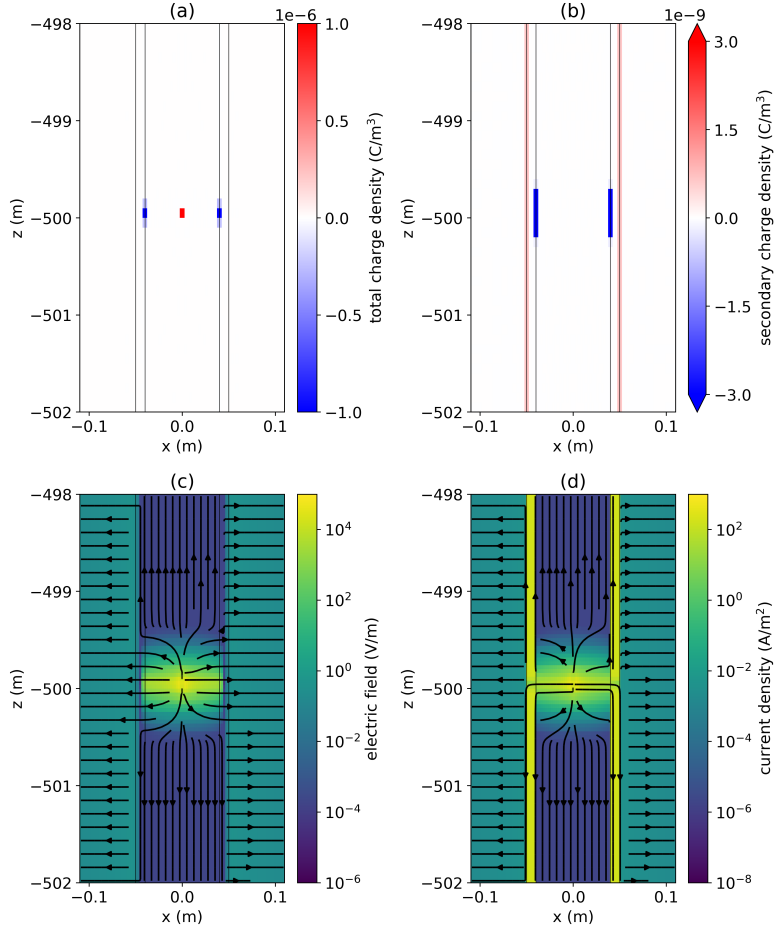


Figure 3.5: (a) Total charge density, (b) secondary charge density, (c) electric field, and (d) current density in a section of the pipe near the source at $z=-500\text{m}$.

fields, and fluxes.

3.3.2 DC Resistivity Part 2: Finite Length Wells

In (Kaufman and Wightman, 1993), the transmission-line analysis was extended to consider finite-length wells. Inspired by the interest in using the casing as an “extended electrode” for delivering current to depth (e.g. Schenkel and Morrison (1994); Um et al. (2015); Weiss et al. (2016); Hoversten et al. (2017)), here we consider a 3D DC resistivity experiment where one electrode is connected to the top of the well. We will examine

the current and charge distribution for wells ranging in length from 250 m to 4000 m and compare those to the observations in (Kaufman and Wightman, 1993). The conductivity of the well is selected to be 10^6 S/m. A uniform background conductivity of 10^{-2} S/m is used and the return electrode is positioned 8000m from the well; this is sufficiently far from the well that we do not need to examine the impact of the return electrode location in this example. A 3D cylindrical mesh was used for the simulation.

Discussion

(Kaufman and Wightman, 1993) derives a solution for the current within a finite length well and discusses two end-member cases: a short well and a long well. “Short” versus “long” are defined on the product of αL_c , where L_c is the length of the casing and $\alpha = 1/\sqrt{ST}$, where S is the cross-sectional conductance of the casing and has units of S·m ($S = \sigma_c 2\pi a \Delta a$, for a casing with radius a and thickness Δa), and T is the transverse resistance. The transverse resistance is approximately equal to the resistivity of the surrounding formation (for more discussion on where this approximation breaks down, see Schenkel and Morrison (1994)). For short wells, $\alpha L_c \ll 1$, the current decreases linearly with distance, whereas for long wells, where $\alpha L_c \gg 1$, the current decays exponentially with distance from the source, with the rate of decay being controlled by the parameter α . In Figure 3.6 (a), we show current in the well for 5 different borehole lengths. The x-axis is the distance from the source normalized by the length of the well. We also show the two end-member solutions (equations 45 and 53) from Kaufman and Wightman (1993). There is significant overlap between the 250m numerical solution and the short well approximation. As the length of the well increases, exponential decay of the currents becomes evident. Since α is quite small, for this example $\alpha = 2 \times 10^{-3} m^{-1}$, the borehole must be very long to reach the other end member which corresponds to the

exponentially decaying solution.

In Figure 3.6 (b), we have plotted the charges along the length of the well. In the short-well regime, the borehole is approximately an equipotential surface and the charges are uniformly distributed; in the long well the charges decay with depth. What was surprising to us was the noticeable increase in charge accumulation that occurs near the bottom of the well. This is especially evident for the short well. Initially, we were suspicious and thought this might be due to problems with our numerical simulation; there was no obvious physical explanation that we were aware of. However, investigation into the literature revealed that the increase in charge density at the ends of a cylinder is a real physical effect, but an exact theoretical solution does still not appear to exist (Griffiths and Li, 1997) (see figure 4, in particular).

The results shown in Figure 3.6 have implications when testing approaches for reducing computational load by approximating a well with a solid tube or prism, as in Um et al. (2015), or replacing the well with a distribution of charges, as in Weiss et al. (2016). For a short well, the behaviour of the currents is independent of conductivity, so, as long as the borehole is approximated by a sufficiently conductive target, the behaviour of the fields and fluxes will be representative of the fine-scale model. However, as the length of the well increases, the cross-sectional conductance of the well, becomes relevant as it controls the rate of decay of the currents in the well and thus the rate that currents leak into the formation. A similar result holds when a line of charges is used to approximate the well as a DC source; a uniform charge is suitable for a sufficiently short or sufficiently conductive well, whereas a distribution of charge which decays exponentially with depth needs to be considered for longer wells. Thus, when attempting to replace a fine-scale model of a well with a coarse-scale model, either with a conductivity structure or by some form of “equivalent source”, validations should be

performed on models that have the same length-scale as the experiment to ensure that both behaviors are being accurately modeled.

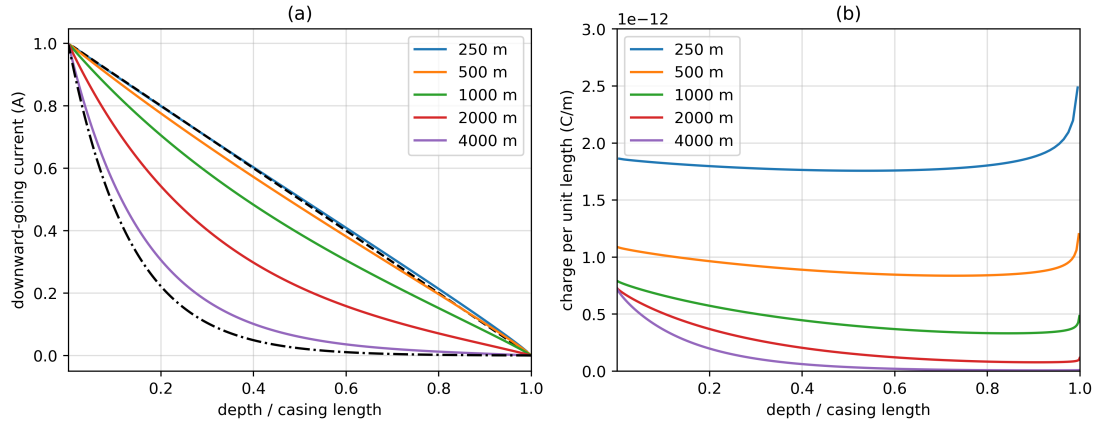


Figure 3.6: (a) Current along a well for 5 different wellbore lengths. The x-axis is depth normalized by the length of the well. The black dashed line shows the short-well approximation (equation 45 in Kaufman and Wightman (1993)) for a 200m long well. The black dash-dot line shows the long-well approximation (equation 53 in Kaufman and Wightman (1993)) for a 4000m well. (b) Charge per unit length along the well for 5 different wellbore lengths.

3.3.3 Time Domain Electromagnetics

In this example, we examine the behaviour of electric currents in an experiment where the casing is used as an “extended electrode”. Although the initial investigations with casings centered around using a DC source, greater information about the subsurface can be had by employing a frequency or time domain source. A particular application is the monitoring of hydraulic fracturing proppant and fluids, or CO₂; this is active research carried out by many groups worldwide (e.g. Hoversten et al. (2015); Um et al. (2015); Puzyrev et al. (2017); Zhang et al. (2018) among others). The challenge is to have efficient and accurate forward modelling; solving the full Maxwell equations is much more demanding than solving the DC problem. For our simulation, a positive

electrode is connected to the top of the casing and a return electrode is positioned 1km away. The well has a conductivity of 10^6 S/m and is 1km long; it has an outer diameter of 10cm and a 1cm thick casing wall. The mud which infills the well has the same conductivity as the background, 10^{-2} S/m. The conductivity of the air is set to 10^{-5} S/m; in numerical experiments, we have observed that contrasts near or larger than $\sim 10^{12}$ S/m leads to erroneous numerical solutions. For this example, we will focus on electrical conductivity only and set the permeability of the well to μ_0 . A step-off waveform is used, and the currents within the formation are plotted through time in Figure 3.7. Panel (a) shows a zoomed-in cross section of the casing, (b) shows a vertical cross section along the line of the wire (c) shows a horizontal depth slice at 50 m depth and (d) shows a depth slice at 800 m depth. The images in panels (b), (c) and (d) are on the same color scale.

Discussion

We begin by examining Figure 3.7 (b), which shows the currents in the formation. The return electrode is positioned at $x=1000$ m. At time $t = 0$ s, we have the DC solution. Currents flow away from the well, and eventually curve back to the return electrode. Immediately after shut-off, we see an image current develop in the formation. The image current flows in the same direction as the original current in the wire; this is opposite to currents in the formation, causing a circulation of current. The center of this circulation is visible as the null propagating downwards and to the right in Figure 3.7 (b). In Figure 3.7 (a), we see the background circulating currents being channeled into the well and propagating downwards. The depth range over which currents enter the casing depends upon time. At $t=0.01$ ms, the zero crossing, which distinguishes the depth between incoming and outgoing current in the casing, occurs at $z=90$ m, at $t=0.1$

ms it is at 225 m and by t=1 ms, the zero crossing approaches the midway point in the casing and is at 470 m depth. At later times, the downward propagation of this null slows as the image currents are channeled into the highly conductive casing; at 5 ms it is at 520 m depth, at 10 ms, 560 m depth and by 100 ms (not shown), it is at 800 m depth.

On the side of the well opposite to the wire, we also see a null develop; it is visible in the cross sections in panel (a). To help understand this, we examine the depth slices in panel (c). Behind the well, we see that as the image currents diffuse downwards and outwards, some of those currents are channeled back towards the well; this is visible in the depth slice at 10^{-4} s. These channeled currents are opposite in direction to those the formation currents set up at t=0, which also are diffusing downwards and outwards; where these two processes intersect, there is a current shadow.

There are a number of points to highlight in this example. The first, which has been noted by several authors (e.g. Schenkel and Morrison (1994); Hoversten et al. (2015)), is that the casing helps increase sensitivity to targets at depth. This occurs by two mechanisms: (1) at DC, prior to shut-off, the casing acts as an “extended electrode” leaking current into the formation along its length; (2) after shut-off, it channels the image currents and increases the current density within the vicinity of the casing. The second point to note is that there are several survey design considerations raised by examining the currents: targets that are positioned where there is significant current will be most illuminated. If the target is near the surface and offset from the well, a survey where the source wire runs along the same line as the target will have the added benefits of the excitation due to the image currents. These benefits are twofold: (1) the passing image-current increases the current density for a period of time, and (2) the changing amplitude and direction of the currents with time generate different excitations of the target. this should provide enhanced information in an inversion, as compared to a single excitation

that is available from a DC survey. For deeper targets in this experiment, the passing image current has diffused significantly, and thus it appears that the wire location has less impact on the magnitude of the current density with location. However, it is possible that increasing the wire-length could be beneficial. This extension is straightforward and could be examined with the provided script. There may also be added benefit by having the target positioned along the same line as the source wire, as at later times, the direction of current reverses, changing the excitation of the target.. The final point to note from this example is that although this is a simple model, the behavior of the currents is not intuitive; visualizations of the currents, fields and fluxes, allow researchers to explore the basic physics and prompts new questions. Such simulations and visualizations have proved valuable in the context of geoscience education (Oldenburg et al., 2017) and can be a useful tool for understanding the physical processes that contribute to the data we observe.

3.3.4 Frequency Domain Electromagnetics Part 1: Comparison with scale model results

In the DC example, we discussed how charges are distributed along the well and currents flow into the formation. The time domain example extended the analysis of grounded sources, showed the potential importance of EM induction effects and illuminated the underlying physics. From a historical perspective, however, practical developments in EM were pursued in the frequency domain; the mathematics is more manageable in the frequency domain, and technological advances were being made in the development of induction well-logging tools (Doll, 1949; Moran and Kunz, 1962). Although conductivity of the pipes is generally plays the most dominant role in attenuating the signal, the magnetic permeability is non-negligible (Wait and Hill, 1977); it is the product of the

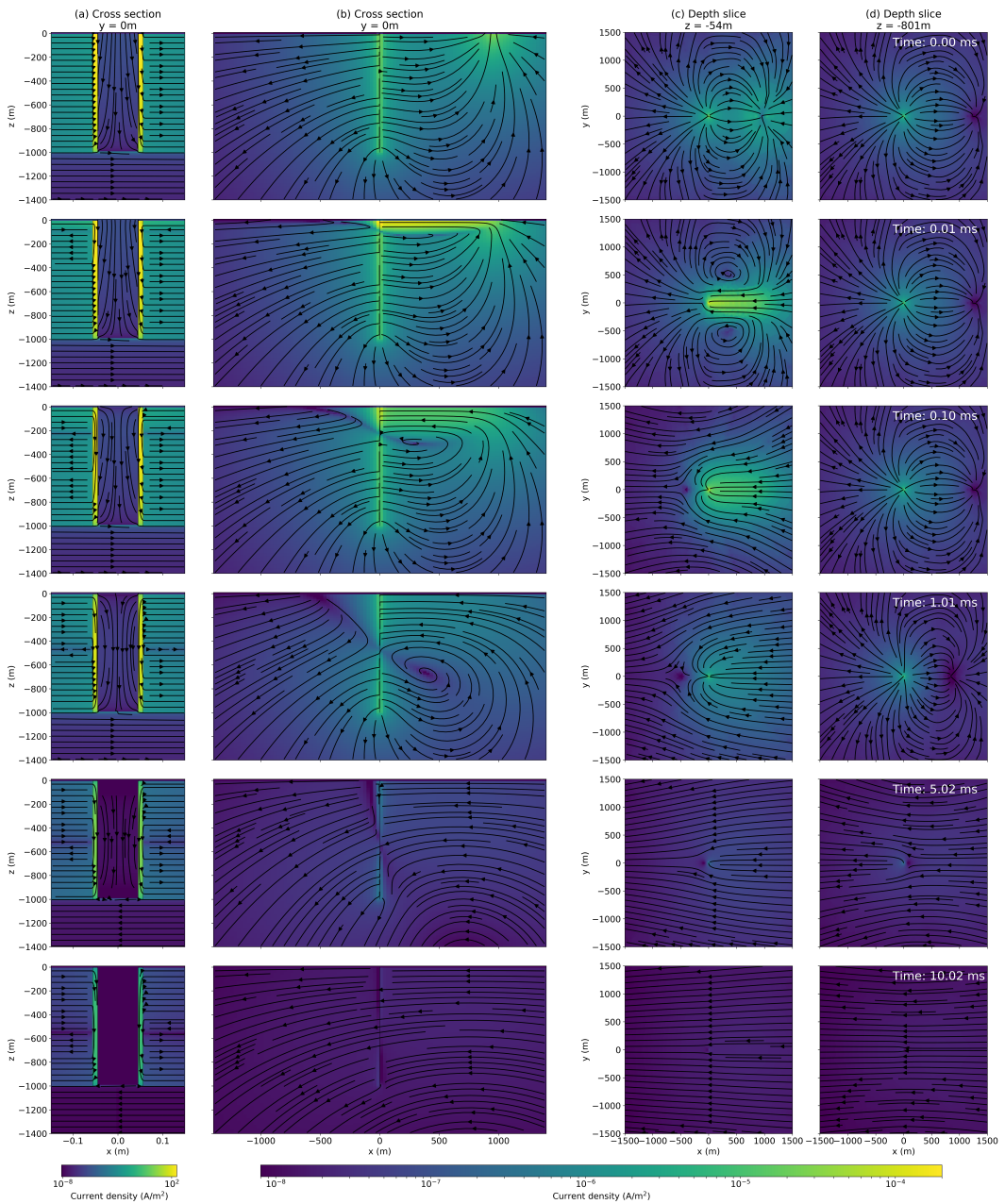


Figure 3.7: Current density for a time domain experiment where one electrode is connected to the top of the casing and a return electrode is on the surface, 1000m away. Six different times are shown, corresponding to each of the six rows; the times are indicated in the plots in panel (d). Panel (a) shows a zoomed-in cross section of the current density in the immediate vicinity of the steel cased well. Panel (b) shows a cross section through the half-space along the same line as the source-wire. Panels (c) and (d) show depth-slices of the currents at 54m and 801m depth.

conductivity and permeability that appears in the description of EM attenuation. Also, the fact that permeable material becomes magnetized in the presence of an external field complicates the problem. Augustin et al. (1989) is one of the first papers on induction logging in the presence of steel cased wells that aims to understand and isolate the EM response of the steel cased well. Using a combination of scale modelling and analytical mathematical modelling, they examine the impacts of conductivity and magnetic permeability on the magnetic field observed in the pipe. In this example and the one that follows, we attempt to unravel this interplay between conductivity and magnetic permeability.

The first experiment Augustin et al. (1989) discuss is a scale model using two different pipes, a conductive copper pipe and a conductive, permeable iron pipe; each pipe is 9 m in length. The copper pipe had an inner diameter of 0.063 m and a thickness of 0.002 m, while the iron pipe had a 0.063 m inner diameter and 0.0043 m wall thickness. A source-loop, with radius 0.6 m was co-axial with the pipe and in one experiment positioned at one end of the pipe (which they refer to as the “semi-infinite pipe” scenario). In another experiment the source loop is positioned at the midpoint of the pipe (which they refer to as the “infinite pipe” scenario); for both experiments, magnetic field data are measured as a function of frequency at the central axis of the pipe. Their results are presented in terms of a Field Strength Ratio (FSR), which is the ratio of the absolute value of the magnetic field at the receiver with the absolute value of the magnetic field if no pipe is present (Figure 3 in Augustin et al. (1989)). At low frequencies, for the data collected within the iron pipe, static shielding ($FSR < 1$) was observed for the measurements where the receiver was in the plane of the source loop for both the “infinite” and “semi-infinite” scenarios. When the receiver was positioned within the pipe, 1.49 m offset from the plane of the source loop, static enhancement effects ($FSR > 1$)

were observed for both the infinite and semi-infinite scenarios. Using this experiment for context, we will compare the behaviour of our numerical simulation with the observations in (Augustin et al., 1989) and examine the nature of the static shielding and enhancement effects.

For our numerical setup, the pipes are 9 m in length and have an inner diameter of 0.06 m. The copper pipe has a casing-wall thickness of 0.002 m and the iron pipe has a thickness of 0.004 m. Following the estimated physical property values from Augustin et al. (1989), we use a conductivity of 3.5×10^7 S/m and a relative permeability of 1 for the copper pipe. For the iron pipe, a conductivity of 8.0×10^6 S/m and a relative permeability of 150 is used. A background conductivity of 10^4 Ωm is assumed. The computed FSR values for the axial magnetic field as a function of frequency are shown in Figure 3.8.

Consider the response of the conductive pipe. At low frequencies, the FSR for the copper pipe (blue lines) is 1 for both the infinite (solid line) and semi-infinite (dashed line) scenarios, as the field inside the copper pipe is equivalent to the free-space field. With increasing frequency, eddy currents are induced in the pipe which generate a magnetic field that opposes the primary, causing a decrease in the observed FSR. When the source and receiver are in the same plane ($L=0.00$ m), the rate of decrease is more rapid in the infinite scenario than the semi-infinite. Since there is conductive material on both sides of the receiver in the infinite case, we would expect attenuation of the fields to occur more rapidly than in the semi-infinite case. This observation is consistent with Figure 3a in Augustin et al. (1989). For the offset receiver ($L=1.49$ m), they observed a slight separation in the infinite and semi-infinite curves which we do not; however, they attributed this to potential errors in magnetometer position. Thus, overall, the numerical results for the copper pipe are in good agreement with the scale model results observed

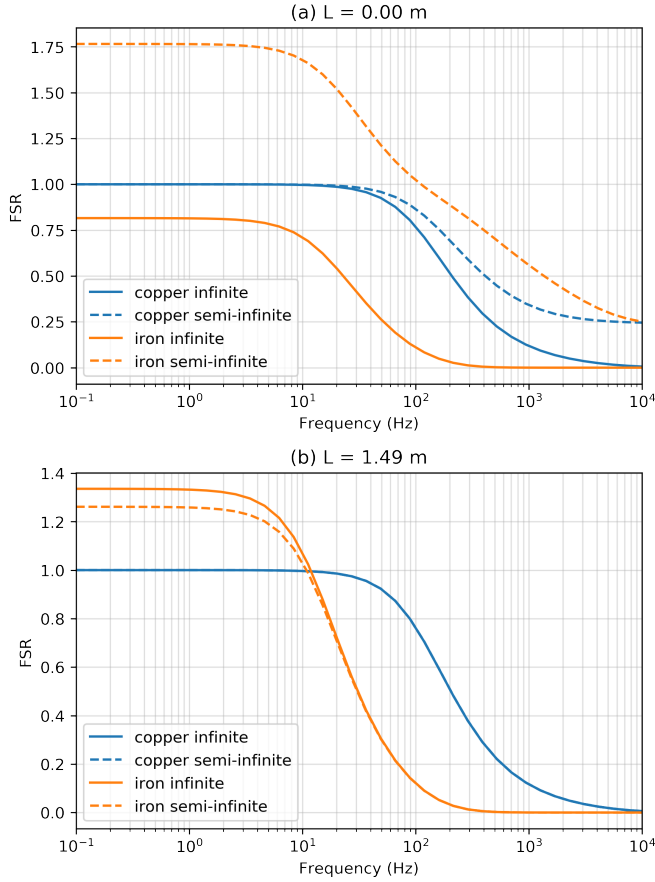


Figure 3.8: Field strength ratio (FSR), the ratio of the measured vertical magnetic field with the free space magnetic field, as a function of frequency for two different receiver locations. In (a), the receiver is in the same plane as the source, in (b), the receiver is 1.49m offset from the source.

by Augustin et al. (1989).

Next, we examine the response of the conductive, permeable pipe. In Figure 3.8b, we observe a static enhancement effect ($FSR > 1$) at low frequencies. The enhancement is larger in the infinite scenario than the semi-infinite scenario; this is in agreement with Figure 3b in Augustin et al. (1989). There is however, a significant discrepancy between our numerical simulations and the scale model for the semi-infinite pipe when the source and receiver lie in the same plane (Figure 3.8a). Augustin et al. (1989) observed a static

shielding effect for both the infinite and semi-infinite scenarios, whereas we observe a static shielding for the infinite scenario, but a significant static enhancement for the semi-infinite case. To examine what might be the cause of this, we will examine the magnetic flux density in this region of the pipe.

In Figure 3.9, we have plotted: (a) the secondary magnetic flux in the infinite-pipe scenario near the source ($z=-4.5$ m), (b) the secondary magnetic flux in the semi-infinite scenario ($z=0$ m for the source), and (c) top 5 cm of the semi-infinite pipe. All plots are at 0.1 Hz. The primary magnetic field is directed upwards within the regions we have plotted, so upward-going magnetic flux indicates a static enhancement effect, and downward-oriented magnetic flux indicates static shielding effects. In (a) we see a transition between the static shielding in the vicinity of the source to a static enhancement approximately 0.5 m above and below the plane of the source. Similarly in (b), we notice a sign-reversal in the z-component of the secondary magnetic flux at a depth of 0.6 m.

Discussion

The behaviors observed in Figure 3.9 are quite comparable to Augustin et al.'s observation of a transition from shielding to enhancement occurring at distances greater than 0.8 m from the source. Numerical experiments show that the vertical extent of the region over which static shielding is occurring increases with increasing pipe diameter, and similarly increases with increasing loop radius while the magnitude of the effect decreases. This can be understood by considering how the pipe is magnetized; for a small loop radius, the magnetization is largely localized near the plane of the source and rapidly falls off with distance from the plane of the source. Localized, large amplitude magnetization causes the casing to act as a collection of dipoles around the circumference

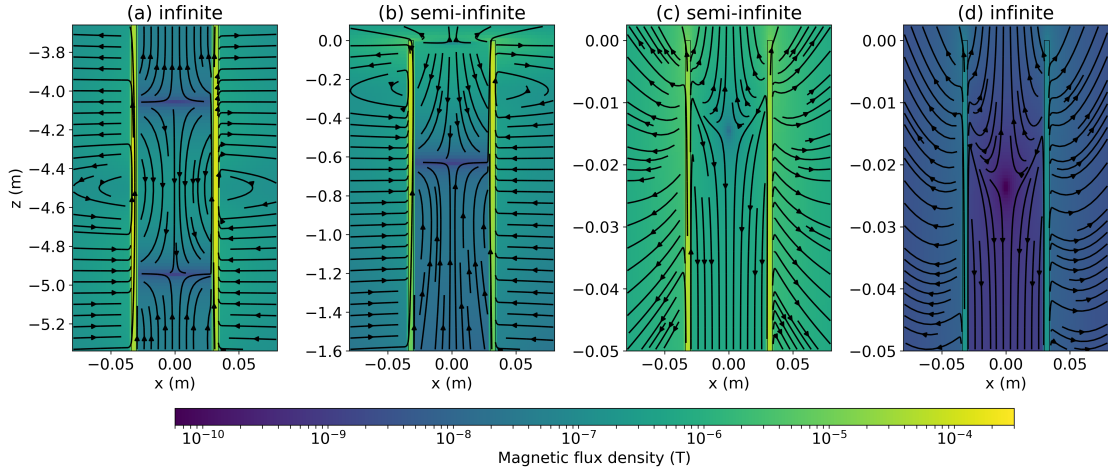


Figure 3.9: Magnetic flux density at 0.1Hz in the region of the pipe near the plane of the source for (a) the “infinite” pipe, where the source is located at -4.5m and the pipe extends from 0m to -9m, (b) a “semi-infinite” pipe, where the source is located at 0m and the pipe extends to -9m. In (c), we zoom in to the top 5cm of the “semi-infinite” pipe, and (d) shows the 5cm at the top-end of the “infinite” pipe.

of the casing. As the radius of the loop increases, the magnetization spreads out along the length of the well resulting in longer, lower-amplitude dipoles, thus both increasing the extent of the region over which static shielding is occurring as well as decreasing its amplitude.

This explains the nature of the static enhancement and static shielding effects, but to explain the discrepancy between the static shielding observed in the semi-infinite pipe when $L=0$ m by Augustin et al., and the static enhancement we observe in Figure 3.8a, we examine the magnetic flux density in the top few centimeters of the pipe. Figure 3.9c shows the top 5 cm of the secondary magnetic flux in the semi-infinite pipe; the source is in the $z=0$ m plane. Zooming in reveals there is yet another sign reversal near the end of the pipe. This is evident even in the infinite-pipe scenario (Figure 3.8d), where the source is offset by several meters from the end of the pipe. This edge-effect

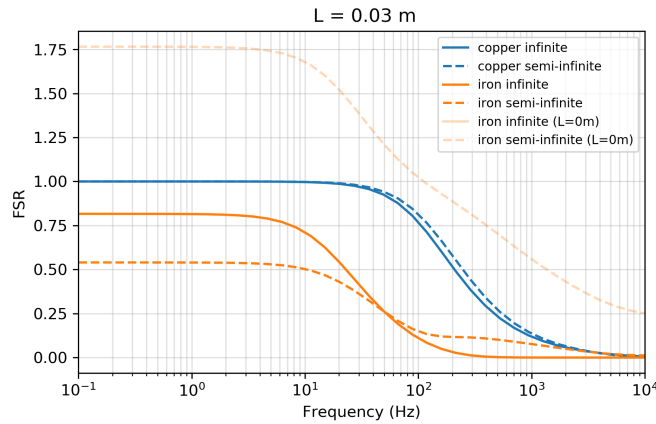


Figure 3.10: Field strength ratio, FSR, for a receiver positioned 3cm beneath the plane of the source. For comparison, we have plotted the FSR for the permeable pipe when the source and receiver lie in the same plane ($L=0.00\text{m}$) with the semi-transparent orange lines. Note that the infinite-pipe solutions for $L=0.03\text{m}$ and $L=0.00\text{m}$ overlap.

perhaps bears some similarities to what we observed in Figure 3.6b, where we saw a build up of charge near the end of the pipe in the DC scenario. At the end of the pipe, we encounter the situation where the normal component of the flux (\vec{j}, \vec{b}) from the pipe to the background needs to be continuous both in the radial and vertical directions at the end of the pipe as does the tangential component of the fields (\vec{e}, \vec{h}). The interplay of these two constraints at the end of the pipe results in more complexity in the resultant fields and fluxes. Within the span of a few centimeters we transition from static enhancement at the top of the pipe to a static shielding further down. An error as small as a few centimeters in the position of the magnetometer causes a reversal in behavior; in Figure 3.10, we have plotted the FSR for a magnetometer positioned 3cm beneath the plane of the source, and the static-shielding behavior observed for the semi-infinite pipe is much more aligned with that observed in Figure 3a in Augustin et al. (1989).

3.3.5 Frequency Domain Electromagnetics Part 2: Conductivity and permeability in the inductive response of a well

The experiments shown in the previous section revealed some insights into the complexity of the fields within the pipe and illustrated the role of permeability in the character of the responses at low frequency. Next, we move to larger scales and examine the role of conductivity and permeability in the responses we observe in the borehole.

In this example, we consider a 2 km long well with an outer diameter of 10 cm and thickness of 1 cm in a whole-space which has a resistivity of $10^4 \Omega\text{m}$. A loop with radius 100 m is coaxial with the well and positioned at the top-end of the well. A receiver measuring the z-component of the magnetic flux density is positioned 500 m below the transmitter loop, along the axis of the well. We will consider both time domain and frequency domain responses.

In electromagnetics, it is often the product of permeability and conductivity that we consider to be the main controlling factor on the EM responses. To assess the contribution of each to the measured responses, we will investigate two scenarios. In the first, the well has a conductivity of 10^8 S/m and a relative permeability of 1, and in the second, the well has a conductivity of 10^6 S/m and a relative permeability of 100; thus the product of conductivity and permeability is equivalent for both wells.

Similar to the analysis done by Augustin et al. (1989) when looking at the role of borehole radius in the behaviour of the magnetic response (e.g. figure 8), we will examine the normalized secondary field (NSF) which is the ratio of the secondary field with the amplitude of the primary, where the primary is defined to be the free-space response. In Figure 3.11, we have plotted the normalized secondary field for the two pipes considered, the conductive pipe (blue) and the conductive, permeable pipe (orange). Let's start by examining the conductivity response in Figure 3.11. Where the value of the NSF

is zero, the primary dominates the response; this is the case at low frequencies where induction is not yet contributing to the response. As frequency increases, currents are induced in the pipe which generate a secondary magnetic field that opposes the primary, hence the NSF becomes negative. When the real part of the NSF (solid line) is -1, the secondary magnetic field is equal in magnitude but opposite in direction to the free-space primary and the measured real field is zero. Values less than -1 indicate a sign reversal in the real magnetic field. Similarly, when the imaginary part of the response function goes above zero, there is a sign reversal in the imaginary component. Note that these sign reversals occur even in a half-space and are a result of sampling the fields within a conductive medium; in this case the receiver was 500 m below the surface.

As compared to the conductive pipe, the frequency at which induction sets in is higher for the conductive, permeable pipe. We also notice that the amplitude variation of both the imaginary and real parts is larger for the permeable pipe. To examine the contribution of conductivity and permeability to the responses, we have plotted the real part of the secondary magnetic flux density, \mathbf{b} , in Figure 3.12. The top row shows the response within the conductive pipe and the bottom row shows the conductive, permeable pipe. The primary magnetic flux is oriented upwards and we can see that all of the secondary fields generated are oriented downwards. Similar to the previous example, we see that at low frequencies, there is magnetostatic response due to the permeable pipe. However, due to the larger length scales of the source loop and the casing in this example, there is no measurable contribution at the receiver. At 1 Hz, we can see that induction is starting to contribute to the signal for the conductive pipe, while for the permeable pipe, it is not until \sim 10 Hz that we begin to observe the contribution of induction. At 100 Hz, the secondary magnetic field is stronger in amplitude than the primary, and the NFS is less than -1 for both the conductive and permeable pipes.

The amplitude of the secondary within the permeable pipe is stronger than that in the conductive pipe. At 1000 Hz, we have reached the asymptote of $\text{NSF}=-1$ for both the conductive and permeable pipes; the secondary magnetic flux is equal in magnitude but opposite in direction to the primary.

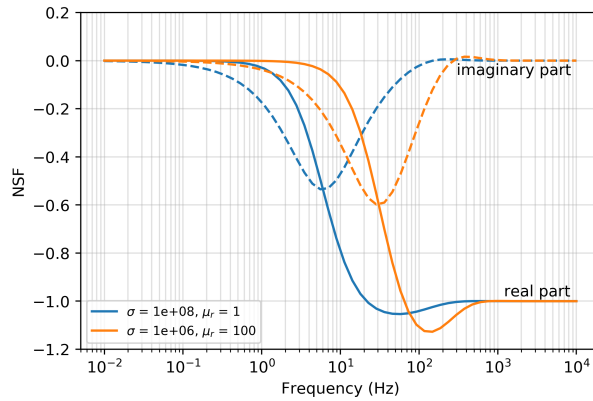


Figure 3.11: Normalized secondary field, NSF, as a function of frequency for two wells. The NSF is the ratio of the secondary vertical magnetic field with the primary magnetic field at the receiver location ($z=-500\text{m}$); the primary is defined as the whole-space primary.

Conducting a similar experiment in the time domain, we can compare the responses as a function of time. For this experiment, a step-off waveform is employed and data are measured after shut-off, the NSF is plotted in Figure 3.13. Note here that the secondary field is in the same direction as the primary, so after the source has been shut off, the secondary field is oriented upwards, as shown in Figure 3.14. Shortly after shut-off, the rate of increase in the secondary field is the same for both the conductive and the conductive, permeable wells. A maximum normalized field strength of approximately 1 is reached for both cases. The responses begin to differ at 10^{-3} s where the conductive well maintains a $\text{NFS} \sim 1$ for approximately 1 ms longer than the permeable well before the fields decay away.

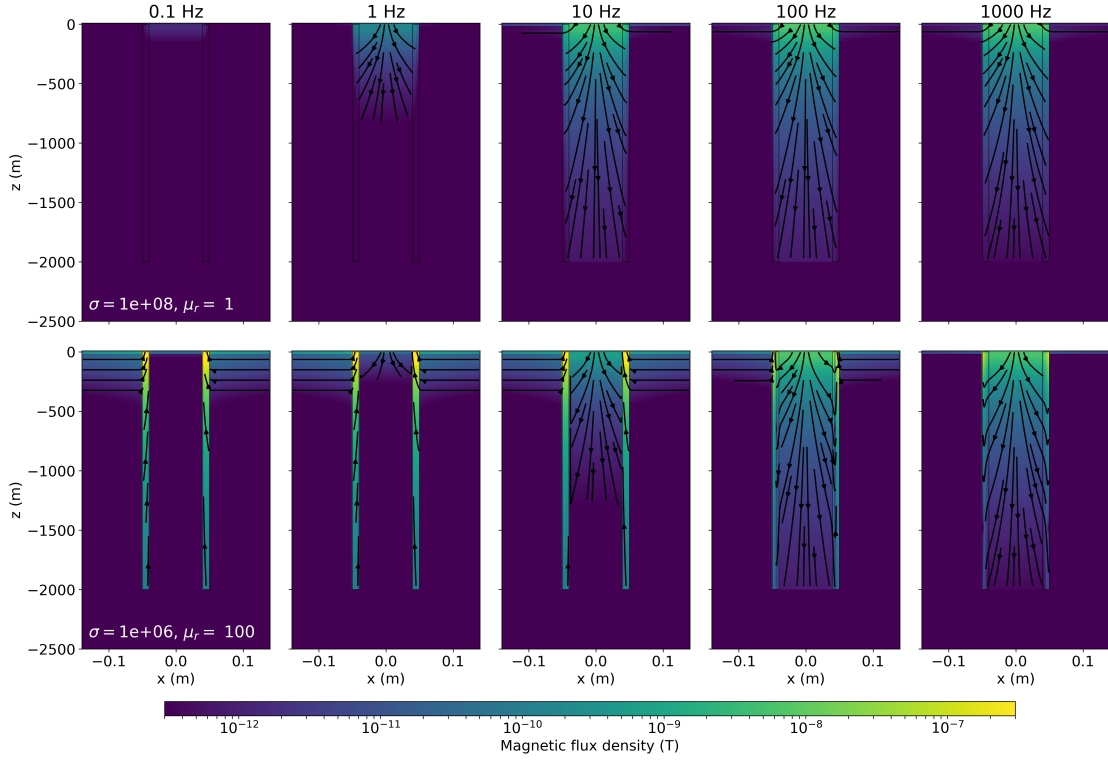


Figure 3.12: Secondary magnetic flux density (with respect to a whole-space primary) at five different frequencies for a conductive pipe (top row) and for a conductive, permeable pipe (bottom row).

Discussion

It is important to note that although the product of the conductivity and permeability is identical for these wells, the geometry of the well and inducing fields results in different couplings for each of the parameters. For a vertical magnetic dipole source, the electric fields are purely rotational while the magnetic fields are primarily vertical. An approximation we can use to understand the implications of these geometric difference is to assume the inducing fields are uniform (e.g. the radius of the source loop is infinite) and to examine the conductance and permeance of the pipe. For rotational electric fields, the

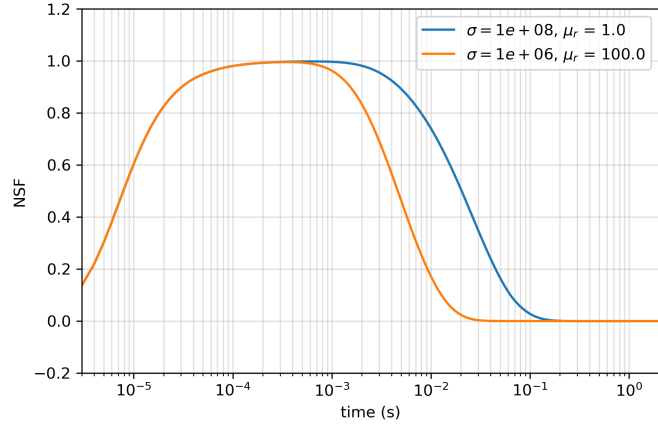


Figure 3.13: Normalized secondary field (NSF) through time. In the time-domain, we compute the NSF by taking the difference between the total magnetic flux at the receiver and the whole-space response and then taking the ratio with the whole-space magnetic flux prior to shutting off the transmitter.

conductance is

$$\mathcal{S} = \sigma \frac{tL}{2\pi r} \quad (3.9)$$

where t is the thickness of the casing, r is the radius of the casing and L is the length-scale of the pipe segment contributing to the signal. For vertical magnetic fields, the permeance is

$$\mathcal{P} = \mu \frac{t2\pi r}{L} \quad (3.10)$$

As the length-scale, L , is larger than the circumference of the pipe ($2\pi r$) the geometric contribution to the conductance is larger than that to the permeance.

An important take-away from this example is that the contributions of conductivity and permeability to the observed EM signals are not simply governed by their product. The geometry of the source fields plays an important role in how each contributes. Thus to accurately model conductive, permeable pipes, over a range of frequencies or times, a numerical code must allow both variable conductivity and variable permeability to be

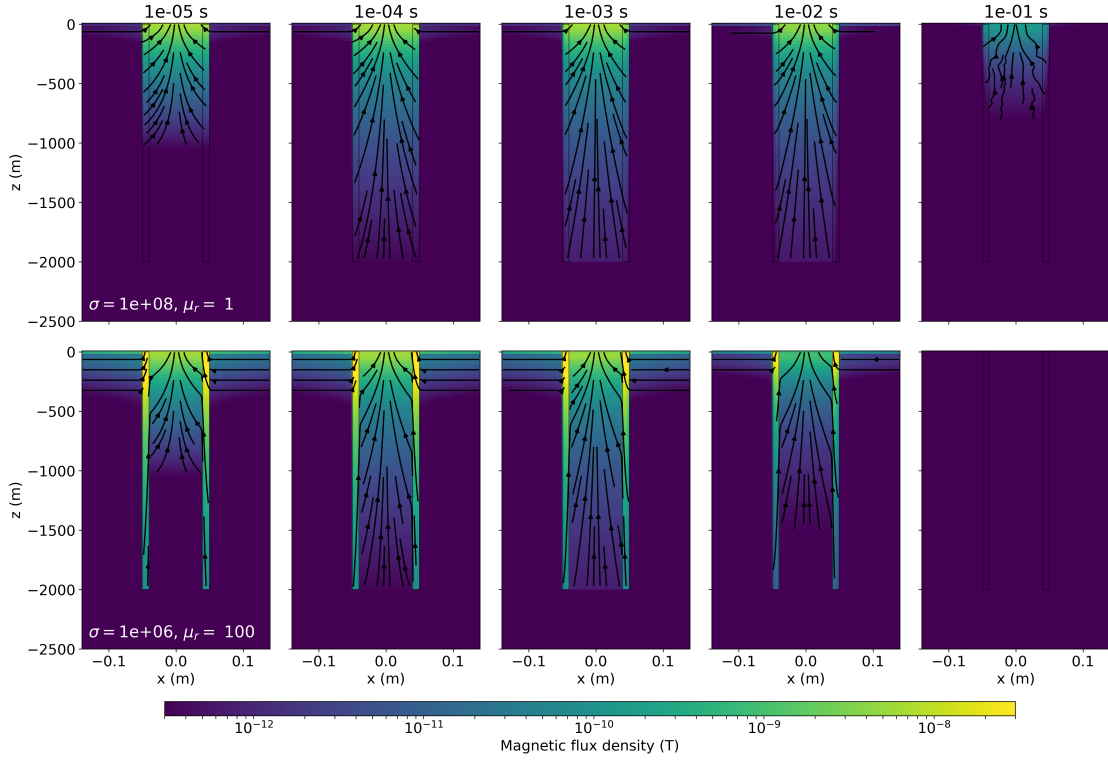


Figure 3.14: Secondary magnetic flux density for a conductive well (top row) and a conductive, permeable well (bottom row) through time. The source waveform is a step-off waveform.

considered.

3.4 Summary and Outlook

We have developed software for solving Maxwell's equations on 2D and 3D cylindrical meshes. The medium can have variable electrical conductivity and magnetic permeability. The 2D solution is especially computationally efficient and has a large number of practical applications. When cylindrical symmetry is not valid, the 3D solution can be implemented; a judicious design of the mesh can often generate a problem with fewer cells than would be required with a tensor or OcTree mesh, thus reducing the computational cost of a simulation. We demonstrated the versatility of the codes by modelling

the electromagnetic fields that result when a highly conductive and permeable casing is embedded in the earth.

We presented a number of different experiments involving DC, frequency-domain, and time-domain sources. The first two examples considered a simple DC resistivity experiment. In the first, we demonstrated that the numerically obtained currents, electric fields, and charges emulated those predicted by the asymptotic analysis in Kaufman (1990) for long wells. The second example looked at the transition in behavior of currents and charges between short and long wells. Even in this relatively simple example, the physics was more complex than we originally anticipated; we had not intuitively expected to see the large increase in charge density that was observed near the ends of the well.

In the subsequent examples, we considered electromagnetic experiments. The third example presented a grounded-source time domain experiment and showed the distribution of currents in the formation through time. It showed that the steel-casing can help excite a target at depth by 2 mechanisms: (1) the casing provides a high-conductivity pathway for bringing DC currents to depth, and (2) the casing channels the image current that is created after shut-off of the source. With respect to survey design, one consequence of the second point is that there may be an advantage to positioning the wire and return electrode along the same line as where the target is expected to be located. In this way, the current direction is reversed as the image current passes; the target is thus excited from multiple excitation directions and the resultant data can be beneficial in an inversion.

The final two examples incorporated magnetic permeability in the simulations. We showed that for a conductive and permeable casing, excited by a circular current source, there is a complicated magnetic field that occurs in the top few centimeters of the pipe.

Furthermore, the role of conductivity and permeability in the observed responses is more complex than their product; the source geometry and coupling with the casing are important to consider.

As new strategies and software are developed to handle more complex well-geometries, such as deviated or horizontal wells, it is important that we establish an understanding of the physics. Of critical importance is the ability to plot the charges, fields, and fluxes in the simulations. This is valuable for understanding the responses obtained from the experiment and it is a solid foundation for designing a field survey. We anticipate that the software provided with this publication can be a resource for building understanding and additionally, serve as a tool for testing 3D simulations with boreholes present.

The software implementation is included as a part of the SimPEG ecosystem. SimPEG also includes finite volume simulations on 3D tensor and OcTree meshes as well as machinery for solving inverse problems. This means that the cylindrical codes can be readily connected to an inversion and additionally, simulations and inversions of more complex 3D geologic settings can be achieved by coupling the cylindrical simulation with a 3D tensor or OcTree mesh using a primary-secondary approach (e.g. example 3 in Heagy et al. (2017a)). Beyond modelling steel cased wells, we envision that the 3D cylindrical mesh could prove to be useful in conducting 3D airborne EM inversions where a domain-decomposition approach, similar to that described in Yang et al. (2014), is adopted.

SimPEG and all of the further developments described in this paper are open source and freely available. The examples have been provided as Jupyter notebooks. This not only allows all of the figures in the paper to be reproduced, but provides an avenue by which the reader can ask questions, change parameters, and use resultant images to confirm (or not) their presumed outcome. We hope that our efforts to make the software

and examples accessible promotes the utility of this work for the wider community.

Chapter 4

Direct current resistivity with steel-cased wells

4.1 Introduction

Subsurface resistivity can be a valuable part of a geologic interpretation, whether that be identifying lithologic units, characterizing changes within a reservoir, or imaging subsurface injections associated with carbon capture and storage or hydraulic fracturing. In many of these settings, steel-cased wellbores are present. Steel has a significant electrical conductivity, which is generally six or more orders of magnitude larger than that of the surrounding of the geologic formation. Clearly, such a large contrast is important to consider when conducting a direct current (DC) resistivity survey. On one-hand, the role of the steel casing may be viewed as “distortion” which complicates the signals of interest (Wait, 1983; Holladay and West, 1984; Johnston et al., 1987). In other scenarios, a wellbore may be beneficial in that it can serve as an “extended electrode” so that current-injection and sampling of the resultant electrical potentials can take place

beneath near surface heterogeneities (Ramirez et al., 1996; Rucker et al., 2010; Rucker, 2012; ?) or so that currents injected at the surface can reach significant depths (Schenkel and Morrison, 1994; Weiss et al., 2016; Hoversten et al., 2017). The use of casings as extended electrodes extends back several decades. Sill and Ward (1978) used the well casing as a buried electrode for their mis-a-la-massé experiment at the Roosevelt Hot Springs geothermal field in Utah, as did Kauahikaua et al. (1980) for their mis-a-la-massé mapping of a high temperature geothermal reservoir in Hawaii. Sill (1983) used the well as a source to monitor an injection test at Raft River, Idaho to determine if measurable changes that might indicate the direction of fluid flow could be observed. Rocroi and Koulikov (1985) delineated a known resistive hydrocarbon deposit in the USSR by injecting current into two cased wells. More recently, applications for hydraulic fracturing, enhanced oil recovery and carbon capture and storage have been of much interest (Commer et al., 2015; Um et al., 2015; Weiss et al., 2016; Hoversten et al., 2017). There has also been an increase in interest in examining the use of electrical or electromagnetic methods deployed on the surface to look for flaws or breaks in the casing (Wilt et al., 2018).

To build a physical understanding of electrical and electromagnetic methods in settings where steel-cased wells are present, there are several areas to be investigated. First, the significant conductivity of the steel will impact the behavior of the charges, currents, and electric fields. This is true at the electrostatic limit, relevant to DC resistivity surveys, as well as when the source fields are time-varying, as in electromagnetic (EM) surveys. When considering EM surveys, induction effects also influence the responses, and magnetic fields and fluxes become relevant, meaning that the magnetic permeability of the steel then introduces further complexity into the signals we measure. This paper is concerned with the first set of physical phenomena: understanding the physics of steel

casings at DC.

Much of the initial theory and understanding of the behavior of electric fields, currents, and charges, was developed in the context of well-logging. Kaufman (1990) and Kaufman and Wightman (1993) provide a theoretical basis for our understanding; the first paper derives an analytical solution for a DC experiment where an electrode is positioned along the axis of an infinite length well, and discusses where charges accumulate and how currents leak into the surrounding formation. From this, Kaufman (1990) shows that by measuring the second derivative of the electric potential, information about the formation resistivity can be obtained. The second paper extends the analysis for finite length wells. Schenkel and Morrison (1990); Schenkel (1991); Schenkel and Morrison (1994) pioneered numerical work analyzing the influence of steel-cased wells on geophysical data using an integral equation approach for solving the DC resistivity problem. They expand upon the logging-through-casing application and discuss limitations of the transmission line solution presented in Kaufman (1990) for this application. They also explored the feasibility of cross-hole and borehole-to-surface surveys where one electrode is placed within, or beneath, a cased borehole. These examples demonstrated that the casing can improve detectability of a conductive target as compared to the scenario where no cased well is present.

With improvements in computing power, it has become possible to perform 3D numerical simulations with steel-cased wells. Simulations which capture the challenging geometry and large physical property contrasts due to well casings have been successfully employed for DC and EM problems (e.g. Swidinsky et al. (2013); Commer et al. (2015); Hoversten et al. (2015); Tang et al. (2015); Um et al. (2015); Weiss et al. (2016); Yang and Oldenburg (2016); Heagy and Oldenburg (2018a)). These advances provide the opportunity to delve further into aspects of the physics governing the behav-

ior of fields, fluxes, and charges when casings are present in an electrical or electromagnetic survey. To develop our understanding we start with DC resistivity.

In this paper, we focus our attention on three aspects of DC resistivity in the presence of steel-cased well. In section 4.3, we examine the feasibility of conducting a surface DC survey to detect a flaw in the casing and discuss factors that influence detectability of a flaw. In section 4.4, we examine the use of DC resistivity for geophysical imaging when a steel-cased well is present. Finally, in section 4.5, we assess strategies applied in the literature for approximating a steel-cased well with a coarse-scale model to reduce computational cost.

Source codes for all of the simulations shown are open source, licensed under the MIT license, and are available as Jupyter notebooks at: <https://github.com/simpeg-research/heagy-2018-dc-casing> (Heagy and Oldenburg, 2018b). The examples in the paper have been selected with an emphasis on examining physical principles; however, we envision that the Jupyter notebooks included with this publication could serve as useful survey design tools.

4.2 Governing equations and numerical modelling

The governing equations for the DC resistivity problem are given by:

$$\begin{aligned} \nabla \cdot \vec{j} &= I(\delta(\vec{r} - \vec{r}_{s+}) - \delta(\vec{r} - \vec{r}_{s-})) \\ \vec{e} &= -\nabla\phi \end{aligned} \tag{4.1}$$

where \vec{j} is the current density, I is the magnitude of the source current, and \vec{r}_{s+} and \vec{r}_{s-} are the location of the positive and negative source electrodes, respectively. In the electrostatic limit, which is applicable for the DC experiment, the electric field \vec{e} is curl-free and can therefore be expressed as the gradient of a scalar potential ϕ , giving the

second equation in equation 4.1. The electric field and the current density are related through Ohms law:

$$\vec{j} = \sigma \vec{e} \quad (4.2)$$

which we invoke to reduce the two first-order partial differential equations in equation 4.1 to a single, second order equation in ϕ :

$$\nabla \cdot \sigma \nabla \phi = -I(\delta(\vec{r} - \vec{r}_{s^+}) - \delta(\vec{r} - \vec{r}_{s^-})) \quad (4.3)$$

In addition to considering the current density and electric fields, we will also present results in terms of charges. The charge density is related to the electric field through

$$\nabla \cdot \vec{e} = \frac{\rho_f}{\epsilon_0} \quad (4.4)$$

To numerically solve equation 4.3, we use a finite volume approach. From the discrete solution for the electric potentials, the discrete electric field, current density and charge density can be computed directly. We employ both cylindrically symmetric and 3D cylindrical meshes, which include an azimuthal discretization. All of the numerical simulations are run with the open source software described in (Heagy and Oldenburg, 2018a), which relies on the electromagnetics module within SimPEG (Cockett et al., 2015; Heagy et al., 2017a).

4.3 DC resistivity for casing integrity

Degraded or impaired wells can pose environmental and public-health hazards. A flaw in the cement or casing can provide a conduit for methane to migrate from depth into groundwater aquifers or into the atmosphere. This is particularly of concern for shale

gas wells. Elevated levels of thermogenic methane, which are attributed to deep sources (rather than biogenic methane which can be generated closer to the surface), in ground-water wells in Pennsylvania has been positively correlated with proximity to shale gas wells in the Marcellus and Utica (Osborn et al., 2011; Jackson et al., 2013), and failure rates of unconventional wells (e.g. shale gas wells) is estimated to be 1.57 times larger than that of a conventional well drilled in the same time-period (Ingraffea et al., 2014). Wells can fail if there is a compromise in the cement or the casing. To diagnose the integrity of a well with electrical methods, we require a contrast in electrical conductivity to be associated with the flaw, thus we will focus our attention to detecting flaws in the highly conductive casing.

Under what circumstances should we be able to detect a flaw in the casing using DC resistivity from the surface? To address this question, we begin by examining how a flaw which comprises the entire circumference of the pipe along some depth interval changes the charge distribution and thus the resultant electric fields we measure on the surface. From there, we investigate the role of parameters including the depth of the flaw and the background conductivity on our ability to detect it from the surface. Finally, we examine the scenario in which only a portion of the circumference of the pipe is flawed.

4.3.1 Basic experiment

The experiment we consider is a “top-casing” DC resistivity experiment where one electrode is connected to the wellbore at the surface and a return electrode is positioned some distance away. The concept and basic physics is the same as a mis-a-la-massé survey in which the positive electrode is connected to a conductive target. When the source is turned on, positive charges are distributed on the interface between the conductive target and the resistive host. Electric potentials are measured on the surface and these data are

then used to infer information about the extent of the conductor (Telford et al., 1990a). Applying the same principles to a casing integrity experiment, we connect a positive electrode to the casing, and for an intact casing, positive charges will be distributed on the outer interface of the casing along its entire length. If corrosion causes a flaw across the diameter of the casing, the continuity of the conductive flow-path for charges is interrupted, thus we expect a larger charge on the top portion of the flawed casing than we would if it were intact. This results in a larger electric field at the surface than would be observed if the casing were intact. The difference in electric field (or electric potentials) from the expected electric field that results from an intact well could then be an indicator that there is a problem with the well.

To demonstrate the principles, we start by considering a simple model of a casing in a half-space. The intact well is 1km long, has an outer diameter of 10cm, a thickness of 1cm and a conductivity of 5×10^6 S/m. The background is 10^{-1} S/m background, and the conductivity of the inside of the well is taken to be equal to that of the background. The positive electrode is connected to the top of the casing and the return electrode is positioned 2km away. To simulate the physics, the 3D cylindrical DC code described in Heagy and Oldenburg (2018a) was employed. In Figure 4.1 we show cross-sections of the: (a) electrical conductivity model, (b) current density, (c) charge density, and (d) electric field for the intact well (top row) and a flawed well (bottom row) that contains a 10m gap in the casing at 500m depth. As expected, the introduction of a resistive flaw prevents currents from reaching the bottom portion of the well. This results in increased currents, charge density and thus electric fields within the top 500m.

To quantify the charge along the length of the well, we have plotted the charge as a function of depth for the intact well (black), flawed well (blue), and also a short well of 500m length (grey dash-dot) in Figure 4.2a. In each of the wells, we observe that there

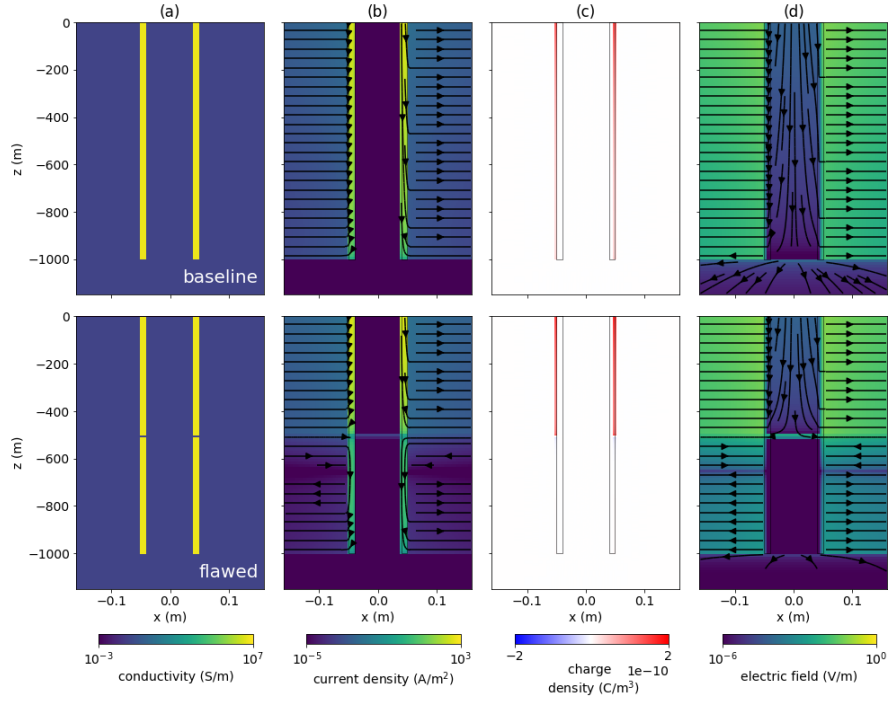


Figure 4.1: Cross section showing: (a) electrical conductivity, (b) current density, (c) charge density, and (d) electric field for a top-casing DC resistivity experiment over (top) an intact 1000m long well and (bottom) a 1000m long well with a 10m flaw at 500m depth.

is an increase in charge density near the end of the discontinuity along the length of the well. This was also noted in Griffiths and Li (1997); Heagy and Oldenburg (2018a) and is attributed to edge-effects. At an interface between materials with two different conductivities, the normal component of the current density must be conserved, as well as the tangential component of the electric field; the discontinuity at the end of the pipe, and at the location of the flaw, means the continuity conditions must be preserved simultaneously in the radial and vertical directions, and this complicates the behavior of the fields, fluxes and charges. Another observation is that the flawed and short wells have nearly identical charge distributions in the top 500m. In the bottom portion of the flawed well, where the remaining conductive material is, a small dipolar charge is introduced,

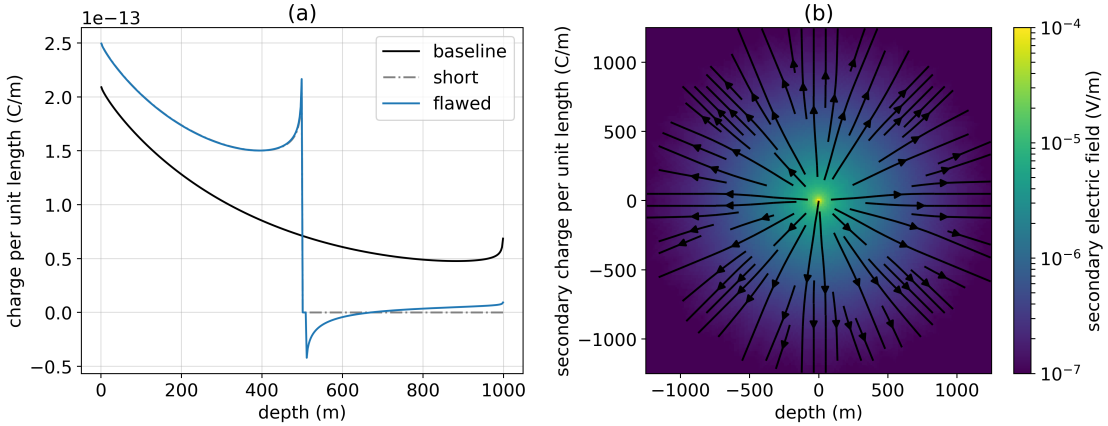


Figure 4.2: (a) Charge along the length of the intact well (black), a 500m well (“short”, grey dash-dot), and a well with a 10m flaw at 500m depth (blue), in a top-casing DC resistivity experiment. (b) Secondary electric field due on the surface of the earth due to the flaw in the casing. The primary is defined as the electric field due to the 1000m long intact well. The return electrode is 2000m away from the well.

but this is nearly an order of magnitude smaller than the charge in the top portion of the pipe. The signal due to the flaw can be defined as the difference between the total response due to a flawed well and the total response due to an intact well (the primary); we will refer to this difference as the secondary response. The secondary charge is dipolar in nature with positive charge above the flaw and negative charge beneath the flaw. We note that the charge distributions along the short well, truncated where the flaw starts at 500m depth, and along the top portion of the flawed well are almost identical; these charges are the source of signal for a surface electric field measurement. This suggests that an inversion strategy, where one attempts to estimate the length of a well, may be an effective approach for characterizing the depth to a flaw.

Impact of the vertical extent of the flaw

A 10m flaw is quite long and it is of interest to see how the results are changed if the flaw has a smaller vertical extent. The distribution of charges shown in Figure 4.2 hints that the flaw may not need to be very long in order to still significantly influence the response. To confirm this, we adopt a much finer vertical discretization in order to model smaller flaws. Here, we use a shorter, 50m long well in order to reduce computational load. The flaw is positioned at 25m depth, and the length of the impairment is varied. This simulation is conducted on a cylindrically symmetric mesh, the positive electrode is connected to the casing, and a return electrode is positioned 50m away.

The resultant charge distributions are shown in Figure 4.3. For comparison, we have again shown the charge on a well that is truncated at the location of the flaw; this is the “short” well and results are displayed using the grey dash-dot line. The charge distribution is similar for all of the flawed-well scenarios, even for flaws smaller than the thickness of the casing (10^{-2} m). We see similar behavior to that shown in Figure 4.2, where positive charge accumulates within the top portion of the well and a small dipole charge is present in the bottom portion of the well. There are minor differences in amplitude as the vertical extent of the flaw is changed; as the extent of the flaw decreases, the amplitude of the dipolar charge on the bottom portion of the well increases slightly while the amplitude of the positive charge on the top portion of the well decreases. These distinctions, however, are small in magnitude, and even if the background is more conductive, the casing is still orders-of-magnitude larger in conductivity than any geologic material we are likely to encounter. Thus, we can conclude that, so long as the impairment affects the entire circumference of the casing, the extent of that flaw has little impact on the charge that accumulates in the top portion of the well. As such, we will proceed in our analysis using a 10m flaw in the 1km well so that a fine vertical

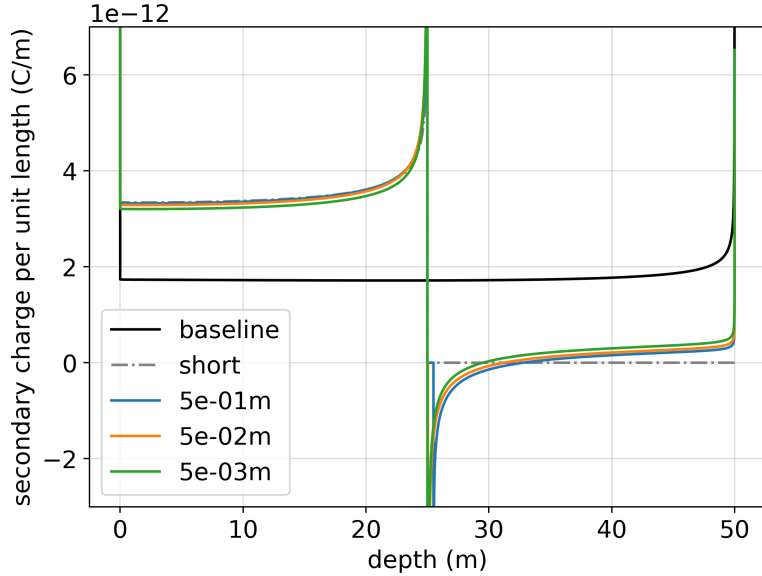


Figure 4.3: Charge along the length of a 50m long intact well (black), a 25m well (“short”, grey dash-dot), and four wells, each with a flaw starting at 25m depth and extending the length indicated by the legend (5×10^{-1} m (blue), 5×10^{-2} m (orange), and 5×10^{-3} m (green)) in a top-casing DC resistivity experiment. For reference, the diameter of the casing is 10^{-1} m and its thickness is 10^{-2} m. The return electrode is 50m away from the well and a cylindrically symmetric mesh was used in the simulation.

discretization is not necessary.

4.3.2 Survey design considerations

When examining detectability of a signal, there are two aspects to consider: (1) the signal must be larger than the noise floor of the instrument, and (2) the signal must be a significant percentage of the primary; for the casing integrity experiment, the primary is the signal due to the intact well. Due to the cylindrical symmetry of the charge on the well, we expect the electric field at the surface to be purely radial, thus only radial electric field data need be collected at the surface.

In Figure 4.4, we have plotted the primary field (top row), secondary field (second

row) and secondary field as a percentage of the primary (third row) for four different return electrode locations. In (a), the return electrode is 2000m offset from the well, in (b) the offset is 750m, in (c) the offset is 500m, and in (d) the offset is 250m. In addition to the plan view, we have plotted the primary electric field (black), total electric field for the flawed well (blue) and secondary radial electric field (orange) along the $\theta = 90^\circ$ azimuth in the fourth row of Figure 4.4. The fifth row shows the secondary as a percentage of the primary.

At the furthest offset (Figure 4.4a), there is nearly complete cylindrical symmetry in the primary field. With complete cylindrical symmetry there is no preferential direction along which to collect data. As we move the return electrode closer, for example to 750m from the well, we notice that the secondary electric field does not change substantially. However, if we examine the ratio of the secondary to the primary (second and fifth rows), we see that the ratio has increased. Although the primary field has similar, if not larger amplitude near the well, it also has considerable curvature. As a result, the proportion of the primary field that is in the radial direction has decreased in amplitude. Hence the important characteristic, the ratio of the secondary to primary of the radial components, has increased. The above principles are further enhanced as the return current is brought closer to the well as in panels (c) and (d), where the return electrode is brought to 500m and 250m from the well. Again, for all of these examples the amplitude of the secondary field at the surface is quite similar. However, the choice of azimuth for the survey line will greatly affect the size of the ratio. In terms of survey design, we can take advantage of the return electrode to reduce coupling with the primary.

For our following examples we will place the return electrode at 500 m from the well and collect radial data along a line that is perpendicular to the source line. We will examine several factors influencing detectability of a flaw, including the depth of

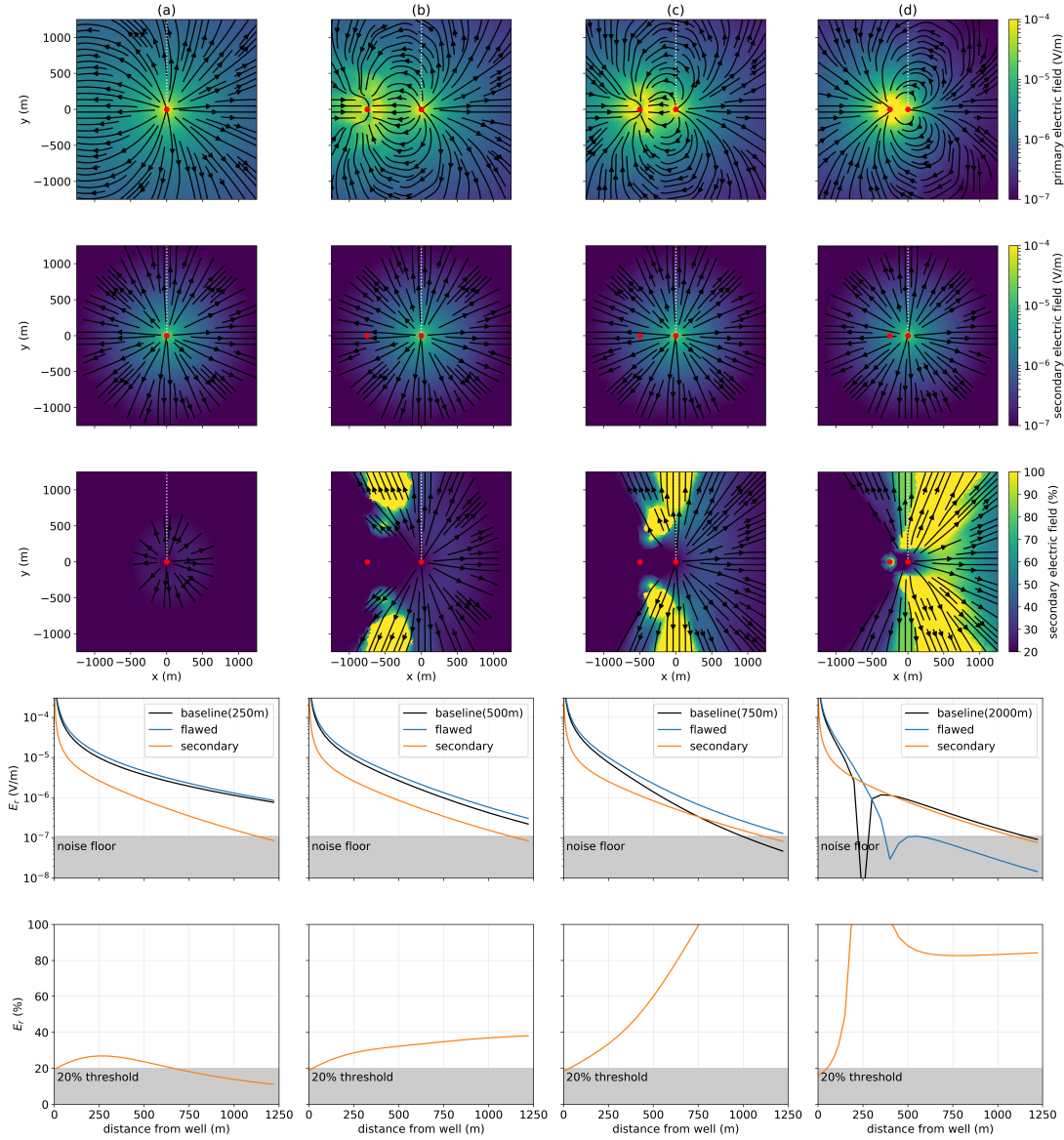


Figure 4.4: (Top row) primary electric field, (second row) secondary electric field, and (third row) secondary electric field as a percentage of the primary radial electric field for a return electrode that is offset (a) 2000m, (b) 750m, (c) 500m, and (d) 250m from the well. The primary is defined as the response due to the 1000m long, intact well. In each figure, the electrode locations are denoted by the red dots. In the third row, the colorbar has been limited between 20% and 100%. The fourth and fifth rows show radial electric field data collected along the $\theta = 90^\circ$ azimuth (the white dotted lines in the top three rows). The fourth row shows the primary (black line), the total electric field due to the flawed well (blue line), and the secondary radial electric field (orange line). The fifth row shows the secondary as a percentage of the primary.

the flaw and the conductivity of the background in the following sections. We will also examine the scenario where only a portion of the circumference of the well has been compromised.

4.3.3 Factors influencing detectability

Depth of the flaw

The introduction of a flaw in the well changes the distribution of charges along the length of the well and causes a secondary dipolar charge centered about the flaw. The position and strength of this dipole will affect our ability to detect the flaw. To examine this, we have taken the same model of a 1km pipe in a 10^{-1} S/m background and varied the depth of the flaw from 300m to 900m. In Figure 4.5, we have plotted radial electric field results along a line perpendicular to the source electrodes; the return electrode is positioned 500m from the well. In (a), we show total radial electric field, in (b) the secondary radial electric field (with the primary being the electric field resulting from the intact well, shown in black in panel a), and in (c) we show the secondary radial electric field as a percentage of the primary. We have also indicated where values fall below a 10^{-7} V/m noise floor on Figure 4.5 (a) and (b), as well as those that fall below a 20% threshold in (c). A threshold of 20% may be conservative, however, it does depend on knowledge of the background conductivity as well as the geometry and physical properties of the well. In many scenarios, these may not be well-constrained, thus we select a conservative threshold for this analysis. Any detectability analysis will be site-dependent and we have therefore made all source-code available so that a similar workflow may be followed and adapted to include setting-specific parameters.

When a well is impaired, the total radial electric field is larger than that due to the baseline, intact well. The strength of the secondary response decreases as the depth of

the flaw increases. For this example of a 1000m long well in a 10^{-2} S/m background, a flaw at 900m depth is not detectable; there is no overlap between the region in which the secondary electric field (Figure 4.5b) is above the noise floor and the region in which the secondary comprises a significant percentage of the primary (Figure 4.5c). This might be expected, as the difference between the charges distributed along a 900m long segment versus the 1000m long well are not drastically different. For a flaw at 700m depth, there is a window between 400m offset and 800m offset over which the radial electric field data are sensitive to the flaw. As the depth to the impairment decreases, both the spatial extent over which data are sensitive to the flaw, and the magnitude of the secondary response in those data, increase.

Background conductivity

The total charge on the well is controlled by the contrast in conductivity between the steel-cased well and the surrounding geology. Increasing the conductivity of the background reduces that contrast thus reducing the amount of charge on the well. The result is a decrease in the total electric field at the surface. Similarly, the strength of the secondary dipolar charge introduced with the presence of an impairment also depends upon the available charge and will also be reduced with increasing background conductivity. In Figure 4.6, we have adopted the same model of a 1km well with a 10m impairment at 500m depth, and show the radial electric field for the flawed (solid lines) and intact (dashed lines) well as the background conductivity is varied. A resistive background promotes the strongest total and secondary signals. As the conductivity increases, detectability becomes more challenging; at a conductivity of 3×10^{-1} S/m, the flaw at 500m depth is undetectable as there is no overlap in the regions where the secondary signal is above the noise floor and where it comprises a significant percentage of the

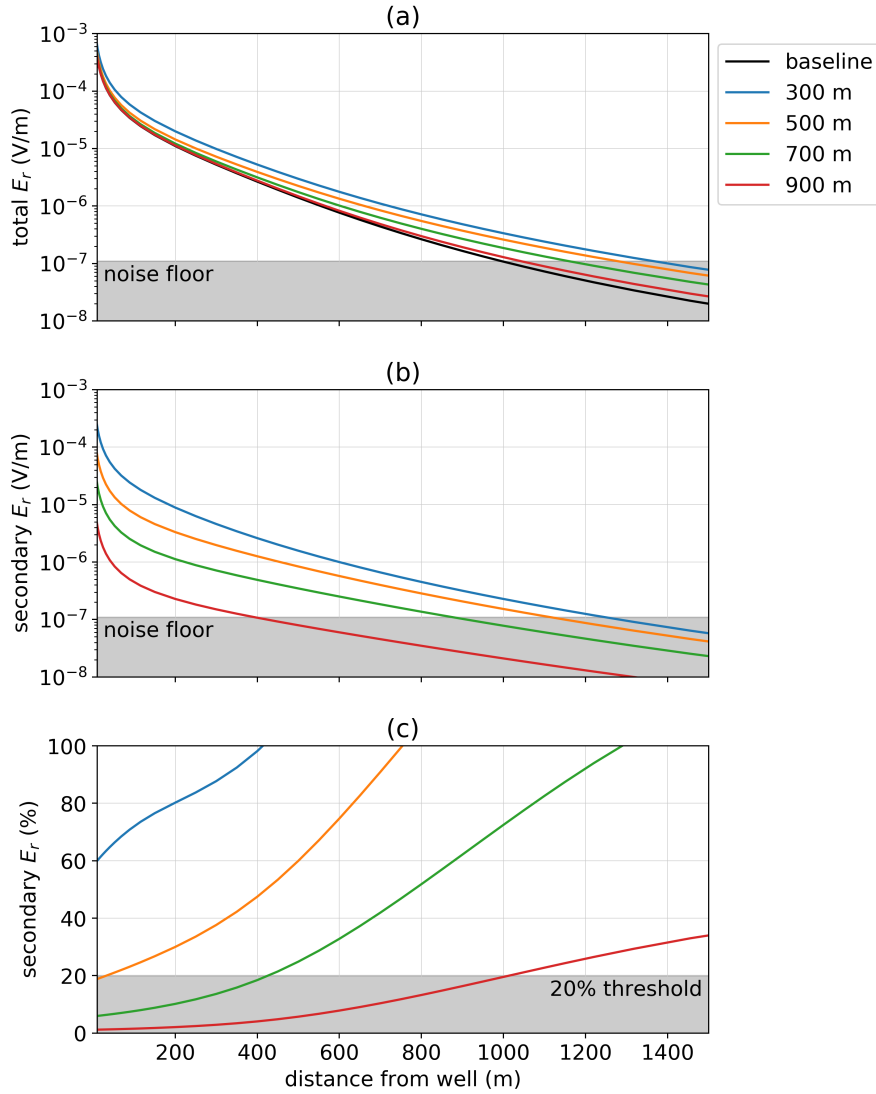


Figure 4.5: Radial electric field as the depth of the flaw along a 1km long well is varied. The positive electrode is connected to the top of the casing, the negative electrode is positioned 500m away and data are measured along a line 90° from the source electrodes. In (a), we show the total electric field for four flawed wells, each with a 10m flaw at the depth indicated on the legend. The black line shows the radial electric field due to an intact well; we define this as the primary. In (b), the secondary radial electric field is plotted and in (c), we show the secondary radial electric field as a percentage of the primary.

primary.

Variations in the background geology will also influence the distribution of charges and thus the measured signal at the surface. To examine the challenges introduced when variable geology is considered, we will introduce a layer into the model and vary its conductivity. The layer is 50m thick and its top is at 400m depth. The flaw will again be positioned at 500m depth, and the background conductivity is 10^{-1} S/m. The return electrode is 500m from the well, and radial electric field data are measured along a line perpendicular to the source. In Figure 4.7, we show data for a flawed well (solid) and intact well (dashed) for scenarios in which a conductive or resistive layer is positioned above the flaw. The presence of a resistive layer improves detectability, while a conductive layer reduces detectability.

To understand the physical phenomena governing this, we have plotted a cross section through: (a) the model, (b) the currents, (c) the charges, and (d) the electric field in Figure 4.8 for (first row) a model of an intact well with a conductive layer present, (second row) a flawed-well model including a conductive layer, (third row) a model of an intact well with a resistive layer, and (fourth row) a flawed-well model including the resistive layer. For the comparison, there is two orders of magnitude difference between the background and the layer. When a conductive layer is present, we see that it acts to “short-circuit” the system as there is significant current leak-off into that layer. This reduces the amount of current that reaches the flawed section of the well and decreases the total charge on the well, which is the source of our signal. Conversely, when a resistive layer is present, there is less leak-off of currents. In fact, Yang and Oldenburg (2016) showed that rather than leaking-off, currents can enter the casing if a resistive layer is present. In terms of detecting a flaw beneath a resistive layer, this means that the current density and charge along the well increases, thus amplifying the response due to

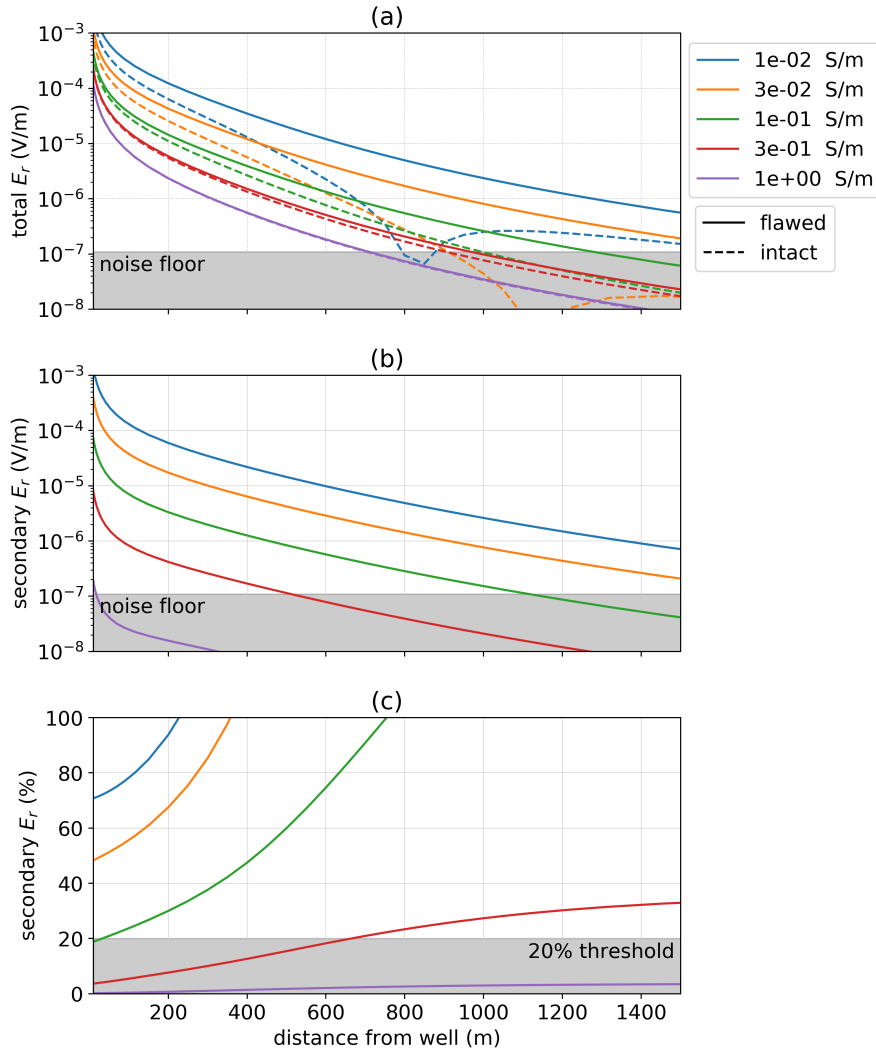


Figure 4.6: Radial electric field as the conductivity of the background is varied for a 1km well with a 10m flaw at 500m depth. The positive electrode is connected to the top of the casing, the negative electrode is positioned 500m away and data are measured along a line 90° from the source electrodes. In (a), we show the total electric field for five different background conductivities, each indicated on the legend. The solid lines indicate the response of the flawed well and the dashed lines indicate the response of the intact well (the primary). In (b), the secondary radial electric field is plotted and in (c), we show the secondary radial electric field as a percentage of the primary.

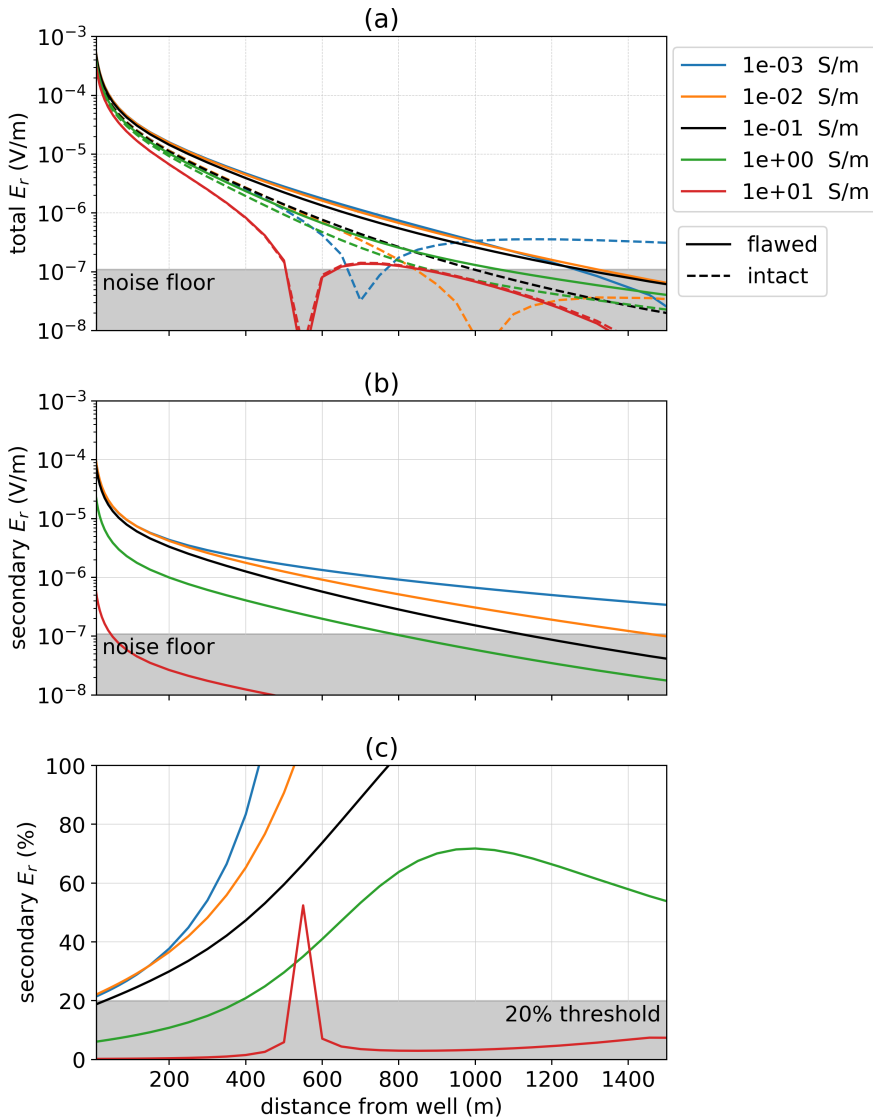


Figure 4.7: Radial electric field as the conductivity of a 50m thick layer positioned at 400m depth is varied. The positive electrode is connected to the top of the casing, the negative electrode is positioned 500m away and data are measured along a line 90° from the source electrodes. In (a), we show the total electric field five different layer conductivities. The black line shows the scenario where the layer has the same conductivity as the background. The dashed-lines indicate the intact well and the solid lines indicate the flawed well. In (b), the secondary radial electric field is plotted (with respect to an intact well primary) and in (c), we show the secondary radial electric field as a percentage of the primary.

the flaw.

Conductivity of the casing

The conductivity of the casing is also relevant to how the charges are distributed along its length. For highly conductive wells, the charge along the length of the well is approximately uniform, for more resistive wells, the charges follow an exponential decay, as shown in Figure 4.9. Schenkel (1991) described the decay of currents, and thus the distribution of charges along the length of a well, in terms of the conduction length,

$$\delta_L = \sqrt{\frac{S_c}{\sigma_0}} = \sqrt{\frac{2\pi r t \sigma_c}{\sigma_0}} \quad (4.5)$$

Where S_c is the cross-sectional conductance of the casing ($S_c = 2\pi r t \sigma_c$ for a casing with radius r , thickness t , conductivity σ_c and has units of $[S \cdot m]$) and σ_0 is the conductivity of the background. The conduction length is akin to skin depth in electromagnetics and is the depth at which the amplitude of currents have decreased by a factor of e^{-1} . Casing conductivities of 5×10^5 S/m, 5×10^6 S/m, and 5×10^7 S/m correspond to conduction lengths of ~ 180 m, 560 m, 1800 m. For the most resistive well shown, 5×10^5 S/m, the vast majority of current has decayed well before it reaches the flaw; the majority of charges are concentrated where the currents leak off, near the top of the well. Correspondingly, there is greater sensitivity to a flaw in a conductive well than in a resistive well, as is reflected in the radial electric field data shown in Figure 4.10.

Partial flaw

The above examples considered an impairment that affects the entire circumference of the casing. This may be suitable in some scenarios where a particular geologic unit subjects the well to corrosive conditions, however, flaws may also be vertical cracks

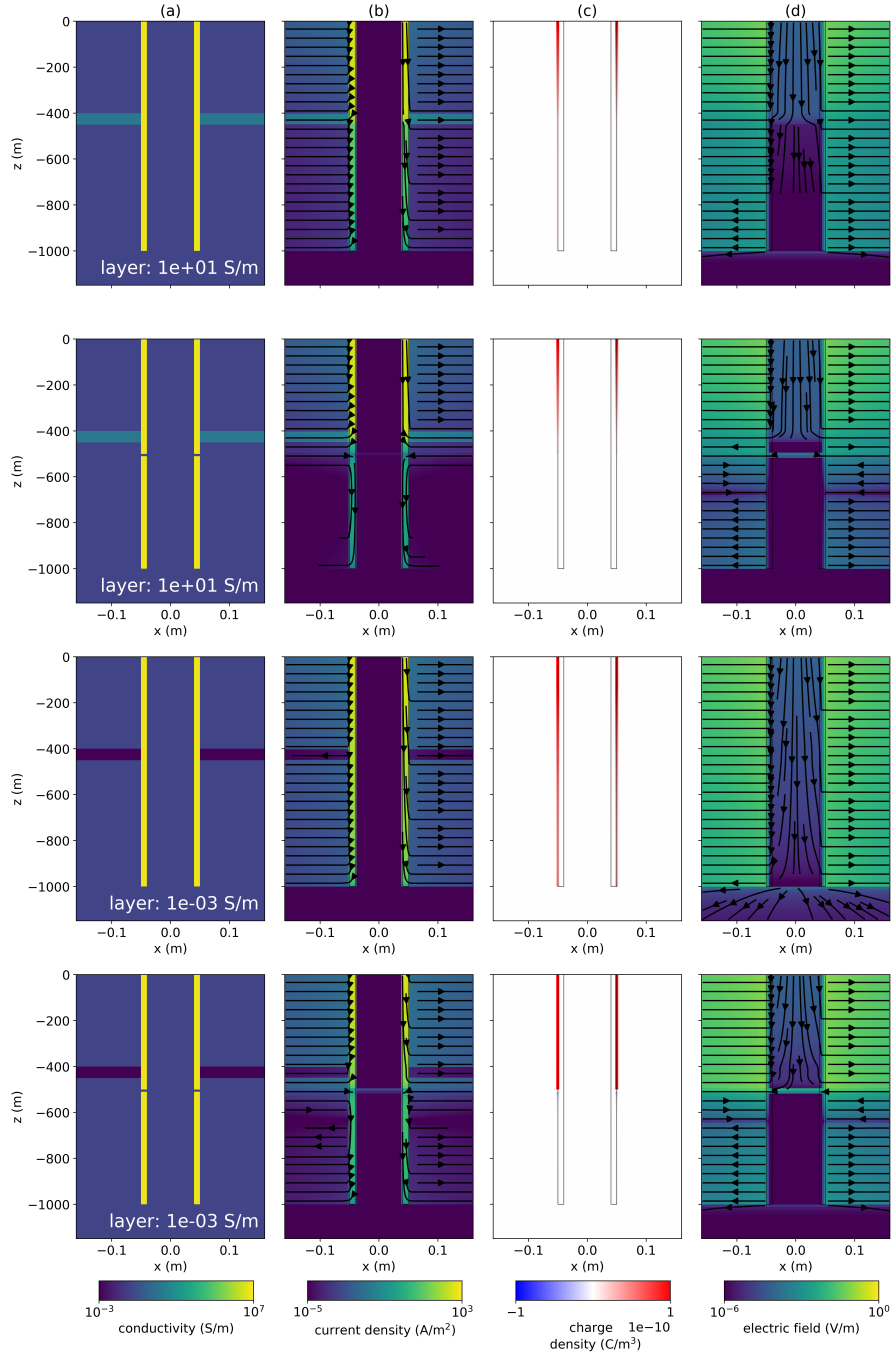


Figure 4.8: Cross section showing: (a) electrical conductivity, (b) current density, (c) charge density, and (d) electric field for a top-casing DC resistivity experiment over models with a conductive layer (top two rows) and a model with a resistive layer (bottom two rows). In all, the layer extends from 400m to 450m depth. The plots in the second and fourth rows show the model, currents, charges and electric fields for a well with a 10m flaw at 500m depth.

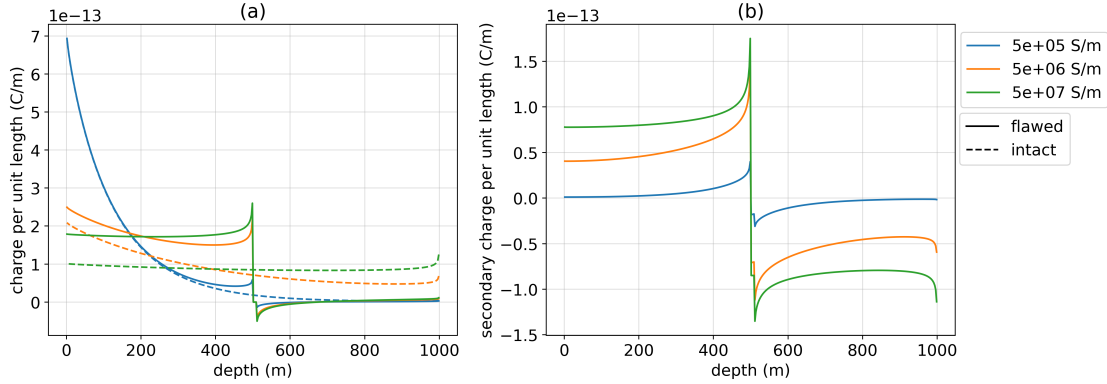


Figure 4.9: (a) Charge along the length of wells with three different conductivities (each indicated by a different color in the legend). The intact wells are denoted with dashed lines and the flawed wells are denoted with solid lines. (b) Secondary charge along the flawed and short wells. The primary is defined as the electric field due to the 1000m long intact well. The return electrode is 2000m away from the well.

along the well (e.g. if pipe burst occurs). This is a much more challenging problem for DC resistivity because, if only a portion of the circumference is impaired, there is still a high-conductivity pathway for currents to flow along the entire length of the well. To examine the feasibility of detecting a partial flaw, we have run simulations where half of the circumference of the casing is compromised, leaving the other-half intact.

We consider four different depth extents of the flaw between 10m and 300m; in all scenarios the top of the flaw is at 500m. In Figure 4.11a, we have plotted the total radial electric field resulting from an intact well (black), wells where the entire circumference is compromised (solid) and wells in which 50% of the circumference has been compromised (dashed); (b) and (c) show the secondary radial electric field and the secondary as a percentage of the primary, respectively. We see that the depth-extent of the flaw has little impact on the fully-compromised wells, which is consistent with the observations in our previous examples. However, if the well is partially flawed, we do see variation

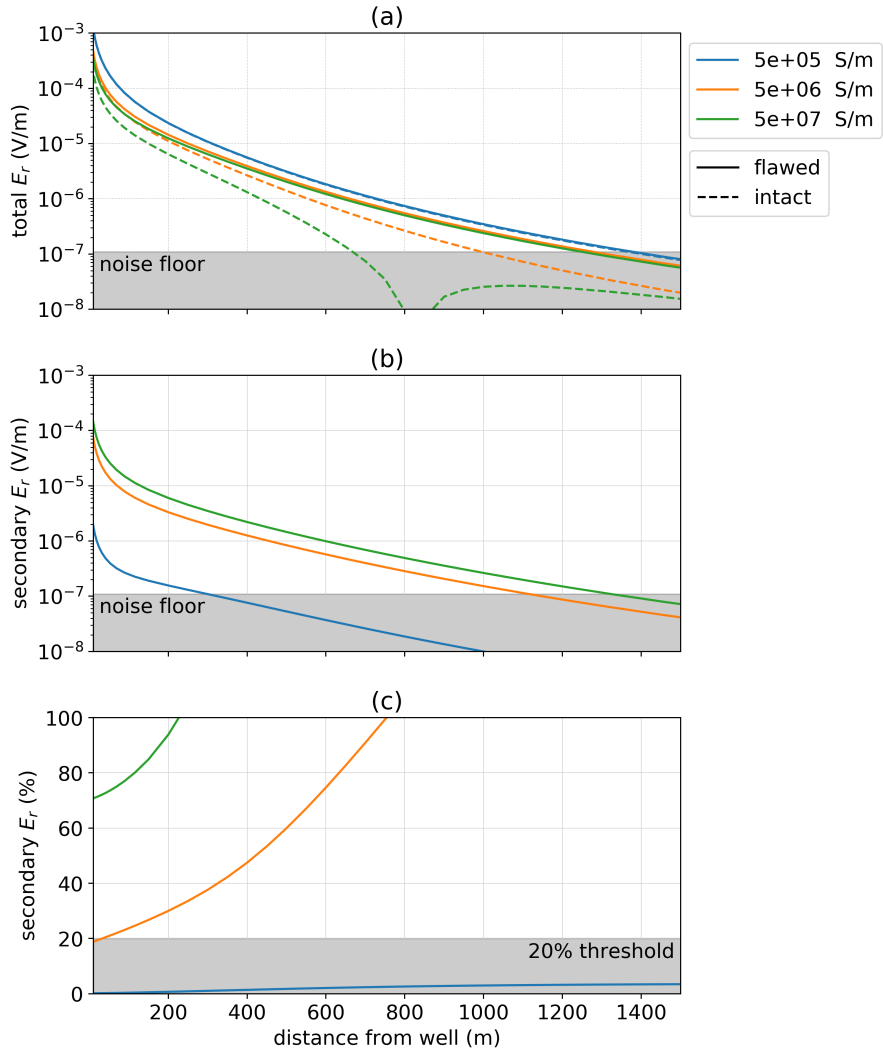


Figure 4.10: Radial electric field as the conductivity of the casing is varied for a 1km well with a 10m flaw at 500m depth. The positive electrode is connected to the top of the casing, the negative electrode is positioned 500m away and data are measured along a line 90° from the source electrodes. In (a), we show the total electric field for three different casing conductivities, each indicated on the legend. The solid lines indicate the response of the flawed well and the dashed lines indicate the response of the intact well (the primary). In (b), the secondary radial electric field is plotted and in (c), we show the secondary radial electric field as a percentage of the primary.

in the secondary response. By compromising 50% of the circumference of the well, we have reduced the effective cross-sectional conductance over that portion of the well. Numerical experiments show that if, instead of introducing a flaw which comprises 50% of the circumference of the well, we reduce the conductivity of the intact well by 50% over the same depth extent as the flaw, we obtain similar, but not identical, responses at the surface. Although for extensive flaws, there is a small region over which the secondary signal is above the noise floor, there are no regions where this coincides with measurements where the secondary fields are a significant percentage of the primary. There may be a subset of circumstances, such as if the flaw is near to the surface, or if the background geology is sufficiently well-known so that the percent threshold can be reduced, where a partial flaw may be diagnosed, however, these results demonstrate that a partial flaw is a challenging target for a DC resistivity survey.

4.3.4 Summary

In summary, we provided an overview of the fundamental physics governing the behavior of currents, charges, and electric fields in a top-casing DC resistivity experiment to detect an impairment in the well. If a flaw comprises the entire circumference of some depth interval along the casing, then the charges are concentrated in the portion of the well above the flaw, and to first approximation, the charge distribution is equal to that of a well which has been truncated at the depth of the flaw. This excess charge is the source of our signal. As it is cylindrically symmetric, the resultant secondary electric fields due to the flaw are purely radial. In terms of survey-design, we can take advantage of this knowledge and use the return electrode location to reduce coupling with the primary electric field in our data (as shown in Figure 4.4). Our ability to detect a flaw across the entire circumference of the casing depends upon the conductivity of the background

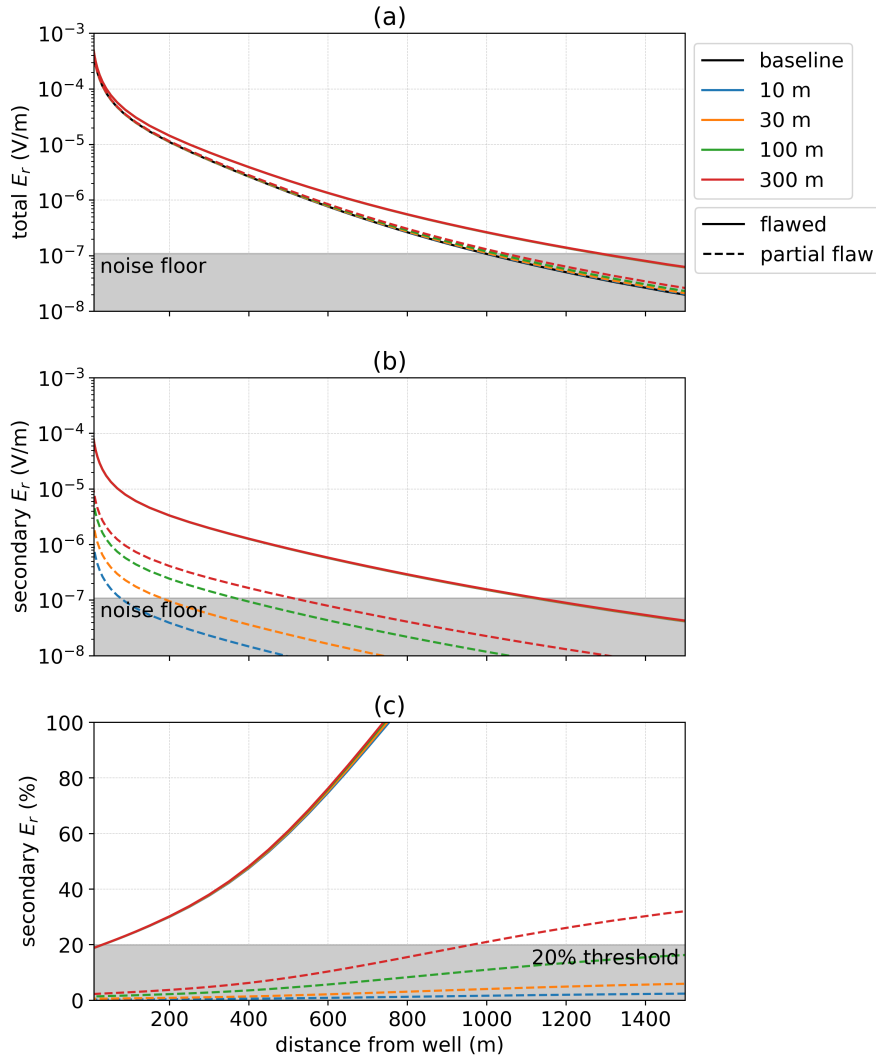


Figure 4.11: Radial electric field as the vertical extent of the flaw is varied. The positive electrode is connected to the top of the casing, the negative electrode is positioned 500m away and data are measured along a line 90° from the source electrodes. In (a), we show the total electric field for four different flaw extents. The black line shows the response of the intact well. The dashed-lines indicate the partially flawed wells (50% of the circumference is compromised) and the solid lines flawed wells in which the entire circumference of the well has been compromised. In (b), the secondary radial electric field is plotted (with respect to an intact well primary) and in (c), we show the secondary radial electric field as a percentage of the primary.

and casing, as well as the depth of the flaw. Larger contrasts between the casing and the background (e.g. a more resistive background and / or a more conductive casing) increase the secondary response, as does decreasing the depth of the flaw. If only a portion of the circumference is impaired, leaving a conductive pathway connecting the top and bottom portions of the casing, the secondary signal is small and thus will be challenging to detect under most circumstances.

For the subset of scenarios where we do have data sensitivity to the flaw, an inverse problem can be solved to estimate the depth of the impairment. One approach would be to use a reduced modeling procedure whereby only a few parameters are sought. For the case presented here, we might invert for a smooth background, the length of the well, and potentially the conductivity of the casing, if it is not known a-priori.

In the next section, we transition from viewing the casing as the target to working on the scale of a geophysical imaging application in reservoir monitoring and viewing the casing as a high-conductivity feature present in that setting.

4.4 Survey design for exciting targets at depth

There are many problems in hydraulic fracturing, carbon capture and storage and enhanced oil recovery that require targets to be illuminated and data to be acquired and inverted. Typically these experiments include steel-cased wells and the target of interest could be resistive or conductive. The target could be immediately adjacent to a well or offset from it, and the survey may employ electrodes on the surface or positioned down-hole. Similarly, receivers may be positioned on the surface or in adjacent boreholes. Each of these factors influences our ability to detect a target in our data.

Detectability of a target requires two steps: (1) source fields must excite the target, and (2) receivers must be positioned so that the secondary response is measurable. In this

section, we focus our attention on the first point, exciting the target. We will examine the impact of source electrode locations, the physical properties of the target and the geometry of the target on our ability to excite a response.

4.4.1 Source location

We begin by examining the impact of the source electrode location on our ability to deliver current to a region of interest in the model. The model we consider is 1km long well in a 10^{-1} S/m background. The well has a conductivity of 5×10^6 S/m, an outer diameter of 10cm thickness, and a 1cm thickness; these are the same parameters used for the casing integrity experiment described in the previous section. The conductivity of the fluid filling the casing is identical to that of the background. We are interested in effects near the well and thus the modeling can be carried out using the 2D cylindrical mesh provided that the return electrode is sufficiently far away. The return electrode is physically a disc of current at a radius equal to the distance of the return electrode from the well, in this case 2km. The assumption of cylindrical symmetry and the use of a distant return electrode has similarly been applied in Schenkel (1991).

To examine the impact that the source electrode location has on our ability to excite a target, we consider the five electrode locations shown in Figure 4.12. Three of the electrodes are connected to the casing (tophole - blue, centered - green, and downhole - red); the remaining electrodes are not connected to the casing; these include the surface electrode (orange) as well as the five electrodes near the end of the pipe (purple - within the pipe, brown, pink, grey and yellow are beneath the end of the pipe). The surface electrode is offset from the well by 0.1m.

To assess the ability of each electrode configuration to excite a geologic target of interest, we will examine the current density in the formation. In Figure 4.13, we have

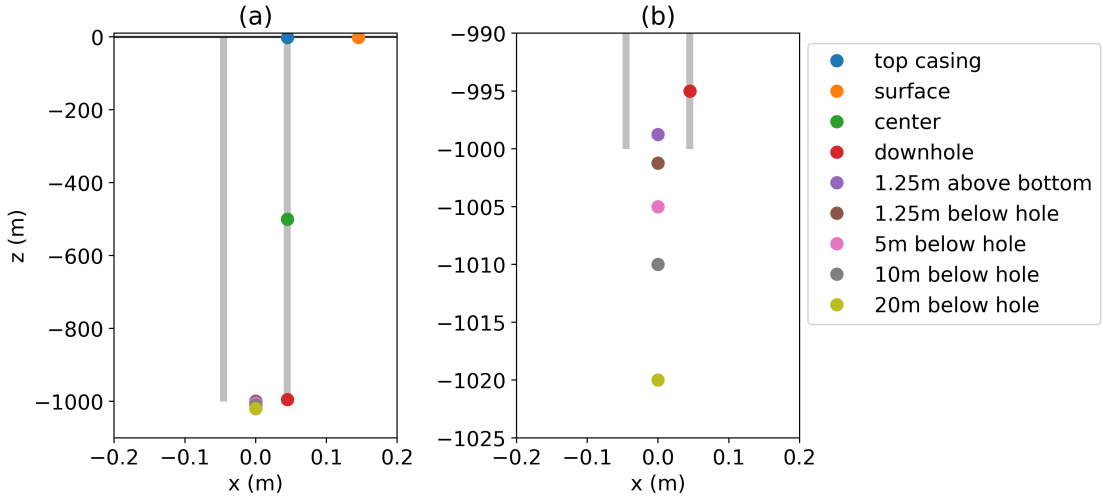


Figure 4.12: Electrode locations to be compared. The top casing electrode (blue), centered electrode (green, 500m depth), and downhole electrode (red, 500m depth) are connected to the casing. The surface electrode (orange) is offset from the well by 0.1m. The remaining electrodes are positioned along the axis of the casing. Panel (a) shows the entire length of the casing, while (b) zooms in to the bottom of the casing to show the separation between the electrodes beneath the casing.

plotted the amplitude of the current density along a vertical line (a) 25m, (b) 50m, and (c) 100m radially offset from the well. In terms of survey design, we wish to choose a source location that maximizes the total current density within the depth region of interest. If the target is near the surface, we choose an electrode which is connected to the top of the casing, or near the casing at the surface. Interestingly, at depth, there is little distinction between these two scenarios. Thus, if one is limited to deploying electrodes at the surface, and for practical purposes, connecting infrastructure to the well-head presents a challenge, then grounding the electrode near the well still results in a survey that benefits from the well acting as a high-conductivity pathway to help deliver current to depth. If the aim however, is to excite a deeper target, we see that positioning the electrode downhole can significantly increase the current density delivered to that

depth. For example, if we have a target near 500m depth, positioning the electrode near that depth nearly doubles the current density as compared to an electrode at the surface. If a target is near the end of the well, between 800m and 1000m depth, then positioning an electrode near the end of the well triples the current density. This effect will be amplified if the well is lengthened, since we observe exponential decay of the currents carried along according to the conduction length (equation 4.5).

Kaufman (1990) pointed out that the difference between an electrode positioned along the axis of the casing and one coupled to the casing at depth is highly localized around the source, and thus is not an important distinction at the scales we consider for a geophysical imaging survey. We can test this numerically by comparing the currents arising from the electrode which is connected to the casing 5m above the bottom of the casing (red in Figures 4.12 and 4.13), and the electrode positioned along the axis of the casing 1.25m above the bottom of the casing (purple in Figures 4.12 and 4.13). Indeed, we see that the red and purple lines overlap for all offsets in Figure 4.13, indicating that both situations result in the same distribution of currents within the formation.

For electrodes beneath the casing, the distribution of currents is significantly different. For electrodes 1.25m, 5m, 10m and 20m below the pipe, we see that within a \sim 100m above and below the electrode location, the currents are nearly symmetric, following the expected response of a point source. We have included a simulation with the electrode 20m below the pipe when there is no casing present; this is shown in black in Figure 4.13. The main difference between the distribution of currents for each of these scenarios is the reduction in current density in the top 1000m, with increasing electrode depth; as the electrode is moved deeper, less current is channeled into the casing. Schenkel and Morrison (1990) noted that for electrodes positioned beneath a well, if the electrode is more than 100 casing diameters beneath the casing, then the casing has little

impact on the fields below or far from the pipe. The current is much more localized if the electrode is beneath the casing, and thus if a target is beneath or very near the end of the well, then it is advantageous to position the electrode beneath the well.

Not surprisingly, if the source electrode can be positioned near the depth region of interest, the current density delivered to that region is larger. Numerical experiments show that the position of the return electrode makes minimal impact on the currents at depth. However, if the return electrode is within 10s of meters of the well, the near surface currents are significantly altered. This is consistent with our observations in section 4.3, where we showed that the return electrode location has little impact on the magnitude of the secondary signals, but its position alters the geometry of the source fields and this can be used to reduce coupling of receivers to the primary field.

4.4.2 Target properties

The physical property contrast between the target and the background, the targets geometry and proximity to the well, all influence our ability to observe its impact on the data we measure. The purpose of this section is to explore the impact of these factors on the excitation and detection of the target. In the first example, we examine the role of the conductivity of a cylindrical target which is in contact with the well. The second example is again a cylindrically symmetric co-axial disc target but there is a gap between the casing and the target. The final example is fully 3D; the target is a block and we look at the excitation as a function of the distance of a block from the well.

Target in contact with the well

First, we consider a cylindrical target that is in contact with the well. Schenkel and Morrison (1994) examined such a scenario for a conductive target (e.g. a steam injection or water flood) in a mis-a-la-massé type experiment where a source electrode is connected

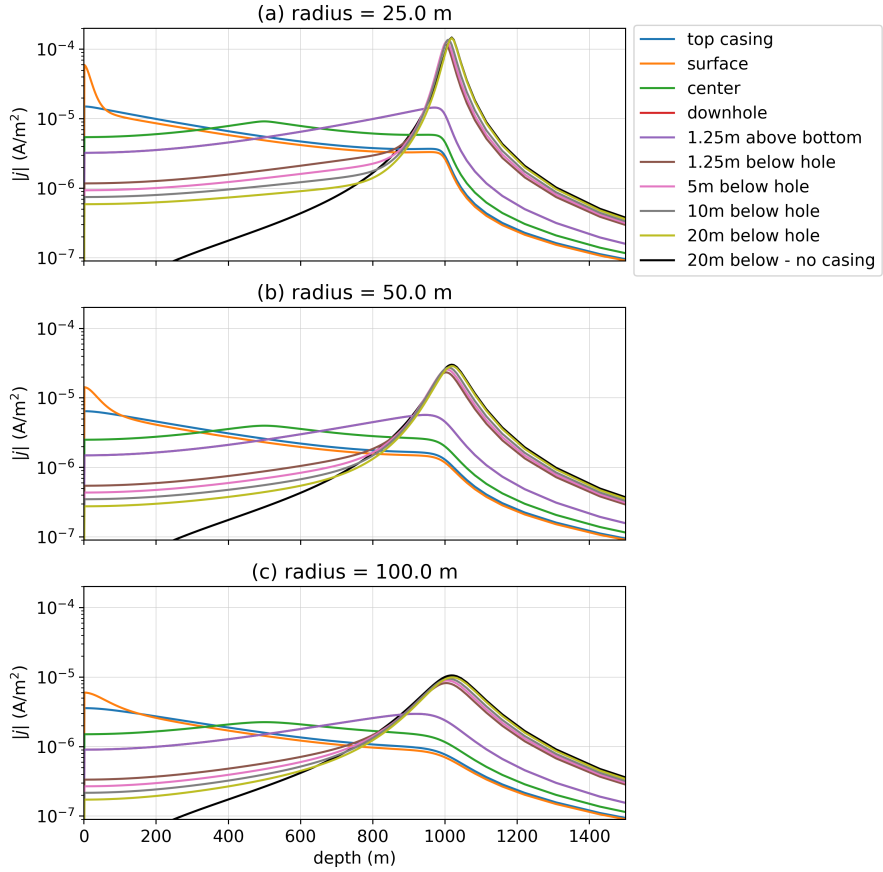


Figure 4.13: Total current density along a vertical line offset (a) 25m, (b) 50m and (c) 100m from the axis of the casing, which extends from the surface (0m) to 1000m depth. The electrode locations correspond to those shown in Figure 4.12. For reference, a simulation with an electrode 20m below the casing when there is no casing present is shown in black.

to the casing at the same depth as the center of the target. They considered a cross-well experiment with potential electrodes in an offset, uncased well, and compared two scenarios for the source well: one in which the source well is an open-hole, and the second in which it was cased. They demonstrated that the casing enhances the response, and thus the data sensitivity to the target, as compared to an experiment where current is injected directly into the target and no casing is present. In this example, we build upon

those findings and examine the role of the conductivity of the target on our ability to excite it as well as the impact on the data if the target is not directly in contact with the well.

The model we use is a 1km casing in a half-space with a target. The target extends 25m vertically and has a 25m radius and the depth to its top is 900m. The model is cylindrically symmetric and thus we expect that the secondary electric field at the surface due to the target will be purely radial. As such, we apply the learnings from the casing integrity example and use the return electrode to reduce coupling with the primary field along a line perpendicular to the source. We position the return electrode 500m from the well-head and we compare both top-casing and down-hole source electrode locations.

We begin by examining the physical behavior governing the DC response of a conductive and resistive target. Figure 4.14 shows the (a) conductivity model, and resultant: (b) current density, (c) charge density, and (d) electric fields for a conductive target (10 S/m , top row) and a resistive target (10^{-3} S/m , bottom row) in a down-hole experiment where the source electrode is positioned at the center of the target. The extent of the steel-cased well is noted by the vertical black line in panel (a). For the conductive target, we see an accumulation of positive charges along the radial and vertical boundaries of the target. This is consistent with currents that have been channeled into the conductor and exit into a more resistive background. Conversely, for the resistive target, we see an accumulation of negative charge on the radial boundary, consistent with current moving from a resistive region to a more conductive material. We also notice some positive charge accumulation on the top and bottom boundaries of the target; some of the currents deflected around the resistor do enter from the top and bottom, resulting in an accumulation of positive charge. This is not observed in a traditional mis-a-la-massé experiment, where a point source is positioned within the target. Figure 4.15 shows the

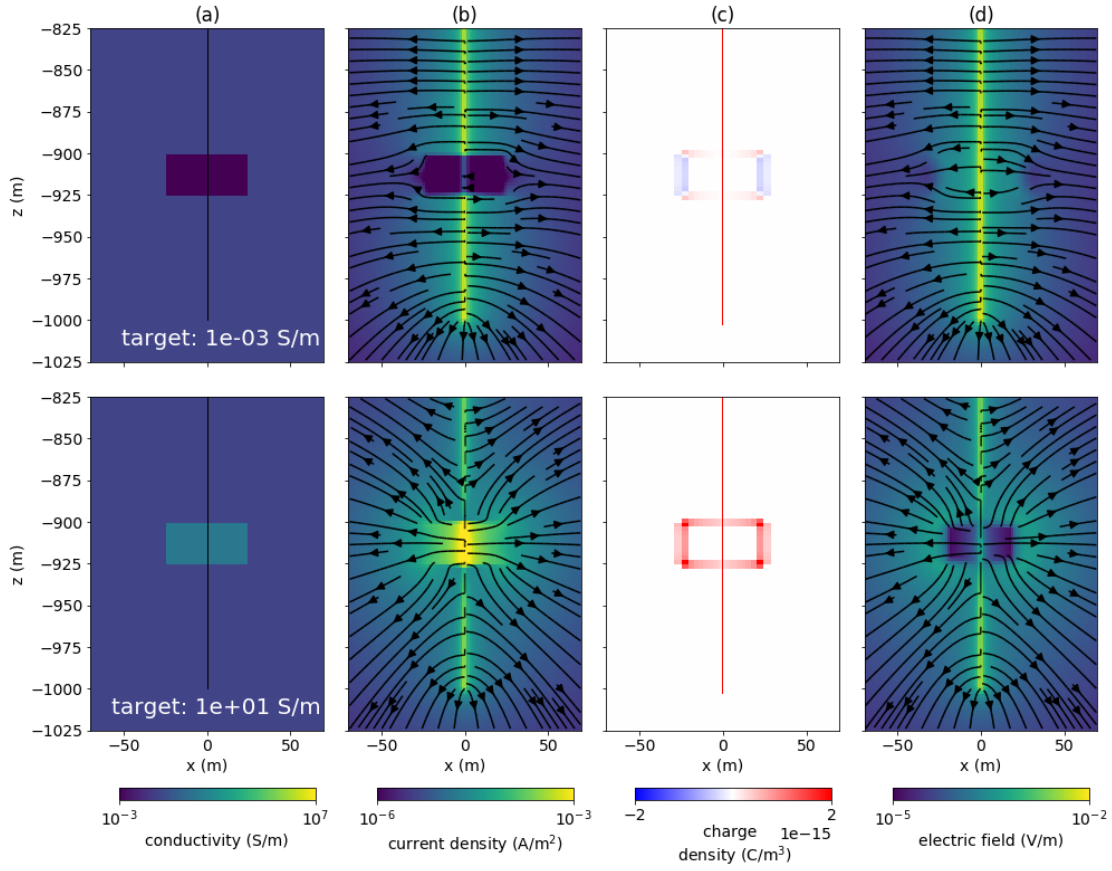


Figure 4.14: Cross section showing: (a) electrical conductivity, (b) current density, (c) charge density, and (d) electric field for a DC resistivity experiment with a conductive target (top) and a resistive target (bottom). The positive electrode is positioned in the casing at the 912.5m depth. The casing is shown by the black line that extends to 1km depth in panel (a).

current density, charges and electric fields for a mis-a-la-massé experiment in which no steel cased well is present.

In a DC experiment, the electric field response we measure is a result of the distribution of charges within the domain. As a metric for quantifying excitation, we integrate the secondary charge over this depth interval containing the target. In Table 4.1, we show the secondary charge integrated over the depth interval containing the target; the

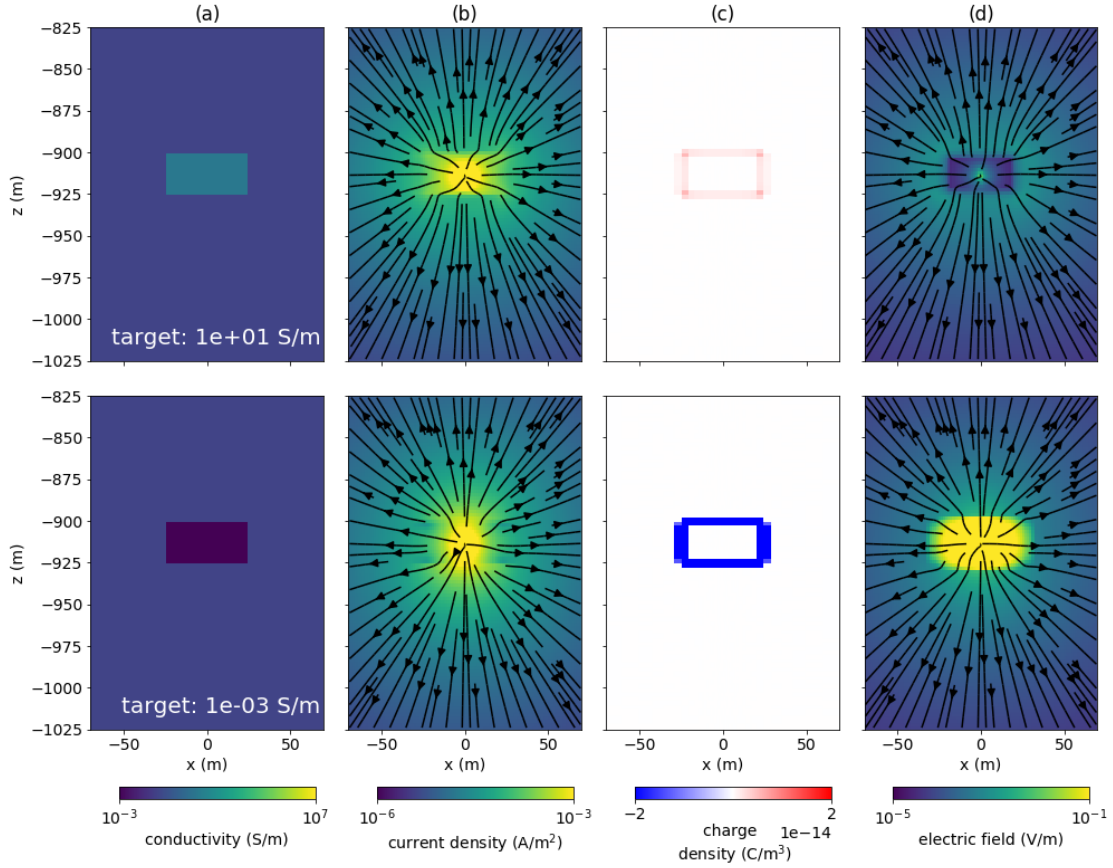


Figure 4.15: Cross section showing: (a) electrical conductivity, (b) current density, (c) charge density, and (d) electric field for a DC resistivity experiment with a conductive target (top) and a resistive target (bottom). The positive electrode is positioned at 912.5m depth. No casing is included in this simulation. Note that the colorbars for the charge density (c) and electric field (d) are different than those used in Figure 4.14. For the resistive target, the colorbar is saturated, the charge density over the resistive target is on the order of 10^{-13} C/m^3 .

Table 4.1: Integrated secondary charge over a target adjacent to the casing, as shown in Figure 4.14.

target conductivity (S/m)	integrated secondary charge (C)	
	downhole source	top-casing source
1e-03	-4.24e-12	-1.08e-12
1e-02	-3.82e-12	-9.68e-13
1e-01	0.00e+00	0.00e+00
1e+00	1.75e-11	4.46e-12
1e+01	3.26e-11	8.28e-12

secondary charge on the casing within this region is included in the calculation. To examine how the charge relates to the electric field data, we have plotted (a) total radial electric field, (b) secondary radial electric field (with respect to a primary that includes the casing in a halfspace), and (c) the secondary radial electric field as a percentage of the primary for a down-hole source and similarly for a top-casing source (d, e, f) in Figure 4.16. We have adopted the same noise floor and percent threshold as in the casing integrity examples (10^{-7} V/m and 20%, respectively). For time-lapse surveys where a baseline survey has been taken and the background is well-characterized, this threshold could likely be reduced. The black line in panels (a) and (d) corresponds to the baseline model in which no target is present; each of the colored lines corresponds to a different target conductivity as indicated in the legend.

First, we examine the impact of the conductivity of the target and notice that there is an asymmetry between secondary charge on conductive targets and resistive targets. For a 1 S/m target, which is one order of magnitude more conductive than the background, the integrated secondary charge is 1.75×10^{-11} C, while for a 1×10^{-2} S/m target, which is one order of magnitude more resistive than the background, the integrated secondary charge is -3.82×10^{-12} C for the downhole casing experiment. Thus, there is a factor of 4.6 between the magnitude of the secondary charge for these targets; this is

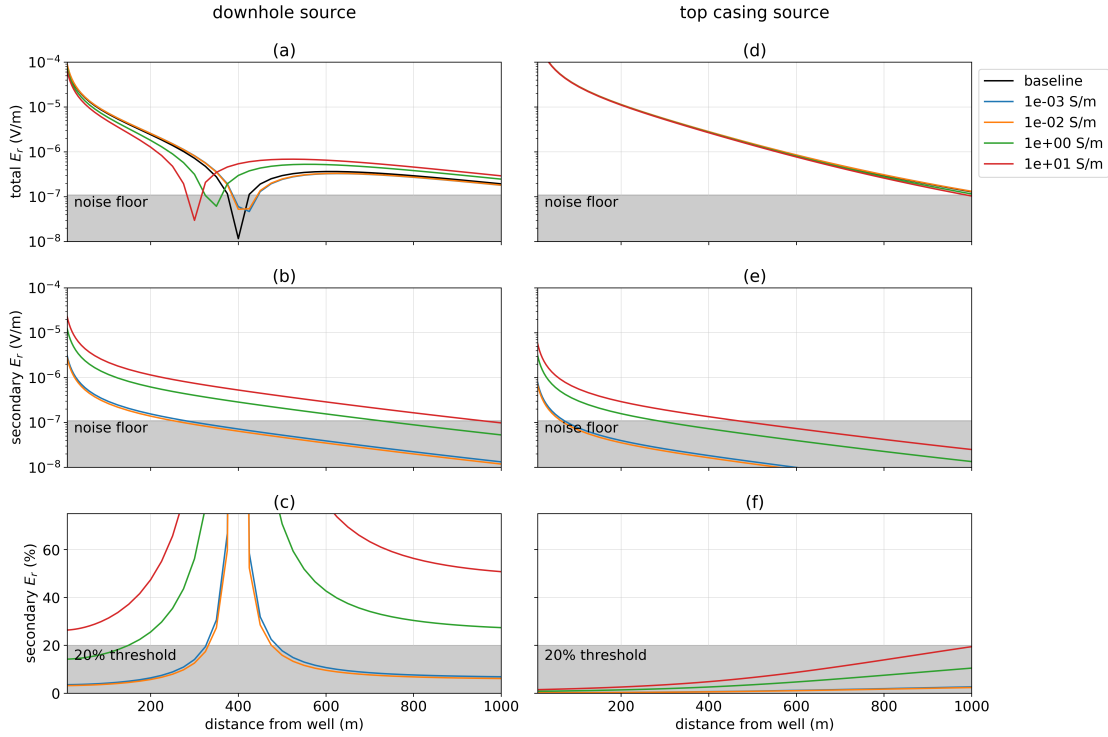


Figure 4.16: Radial electric field at the surface as the conductivity of a cylindrical target, in contact with the well, is varied. The target has a radius of 25m and extends in depth from 900m to 925m. The return electrode is on the surface, 500m from the well and data are measured along a line perpendicular to the source. The panels on the left show (a) the total electric field, (b) the secondary electric field with respect to a primary that does not include the target, and (c) the secondary electric field as a percentage of the primary for a survey in which the positive electrode is positioned downhole at 912.5m depth. The panels on the right similarly show (d) the total electric field, (e) the secondary electric field, and (f) the secondary electric field as a percentage of the primary for a top-casing experiment.

equivalent to the ratio we see between the secondary electric field measurements at the surface observed in Figure 4.16b. When also considering the influence of the primary electric field on our ability to detect a target, we see that for a down-hole casing experiment, the conductive targets are detectable; they both have a significant region where the secondary is above the noise floor and the secondary comprises a significant percentage of the primary. The resistive targets, however, are not. Although within 200m of the well, the secondary signal is above the noise floor, this also corresponds to where the primary field is large; the percent threshold would need to be reduced to less than 5% in order to have confidence in the signals due to the resistive targets.

When comparing the downhole source to the top-casing source experiments for a fixed conductivity, there is a factor of 3.9 between the integrated secondary charge shown in 4.1; this is reflected in the secondary electric field data in Figure 4.16b & e. For the top-casing experiment, none of the targets is detectable. There are two factors that make this a more challenging experiment than the downhole scenario: (1) less current is available to excite the target, as reflected in Table 4.1 and (2) the primary field is stronger at the receivers (200m from the well the primary field has an amplitude of 10^{-5} V/m, while for the down-hole source experiment, the primary has an amplitude of 2×10^{-6} V/m). Addressing the excitation of the target requires that the source electrode be positioned downhole, closer to the target. The second point may be overcome if receivers can be positioned closer to the target, for example within an adjacent borehole.

In summary, the integrated secondary charge provides a metric for a survey's ability to excite a target, and shows that conductive targets are easier to excite than resistive targets. As expected, if the source electrode can be positioned near the target, excitation is enhanced. This also has the added benefit of reducing the strength of the primary electric field at the surface, as compared to a top-casing survey; this increases the potential

for detecting a target with surface-based receivers. In the next section, we examine the significance of the electrical connection between the casing and the target.

Target not in contact with the well

How significant is the electrical connection between the casing and the target for our ability to excite a response? To examine this, we introduce a small gap equal to the thickness of the casing (1cm) between the casing and the target. This has negligible effect on the volume of the target, but it changes the electrical characteristics of the problem. Consider a conductive target; if it is in-contact with the well, we are effectively conducting a mis-a-la-massé experiment, and the conductor will have a net positive charge. When the target is isolated from the casing, the total charge on the target must be zero, and thus dipolar effects, in which negative charges build up on the inner interface of the cylinder target and positive charges build up on the outer interface of the target, will be the source of our signal. This is demonstrated in Figure 4.17.

The corresponding secondary charge integrated over the target depth and radial electric field data are shown in Table 4.2 and Figure 4.18. For comparison, the data resulting from the target in contact with the well are plotted in the dashed, semi-transparent lines. While there is little difference in the integrated secondary charge or the electric field measurements for the resistive targets, we see that there is a factor of 1.3 difference (i.e. 30%) between the integrated secondary charges and correspondingly, the secondary electric fields, from a 10 S/m target in contact with the well versus not. Similarly, there is a factor of 1.2 between a 1 S/m target in contact with the well versus not for both the downhole and top-casing sources. Increasing the gap between the target and the casing decreases the integrated charge and correspondingly reduces the secondary electric field at the surface. The integrated secondary charge for a 10 S/m target with a 10cm gap be-

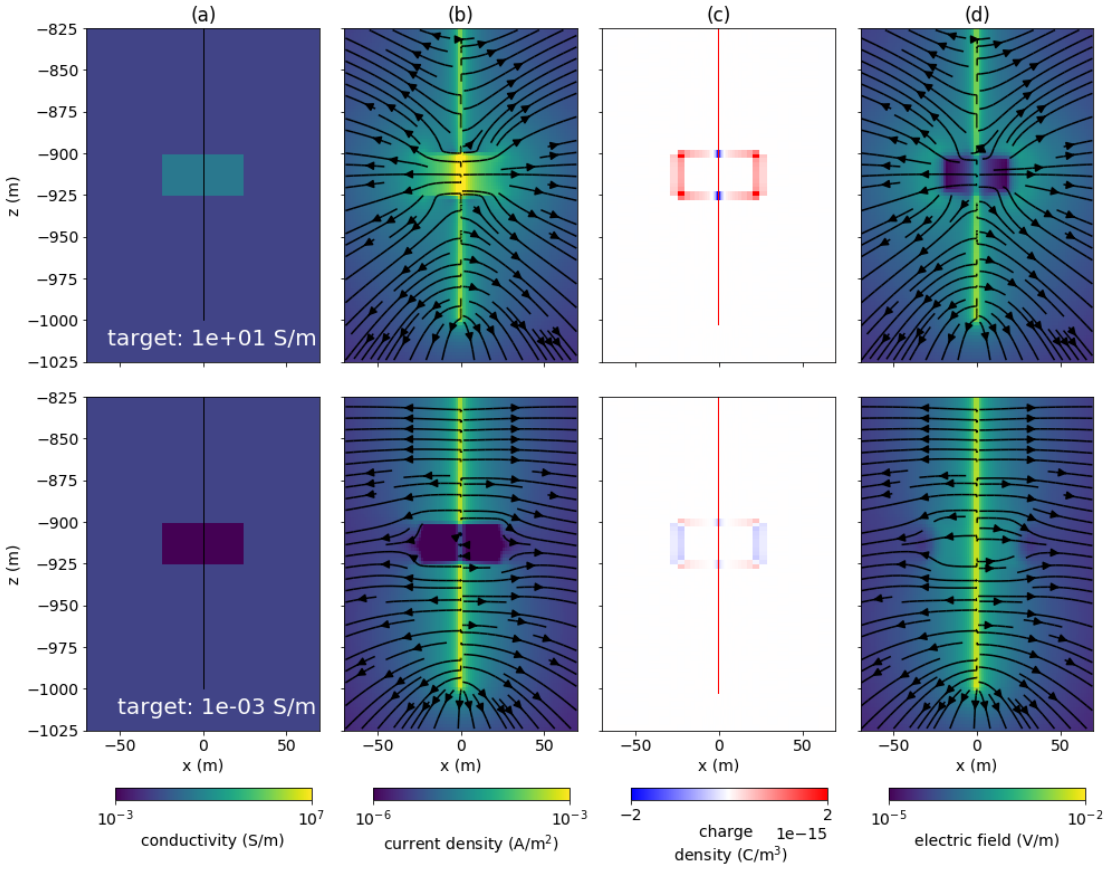


Figure 4.17: Cross section showing: (a) electrical conductivity, (b) current density, (c) charge density, and (d) electric field for a DC resistivity experiment with a conductive target (top) and a resistive target (bottom) which is not in contact with the well. The positive electrode is positioned in the casing at the 912.5m depth. The casing is shown by the black line that extends to 1km depth in panel (a).

tween the target and casing in a downhole source experiment is $1.7 \times 10^{-11} \text{ C}$, which is a factor of 2.2 smaller than the connected target; correspondingly the electric field data at the surface are reduced by a factor of 2.2 as compared to the connected target. Thus, a direct, electrical connection between the target and the well in which we connect the source is preferable for exciting and detecting conductive targets. In the next section, we further examine the impact of the separation between the target and casing.

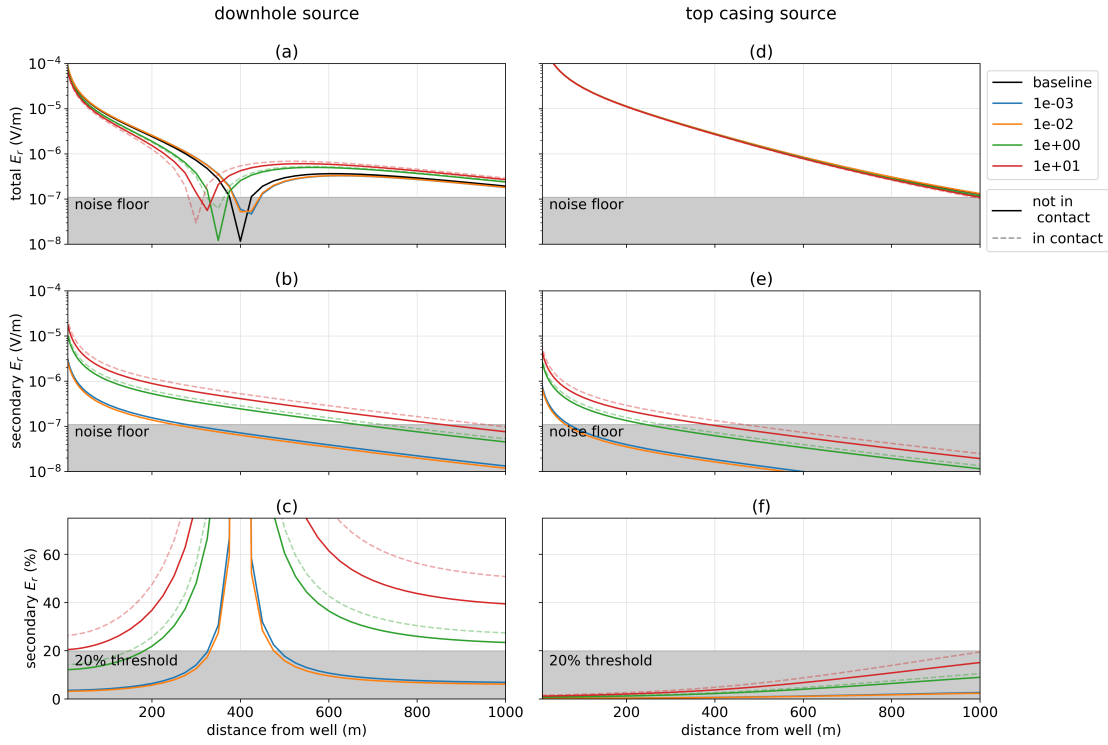


Figure 4.18: Radial electric field at the surface as the conductivity of a cylindrical target, which is not contact with the well, is varied. The target has a radius of 25m and extends in depth from 900m to 925m. The return electrode is on the surface, 500m from the well and data are measured along a line perpendicular to the source. The panels on the left show (a) the total electric field, (b) the secondary electric field with respect to a primary that does not include the target, and (c) the secondary electric field as a percentage of the primary for a survey in which the positive electrode is positioned downhole at 912.5m depth. The panels on the right similarly show (d) the total electric field, (e) the secondary electric field, and (f) the secondary electric field as a percentage of the primary for a top-casing experiment. The data shown in Figure 4.16, for the target in contact with the well, are plotted in the dashed, semi-transparent lines for reference.

Table 4.2: Integrated secondary charge over a target that is not electrically connected to the casing, as shown in Figure 4.17.

target conductivity (S/m)	integrated secondary charge (C)	
	downhole source	top-casing source
1e-03	-4.24e-12	-1.08e-12
1e-02	-3.80e-12	-9.64e-13
1e-01	0.00e+00	0.00e+00
1e+00	1.49e-11	3.79e-12
1e+01	2.51e-11	6.39e-12

Target offset from the well

The examples thus far have focused on a particular geometry where the target is symmetric about the well and is either connected or not. The more general case is where there is a target located anywhere in the medium and we wish to use DC or EM to characterize it. For example, in some scenarios, instrumenting a well for a geophysical survey may not be possible if it is also actively being used for an injection. Using another well, offset from the injection well, may then be preferable for positioning electrodes. In such circumstances, the physical property model is fully 3D and there are more factors that influence our ability to excite the target; in addition to the conductivity and geometry of the target, the distance between the well where the source electrode is positioned is now relevant. To address these potential applications, we examine a fully 3D scenario in which a target block is located away from the source well. Our primary goal is compare relative excitations that arise from using different survey parameters. It is sufficient to evaluate an electric dipole moment of the target that is evaluated with a Born approximation.

For a target offset from the pipe, we expect the secondary response due to that target to be dipolar. Thus, a natural proxy for excitation is the dipole moment of the target. We will adopt a Born-approximation approach to quantify the excitation and take the norm

of the integrated anomalous current density over the target volume, that is,

$$\begin{aligned} m &= \left\| \int \vec{j}_a \, dV \right\| \\ &= \left\| \int \sigma_s \vec{e}_p \, dV \right\| \end{aligned} \quad (4.6)$$

where $\sigma_s = \sigma - \sigma_p$ is the secondary conductivity (the difference between the conductivity of the target and the conductivity of the background), \vec{e}_p is the primary electric field (the electric field due to the source, casing, and half-space background), and \vec{j}_a is the anomalous current density which is non-zero only over the volume where the target is located.

The target we consider is 50m wide in both horizontal dimensions and is 25m in height. Its top is at 900m depth, as in the previous examples. We will examine both downhole source and top-casing experiments. A depth slice showing the primary electric field for the downhole electrode is shown in Figure 4.19; the return electrode is on the surface at $x=-500$ m, $y=0$ m. The three different target positions relative to the borehole are outlined in white. The solid line shows the target which is inline with the return electrode, the dashed is 90° from the source electrode and the dotted line shows the target which is 180° from the return electrode. We vary the distance from the well to the target and have plotted the Born-approximated dipole moment for four different target conductivities in Figure 4.20 for a (a) downhole experiment, and (b) a top-casing experiment. The offset is calculated from the center of the well to the nearest edge of the target that is excited by a downhole source. As before, conductive targets are much easier to excite than resistive targets, and for a given conductivity, a downhole source provides greater excitation than a top-casing source. Naturally, as the target is moved further from the well, the geometric decay of source fields reduces our ability to excite

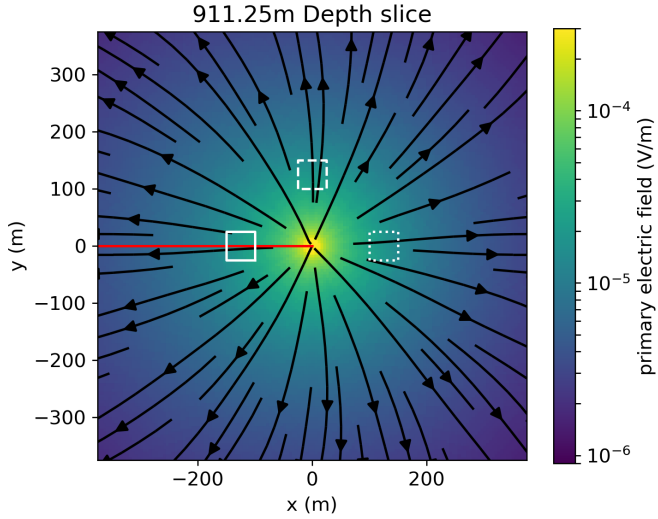


Figure 4.19: Depth slice showing the primary electric field due to a downhole electrode and a return electrode located on the surface at $x=-500\text{m}$, $y=0\text{m}$. The red line indicates the azimuth of the source. We examine the 3 different target azimuths shown by the white outlines. The solid line indicates the target inline with the source, the dashed is 90° from the source line, and the dotted line is 180° from the source line.

the target. Positioning the return electrode along the same azimuth as the target acts to mitigate some of these effects for targets that are at distances greater than 200m from the well, while for targets nearer to the well, the return electrode location has little effect on the excitation.

The next step to consider is detection of the secondary response due to this target. Consistent with the Born-approximation approach, we simulate the target as a dipole with a moment computed with equation 4.6 and compare the secondary electric field data at the surface for models with, and without, the casing. For this example, we select the model of a conductive target (10 S/m) with center 50m offset from the well. The target is along a line 90° from the source (e.g. along the same line as the dashed-outline in Figure 4.19). This gives a dipole moment of 38 Am for the target. The electric

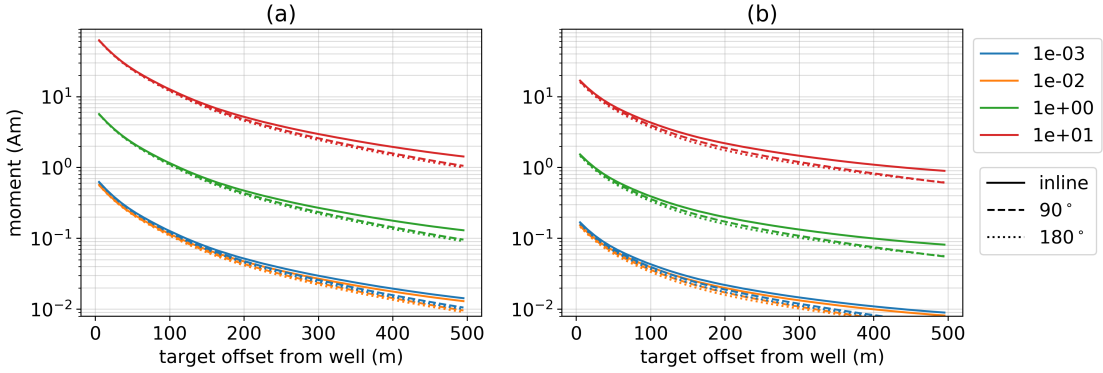


Figure 4.20: Integrated anomalous current density (excitation), as defined in equation 4.6, for a $50\text{m} \times 50\text{m} \times 25\text{m}$ target at 900m depth in a DC experiment with the positive electrode (a) downhole at 912.5m depth, and (b) a top-casing electrode. The return electrode is positioned on the surface 500m from the well. Each line color indicates a different target conductivity. The different line styles correspond to different target azimuths relative to the plane of the source electrodes and correspond to those shown in Figure 4.19. The solid line indicates a target inline with the source, the dashed is 90° from the source, and the dotted line is 180° from the source. Offset is calculated from the center of the well to the edge of the target closest to the well.

field data, measured along the same line as the target, are shown in Figure 4.21. The secondary response with the casing is shown in blue, and the response of the same dipole in a half-space is shown in orange. The secondary response due to the dipole in a half-space falls below the 10^{-7} V/m noise floor for all offsets, whereas, when the casing is included, the secondary response is above the noise floor until beyond offsets of 600m from the well. The casing not only helps excite a target, as was demonstrated in Schenkel and Morrison (1994), it also provides a conductive pathway for the secondary currents, thus increasing the secondary signal observed at the surface; this was similarly noted in Yang and Oldenburg (2016). In the model with the casing, the secondary signal comprises a significant percentage of the primary between offsets of $\sim 200\text{m}$ and $\sim 650\text{m}$, providing a window between 200m and 600m where the secondary electric field

is above the noise floor and comprises a significant percentage of the primary.

If we move the target further from the well, positioning its center 75m from the well, then the dipole moment is reduced to 24 Am. If we use our criteria that the secondary electric field must be above the noise floor and be at least 20% of the primary field, then the region over which we can expect to collect data is reduced to a 50m window between 300m and 350m offset from the well. For this given survey, then, we can consider ~ 25 Am as a threshold for detectability of a target.

Summary

The examples presented here showed that conductive targets are much easier to excite than resistive targets. For deep targets, a downhole electrode is preferable to a top-casing source as it delivers more current at depth to excite the target and reduces the strength of the primary at the surface; this makes the secondary field a larger percentage of the primary. For targets in close proximity to the well, if the target is in contact with the well, that electrical connection enhances the response. Additionally, we showed that beyond helping excite a target, as was demonstrated by Schenkel and Morrison (1994), the casing also improves detectability of secondary signals at the surface.

Designing a survey for a specific setting may require incorporation of 3D geologic structures and may include inversions to examine a survey's ability to recover a target. In this case, it is desirable to have a coarse-scale representation the steel-cased well on the simulation mesh. This is the topic of the next section.

4.5 Coarse-scale approximations of the well

When approaching the inverse problem, many forward simulations are required, and typically, a 3D cartesian mesh, with cells that vary on the length scales of the geol-

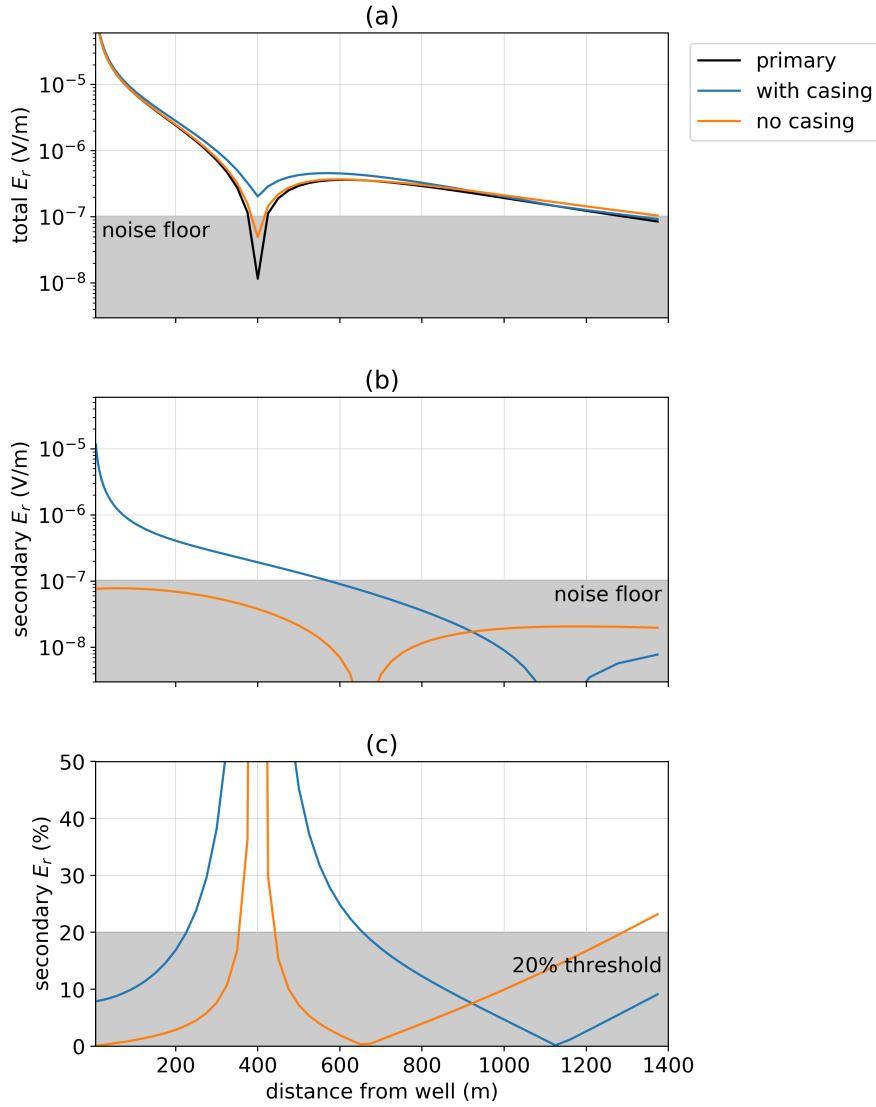


Figure 4.21: (a) Sum of the primary and secondary radial electric field due to a dipolar target with moment of 38 Am centered 50m from the well, either calculated with the casing (blue) or simply a dipole in a half-space (orange). (b) Secondary radial electric field due to a dipolar target in a halfspace with casing (blue) and without casing (orange). Secondary radial electric field as a percentage of the primary. The target is along a line 90° from the source electrodes; this is the same line along which we measure data at the surface.

ogy, is desired. Thus, rather than performing a fine-scale simulation of the steel-cased well, we may wish to represent the well on a coarse mesh. In the literature, two main approaches arise: the first approximates the well as some form of “equivalent source,” such as a charge distribution (e.g. Weiss et al. (2016)); the second approach represents the well as a conductivity feature on the coarse-mesh (e.g. Swidinsky et al. (2013); Um et al. (2015); Yang and Oldenburg (2016); Kohnke et al. (2017); Puzyrev et al. (2017), among others). Here, we will focus our attention to the second approach, noting that a charge distribution along the length of the well can be computed with the 2D or 3D cylindrical code described in Heagy and Oldenburg (2018a). Within the literature, there is disagreement among approaches for selecting the conductivity of the coarse-scale feature approximating the well. Um et al. (2015) replaces the fluid-filled cylinder with a solid rod having the same conductivity as the casing, arguing that it is the contrast between the conductivity of the well and the conductivity of the surrounding geology that is the most important factor; Puzyrev et al. (2017) also adopts this approach. Other authors have opted to preserve the cross-sectional conductance of the well (Swidinsky et al., 2013; Kohnke et al., 2017); this is consistent with the transmission-line model of the well discussed in Kaufman (1990). The aim of this section is to analyze these approaches.

4.5.1 Replacing a hollow-cased well with a solid cylinder

We consider a steel-cased well with a conductivity of 5×10^6 S/m that is embedded in a 0.1 S/m halfspace; the conductivity of the material that fills the well is the same as the background. The well has an outer diameter of 10cm and a thickness of 1cm, and we will vary its length. We will perform a top-casing experiment, where the positive electrode is connected to the casing at the surface. The return electrode is positioned

8km away, and a cylindrically symmetric mesh is used in the simulations. We examine approximations that treat the casing as a solid cylinder with the same outer-diameter as the true, hollow-cased well.

The distribution of charges, or equivalently, the current in the casing, is the source of the electric response of the casing. Thus to judge if two models of the casing are “equivalent”, we examine the current and charges as a function of depth. In Figure 4.22, we have plotted the vertical current and charges along the casing for the true, hollow cased well (solid), solid cylinder with conductivity equal to that of the casing, 5×10^6 S/m (dashed), and solid cylinder with a conductivity that preserves the product of the conductivity and the cross-sectional area of the conductor, 1.8×10^6 (dotted), for four different casing lengths, each indicated by a different color. Figure 4.22 shows: (a) the vertical current along the casing, (b) the difference in current between the approximate model and the true model, (c) that difference as a percentage of the true solution (d) the charge per unit length, (e) difference in charge per unit length and (f) difference in charge per unit length as a percentage of the true solution.

For short wells, we see that the current decays linearly and that the charge distribution is nearly uniform above the end of the well, while for longer wells, the decay of the current is exponential in nature, as is the charge distribution. This behavior is consistent with that predicted by the transmission line solution described in Kaufman and Wightman (1993). Kaufman and Wightman (1993) showed that the transition between the linear decay of currents and the exponential decay of currents is controlled by three factors: the cross sectional conductance of the well, the resistivity of the surrounding formation, and the length of the well. Schenkel (1991) similarly summarized this behavior in the definition of the conduction length (equation 4.5), which is the length over which the currents in the casing have decayed by a factor of $1/e$. For sufficiently

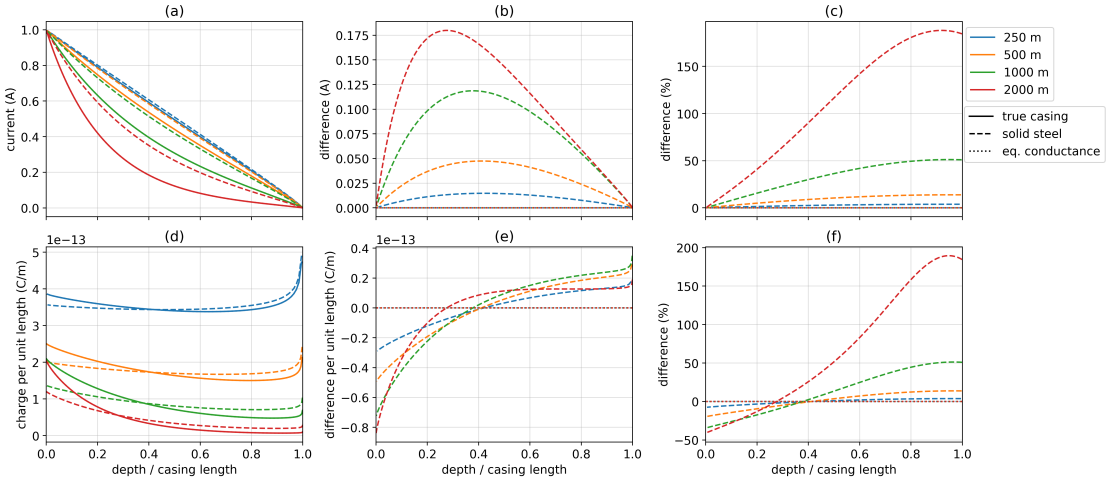


Figure 4.22: Currents (top row) and charges (bottom row) along the length of a hollow steel-cased well (solid lines), solid cylinder with conductivity equal to that of the steel-cased well (dashed-lines), and a solid cylinder with a conductivity such that the product of the conductivity and the cross sectional area of the cylinder is equal to that of the hollow-pipe (dotted lines). Each of the line-colors corresponds to a different casing length, as indicated in the legend. In (a), we show the vertical current in the casing, (b) shows the difference from the true, hollow-cased well in the vertical current within the casing, and (c) shows that difference as a percentage of the true currents. In (d), we show the charge per unit length along the casing, (e) shows the difference from the true, hollow-cased well and (e) shows that differences as a percentage of the true charge distribution. The x-axis on all plots is depth normalized by the length of the casing.

conductive and short wells (e.g. $L_c/\delta \ll 1$, where L_c is the length of the casing), the current decay is linear and independent of the conductivity, whereas for longer wells, ($L_c/\delta \gg 1$), the rate of decay of the currents is controlled by the conduction length (see equations 45 and 53 in Kaufman and Wightman (1993)).

In preserving the cross-sectional conductance, we see that the difference in currents and charges along the length of the well is negligible; the maximum difference in currents for the 2000m long well which has equivalent cross-sectional conductance is 7×10^{-7} A as compared to the difference of 0.18 A when using the conductivity of

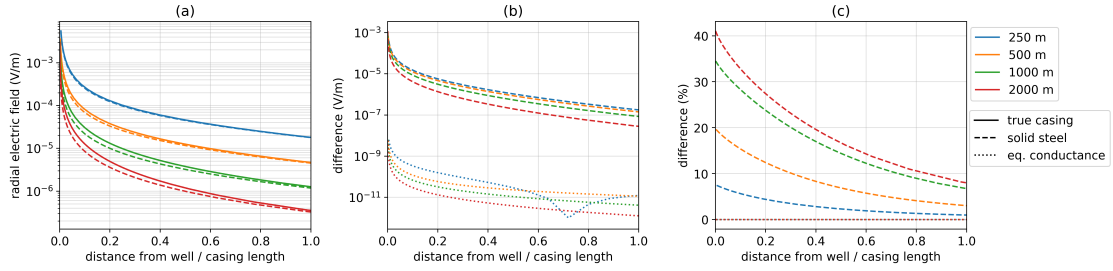


Figure 4.23: Radial electric field measured at the surface for a model of a hollow steel-cased well (solid lines), a solid cylinder with conductivity equal to that of the steel-cased well (dashed-lines), and a solid cylinder with a conductivity such that the product of the conductivity and the cross sectional area of the cylinder is equal to that of the hollow-pipe (dotted lines). Each of the line-colors corresponds to a different casing length, as indicated in the legend. In (a), we show the total radial electric field, (b) shows the difference in electric field from that due to the true, hollow-cased well, and (c) shows that difference as a percentage of the true electric fields. The x-axis on all plots is distance from the well normalized by the length of the casing.

the casing. This difference is important as it changes how much current is available to excite a target at depth. For a 2000m long well, the current is overestimated by > 150% if the well is replaced by a solid cylinder with the same conductivity of the steel-cased well. It also changes the distribution of charges and thus the electric field due to the well. Figure 4.22e shows us that the extra conductance introduced when approximating the well using the conductivity equal to the casing results in a secondary dipolar charge on the casing. This in turn reduces the electric field we observe at the surface, as shown in Figure 4.23. For a long well, the difference can be as large as 40% near the well.

The numerical time-domain EM experiment used in Um et al. (2015) to justify the approximation of the well by a solid, conductive rod having the same conductivity as the steel-cased well used a 200m long well with a thickness of 12.223mm, outer diameter of 135mm, conductivity of 10^6 S/m in 0.033 S/m half-space. The conduction length of this well is 560m; this is more than twice the length of the well. Therefore, the

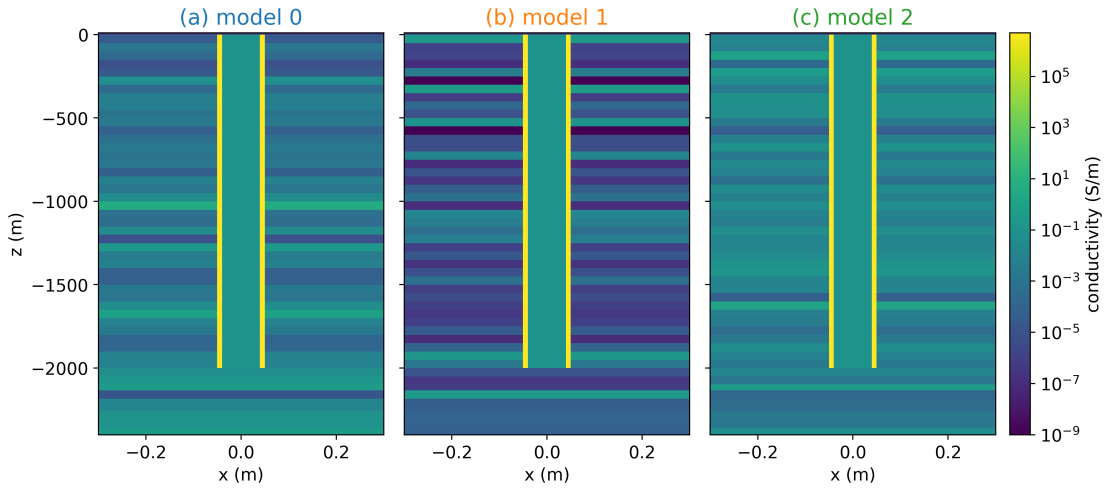


Figure 4.24: Three realizations of a 2km long casing in a layered background, where the conductivity of the layers is assigned randomly. Each layer is 50m thick, and the mean conductivity of the background is 0.1 S/m. The color of the title corresponds to the plots of the currents and charges in Figure 4.25

behavior of the currents falls into the linear regime, where the decay of currents is mostly independent of the conductivity, and thus the difference between using the conductivity of the casing or preserving cross-sectional conductance is less significant. However, if longer wells such as those typically employed in hydrocarbon settings, are considered, the behavior of the currents and charges depends upon the conductance of the casing, and thus that is the quantity that should be conserved in an approximation of the hollow-cased well by a solid rod.

In order to confirm that this conclusion is valid for variable geology, we have included a simulation with a 2km long casing in a layered background. Each layer is 50m thick and the conductivity was assigned randomly; three instances are included, as shown in Figure 4.24. The mean of the background conductivity is 0.1 S/m for each of the models.

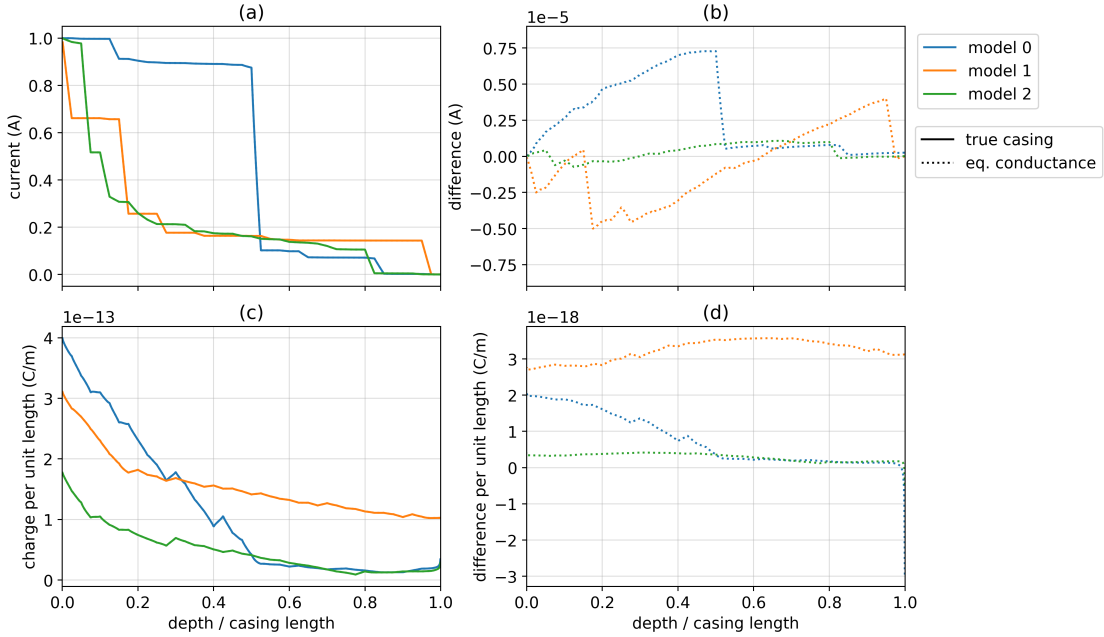


Figure 4.25: (a) Total vertical current through the casing for the three layered-earth models shown in Figure 4.24. The solid lines indicate the response of the true, hollow steel cased-well and the dotted lines indicate the response of a solid cylinder having the same cross-sectional conductance as the hollow well. (b) Difference between the currents along the casing in the solid well approximation and the true, hollow well. (c) Charge per unit length for each of the models. (d) Difference in charge per unit length between the true model of the casing and the approximation which preserves cross-sectional conductance.

The currents and charges along the length of the well for the true model, and a model approximating the well as a solid cylinder with equal cross-sectional conductance, are shown in Figure 4.25. For all of the models shown, the difference in both the casing currents and the charges are 5 orders of magnitude less than the amplitude of the total currents and charges; thus we conclude that approximating a hollow cylindrical steel casing by a solid cylinder with a conductivity that preserves cross-sectional conductance is valid for models with variable geology.

4.5.2 Cartesian grid

In the previous section, we showed that a hollow, cylindrical steel-cased well can be approximated by a solid cylinder with equal cross-sectional conductance. In this section, we move to a coarser, cartesian mesh, such as might be employed when solving a 3D inverse problem. We examine a simple approximation of a steel cased well on a cartesian grid. We employ 4 tensor meshes, each with progressively larger cell widths for the finest cells that capture the casing. On each of the cartesian meshes, we approximate the casing by preserving the product of the conductivity and the cross sectional area on the mesh. For comparison, we run a fine-scale simulation on a 3D cylindrical mesh that accurately discretizes the casing; it uses 4 cells across the casing-wall. The casing model is similar to that used in previous examples: it is 1km long, has an outer diameter of 10cm, a thickness of 1cm, and is embedded in a 0.1 S/m half-space. The positive electrode is connected to the top of the casing and a return electrode is positioned 1km from the well-head.

The resultant currents and charge per unit length are shown in Figure 4.26. In the top row, panel (a) shows the total current in a region approximating the well, along with the total current in the “true” cylindrical well (black line), (b) shows the difference between the current through the cartesian cells and the true model, and (c) shows the difference as a percentage. Similarly, in the bottom row, we show (d) the charge per unit length along the cylindrical well (black line) and cartesian-prism approximations, (e) the difference in charge per unit length from the charge per unit length on the true cylindrical model, and (f) that difference as a percentage of the charge per unit length on the cylindrical well.

The approximation of the cylindrical well by a rectangular prism with width equal to the diameter of the casing introduces minimal error in the currents and charges com-

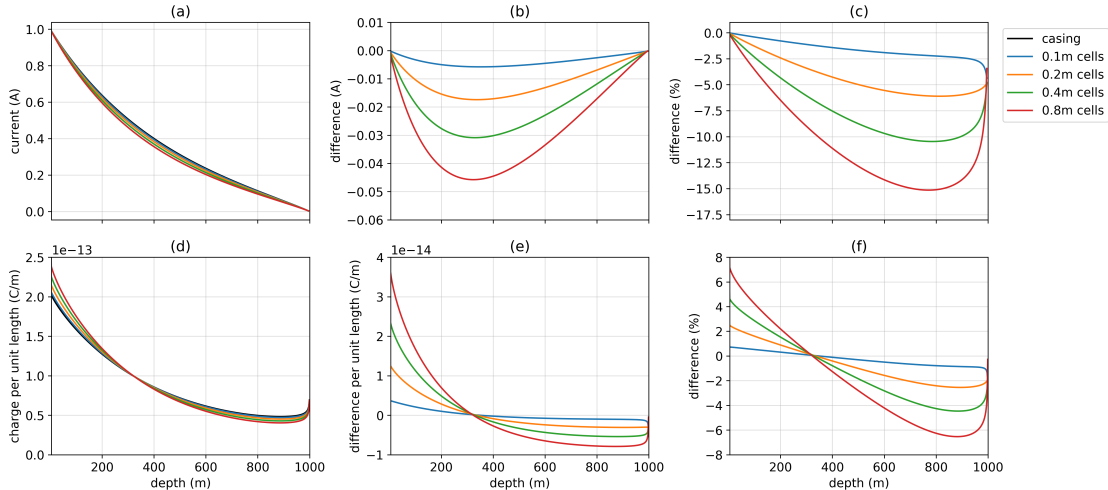


Figure 4.26: Currents (top row) and charges (bottom row) along the length of a steel cased well. The “true” hollow-cased well is simulated on a 3D cylindrical mesh and has 4 cells across the width of the casing thickness (black line). The colored lines correspond to the currents and charges computed along the well represented on a cartesian mesh with cell widths shown in the legend. The finest vertical discretization is 2.5m in all simulations. To represent the hollow cased well on the cartesian mesh, the cells intersected by the casing are assigned a conductivity that preserves the product of the conductivity and cross-sectional area of the well. In (a), we show the vertical current in the casing, (b) shows the difference from the true, hollow-cased well in the vertical current within the casing, and (c) shows that difference as a percentage of the true currents. In (d), we show the charge per unit length along the casing, (e) shows the difference from the true, hollow-cased well and (e) shows that differences as a percentage of the true charge distribution.

puted using a finite volume approach, even though the casing is only captured by one cell across its width. Comparing the current along the length of the well for the 3D cylindrical well and the cartesian simulation with 0.1m cells, we see that the error introduced is $< 2.5\%$ (until the end of the well where the current approaches zero). Similarly, the difference in the charge per unit length is $< \pm 1.25\%$. As successively coarser discretizations are used, accuracy is gradually lost; by doubling the cell sizes to 0.2m, the

error in the currents is 6% at its maximum and $< \pm 3\%$ in the charge along the casing. A factor of 8 increase in cell size (0.8m cells) results in a maximum error of 15% in the currents. It is important to note that the forward simulation is conducted using a finite volume approach; other approaches such as finite difference or integral equation approaches may have worse agreement if care is not taken to handle large physical property contrasts, captured by a single cell, in the simulation. Note that the behavior of the errors depends upon the properties of the casing (e.g. conductivity and length) as well as the conductivity of the background. This might be expected from the description of the casing conduction length (equation 4.5). If the conduction length is large relative to the length of the well, the currents decay linearly, and the geometry and conductivity of the well are less significant in the behavior of the currents. Alternatively, if the conduction length is comparable to the length of the well, the currents decay exponentially with a decay rate that depends on the geometry and conductivity of the well. For example, if the background is more resistive, increasing the contrast between the casing and background, the reduces the errors. Using a background conductivity of $100\Omega m$, the maximum error introduced in the current is $< 1\%$ with 0.1m cells and $< 2\%$ with 0.8m cells.

Depending on the level of accuracy required in a 3D simulation, there are several strategies that one might take to reduce this error. In some cases, local refinement can be achieved with a tetrahedral mesh, as is often employed when using finite element techniques (e.g. Weiss et al. (2016)), or an OcTree mesh (Haber et al., 2007). Other, more advanced approaches including upscaling and multiscale could also be considered. In an upscaling approach, one inverts for a conductivity model, which might be anisotropic, that replicates the physical behavior of interest (Caudillo-Mata et al., 2017a). Multiscale techniques translate conductivity information from a fine-scale mesh to a coarse-scale

mesh, on which the full simulation is to be solved, using a coarse-to-fine interpolation that is found by solving Maxwell's equations on the fine mesh locally for each coarse grid cell (Haber, 2014b; Caudillo-Mata et al., 2017b). The 3D cylindrical forward simulation code described in Heagy and Oldenburg (2018a) and used in this example can serve a tool for validating and refining an approach to achieve the desired level of accuracy.

4.6 Conclusion

The work in this paper is motivated by the increasing use of steel cased wells in geoscience problems, including monitoring applications such as carbon capture and storage and hydraulic fracturing. For geophysical imaging of targets at depth, the wells are beneficial as they can be used to channel currents to depth and enhance signals at the surface for targets that otherwise would be undetectable from a surface-based survey. Additionally, there is interest in considering the casing itself as the target of the geophysical target in casing integrity experiments; here the aim is to detect flaws or breaks in the casing. These applications, coupled with advances in modeling capabilities, open up the potential for advancing the utility of electrical and electromagnetic imaging in settings with metallic-cased wells.

Despite this potential, the reality is that electric field fields, especially if measured at the earth's surface, are small. Secondary fields might only be a few percent of the primary field, and thus too insignificant to reliably detect the target of interest. The success of using a DC or EM survey then depends upon many details that pertain to understanding the basic physics, the effects of parameters of the casing, the background conductivity, location of the current electrodes, and discerning which fields should be measured. DC resistivity is the starting point, as it allows us to examine the currents, charges, and electric fields in the electrostatic limit, prior to introducing inductive effects

and the influence of magnetic permeability in an EM signal, and as such, was the focus of this paper. Regarding the physics, a DC survey involves attaching a current generator to a conductive medium. This establishes a steady state current; the signal to which we are sensitive is the electric field that arises from charges that accumulate at interfaces separating regions of different conductivity. For this reason, most of our results are first presented as currents and charges.

The large contrasts in physical properties and significant variation in length scales due to long, thin, cylindrical, steel-cased wells prompt a number of questions about how the EM fields behave. In many cases, the finer details about the physical responses has challenged our intuition. With respect to the casing integrity application there were basic questions: how does a flaw in the pipe affect the currents and electric fields measured at the surface? Does the extent of the flaw change our ability to detect it (e.g. if it has a vertical extent of several meters versus a vertical extent of centimeters)? What happens if the flaw only comprises a part of the well, leaving some connectedness in the casing? When considering a geophysical experiment for imaging a target: is there a significant difference in the currents at depth between scenarios where a source electrode is connected to the well-head at the surface and one where the source electrode is offset from the well by a few meters? The surface signals are small; are there preferential geometries for the source and receiver electrodes that maximize signal/noise? A major goal of the DC survey will be to excite and detect target bodies. For problems, such as CO₂ sequestration, enhanced oil recovery, or hydraulic fracturing, the target may or may not be in contact with the well; how significant is an electrical contact between a target and the well in the data we measure at the surface?

Looking towards solving inverse problems in settings with steel-cased wells, it is advantageous to reduce the computational cost of the forward simulation because an

inversion requires many forward simulations. There are several approaches that can be taken to achieve this; one common approach is to approximate the finely-discretized well with an approximation on a coarse-scale mesh. Currently, there is disagreement within the literature as to how this should be done. Some authors have advocated that the conductivity contrast between the casing and the background should be preserved and thus replace a hollow steel-cased well with a solid rod that has a conductivity equal to that of the casing. Other authors have opted to preserve the product of the conductivity and cross-sectional area of the casing, following the conclusions of the transmission-line solution shown in Kaufman (1990). What is the correct conductivity needed for substitution?

Some of the above questions have been addressed in theoretical papers extending back a few decades but numerical verification was often limited or carried out with simplifying assumptions. Other questions require the ability to carry out numerical modeling in 2D or 3D environments – these tools are just now becoming available. Our goal with this paper has been to examine the scientific questions above and to promote insight about the solution by plotting the currents, charges, and electric fields. This analysis has benefited from the ease with which fields, fluxes and charges are readily calculated and visualized within the SimPEG framework, particularly when used in conjunction with Jupyter notebooks. Source codes for all of the examples in this paper are available in the form of Jupyter notebooks at <https://github.com/simpeg-research/heagy-2018-dc-casing> (Heagy and Oldenburg, 2018b); our aim in providing these notebooks is to allow readers to reproduce the results shown and also adapt the parameters and extend the analysis to address their questions.

Chapter 5

Electromagnetics with steel cased wells

Chapter 6

An inversion approach for subsurface injections

6.1 Introduction

The previous three chapters have focussed on understanding the physics of electromagnetics over conductive, permeable, steel-cased wells. In this chapter, we return to the goal of imaging subsurface injections through geophysical inversion. We view this as a time-lapse problem, in which one data set is obtained prior to the injection and second data set is obtained after the injection. The aim of the inversion, then, is to characterize the changes in the earth model due to the injection.

Time-lapse direct current (DC) resistivity, and in some cases electromagnetics (EM), is commonly used in the groundwater hydrology community. In particular, DC resistivity has been used, in salt-tracer experiments aimed at understanding groundwater flow (e.g. Slater et al. (2002); Kemna et al. (2002); Singha and Gorelick (2005); Doetsch et al. (2012)) and for characterizing time-lapse vadose zone processes (e.g. Daily et al.

(1992); Park (1998); Binley et al. (2002)). Within the context of hydrogeophysics, typically multiple time-lapse surveys are conducted. A range of interpretation techniques have been applied. In terms of algorithmic complexity, the most straightforward approach is to invert each time-snapshot independently. The recovered models can then be differenced and the difference interpreted (Cassiani et al., 2006), or an intermediate interpretation, for example estimating the center of mass of a plume (Singha and Gorelick, 2006; Doetsch et al., 2012), can serve as an indicator that is tracked through time. Daily et al. (1992) presented an approach for inverting ratios between initial and subsequent datasets, and (?) proposed an inversion for the resistivity difference between two subsequent data sets by inverting the difference between the two data sets. A common approach is to use the inversion result from an initial timestep as a reference and starting model for the following datasets (?Oldenborger et al., 2007), this is sometimes referred to as a “cascaded inversion” (?). More advanced techniques simultaneously invert all of the time-snapshots and apply both spatial and temporal regularization (Kim et al., 2009; ?; Loke et al., 2014). Hayley et al. (2011) provides an overview and comparison of common time-lapse inversion approaches and demonstrates a comparison of several approaches for a synthetic example of the remediation of a saline plume.

In the context of reservoir imaging applications, the “time-lapse” aspect of the problem is somewhat simpler than that typically encountered in hydrogeophysics. Very few temporally-dense DC or EM data sets have been collected for reservoir imaging. Notable exceptions include the cross-well DC resistivity surveys described in ? and Tøndel et al. (2014), for monitoring of a deep CO₂ injection in a gas field and monitoring steam chamber growth in a steam-assisted gravity drainage operation in the Athabasca Oil sands, respectively. Much more common are time-lapse data sets consisting of only two times: pre-injection and post-injection. Cross-well EM has been applied for such

surveys in to monitor water-floods (?Wilt et al., 2012) and steam injections (Wilt et al., 1996, 1997; ?). By far, the most common inversion approach involves inverting for a background model with the initial data set, typically including constraints from well-logs and potentially interfaces from seismic data and using this as the starting model for the inversion, typically in 2D (e.g. Wilt et al. (2012)).

Although the “time-lapse” aspect of injection-monitoring applications is generally simpler than applications in hydrogeophysics, the large depths considered in reservoir applications means that we are usually working with small signals. Furthermore, the presence of steel cased wells complicates signals. Efforts to reduce the impact of steel cased wells on DC surveys include using a coating on the casing which the electrodes are connected to insulate the casing from the survey (Tøndel et al., 2014). For cross-well EM applications, fibreglass casings may sometimes be used (Wilt et al., 2012), or when a single well is cased, a “casing-correction” is applied to the data collected at a fixed frequency (?).

For the emerging application of grounded-source DC or EM in the monitoring of subsurface injections, very few inversions of synthetic or field studies have been published and there are many open questions. How does the casing affect our sensitivities in the inversion? In particular, , have shown that in near surface studies, where forward modelling shows that the currents spread out along the length of the well, can we expect to resolve the location of the target along the well? Specific to subsurface injections, there is also further a-priori information that may be included, for example the conductivity of the injected material and the volume of material injected can be considered known. How best do we include this information in the inversion?

To focus discussion, we will consider synthetic examples related to hydraulic fracturing. The goal of the inversion in this case is to delineate the extent and geometry

of the propped region of the fractured reservoir. Changes in electrical conductivity are viewed as a proxy for estimating the concentration of propped fractures.

We will consider voxel based, parametric alternative model parameterizations using effective medium theory

Incorporate volume information about the subsurface injection

Notebooks are available at <https://github.com/simpeg-research/heagy-2018-injection-inversions>

6.2 Geophysical Inversions

In this section, we provide a brief overview of geophysical inversions, adapted from Cockett et al. (2015); for more detail and examples, the reader is referred to Oldenburg and Li (2005b); Cockett et al. (2015) as well as Appendix C for details specific to forward and inverse modelling in electromagnetics.

The aim of a geophysical inversion is to use the collected data to extract information about the subsurface. In a given survey, a datum can be written as

$$F_i[\mathbf{m}] + \boldsymbol{\varepsilon}_i = d_i \quad (6.1)$$

where $F[\cdot]$ is the forward simulation operator; for an electromagnetic problem, it simulates Maxwell's equations given a source and samples the relevant fields and fluxes at the receiver locations. The physical properties of the subsurface are captured by the variable \mathbf{m} , which we refer to as the inversion model. The noise is described by $\boldsymbol{\varepsilon}_i$, and d_i is the observed datum. A survey usually includes multiple sources and receivers, resulting in the observed data $\mathbf{d}_{\text{obs}} = [d_1, \dots, d_N]$ and some estimate of their uncertainties – often assumed to be Gaussian. If the noise is Gaussian, then an appropriate measure of the data misfit is the l_2 -norm of the difference between the predicted data obtained through

a forward simulation and the observed data, namely

$$\phi_d(\mathbf{m}) = \frac{1}{2} \|\mathbf{W}_d(F[\mathbf{m}] - \mathbf{d}_{\text{obs}})\|^2 \quad (6.2)$$

\mathbf{W}_d is a diagonal matrix whose elements are equal to $\mathbf{W}_{d_{ii}} = 1/\varepsilon_i$ where ε_i is an estimated standard deviation of the i^{th} datum. A good option is to assign a $\varepsilon_i = \text{floor} + \%|d_i|$. Percentages are generally required when there is a large dynamic range of the data. A percentage alone can cause great difficulty for the inversion if a particular datum acquires a value close to zero, and therefore we include a floor.

In addition to a metric that evaluates the size of the misfit, it is also required that we have a tolerance, ϕ_d^* ; models satisfying $\phi_d(\mathbf{m}) \leq \phi_d^*$ are considered to adequately fit the data (Parker, 1994a). If the data errors are Gaussian and we have assigned the correct standard deviations, then the expected value of $\phi_d^* \sim N/2$, where N is the number of data. Finding a model that has a misfit substantially lower than this will result in a solution that has excessive and erroneous structure, that is, we are fitting the noise. Finding a model that has a misfit substantially larger than this will yield a model that is missing structure that could have been extracted from the data (see Oldenburg and Li (2005b) for a tutorial).

The goal of an inversion is to estimate the earth-model, m from the data. In reality, the physical property distribution of the subsurface is continuous; therefore, estimating this model from a finite number of data is an ill-posed problem, meaning no unique model explains the data. Thus, in order to obtain a meaningful model from the data, assumptions and additional information must be included. There are several mechanisms by which this can be achieved. One of the most common is to include consideration of a model regularization, ϕ_m in the inverse problem. This norm can penalize variation from a reference model, spatial derivatives of the model, or some combination of these. For

example, the Tikhonov-style regularization function can be expressed as

$$\phi_m(\mathbf{m}) = \frac{\alpha_s}{2} \|\mathbf{W}_s(\mathbf{m} - \mathbf{m}_{ref})\|^2 + \frac{\alpha_x}{2} \|\mathbf{W}_x \mathbf{m}\|^2 + \frac{\alpha_y}{2} \|\mathbf{W}_y \mathbf{m}\|^2 + \frac{\alpha_z}{2} \|\mathbf{W}_z \mathbf{m}\|^2 \quad (6.3)$$

The first term is referred to as the “smallness” and penalizes difference between the inversion model and a reference model \mathbf{m}_{ref} . The matrix \mathbf{W}_s is a diagonal matrix; in the simplest case it is the identity matrix. The remaining three terms are the first-order smoothness in the x, y, and z directions; the matrices \mathbf{W}_x , \mathbf{W}_y , \mathbf{W}_y and \mathbf{W}_z approximate the first order spatial derivatives in each direction. The α parameters weight the relative contribution of each term to the regularization. Their values should consider the length-scales in the problem (c.f. Oldenburg and Li (2005b)); for a typical 3D problem $\alpha_x = \alpha_y = \alpha_z = 1$ and α_s is generally chosen to be several orders of magnitude smaller than the smoothness weights.

To define the inverse problem, we take a deterministic approach to the inversion and treat the it as an optimization problem. Additional strong constraints on the model such as upper and lower bounds (\mathbf{m}_u , \mathbf{m}_l) are also considered. The general form of the objective function we use combines the data misfit and regularization with a trade-off parameter, β , between them, giving a problem of the form

$$\begin{aligned} & \underset{\mathbf{m}}{\text{minimize}} \quad \phi(\mathbf{m}) = \phi_d(\mathbf{m}) + \beta \phi_m(\mathbf{m}) \\ & \text{such that} \quad \phi_d \leq \phi_d^*, \quad \mathbf{m}_l \leq \mathbf{m} \leq \mathbf{m}_u \end{aligned} \quad (6.4)$$

Since the value of β is not known *a priori*, the above optimization problem can be solved at many values of β to produce a trade-off, or Tikhonov, curve (cf. Parker (1994a)). An

optimum value, β^* , can be found so that solving equation 6.4 with β^* produces a model with misfit ϕ_d^* . One approach to finding the value of β^* is to use cooling techniques where the β is progressively reduced from some high value and the process stopped when the tolerance is reached.

The optimization problem posed equation 6.4 is non-linear for DC resistivity and electromagnetic forward simulations requiring that iterative optimization techniques be employed (c.f. ?). Gradient-based techniques are commonly employed. In particular, Gauss-Newton methods are effective in geophysical inversions. To ease notation, we consider a more compact description of the model regularization, and write our objective function as

$$\phi(\mathbf{m}) = \frac{1}{2} \|\mathbf{W}_d(F[\mathbf{m}] - \mathbf{d}_{\text{obs}})\|^2 + \frac{\beta}{2} \|\mathbf{W}_m \mathbf{m}\|^2 \quad (6.5)$$

Note that if $\mathbf{m}_{\text{ref}} = \mathbf{0}$ and $\mathbf{W}_m = [\mathbf{W}_s^\top, \mathbf{W}_x^\top, \mathbf{W}_y^\top, \mathbf{W}_z^\top]^\top$, then the regularization is equivalent to that stated in equation 6.3. The gradient is given by

$$\mathbf{g}(\mathbf{m}) = J[\mathbf{m}]^\top \mathbf{W}_d^\top \mathbf{W}_d(F[\mathbf{m}] - \mathbf{d}_{\text{obs}}) + \beta \mathbf{W}_m^\top \mathbf{W}_m(\mathbf{m}) \quad (6.6)$$

where $J[\mathbf{m}]$ is the sensitivity or Jacobian. The components $J[\mathbf{m}]_{ij}$ specify how the i^{th} datum changes with respect to the j^{th} model parameter,

$$J[\mathbf{m}] = \frac{dF[\mathbf{m}]}{d\mathbf{m}} \quad (6.7)$$

We discuss the derivation of the sensitivity for time and frequency domain electromagnetic problems in depth in Appendix C.

At the k^{th} iteration, beginning with a model \mathbf{m}^k , we search for a perturbation $\delta\mathbf{m}$ that reduces the objective function. Linearizing the forward simulation by Taylor expansion,

$$F[\mathbf{m}^k + \delta\mathbf{m}] \simeq F[\mathbf{m}^k] + J[\mathbf{m}^k]\delta\mathbf{m} + \mathcal{O}(\delta\mathbf{m})^2 \quad (6.8)$$

and setting the gradient equal to zero yields the standard Gauss-Newton equations to be solved for the perturbation $\delta\mathbf{m}$:

$$(J[\mathbf{m}]^\top \mathbf{W}_d^\top \mathbf{W}_d J[\mathbf{m}] + \beta \mathbf{W}_m^\top \mathbf{W}_m) \delta\mathbf{m} = -\mathbf{g}(\mathbf{m}) \quad (6.9)$$

The updated model is given by

$$\mathbf{m}^{k+1} = \mathbf{m}^k + \gamma\delta\mathbf{m} \quad (6.10)$$

where $\gamma \in (0, 1]$ is a coefficient that can be found by a line search. Setting $\gamma = 1$ is the default and a line search is necessary if $\phi(\mathbf{m}^{k+1}) \geq \phi(\mathbf{m}^k)$.

The iterative optimization process is continued until a suitable stopping criterion is reached. Completion of this iterative process yields a minimization for particular value of the trade-off parameter, β . If we are invoking a cooling schedule, and if the desired misfit tolerance is not yet achieved, β is reduced and the iterative numerical optimization procedure is repeated.

The forward simulation, computation of the sensitivities, and inversion machinery that we use throughout this chapter are implemented in the open source software package, SimPEG (Cockett et al., 2015; Heagy et al., 2017a).

6.2.1 Choosing an inversion model

At this stage, we have laid out a strategy for inverting for the inversion model \mathbf{m} , but we have yet to specify how we define \mathbf{m} . The physical property to which aim to characterize in an electromagnetic inversion is electrical conductivity σ (or equivalently, its inverse,

resistivity ρ). In a DC or an EM inversion, however, it is common to invert for log-conductivity on the forward simulation mesh, that is

$$\sigma = \mathcal{M}(\mathbf{m}) \quad (6.11)$$

where $(\mathbf{m}) = \exp \mathbf{m}$. We refer to $\mathcal{M}(\cdot)$ as a mapping. Mappings have two implications in the inversion. One implication is in the model regularization: we have changed the space in which we are applying the regularization, for this example, we regularize on log-conductivity values rather than linear conductivity. As the conductivity of common earth materials varies over several orders of magnitude, it is preferable to penalize jumps in orders of magnitude between voxels rather than penalizing linear values. The second implication is in the computation of the sensitivity. The forward simulation in an EM or DC problem depends upon electrical conductivity, thus the mapping modifies the sensitivity via the chain rule

$$J[\mathbf{m}] = \frac{dF[\mathcal{M}(\mathbf{m})]}{d\mathcal{M}(\mathbf{m})} \frac{d\mathcal{M}(\mathbf{m})}{d\mathbf{m}} = \frac{dF[\sigma(\mathbf{m})]}{d\sigma} \frac{d\sigma}{d\mathbf{m}} \quad (6.12)$$

Mappings can be composed, for example if inactive cells are included in the modelling domain, such as air cells or cells capturing known structures such as a steel-cased well, then

$$\sigma = \mathcal{M}_2(\mathcal{M}_1(\mathbf{m})) \quad (6.13)$$

where \mathcal{M}_1 injects in the log-conductivity values of the inactive cells and \mathcal{M}_2 takes the exponential. The sensitivity is appropriately modified by adding another step to the chain rule.

In addition to mappings routinely employed in electromagnetic inversions, such as

those used for working with log-conductivity values and handling inactive cells in the modelling domain, there are two mapping which we will make use of in this chapter: an effective medium theory mapping, based on the homogenization technique for propped, fractured reservoirs discussed in chapter 2 and parametric mappings.

Parametric mappings

The other type of mapping will make extensive use of in this chapter are parametric maps. We consider the model parameterizations of blocks and ellipsoids, similar to that described in McMillan et al. (2015a); McMillan (2017). For example, using a simple parametrization of a block, the model is

$$\mathbf{m} = [m_{\text{back}}, m_{\text{block}}, x_0, \Delta x, y_0, \Delta y, z_0, \Delta z]^{\top} \quad (6.14)$$

where m_{back} is the model value of the background, m_{block} , (x_0, y_0, z_0) is the center of the block and $(\Delta x, \Delta y, \Delta z)$ are the widths of the block in each dimension. The mapping is then

$$\mathcal{M}(\mathbf{m}) = m_{\text{back}} + (m_{\text{block}} - m_{\text{back}}) s(\tau(\mathbf{m})) \quad (6.15)$$

where $s(\cdot)$ is a differentiable approximation to a step-function and τ is a level set function of the block. To approximate a step function, we use the arctangent function,

$$s(\tau) = \frac{1}{\pi} \tan^{-1}(a\tau) + \frac{1}{2} \quad (6.16)$$

where a controls the slope of the transition between 0 and 1. Small values of a result in a gradual transition while larger values give a sharper transition. For more robust performance of the Gauss-Newton inversion, we choose a such that the transition happens

over a multiple cells in the simulation mesh (McMillan, 2017).

A block is defined by the infinity norm,

$$\tau = 1 - \left(\left\| \frac{x-x_0}{\Delta x/2} \right\|_{\infty}^2 + \left\| \frac{y-y_0}{\Delta y/2} \right\|_{\infty}^2 + \left\| \frac{z-z_0}{\Delta z/2} \right\|_{\infty}^2 \right) \quad (6.17)$$

however the infinity norm is not differentiable. Thus, we approximate the infinity norm using an ekblom norm

$$\tau = 1 - \left(\left[\left(\frac{x-x_0}{\Delta x/2} \right)^2 + \varepsilon^2 \right]^{p/2} + \left[\left(\frac{y-y_0}{\Delta y/2} \right)^2 + \varepsilon^2 \right]^{p/2} + \left[\left(\frac{z-z_0}{\Delta z/2} \right)^2 + \varepsilon^2 \right]^{p/2} \right) \quad (6.18)$$

where ε is a small constant and p is a constant describing the approximate norm, for example, if $p = 2$, then equation 6.18 describes an ellipsoid. To represent a block, we choose a p that is sufficiently large. For the length scales we consider, a value of $p = 4$ is appropriate. The value of ε is chosen to be large enough, and the value of p small enough so that the derivatives of the mapping are stable and second-order for the length scales of the problem. In addition, rotations can be included in the model, as described in McMillan (2017)¹.

When employing parametric mappings, there are two important implications to note in the setup of the inversion. Since the mathematical statement of the inverse problem is overdetermined, there are more data than model parameters, we fix the value of β at zero and do not employ a regularization. The second point is that for a starting model, it is important to start with the block and background having different conductivities. This was similarly discussed in McMillan (2017).

¹McMillan (2017) also employs a weighting scheme to scale the model parameters. We have not found this to be necessary for the examples we consider and thus do not use any weights or scaling

Effective medium theory mapping

In chapter 2, we introduced a two-step process for estimating the electrical conductivity of a propped, fractured volume of rock. The first step involved estimating the effective conductivity of a mixture of electrically conductive proppant and fluid, and in the second step, we estimated the effective conductivity of a volume of rock which has fractures filled with the proppant-fluid composite.

Assuming the electrical conductivity of the fluid and proppant are known, then rather than inverting for electrical conductivity, we can invert for the concentration of conductive fractures. To avoid introducing additional non-uniqueness into the problem, we use a fixed ratio of proppant and fluid in within the propped region of the reservoir and treat the fracture concentration φ as the inversion model. In a voxel-based inversion, φ is a vector with a value for the concentration in each cell. For simplicity, we assume that the fractures are randomly oriented and work only with isotropic conductivities. In this case, the mapping requires that we solve the two-phase effective medium theory approximation,

$$(1 - \varphi)(\sigma^* - \sigma_0)R^{(0,*)} + \varphi(\sigma^* - \sigma_1)R^{(1,*)} = 0 \quad (6.19)$$

for the effective conductivity, σ^* . The background has conductivity σ_0 and the conductive, proppant-filled cracks have conductivity σ_1 . Note that σ_0 , the conductivity of the background, does not need to be a scalar, it can be a vector with a background conductivity value for each voxel in the mesh. These values can be obtained by first inverting the pre-fracture data. The electric field concentration tensor $R^{(i,*)}$ captures the geometry of the particles that compose each phase. Note that for randomly oriented fractures $R^{(i,*)}$ is a scalar ($1/3\text{trace}\mathbf{R}^{(i,*)}$), where $\mathbf{R}^{(i,*)}$ is given in equation ???. For the background, we

use an aspect ratio of 1, assuming a spherical geometry for the particles that compose it, and for the fractures, we use a small aspect ratio ($\sim 10^{-4} - 10^{-3}$) and treat them as ellipsoidal cracks. In Chapter 2, we demonstrated that for sufficiently thin fractures, the exact aspect ratio is not significant. For a gradient based inversion, we also require the derivative of the effective conductivity with respect to the fracture concentration; the derivation is outlined in Appendix B.

Self-consistent effective medium theory is the method we adopt to connect the concentration of fractures with the effective conductivity of a fractured volume of rock, however, other relationships, such as an empirical relationship estimated from a lab study, could equally be employed. One interesting implication of relating the concentration of the fractures to the change in conductivity is that this provides a conduit for bringing in a-priori information about the volume of proppant injected into the reservoir.

The predicted volume is

$$V_{\text{pred}} = \int \varphi \, dV \quad (6.20)$$

We can then define a volume data misfit term,

$$\phi_V = \frac{1}{2} \left\| \frac{1}{\varepsilon_V} (V_{\text{pred}} - V_{\text{obs}}) \right\|^2 \quad (6.21)$$

where V_{obs} is the known volume terms which accounts for the estimated ratio of proppant and fluid and ε_V is an uncertainty term. We note that we are assuming a fixed ratio of proppant and fluid within the cracks. In reality, this will be variable, thus we use an sufficiently large ε_V as not to over-fit this assumption.

In the implementation the inclusion of an additional data misfit term is handled by a combo-objective function which enables joint inversions in the SimPEG framework.

6.3 Inversions with steel-cased wells

In the Chapter 4, we saw that the current spreads out along the length of the casing, decaying as we move away from the source. In the inversion, this raises questions about our ability to resolve the depth and vertical extent of the target. In this section, we start from a simple model of a vertical well with a conductive target and examine our ability to recover that target. Although most fracture operations are conducted in horizontal wells, we start by considering a vertical well as this reduces computational cost and allows us to explore aspects of the behavior of inversion prior to moving to the more fully 3D, more computationally intensive scenario.

We start by considering a DC experiment with a simple cylindrically symmetric model, shown in Figure 6.1. A 1km long casing is embedded in a background that has a resistivity of $100 \Omega\text{m}$. The casing has an outer diameter of 10cm, a thickness of 1 cm and a conductivity of $5 \times 10^6 \text{ S/m}$. For modelling, we approximate the hollow-cased well as solid cylinder with a conductivity of $1.4 \times 10^4 \text{ S/m}$, which preserves the product of the conductivity and the cross sectional area. This was shown to be a valid approximation in Chapter 4 and allows us to reduce the number of cells in the mesh, thus speeding up the computation of the forward simulation and sensitivities. Similar to the model used in ??, we assume a moderately-sized fracture operation which uses an 800m^3 slurry comprised of 15% proppant by volume. We assume leak-off of some of the fluid, leaving a mixture of 50% fluid and 50% proppant, by volume, in the fractures. This gives a total fracture volume of 240 m^3 which we distribute among 10 each with 3mm width are positioned within a 10m interval along the well. Conserving volume gives a 50m radius for the fractures. Using a fluid conductivity of 3 S/m and a proppant conductivity of 10^5 S/m , the conductivity of the 50/50 proppant-fluid mixture found using self-consistent effective medium theory (equation 2.1) is 2500 S/m. Using a fracture aspect ratio of

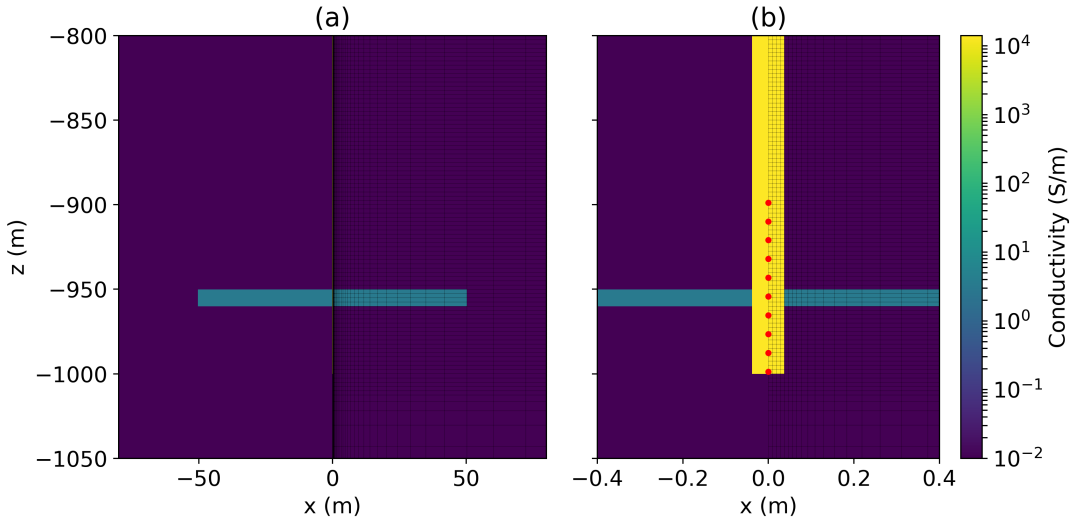


Figure 6.1: Model of an electrically conductive propped fracture zone (3 S/m) in a halfspace ($100 \Omega \text{ m}$) with a steel-cased well. The well is modelled as a solid cylinder with a conductivity of $1.4 \times 10^4 \text{ S/m}$. The mesh has 4 cells across the radius of the casing. The fractured region extends vertically from 950 to 960 m depth and has a radius of 50m. Panel (a) has a radial extent of 80 m to show the fractured zone and panel (b) has a radius of 0.4m to show the casing. The a-electrode locations are shown in panel (b).

3×10^{-5} and assuming randomly-oriented fractures, we obtain a conductivity of 3 S/m for the propped region of the reservoir.

The survey we use employs a downhole electrode and a distant return electrode. There are 10 down-hole source locations from 900 m depth to 1000 m depth, as shown by the red dots in Figure 6.1b. Radial electric field data are collected at the surface; there are 40 receiver locations from 25 m to 1000 m radially away from the well. In total, the survey consists of 400 data. Figure ?? shows the simulated data for both the background (prior to the fracture) and the fracture. The difference between the two is significant both in magnitude and in percentage and thus can expect that the inversion will introduce structure in order to fit the fracture data. In the following sections, we will

explore several approaches to the inverse problem for obtaining meaningful information from the data.

6.3.1 Standard Tikhonov inversion

We begin by applying standard inversion techniques and perform a voxel inversion using a Tikhonov regularization. As the simulation is cylindrically symmetric, we invert for a 2D model which varies radially and vertically. Our aim in this inversion and the ones that follow is to examine, under ideal circumstances, what information we can obtain from the data using a given inversion approach. We therefore do not add noise to the data and assign low uncertainties: 1% with a 10^{-9} V/m floor.

The choice of parameters is quite standard, similar to how one would approach a blind inversion. In the regularization, we use $\alpha_s = 10^{-3}$, $\alpha_x = \alpha_z = 1$. We adopt a β -cooling schedule that reduces the value of β by a factor of 8 every 3 iterations. The initial β is chosen by estimating the largest eigenvalue of the model regularization and data misfit through one iteration of the power method and taking their ratio; β_0 is then a scalar multiple of that. For the following inversions, we use a factor of 10. The initial and reference model are equal to the half-space resistivity of 100 Ωm .

The results of the first inversion we run are shown in Figure ???. This inversion reached a global χ -factor of < 0.1 and fits all data points within 5% (Figure 6.3c). It converged in two iterations. As expected in an Tikhonov-style inversion, the recovered model is smooth and diffuse. Perhaps unexpected is the location of the center of the recovered target; its depth is shifted below the true location, closer to the end of the well. Typically, we might expect that if the inversion were to shift the location of a target, it would be shifted up, closer to the receivers, where we have greater sensitivity. However, the presence of the casing alters the sensitivity. In Chapter ??, we demonstrated that

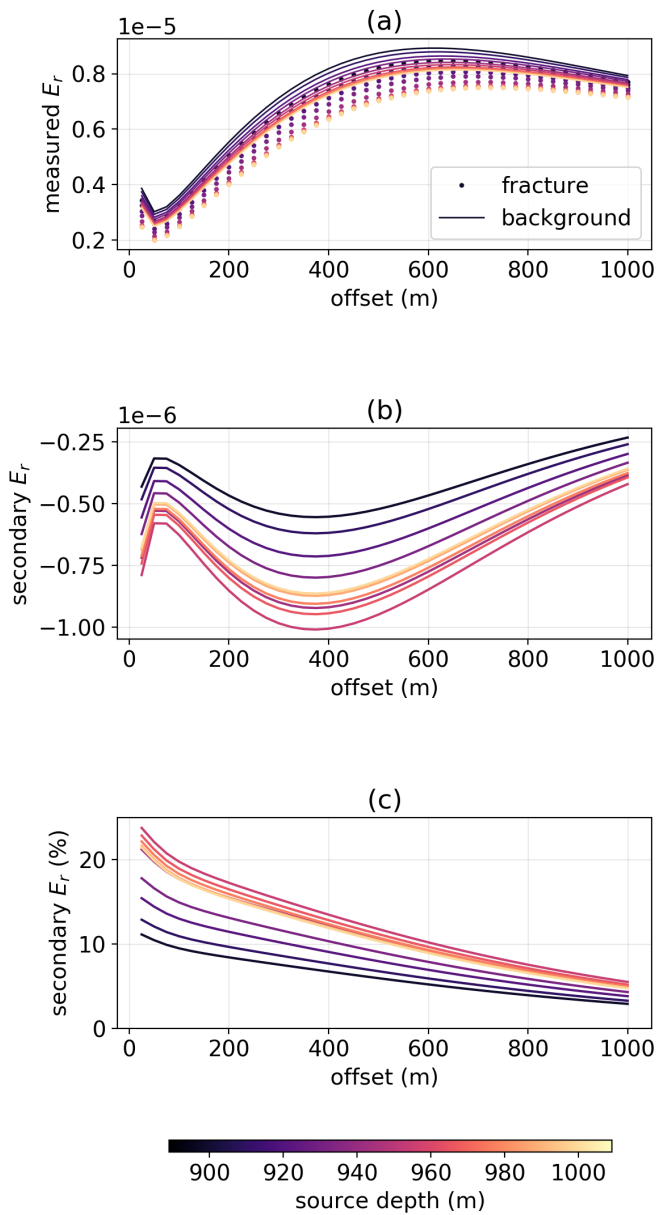


Figure 6.2: (a) Synthetic data for the down-hole casing experiment for the background, prior to the fracture (solid lines), and after the fracture (dots), (b) secondary electric field (fracture - background), and (c) secondary electric field as a percentage of the primary (background). The color of the lines or dots indicates the depth of the source.

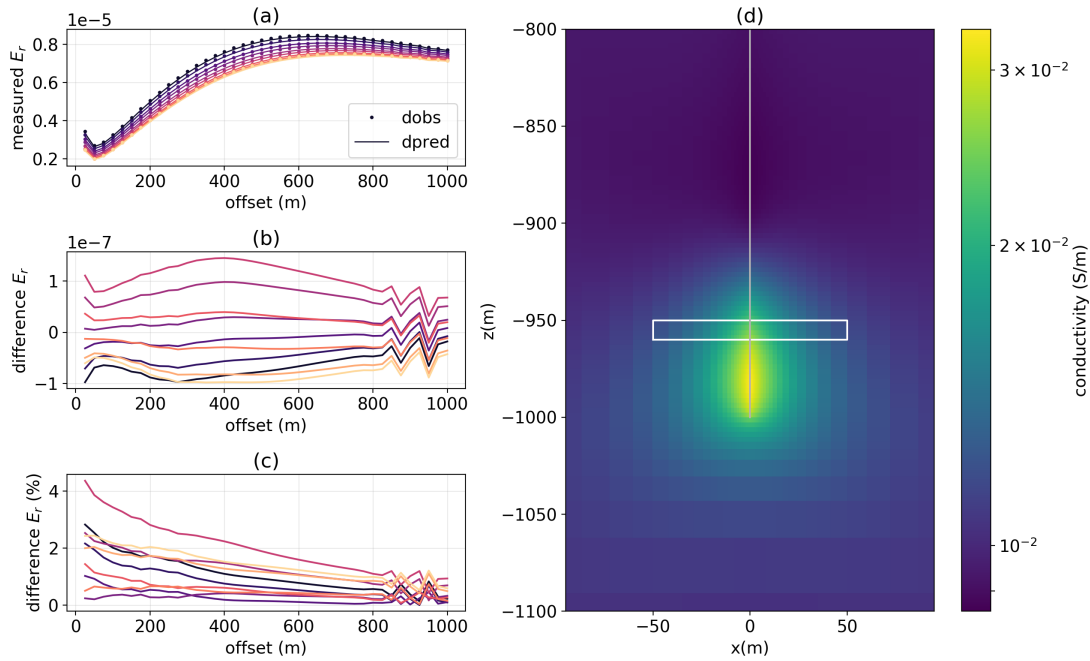


Figure 6.3: (a) Observed and predicted radial electric field data, (b) difference between the observed and predicted data (V/m), (c) difference between the observed and predicted data as a percentage of the observed data, and (d) conductivity model recovered in the inversion. The colors in (a), (b), and (c) indicate the source location as shown in Figure 6.2. The white outline in (d) outlines the true geometry of the fracture zone and the grey line shows the location of the wellbore. The data are fit to a global χ -factor < 0.1 .

there is an increase in charge near the ends of the well (see Figure 3.6, in particular), for the DC problem, this translates to an increase in sensitivity near the end of the well.

If we push the inversion harder, the depth of the target is better-resolved, as shown in Figure 6.4. In practice, this requires very high data quality; here we fit all data points within $\sim 2\%$ and reach a global χ -factor < 0.05 . The geometry of the target that we recover is elongated vertically; this is consistent with having larger sensitivity near the well. We also notice that the conductivity of the background above the target drops beneath that of the background – this is a common effect in smooth inversions when con-

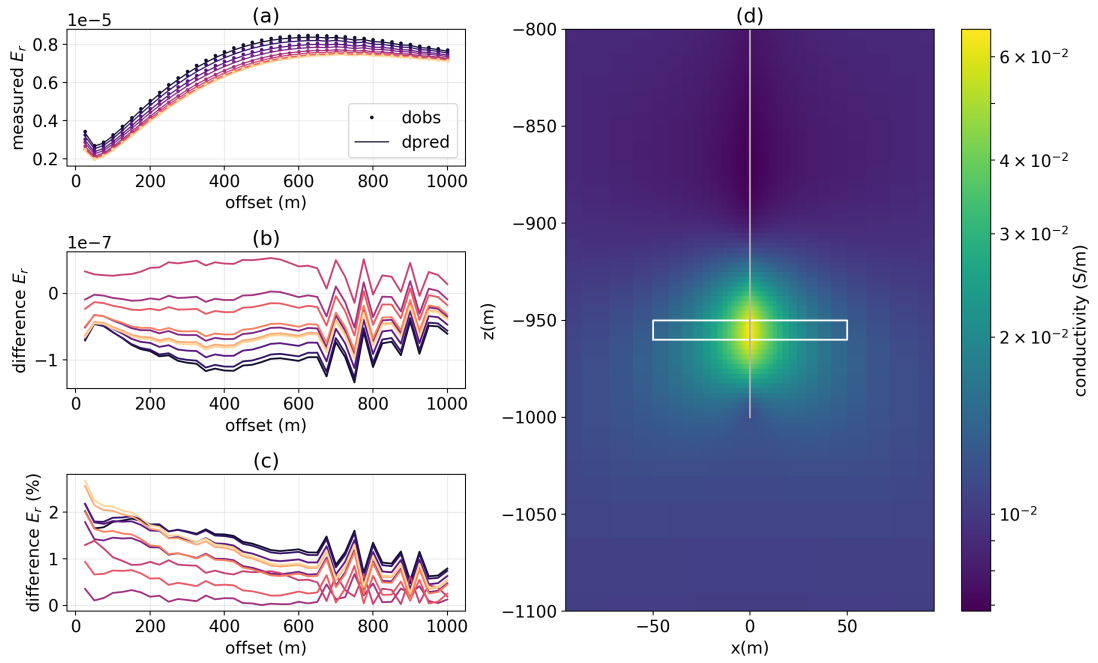


Figure 6.4: Tikhonov inversion result, similar to that shown in 6.3 that fits the data to a global χ -factor < 0.05 .

ductive targets are present. In this case, we know that the changes due to the conductive proppant and fluid should only increase the conductivity with respect to the background. We could impose a lower-bound on the conductivity of the inversion model, however, experimentation shows that this tends to push the center of the conductive anomaly beneath the true target depth.

To counter the vertical elongation of the target, we can always promote more horizontally elongated structures by altering the regularization. Figure 6.5 demonstrates an inversion using $\alpha_x = 100$ and fitting the data to a χ -factor $\downarrow 0.05$.

In summary, assuming high data quality, we can recover a conductive structure centered at the correct depth using a standard Tikhonov-style inversion. This, however, is not a particularly effective approach for delineating the extent of the fractured region of

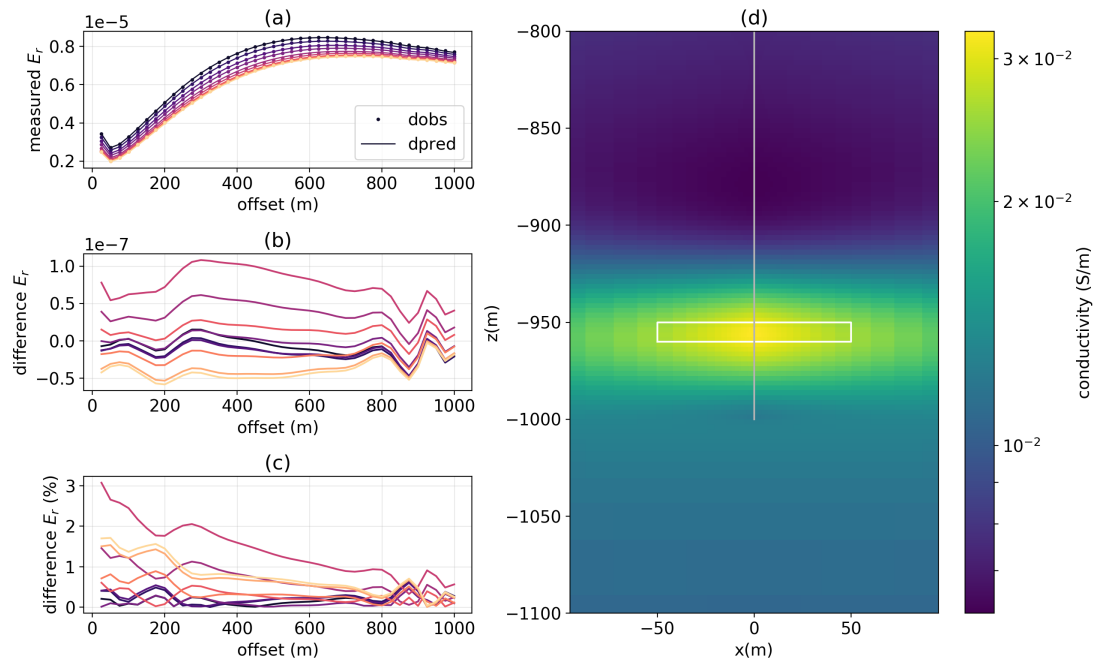


Figure 6.5: Tikhonov inversion result, similar to that shown in 6.4 that uses $\alpha_x = 100$.

the reservoir. With the aim of using the inversion to obtain parameters indicative of the injection, we next examine an approach using a parametric inversion.

Chapter 7

Conclusions and Future Work

Bibliography

- Aghasi, A., Kilmer, M., Miller, E., 2011. Parametric level set methods for inverse problems. *SIAM J. Imaging Sci.* 4 (2), 618–650. → pages 246
- Aldridge, D. F., Weiss, C. J., Knox, H. A., Schramm, K. A., Bartel, L. C., 2015. Is a Steel-Cased Borehole an Electrical Transmission Line? *SEG Technical Program Expanded Abstracts 2015*, 736–741.
URL <http://library.seg.org/doi/10.1190/segam2015-5927874.1> → pages 56
- Amestoy, P. R., Duff, I. S., L'Excellent, J.-Y., Koster, J., jan 2001. A Fully Asynchronous Multifrontal Solver Using Distributed Dynamic Scheduling. *SIAM Journal on Matrix Analysis and Applications* 23 (1), 15–41.
URL <http://epubs.siam.org/doi/abs/10.1137/S0895479899358194> → pages 226
- Amestoy, P. R., Guermouche, A., L'Excellent, J.-Y., Pralet, S., feb 2006. Hybrid scheduling for the parallel solution of linear systems. *Parallel Computing* 32 (2), 136–156.
URL <http://linkinghub.elsevier.com/retrieve/pii/S0167819105001328> → pages 226
- Archie, G., 1942. The Electrical Resistivity Log as an Aid in Determining Some Reservoir Characteristics. *Transactions of the AIME* 146 (01), 54–62.
URL <http://www.onepetro.org/doi/10.2118/942054-G> → pages 13
- Ascher, U. M., jan 2008. Numerical Methods for Evolutionary Differential Equations. Society for Industrial and Applied Mathematics.
URL <http://epubs.siam.org/doi/book/10.1137/1.9780898718911> → pages 226
- Augustin, A. M., Kennedy, W. D., Morrison, H. F., Lee, K. H., jan 1989. A theoretical study of surfacetoborehole electromagnetic logging in cased holes. *Geophysics* 54 (1), 90–99.
URL <http://library.seg.org/doi/10.1190/1.1442581http://library.seg.org/doi/abs/10.1190/1.1442581> → pages 39, 40, 41, 44, 65, 66, 67, 70, 71
- Barree, R., Fisher, M., Woodroof, R., sep 2002. A Practical Guide to Hydraulic Fracture Diagnostic Technologies. Paper SPE 77442, presented at the SPE Annual

Technical Conference and Exhibition held in San Antonio, Texas, 29 September - 2 October.

URL <http://www.spe.org/elibrary/servlet/spepreview?id=00077442> → pages 2, 3

Berryman, J. G., Hoversten, G. M., mar 2013. Modelling electrical conductivity for earth media with macroscopic fluid-filled fractures. *Geophysical Prospecting* 61 (2), 471–493.

URL <http://doi.wiley.com/10.1111/j.1365-2478.2012.01135.x> → pages 11, 13, 15, 16, 17

Bevc, D., Morrison, H. F., jun 1991. Borehole-to-surface electrical resistivity monitoring of a salt water injection experiment. *Geophysics* 56 (6), 769–777.

URL <http://library.seg.org/doi/abs/10.1190/1.1443094> → pages 4

Binley, A., Cassiani, G., Middleton, R., Winship, P., 2002. Vadose zone flow model parameterisation using cross-borehole radar and resistivity imaging. *Journal of Hydrology* 267 (3-4), 147–159. → pages 140

Börner, J. H., Wang, F., Weißflog, J., Bär, M., Görz, I., Spitzer, K., 2015. Multi-method virtual electromagnetic experiments for developing suitable monitoring designs: A fictitious CO₂ sequestration scenario in Northern Germany. *Geophysical Prospecting* 63 (6), 1430–1449. → pages 39

Brandl, G., 2010. Sphinx documentation. URL <http://sphinx-doc.org/sphinx.pdf>. → pages 209

Brannon, H. D., Starks, T. R., apr 2008. The Impact of Effective Fracture Area and Conductivity on Fracture Deliverability and Stimulation Value. In: SPE Annual Technical Conference and Exhibition. Society of Petroleum Engineers.

URL <http://www.onepetro.org/doi/10.2118/116057-MS> → pages 2

Brill, T. M., Le Calvez, J. L., Demichel, C., Nichols, E., Zapata Bermudez, F., 2012. Electromagnetic casing inspection tool for corrosion evaluation. Society of Petroleum Engineers - International Petroleum Technology Conference 2012, IPTC 2012 3 (February), 2109–2122.

URL <http://www.scopus.com/inward/record.url?eid=2-s2.0-84861374490&partnerID=40&md5=28a70a70a82662404aeb914e743f4cbc> → pages 208

Bruggeman, D. A. G., 1935. The calculation of various physical constants of heterogeneous substances. I. The dielectric constants and conductivities of mixtures composed of isotropic substances. *Annalen der Physik* 416 (7), 636–664. → pages 14

- Cannan, C., Bartel, L., Palisch, T., Aldridge, D., 2014. Electrically conductive proppant and methods for detecting, locating and characterizing the electrically conductive proppant.
 URL <http://www.google.com/patents/WO2014107608A1?cl=en> → pages 4
- Cassiani, G., Bruno, V., Villa, A., Fusi, N., Binley, A. M., 2006. A saline trace test monitored via time-lapse surface electrical resistivity tomography. *Journal of Applied Geophysics* 59 (3), 244–259. → pages 140
- Caudillo-Mata, L., Haber, E., Heagy, L., Schwarzbach, C., 2017a. A framework for the upscaling of the electrical conductivity in the quasi-static Maxwell's equations. *Journal of Computational and Applied Mathematics* 317. → pages 134
- Caudillo-Mata, L. A., Haber, E., Heagy, L. J., Oldenburg, D. W., aug 2014. Numerical upscaling of electrical conductivity: A problem specific approach to generate coarse-scale models. In: SEG Technical Program Expanded Abstracts 2014. No. 4. Society of Exploration Geophysicists, pp. 680–684.
 URL <http://library.seg.org/doi/abs/10.1190/segam2014-1488.1> → pages 11, 208
- Caudillo-mata, L. A., Haber, E., Heagy, L. J., Schwarzbach, C., 2016. A Framework for the Upscaling of the Electrical Conductivity in the Quasi-static Maxwell ' s Equations. (in review), 1–29. → pages 11
- Caudillo-Mata, L. A., Haber, E., Schwarzbach, C., 2017b. An oversampling technique for the multiscale finite volume method to simulate electromagnetic responses in the frequency domain. *Computational Geosciences* 21 (5-6), 963–980. → pages 135
- Cipolla, C., Warpinski, N., Mayerhofer, M., apr 2008a. Hydraulic Fracture Complexity: Diagnosis Remediation And Explotation. SPE Asia Pacific Oil and ... (October), 20–22.
 URL <http://www.onepetro.org/doi/10.2118/115771-MS> → pages 11
- Cipolla, C., Wright, C., feb 2002. Diagnostic Techniques To Understand Hydraulic Fracturing: What? Why? and How? *SPE Production & Facilities* 17 (01), 23–35.
 URL <http://www.onepetro.org/doi/10.2118/75359-PA> → pages 2, 3
- Cipolla, C. L., Lolon, E., Mayerhofer, M. J., Warpinski, N. R., apr 2009. The Effect of Proppant Distribution and Un-Propped Fracture Conductivity on Well Performance in Unconventional Gas Reservoirs. In: *SPE Hydraulic Fracturing Technology Conference*. Society of Petroleum Engineers.
 URL <http://www.onepetro.org/doi/10.2118/119368-MS> → pages 2, 3
- Cipolla, C. L., Warpinski, N. R., Mayerhofer, M. J., Lolon, E., Vincent, M. C., apr 2008b. The Relationship Between Fracture Complexity, Reservoir Properties, and

- Fracture Treatment Design. In: SPE Annual Technical Conference and Exhibition. Society of Petroleum Engineers, pp. 1–25.
 URL <https://www.onepetro.org/conference-paper/SPE-115769-MS>
<http://www.onepetro.org/doi/10.2118/115769-MS> → pages 11
- Cockett, R., Heagy, L. J., Oldenburg, D. W., aug 2016a. Pixels and their neighbors : Finite volume. *The Leading Edge* (August), 703–706.
 URL <http://dx.doi.org/10.1190/tle35080703.1>
<http://library.seg.org/doi/10.1190/tle35080703.1>
<http://tle.geoscienceworld.org/content/35/8/703> → pages 217, 224
- Cockett, R., Heagy, L. J., Oldenburg, D. W., aug 2016b. Pixels and their neighbors: Finite volume. *The Leading Edge* 35 (8), 703–706.
 URL <http://library.seg.org/doi/10.1190/tle35080703.1> → pages 48
- Cockett, R., Kang, S., Heagy, L. J., Pidlisecky, A., Oldenburg, D. W., dec 2015. SimPEG: An open source framework for simulation and gradient based parameter estimation in geophysical applications. *Computers & Geosciences* 85, 142–154.
 URL <http://linkinghub.elsevier.com/retrieve/pii/S009830041530056X> → pages x, xxviii, 6, 43, 50, 84, 142, 146, 209, 210, 211, 212, 215, 217, 218, 224
- Coggon, J. H., 1971. Electromagnetic and electrical modeling by the finite element method. *GEOPHYSICS* 36 (1), 132–155.
 URL <http://dx.doi.org/10.1190/1.1440151> → pages 221, 228, 229
- Commer, M., Hoversten, G. M., Um, E. S., mar 2015. Transient-electromagnetic finite-difference time-domain earth modeling over steel infrastructure. *Geophysics* 80 (2), E147–E162.
 URL <http://library.seg.org/doi/pdf/10.1190/geo2014-0324.1>
<http://library.seg.org/doi/abs/10.1190/geo2014-0324.1> → pages xiv, 42, 44, 51, 52, 53, 54, 81, 82, 208, 242
- Constable, S. C., Parker, R. L., Constable, C. G., 1987. Models From Electromagnetic Sounding Data. *Geophysics* 52 (3), 289–300. → pages 207
- Cosmin, G., Schenk, O., Lubin, M., Gäertner, K., 2016. An Augmented Incomplete Factorization Approach for Computing the Schur Complement in Stochastic Optimization The MIT Faculty has made this article openly available . Please share how this access benefits you . Your story matters . Citation An Augmented . → pages 52
- Cuevas, N., 2014a. Energizing a Bipole Casing Electromagnetic Source - Sensitivity Analysis. In: 76th EAGE Conference and Exhibition 2014. No. June 2014. pp. 16–19.
 URL <http://www.earthdoc.org/publication/publicationdetails/?publication=75967>

//earthdoc.eage.org/publication/publicationdetails/?publication=75967http://www.earthdoc.org/publication/publicationdetails/?publication=75967\$\\ delimiter"026E30F\$nhttp://earthdoc.eage.org/public → pages 242

Cuevas, N. H., sep 2014b. Analytical solutions of EM fields due to a dipolar source inside an infinite casing. *Geophysics* 79 (5), E231–E241.
URL <http://library.seg.org/doi/pdf/10.1190/geo2013-0223.1> → pages 42, 208

Daily, W., Ramirez, A., LaBrecque, D., Nitao, J., may 1992. Electrical resistivity tomography of vadose water movement. *Water Resources Research* 28 (5), 1429–1442.
URL <http://doi.wiley.com/10.1029/91WR03087> → pages 139, 140

Devriese, S. G. R., Oldenburg, D. W., 2016. Feasibility of electromagnetic methods to detect and image steam-assisted gravity drainage steam chambers. *Geophysics* 81 (4), E227–E241.
URL <http://library.seg.org/doi/10.1190/geo2015-0451.1> → pages 208

Doetsch, J., Linde, N., Vogt, T., Binley, A., Green, A. G., 2012. Imaging and quantifying salt-tracer transport in a riparian groundwater system by means of 3D ERT monitoring. *Geophysics* 77 (5), B207–B218.
URL <http://library.seg.org/doi/10.1190/geo2012-0046.1> → pages 139, 140

Doll, H., 1949. Introduction to Induction Logging and Application to Logging of Wells Drilled With Oil Base Mud. *Journal of Petroleum Technology* 1 (6). → pages 63

Durlofsky, L. J., 2003. Upscaling of Geocellular Models for Reservoir Flow Simulation : A Review of Recent Progress. Paper presented at the 7th International Forum on Reservoir Simulation Buhl/Baden-Baden, Germany, June 23-27. → pages 11

Griffiths, D. J., 2007. An Introduction to Electrodynamics. Vol. 110.
URL
[http://books.google.com/books?id=x0akQgAACAAJ\\$\\ delimiter"026E30F\\$nhttp://www.nature.com/doifinder/10.1038/110509b0](http://books.google.com/books?id=x0akQgAACAAJ$\\ delimiter) → pages 229

Griffiths, D. J., Li, Y., 1997. Charge density on a conducting needle.
URL <http://aapt.scitation.org/doi/10.1119/1.18671> → pages 59, 87

Haber, E., dec 2014a. Computational Methods in Geophysical Electromagnetics. Society for Industrial and Applied Mathematics, Philadelphia, PA.
URL <http://pubs.siam.org/doi/book/10.1137/1.9781611973808> → pages 6, 207, 213, 217, 219, 221, 225, 228, 229, 247, 250

- Haber, E., 2014b. Computational Methods in Geophysical Electromagnetics.
 URL <http://pubs.siam.org/doi/book/10.1137/1.9781611973808> → pages 11, 46, 47, 49, 50, 135
- Haber, E., Ascher, U. M., 2001. Fast Finite Volume Simulation of 3D Electromagnetic Problems With Highly Discontinuous Coefficients 22 (6), 1943–1961. → pages 207
- Haber, E., Ascher, U. M., Oldenburg, D. W., 2004. Inversion of 3D electromagnetic data in frequency and time domain using an inexact allatonce approach. *Geophysics* 69 (5), 1216–1228.
 URL <http://library.seg.org/doi/10.1190/1.1801938> → pages 47
- Haber, E., Heldmann, S., Ascher, U., 2007. Adaptive finite volume method for distributed non-smooth parameter identification. *Inverse Problems* 23 (4), 1659–1676. → pages 44, 51, 134
- Haber, E., Oldenburg, D., 1998. Joint Inversion: A Structural Approach. Unknown 63. → pages 207
- Hashin, Z., Shtrikman, S., 1962. A Variational approach to the theory of the effective magnetic permeability of multiphase materials. *Journal of Applied Physics* 33 (10), 3125–3131. → pages 26
- Hayley, K., Pidlisecky, A., Bentley, L. R., 2011. Simultaneous time-lapse electrical resistivity inversion. *Journal of Applied Geophysics* 75 (2), 401–411.
 URL <http://dx.doi.org/10.1016/j.jappgeo.2011.06.035> → pages 140
- Heagy, L., apr 2018. simpeg-research/heagy_2018_emcyl. Zenodo.
 URL <https://doi.org/10.5281/zenodo.1220427> → pages 43
- Heagy, L., Oldenburg, D., Chen, J., 2014a. Where does the proppant go? Examining the application of electromagnetic methods for hydraulic fracture characterization. Geoconvention.Com, 1–7.
 URL http://www.geoconvention.com/uploads/abstracts/334_{-}GC2014{-}Where{-}does{-}the{-}proppant{-}go.pdf → pages iii
- Heagy, L. J., Cockett, A. R., Oldenburg, D. W., aug 2014b. Parametrized Inversion Framework for Proppant Volume in a Hydraulically Fractured Reservoir.
 URL <http://library.seg.org/doi/abs/10.1190/segam2014-1639.1> → pages 223
- Heagy, L. J., Cockett, R., Kang, S., Rosenkjaer, G. K., Oldenburg, D. W., 2017a. A framework for simulation and inversion in electromagnetics. *Computers and Geosciences* 107 (July), 1–19.
 URL <http://dx.doi.org/10.1016/j.cageo.2017.06.018> → pages iii, 43, 47, 50, 78, 84, 146

- Heagy, L. J., Cockett, R., Oldenburg, D. W., 2017b. Modular electromagnetic simulations with applications to steel cased wells. Proceedings of the Sixth International Symposium in Three-Dimensional Electromagnetics, 125–129.
 URL <http://www.gwhohmann.org/3dem-6-proceedings-download.html> → pages iii
- Heagy, L. J., Cockett, R., Oldenburg, D. W., Wilt, M., aug 2015. Modelling electromagnetic problems in the presence of cased wells. In: SEG Technical Program Expanded Abstracts 2015. Society of Exploration Geophysicists, pp. 699–703.
 URL <http://library.seg.org/doi/10.1190/segam2015-5931035.1> → pages iii, xxviii, 42, 208, 218, 221, 224, 228, 229, 243
- Heagy, L. J., Oldenburg, D. W., sep 2013. Investigating the potential of using conductive or permeable proppant particles for hydraulic fracture characterization. In: SEG Technical Program Expanded Abstracts 2013. Vol. i. Society of Exploration Geophysicists, pp. 576–580.
 URL <http://library.seg.org/doi/abs/10.1190/segam2013-1372.1> → pages iii
- Heagy, L. J., Oldenburg, D. W., 2018a. Finite volume electromagnetic modelling on 2D and 3D cylindrical meshes with applications to steel cased wells, 1–31.
 URL <http://arxiv.org/abs/1804.07991> → pages 82, 84, 86, 87, 126, 135
- Heagy, L. J., Oldenburg, D. W., apr 2018b. Finite volume electromagnetic modelling on 2D and 3D cylindrical meshes with applications to steel cased wells.
 URL <http://arxiv.org/abs/1804.07991> → pages 83, 137
- Holladay, J. S., West, G. F., 1984. Effect of well casings on surface electrical surveys. *Geophysics* 49 (2), 177–188.
 URL <http://library.seg.org/doi/10.1190/1.1441649> → pages 40, 80
- Horesh, L., Haber, E., jan 2011. A Second Order Discretization of Maxwell's Equations in the Quasi-Static Regime on OcTree Grids. *SIAM Journal on Scientific Computing* 33 (5), 2805–2822.
 URL <http://pubs.siam.org/doi/10.1137/100798508> → pages 46
- Hoversten, G., Commer, M., Haber, E., Schwarzbach, C., 2014. Hydro-frac Monitoring Using Ground Time-domain EM. In: 76th EAGE Conference and Exhibition. No. June 2014. pp. 76–78.
 URL <http://www.earthdoc.org/publication/publicationdetails/?publication=75475> → pages 208, 242
- Hoversten, G. M., Commer, M., Haber, E., Schwarzbach, C., nov 2015. Hydro-frac monitoring using ground time-domain electromagnetics. *Geophysical Prospecting* 63 (6), 1508–1526.

URL <http://doi.wiley.com/10.1111/1365-2478.12300> → pages 10, 19, 31, 60, 62, 82, 208, 242

Hoversten, G. M., Schwarzbach, C., Belliveau, P., Haber, E., Shekhtman, R., 2017. Borehole to Surface Electromagnetic Monitoring of Hydraulic Fractures. In: 79th EAGE Conference and Exhibition 2017. → pages 39, 41, 57, 81

Hu, Y., Fang, Y., LaBrecque, D., Ahmadian, M., Liu, Q. H., 2018. Reconstruction of high-contrast proppant in hydraulic fractures with galvanic measurements. IEEE Transactions on Geoscience and Remote Sensing 56 (4), 2066–2073. → pages 10

Hunter, J. D., 2007. Matplotlib: A 2D graphics environment. Computing In Science & Engineering 9 (3), 90–95. → pages 209

Hyman, J., Morel, J., Shashkov, M., Steinberg, S., 2002. Mimetic finite difference methods for diffusion equations , 333–352. → pages 217

Hyman, J. M., Shashkov, M., 1999. Mimetic Discretizations for Maxwell ' s Equations 909, 881–909. → pages 46, 217

Ingraffea, A. R., Wells, M. T., Santoro, R. L., Shonkoff, S. B. C., 2014. Assessment and risk analysis of casing and cement impairment in oil and gas wells in Pennsylvania, 2000-2012. Proceedings of the National Academy of Sciences 111 (30), 10955–10960.

URL <http://www.pnas.org/cgi/doi/10.1073/pnas.1323422111> → pages 85

Jackson, R. B., Vengosh, A., Darrah, T. H., Warner, N. R., Down, A., Poreda, R. J., Oshborn, S. G., Zhao, K., Karr, J. D., 2013. Increased stray gas abundance in a subset of drkng water wells. Proceedings of the National Academy of Sciences of the United States of America 110 (28), 11250–11255. → pages 85

Jahandari, H., Farquharson, C. G., 2014. A finite-volume solution to the geophysical electromagnetic forward problem using unstructured grids. Geophysics 79 (6), E287–E302.

URL <http://library.seg.org/doi/10.1190/geo2013-0312.1> → pages 46

Johnston, R., Trofimenkoff, F., Haslett, J., jul 1987. Resistivity Response of a Homogeneous Earth with a Finite-Length Contained Vertical Conductor. IEEE Transactions on Geoscience and Remote Sensing GE-25 (4), 414–421.

URL <http://ieeexplore.ieee.org/document/4072660/> → pages 40, 80

Johnston, R. H., Trofimenkoff, F. N., Haslett, J. W., 1992. The Complex Resistivity Response of a Homogeneous Earth with a Finite-Length Contained Vertical Conductor. IEEE Transactions on Geoscience and Remote Sensing 30 (1), 46–54. → pages 40

- Kalderimis, J., Meyer, M., 2011. Travis CI GmbH.
 URL <https://travis-ci.org> → pages 209, 232
- Kang, S., Cockett, R., Heagy, L. J., Oldenburg, D. W., Facility, G. I., 2015. Moving between dimensions in electromagnetic inversions (2), 5000–5004. → pages 207, 218, 222, 223
- Kaufman, A. A., jan 1990. The electrical field in a borehole with a casing. *Geophysics* 55 (1), 29–38.
 URL <http://link.aip.org/link/?GPY/55/29/1{&}Agg=doihttp://library.seg.org/doi/abs/10.1190/1.1442769> → pages 39, 40, 44, 54, 55, 56, 77, 82, 108, 126, 137
- Kaufman, A. A., Wightman, E. W., 1993. A transmission-line model for electrical logging through casing. *Geophysics* 58 (12), 1739. → pages xiv, 39, 40, 44, 54, 55, 57, 58, 60, 82, 127, 128
- Kelbert, A., Meqbel, N., Egbert, G. D., Tandon, K., 2014. ModEM: A modular system for inversion of electromagnetic geophysical data. *Computers and Geosciences* 66, 40–53.
 URL <http://dx.doi.org/10.1016/j.cageo.2014.01.010> → pages 207
- Kemna, A., Kulessa, B., Vereecken, H., 2002. Imaging and characterisation of subsurface solute transport using electrical resistivity tomography (ERT) and equivalent transport models. *Journal of Hydrology* 267 (3-4), 125–146. → pages 139
- Kim, J. H., Yi, M. J., Park, S. G., Kim, J. G., 2009. 4-D inversion of DC resistivity monitoring data acquired over a dynamically changing earth model. *Journal of Applied Geophysics* 68 (4), 522–532.
 URL <http://dx.doi.org/10.1016/j.jappgeo.2009.03.002> → pages 140
- King, G. E., apr 2010. Thirty Years of Gas Shale Fracturing: What Have We Learned? In: SPE Annual Technical Conference and Exhibition. Society of Petroleum Engineers.
 URL <http://www.onepetro.org/doi/10.2118/133456-MS> → pages 4
- Kohnke, C., Liu, L., Streich, R., Swidinsky, A., 2017. A method of moments approach to modeling the electromagnetic response of multiple steel casings in a layered earth. *Geophysics*, 1–72.
 URL <https://library.seg.org/doi/10.1190/geo2017-0303.1> → pages 42, 126
- Kong, F. N., Roth, F., Olsen, P. A., Stalheim, S. O., 2009. Casing effects in the sea-to-borehole electromagnetic method. *Geophysics* 74 (5), F77–F87.
 URL <http://library.seg.org/doi/10.1190/1.3173807> → pages 39, 56

- Labrecque, D., Brigham, R., Liu, Q. H., Fang, Y., Dai, J., Hu, Y., Yu, Z., Kleinhammes, A., Doyle, P., Wu, Y., 2016. SPE-179170-MS Remote Imaging of Proppants in Hydraulic Fracture Networks Using Electromagnetic Methods: Results of Small-Scale Field Experiments, 9–11. → pages 10
- Landauer, R., 1952. The electrical resistance of binary metallic mixtures. *Journal of Applied Physics* 23 (7), 779–784. → pages 14
- Landauer, R., 1978. Electrical conductivity in inhomogeneous media. *AIP Conference Proceedings* 40 (1978), 2–45.
 URL <http://aip.scitation.org/doi/abs/10.1063/1.31150> → pages 14
- Li, M., Abubakar, A., Habashy, T. M., 2010. Application of a two-and-a-half dimensional model-based algorithm to crosswell electromagnetic data inversion. *Inverse Problems* 26 (7), 074013.
 URL <http://stacks.iop.org/0266-5611/26/i=7/a=074013> → pages 222
- Li, Y., Key, K., 2007. 2D marine controlled-source electromagnetic modeling: Part 1 An adaptive finite-element algorithm. *GEOPHYSICS* 72 (2), WA51–WA62.
 URL <http://dx.doi.org/10.1190/1.2432262> → pages 207
- Loke, M. H., Dahlin, T., Rucker, D. F., 2014. Smoothness-constrained time-lapse inversion of data from 3D resistivity surveys. *Near Surface Geophysics* 12 (1), 5–24. → pages 140
- Marsala, A. F., Al-Buali, M., Zaki Ali, Ma, S. M., He, Z., Biyan, T., Guo, Z., He, T., apr 2011. First Borehole to Surface Electromagnetic Survey in KSA: Reservoir Mapping and Monitoring at a New Scale. In: *SPE Annual Technical Conference and Exhibition*. Society of Petroleum Engineers, p. SPE 146348.
 URL <http://www.onepetro.org/doi/10.2118/146348-MS> → pages 4
- Marsala, A. F., Al-Ruwaili, S. B., Shouxiang, M. M., Al-Ali, Z. A., Al-Buali, M. H., Donadille, J.-M., Crary, S. F., Wilt, M., apr 2008. Crosswell Electromagnetic Tomography: from Resistivity Mapping to Interwell Fluid Distribution. In: *International Petroleum Technology Conference*. International Petroleum Technology Conference, pp. 1–6.
 URL <http://www.onepetro.org/doi/10.2523/12229-MS> → pages 4
- Marsala, A. F., Hibbs, A. D., Morrison, H. F., dec 2014. Evaluation of Borehole Casing Sources for Electromagnetic Imaging of Deep Formations. In: *International Petroleum Technology Conference*. International Petroleum Technology Conference.
 URL <http://www.onepetro.org/doi/10.2523/IPTC-17845-MS> → pages 4

- Marsala, A. F., Lyngra, S., Aramco, S., Safdar, M., Zhang, P., Wilt, M., 2015. Crosswell electromagnetic induction between two widely spaced horizontal wells : Coiled-tubing conveyed data collection and 3D inversion from a carbonate reservoir in Saudi Arabia, 2848–2852. → pages 30, 208, 242
- Marsala*, A. F., Lyngra, S., Safdar, M., Zhang, P., Wilt, M., aug 2015. Crosswell electromagnetic induction between two widely spaced horizontal wells: Coiled-tubing conveyed data collection and 3D inversion from a carbonate reservoir in Saudi Arabia. In: SEG Technical Program Expanded Abstracts 2015. Society of Exploration Geophysicists, pp. 2848–2852.
 URL <http://library.seg.org/doi/10.1190/segam2015-5891203.1> → pages 30, 33
- Maxwell, J. C., 1873. A Treatise on Electricity and Magnetism, Vol.1. Clarendon Press (Oxford). → pages 13
- Maxwell, S., 2014. Microseismic Imaging of Hydraulic Fracturing : Improved Engineering of Unconventional Shale Reservoirs. No. 17. → pages 2
- Maxwell, S., Urbancic, T., Steinsberger, N., Zinno, R., sep 2002. Microseismic Imaging of Hydraulic Fracture Complexity in the Barnett Shale. In: Proceedings of SPE Annual Technical Conference and Exhibition. Society of Petroleum Engineers, pp. 1–9.
 URL <https://www.onepetro.org/conference-paper/SPE-77440-MS>
<http://www.onepetro.org/doi/10.2118/77440-MS>
<http://www.spe.org/elibrary/servlet/spepreview?id=00077440> → pages 2
- McMillan, M. S., Oldenburg, D. W., Haber, E., Christoph, 2015a. Parametric 3D inversion of airborne time domain electromagnetics. 24th International Geophysical Conference and Exhibition, 1–5. → pages 148, 207
- McMillan, M. S., Schwarzbach, C., Haber, E., Oldenburg, D. W., 2015b. 3D parametric hybrid inversion of time-domain airborne electromagnetic data. *Geophysics* 80 (6), K25–K36.
 URL <http://library.seg.org/doi/10.1190/geo2015-0141.1> → pages 207, 222, 246
- McMillan, M. S. G., 2017. Cooperative and parametric strategies for 3D airborne electromagnetic inversion (April). → pages 148, 149
- Merwin, N., Donahoe, L., Mcangus, E., 2015. Coveralls.
 URL <https://coveralls.io> → pages 209
- Milton, G. W., 1985. The coherent potential approximation is a realizable effective medium scheme. *Communications in Mathematical Physics* 99 (4), 463–500. → pages 13

- Milton, G. W., 2002. The Theory of Composites. Cambridge University Press, Cambridge.
 URL <http://ebooks.cambridge.org/ref/id/CBO9780511613357> → pages 11, 13
- Moran, J. H., Kunz, K. S., dec 1962. Basic theory of induction logging and application to study of two-coil sondes. *GEOPHYSICS* 27 (6), 829–858.
 URL <http://library.seg.org/doi/10.1190/1.1439108> → pages 63
- Munday, T. J., Doble, R., Berens, V., Fitzpatrick, A., 2006. The Application of Air, Ground and In River' Electromagnetics in the Definition of Spatial Patterns of Groundwater Induced Salt Accumulation in a Salinising Floodplain, Lower River Murray, South Australia. Symposium on the Application of Geophysics to Engineering and Environmental Problems, 886–891.
 URL <http://link.aip.org/link/SAGEEP/v19/i1/p886/s1{&}Agg=doi> → pages 236, 241
- Nekut, A. G., 1995. Crosswell electromagnetic tomography in steelcased wells. *Geophysics* 60 (3), 912–920.
 URL <http://library.seg.org/doi/10.1190/1.1443826> → pages 41
- Newman, G. A., Alumbaugh, D. L., jan 1999. 20. Electromagnetic Modeling and Inversion on Massively Parallel Computers. Society of Exploration Geophysicists, Ch. 20, pp. 299–321.
 URL <http://library.seg.org/doi/abs/10.1190/1.9781560802154.ch20> → pages 207
- Novotny, E., 1977. Proppant Transport. SPE Annual Fall Technical Conference and Exhibition.
 URL <http://op.spe.semcs.net/doi/10.2118/6813-MS> → pages 19, 31
- Oldenborger, G. a., Knoll, M. D., Routh, P. S., LaBrecque, D. J., 2007. Time-lapse ERT monitoring of an injection/withdrawal experiment in a shallow unconfined aquifer. *Geophysics* 72 (4), F177–F187.
 URL <http://library.seg.org/doi/abs/10.1190/1.2734365> → pages 140
- Oldenburg, D. D. W., Li, Y., jan 2005a. Inversion for applied geophysics: A tutorial. *Investigations in geophysics* 13, 1–85.
 URL <http://www.eoas.ubc.ca/courses/eosc454/content/Papers/CaseHistories/InversionTutorialOldenburgandLi2005.pdf>
<http://library.seg.org/doi/book/10.1190/1.9781560801719> → pages 207, 212
- Oldenburg, D. W., Haber, E., Shekhtman, R., 2013. Three dimensional inversion of multisource time domain electromagnetic data. *Geophysics* 78 (1), E47–E57.
 URL [http://apps.webofknowledge.com/full{_}record.do?product=WOS{&}search{_}mode="](http://apps.webofknowledge.com/full{_}record.do?product=WOS{&}search{_}mode=)

GeneralSearch{&}qid=4{&}SID=3D9g64O1pAi9CCJ9N1a{&}page=1{&}doc=3
→ pages 219

Oldenburg, D. W., Heagy, L. J., Kang, S., 2017. Geophysical Electromagnetics: Fundamentals and Applications. SEG Distinguished Instructor Short Course.
URL <https://seg.org/Education/Courses/DISC/2017-DISC-Doug-Oldenburg> →
pages 38, 63

Oldenburg, D. W., Li, Y., jan 2005b. 5. Inversion for Applied Geophysics: A Tutorial.
In: Butler, D. K. (Ed.), Near-Surface Geophysics. Vol. 13. Society of Exploration
Geophysicists, pp. 89–150.
URL <http://www.eoas.ubc.ca/courses/eosc454/content/Papers/CaseHistories/InversionTutorialOldenburgandLi2005.pdf> http:
[//library.seg.org/doi/book/10.1190/1.9781560801719](https://library.seg.org/doi/book/10.1190/1.9781560801719) https:
[//library.seg.org/doi/10.1190/1.9781560801719](https://library.seg.org/doi/10.1190/1.9781560801719) https://library.seg.org/doi/ →
pages 6, 142, 143, 144

Oliphant, T. E., may 2007. Python for Scientific Computing. Computing in Science
Engineering 9 (3), 10–20. → pages 209, 226

Osborn, S. G., Vengosh, A., Warner, N. R., Jackson, R. B., 2011. Methane
contamination of drinking water accompanying gas-well drilling and hydraulic
fracturing. Proceedings of the National Academy of Sciences 108 (37), E665–E666.
URL <http://www.pnas.org/cgi/doi/10.1073/pnas.1109270108> → pages 85

Overton, I. C., Jolly, I. D., Slavich, P. G., Lewis, M. M., Walker, G. R., 2004.
Modelling vegetation health from the interaction of saline groundwater and flooding
on the Chowilla floodplain, South Australia. Australian Journal of Botany 54 (2),
207–220. → pages 236

Pardo, D., Torres-Verdin, C., 2013. Sensitivity analysis for the appraisal of
hydrofractures in horizontal wells with borehole resistivity measurements.
Geophysics 78 (4), D209–D222. → pages 10, 18, 39, 42, 208

Park, S., 1998. Fluid migration in the vadose zone from 3-D inversion of resistivity
monitoring data. Geophysics 63 (1), 41–51.
URL <http://library.seg.org/doi/10.1190/1.1444326> → pages 140

Parker, R. L., aug 1980. The inverse problem of electromagnetic induction: Existence
and construction of solutions based on incomplete data. Journal of Geophysical
Research: Solid Earth 85 (B8), 4421–4428.
URL <http://doi.wiley.com/10.1029/JB085iB08p04421> → pages 207

Parker, R. L., 1994a. Geophysical inverse theory. Princeton university press. → pages
143, 144

- Parker, R. L., 1994b. Geophysical inverse theory. Princeton university press. → pages 212
- Perez, F., Berkeley, L., Granger, B. E., 2015. Project Jupyter : Computational Narratives as the Engine of Collaborative Data Science (April), 1–24. → pages 43
- Petra, C. G., Schenk, O., Anitescu, M., 2014. Real-time stochastic optimization of complex energy systems on high-performance computers. Computing in Science and Engineering 16 (5), 32–42. → pages 52
- Pidlisecky, A., Singha, K., Day-Lewis, F. D., 2011. A distribution-based parametrization for improved tomographic imaging of solute plumes. Geophysical Journal International 187 (1), 214–224. → pages 207, 222
- Puzyrev, V., Vilamajo, E., Queralt, P., Ledo, J., Marcuello, A., 2017. Three-Dimensional Modeling of the Casing Effect in Onshore Controlled-Source Electromagnetic Surveys. Surveys in Geophysics 38 (2), 527–545. → pages 42, 60, 126
- Rahmani, A. R., Athey, A. E., Chen, J., Wilt, M. J., 2014. Sensitivity of dipole magnetic tomography to magnetic nanoparticle injectates. Journal of Applied Geophysics 103, 199–214.
 URL <http://dx.doi.org/10.1016/j.jappgeo.2014.01.019> → pages 10
- Ramirez, A., Daily, W., Binley, A., LaBrecque, D., Roelant, D., 1996. Detection of Leaks in Underground Storage Tanks Using Electrical Resistance Methods. Journal of Environmental and Engineering Geophysics 1 (3), 189–203.
 URL <http://library.seg.org/doi/abs/10.4133/JEEG1.3.189> → pages 41, 81
- Rivera Rios, A., 2014. Multi-order Vector Finite Element Modelling of 3D Magnetotelluric Data including complex geometry and anisotropic earth. Ph.D. thesis, The University of Adelaide. → pages 225
- Rocroi, J. P., Koulikov, A. V., feb 1985. The use of vertical line sources in electrical prospecting for hydrocarbon. Geophysical Prospecting 33 (1), 138–152.
 URL <http://doi.wiley.com/10.1111/j.1365-2478.1985.tb00426.x> → pages 41
- Rucker, D. F., 2012. Enhanced resolution for long electrode ERT. Geophysical Journal International 191 (1), 101–111. → pages 41, 81
- Rucker, D. F., Loke, M. H., Levitt, M. T., Noonan, G. E., 2010. Electrical-resistivity characterization of an industrial site using long electrodes. Geophysics 75 (4), WA95. → pages 41, 81

- Schenkel, C., 1991. The Electrical Resistivity Method in Cased Boreholes. PhD Thesis, Lawrence Berkeley National Laboratory LBL-31139.
URL <https://escholarship.org/uc/item/0cf136z6> → pages 82, 99, 106, 127
- Schenkel, C. J., Morrison, H. F., aug 1990. Effects of well casing on potential field measurements using downhole current sources. *Geophysical Prospecting* 38 (6), 663–686.
URL <http://onlinelibrary.wiley.com/doi/10.1111/j.1365-2478.1990.tb01868.x/abstract> → pages 40, 82, 108
- Schenkel, C. J., Morrison, H. F., 1994. Electrical resistivity measurement through metal casing. *Geophysics* 59 (7), 1072–1082. → pages 40, 57, 58, 62, 81, 82, 109, 123, 124
- Singha, K., Gorelick, S. M., 2005. Saline tracer visualized with three-dimensional electrical resistivity tomography: Field-scale spatial moment analysis. *Water Resources Research* 41 (5), 1–17. → pages 139
- Singha, K., Gorelick, S. M., 2006. Effects of spatially variable resolution on field-scale estimates of tracer concentration from electrical inversions using Archie's law. *Geophysics* 71 (3), G83–G91.
URL <http://library.seg.org/doi/10.1190/1.2194900> → pages 140
- Slater, L., Binley, A., Versteeg, R., Cassiani, G., Birken, R., Sandberg, S., 2002. A 3D ERT study of solute transport in a large experimental tank. *Journal of Applied Geophysics* 49 (4), 211–229. → pages 139
- Sørensen, K. I., Auken, E., 2004. SkyTEM-a new high-resolution helicopter transient electromagnetic system. *Exploration Geophysics* 35 (3), 191–199. → pages 238
- Swidinsky, A., Edwards, R. N., Jegen, M., 2013. The marine controlled source electromagnetic response of a steel borehole casing: Applications for the NEPTUNE Canada gas hydrate observatory. *Geophysical Prospecting* 61 (4), 842–856. → pages 39, 42, 82, 126
- Tang, W., Li, Y., Swidinsky, A., Liu, J., nov 2015. Three-dimensional controlled-source electromagnetic modelling with a well casing as a grounded source: a hybrid method of moments and finite element scheme. *Geophysical Prospecting* 63 (6), 1491–1507.
URL <http://doi.wiley.com/10.1111/1365-2478.12330> → pages 82
- Telford, W. M., Geldart, L. P., Sheriff, R. E., 1990a. *Applied geophysics*. Vol. 1. Cambridge university press. → pages 10, 86

- Telford, W. M., Geldart, L. P., Sheriff, R. E., 1990b. Applied geophysics. Vol. 1. Cambridge university press. → pages 213
- Tietze, K., Ritter, O., Veeken, P., 2015. Controlled-source electromagnetic monitoring of reservoir oil saturation using a novel borehole-to-surface configuration. *Geophysical Prospecting* 63 (6), 1468–1490. → pages 39
- Tikhonov, A. N., Arsenin, V. Y., 1977. Solutions of Ill-Posed Problems. SIAM Review 32, 1320–1322.
 URL <http://www.getcited.org/pub/101760676> → pages 207
- Tøndel, R., Schütt, H., Dümmong, S., Ducrocq, A., Godfrey, R., Labrecque, D., Nutt, L., Campbell, A., Rufino, R., 2014. Reservoir monitoring of steam-assisted gravity drainage using borehole measurements. *Geophysical Prospecting* 62 (4), 760–778. → pages 140, 141
- Torquato, S., 2002. Random Heterogeneous Materials: Microstructure and Macroscopic Properties. Vol. 16. Springer. → pages 11, 13, 15, 16, 25
- Uchida, T., Lee, K. H., Wilt, M. J., 1991. Effect of a steel casing on crosshole EM measurement. SEG Technical Program Expanded Abstracts 1991, 442–445.
 URL <http://library.seg.org/doi/abs/10.1190/1.1889151> → pages 41
- Um, E. S., Commer, M., Newman, G. A., Hoversten, G. M., jun 2015. Finite element modelling of transient electromagnetic fields near steel-cased wells. *Geophysical Journal International* 202 (2), 901–913.
 URL <http://gji.oxfordjournals.org/cgi/doi/10.1093/gji/ggv193> → pages 39, 42, 57, 59, 60, 81, 82, 126, 129, 208, 242
- van der Walt, S., Colbert, S. C., Varoquaux, G., mar 2011. The NumPy Array: A Structure for Efficient Numerical Computation. *Computing in Science Engineering* 13 (2), 22–30. → pages 209
- Vengosh, A., Jackson, R. B., Warner, N., Darrah, T. H., Kondash, A., aug 2014. A Critical Review of the Risks to Water Resources from Unconventional Shale Gas Development and Hydraulic Fracturing in the United States. *Environmental Science & Technology* 48 (15), 8334–8348.
 URL <http://pubs.acs.org/doi/abs/10.1021/es405118y> → pages 4
- Viezzoli, A., Auken, E., Munday, T., 2009. Spatially constrained inversion for quasi 3D modeling of airborne electromagnetic data - an application for environmental assessment in the Lower Murray Region of South Australia. *Exploration Geophysics* 40 (2008), 173–183. → pages 238

- Viezzoli, A., Munday, T., Auken, E., Christiansen, A. V., 2010. Accurate quasi 3D versus practical full 3D inversion of AEM data {‐} the Bookpurnong case study. Preview 2010 (149), 23–31. → pages 237, 238, 241
- Wait, J., Hill, D., apr 1977. Electromagnetic Shielding of Sources within a Metal-Cased Bore Hole. IEEE Transactions on Geoscience Electronics 15 (2), 108–112.
 URL <http://ieeexplore.ieee.org/lpdocs/epic03/wrapper.htm?arnumber=4071844> → pages 63
- Wait, J. R., 1983. Resistivity Response of a Homogeneous Earth with a Contained Vertical Conductor (1). → pages 40, 80
- Wait, J. R., Williams, J. T., aug 1985. EM AND IP RESPONSE OF A STEEL WELL CASING FOR A FOURELECTRODE SURFACE ARRAY. PART I: THEORY. Geophysical Prospecting 33 (5), 723–735.
 URL <http://doi.wiley.com/10.1111/j.1365-2478.1985.tb00775.x> → pages 40
- Ward, S. H., Hohmann, G. W., 1988. Electromagnetic Theory for Geophysical Applications. In: Electromagnetic Methods in Applied Geophysics, 1st Edition. Society of Exploration Geophysicists, Ch. 4, pp. 130–311.
 URL <http://library.seg.org/doi/abs/10.1190/1.9781560802631.ch4> → pages 44, 213
- Warpinski, N. R., oct 1996. Hydraulic Fracture Diagnostics. Journal of Petroleum Technology 48 (10), 907–910.
 URL <http://www.onepetro.org/doi/10.2118/36361-JPT> → pages 2, 3
- Weiss, C. J., Aldridge, D. F., Knox, H. A., Schramm, K. A., Bartel, L. C., aug 2015. The DC response of electrically conducting fractures excited by a grounded current source. SEG Technical Program Expanded Abstracts 2015 81 (3), 930–936.
 URL <http://library.seg.org/doi/10.1190/segam2015-5870407.1> → pages 10, 18, 242
- Weiss, C. J., Aldridge, D. F., Knox, H. A., Schramm, K. A., Bartel, L. C., 2016. The direct-current response of electrically conducting fractures excited by a grounded current source. Geophysics 81 (3), E201–E210.
 URL <http://library.seg.org/doi/10.1190/geo2015-0262.1> → pages 39, 41, 42, 57, 59, 81, 82, 126, 134
- Wiener, O., 1912. Die Theorie des Mischkörpers für das Feld der stationären Stromung. Abhandlungen der Sachsischen Gesellschaft der Akademischen Wissenschaften in Mathematik und Physik 32, 507—604. → pages 25
- Williams, J. T., Wait, J. R., aug 1985. EM and IP response of a steel well casing for a four-electrode surface array. Part II: Numerical results. Geophysical Prospecting 33 (5), 736–745.
 URL <http://doi.wiley.com/10.1111/j.1365-2478.1985.tb00776.x> → pages 40

- Wilson, G. A., Cox, L. H., Zhdanov, M. S., 2010. Practical 3D inversion of entire airborne electromagnetic surveys. Preview (146), 29–33. → pages 238
- Wilt, M., 2003. Oil Reservoir Characterization and CO₂ injection monitoring in the Permean Basing with crosswell electromagnetic imaging. Tech. rep. → pages 32
- Wilt, M., Cuevas, N., Heagy, L., 2015. Determining Proppant and Fluid Distribution, US 2015/0083404 A1.
URL <https://www.google.com/patents/US20150083404> → pages iii
- Wilt, M., Heagy, L., Chen, J., 2014. Hydrofracture mapping and monitoring with borehole electromagnetic (EM) methods. In: 76th European Association of Geoscientists and Engineers Conference and Exhibition 2014: Experience the Energy - Incorporating SPE EUROPEC 2014. → pages iii
- Wilt, M., Lee, K. H., Becker, A., Spies, B., Wang, S., jan 1996. Crosshole EM in steelcased boreholes. In: SEG Technical Program Expanded Abstracts 1996. Society of Exploration Geophysicists, pp. 230–233.
URL <http://library.seg.org/doi/abs/10.1190/1.1826605> → pages 41, 141
- Wilt, M., Schenkel, C., Daley, T., Peterson, J., Majer, E., Murer, A. S., Johnston, R. M., Klonsky, L., 1997. Mapping Steam and Water Flow in Petroleum Reservoirs. SPE Reservoir Engineering 12 (November), 284–287. → pages 30, 141
- Wilt, M., Um, E., Weiss, C., Vasco, D., Petrov, P., Newman, G., Wu, Y., 2018. Wellbore Integrity Assessment with Casing-Based Advanced Sensing (Figure 1), 1–7. → pages 41, 81
- Wilt, M., Zhang, P., Maeki, J., Netto, P., Queiroz, J. L. S., Santos, J. B., Oliveira, V., 2012. Monitoring a Water Flood of Moderate Saturation Changes with Crosswell Electromagnetics (EM): A Case Study from Dom Joao Brazil. SEG Technical Program Expanded Abstracts 2012, 1–5.
URL <http://library.seg.org/doi/abs/10.1190/segam2012-1226.1> → pages 30, 141
- Wilt, M. J., Alumbaugh, D. L., Morrison, H. F., Becker, A., Lee, K. H., DeszczaPan, M., may 1995. Crosswell electromagnetic tomography: System design considerations and field results. Geophysics 60 (3), 871–885.
URL <http://library.seg.org/doi/abs/10.1190/1.1443823> → pages 4, 30, 32
- Wright, C., Davis, E., Weijers, L., Golich, G., Ward, J., Demetrius, S., Minner, W., apr 1998. Downhole Tiltmeter Fracture Mapping: A New Tool for Directly Measuring Hydraulic Fracture Dimensions. In: SPE Annual Technical Conference and Exhibition. Society of Petroleum Engineers, pp. 585–597.
URL <http://www.onepetro.org/doi/10.2118/49193-MS> → pages 3

- Wu, X., Habashy, T. M., mar 1994. Influence of steel casings on electromagnetic signals. *Geophysics* 59 (3), 378–390.
 URL <http://library.seg.org/doi/pdf/10.1190/1.1443600> → pages 39, 208, 242
- Yang, D., 2017. Airborne electromagnetic data inversion for floodplain salinization investigation at Bookpurnong, South Australia.
 URL https://figshare.com/articles/Airborne_{-}electromagnetic_{-}data_{-}inversion_{-}for_{-}floodplain_{-}salinization_{-}investigation_{-}at_{-}Bookpurnong_{-}South_{-}Australia/5071573 → pages 238, 241
- Yang, D., Oldenburg, D. W., 2016. Survey decomposition : A scalable framework for 3D controlled-source electromagnetic inversion. *Geophysics* 81 (2), E69–E87. → pages 42, 51, 82, 96, 123, 126
- Yang, D., Oldenburg, D. W., Haber, E., 2014. 3-D inversion of airborne electromagnetic data parallelized and accelerated by local mesh and adaptive soundings. *Geophysical Journal International* 196 (3), 1492–1507. → pages 78, 207
- Yang, D., Oldenburg, D. W., Heagy, L. J., sep 2016. 3D DC resistivity modeling of steel casing for reservoir monitoring using equivalent resistor network. *SEG Technical Program Expanded Abstracts 2016*, 932–936.
 URL <http://library.seg.org/doi/10.1190/segam2016-13868475.1> → pages 242
- Yee, K., may 1966. Numerical solution of initial boundary value problems involving maxwell's equations in isotropic media. *IEEE Transactions on Antennas and Propagation* 14 (3), 302–307.
 URL [http://ieeexplore.ieee.org/lpdocs/epic03/wrapper.htm?arnumber=1138693\\$delimiter\\$026E30F\\$nhttp://ieeexplore.ieee.org/xpls/abs_{-}all.jsp?arnumber=1138693](http://ieeexplore.ieee.org/lpdocs/epic03/wrapper.htm?arnumber=1138693$delimiter$026E30F$nhttp://ieeexplore.ieee.org/xpls/abs_{-}all.jsp?arnumber=1138693) → pages 46, 207, 217
- Zawadzki, J., Bogacki, J., 2016. Smart magnetic markers use in hydraulic fracturing. *Chemosphere* 162, 23–30. → pages 9
- Zhang, P., Brick, Y., Sharma, M. M., 2018. Numerical study of an electrode-based resistivity tool for fracture diagnostics in steel-cased wellbores 83 (2). → pages 39, 41, 60
- Zhang, P., Shiriyev, J., Torres-Verdín, C., Sharma, M. M., Brick, Y., Massey, J. W., Yilmaz, A. E., 2016. Fracture diagnostics using a low-frequency electromagnetic induction method. *50th ARMA US Rock Mechanics/Geomechanics Symp.*, 1–10.
 URL <https://www.onepetro.org/conference-paper/ARMA-2016-862> → pages 23, 37

Appendix A

Concentric spheres in a uniform electrostatic field

Coating proppant particles with a conductive material is one potential strategy for generating an electrically conductive proppant pack. In this appendix, we work through a derivation of the electric potential outside of two concentric spheres in the presence of a uniform electrostatic field. Using this solution, we estimate an effective electrical conductivity of a composite particle.

A.1 Setup

The set-up is shown in Figure A.1

- primary electric field $\mathbf{E}_0 = E_0 \hat{x}$
- background conductivity σ_0 ,
- outer shell conductivity σ_1 and radius R_1
- inner sphere conductivity σ_2 and radius R_2

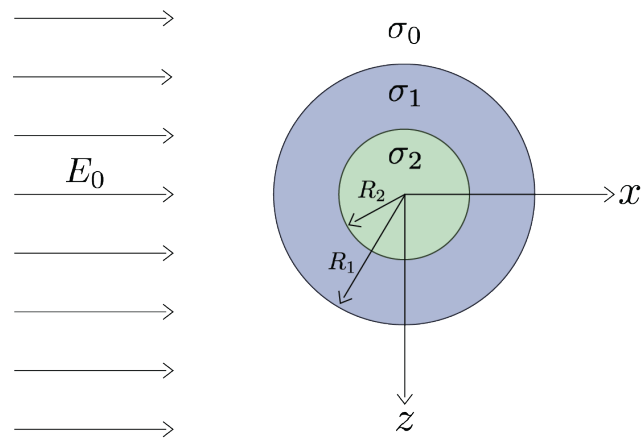


Figure A.1: Problem setup. Concentric spheres in a uniform electric field.

The basic equations are

$$\nabla \times \mathbf{E} = 0 \quad (\text{A.1})$$

$$\nabla \times \mathbf{H} = \mathbf{J} \quad (\text{A.2})$$

$$\mathbf{J} = \sigma \mathbf{E} \quad (\text{A.3})$$

By equation A.1, we can express \mathbf{E} as a gradient of a potential

$$\mathbf{E} = -\nabla V \quad (\text{A.4})$$

and combining equations A.1, A.2 and A.3, we see

$$\nabla \times \mathbf{H} = -\sigma \nabla V$$

Taking the divergence gives

$$0 = -\nabla \cdot \sigma \nabla V$$

and in a region with constant σ

$$\nabla^2 V = 0 \quad (\text{A.5})$$

At each of the conductivity interfaces, we have continuity of the normal component of the current density, and continuity of the electric potential. Continuity of the normal current density gives

$$\sigma_0 \frac{\partial V_0}{\partial r} = \sigma_1 \frac{\partial V_1}{\partial r} \quad \text{at } r = R_1 \quad (\text{A.6})$$

$$\sigma_1 \frac{\partial V_1}{\partial r} = \sigma_2 \frac{\partial V_2}{\partial r} \quad \text{at } r = R_2 \quad (\text{A.7})$$

Continuity of the potential gives

$$V_0 = V_1 \quad \text{at } r = R_1 \quad (\text{A.8})$$

$$V_1 = V_2 \quad \text{at } r = R_2 \quad (\text{A.9})$$

A.2 Solving for the Potential

The primary potential is given by

$$E_0 \hat{x} = -\frac{\partial V^P}{\partial x} \hat{x} \Rightarrow E_0 = -\frac{\partial V^P}{\partial x}$$

By integrating in x and setting the reference point to $V^P(r = 0) = 0$, we see

$$\begin{aligned} \int_0^x E_0 dx &= - \int_0^x \frac{\partial V^P}{\partial x} dx \\ E_0 x &= -V^P \end{aligned}$$

which gives a primary potential of

$$V^P = E_0 x = E_0 r \cos \theta \quad (\text{A.10})$$

In spherical coordinates, the Laplace equation, equation A.5, is given by

$$\left(\frac{\partial}{\partial r} \left(r^2 \frac{\partial}{\partial r} \right) + \frac{1}{\sin \theta} \frac{\partial}{\partial \theta} \left(\sin \theta \frac{\partial}{\partial \theta} \right) + \frac{1}{\sin^2 \theta} \frac{\partial^2}{\partial \phi^2} \right) V(r, \theta, \phi) = 0$$

by symmetry, $V = V(r, \theta)$, so the above equation simplifies to:

$$\left(\frac{\partial}{\partial r} \left(r^2 \frac{\partial}{\partial r} \right) + \frac{1}{\sin \theta} \frac{\partial}{\partial \theta} \left(\sin \theta \frac{\partial}{\partial \theta} \right) \right) V(r, \theta) = 0 \quad (\text{A.11})$$

which has general solution

$$V = \sum_{n=0}^{\infty} \left(A_n r^n + \frac{B_n}{r^{n+1}} \right) P_n(\cos \theta) \quad (\text{A.12})$$

A.2.1 Solving for the coefficients

Regarding notation, on the coefficients A, B the subscript denotes the order of the Legendre polynomial and the superscript denotes the region where that coefficient is applicable (i.e. 0: outside the sphere, 1: in the shell, 2: in the inner sphere). On the radius, R , the subscript denotes the region (1: outer shell, 2: inner sphere), while the superscript is an exponent.

Outside the sphere

Outside the spheres ($r > R_1$), we require that $V \Rightarrow V^P$ for $r \gg R_1$

$$V_0 = A_0^0 + A_1^0 r \cos \theta + \sum_{n=2}^{\infty} A_n^0 r^n P_n(\cos \theta) + \sum_{n=0}^{\infty} \frac{B_n^0}{r^{n+1}} P_n(\cos \theta)$$

for $r \gg R_1$

$$V_0 \Rightarrow A_0^0 + A_1^0 r \cos \theta + \sum_{n=2}^{\infty} A_n^0 r^n P_n(\cos \theta) + \sum_{n=0}^{\infty}$$

Since the Legendre polynomials, $P_n(\cos \theta)$, are orthogonal, then $A_0^0, A_n^0 = 0 \ \forall n$, and

$A_1^0 = -E_0$. So

$$V_0 = -E_0 r \cos \theta + \sum_{n=0}^{\infty} \frac{B_n^0}{r^{n+1}} P_n(\cos \theta) \quad (\text{A.13})$$

In the outer shell

In the outer shell ($R_2 < r < R_1$)

$$V_1 = \sum_{n=0}^{\infty} \left(A_n^1 r^n + \frac{B_n^1}{r^{n+1}} \right) P_n(\cos \theta) \quad (\text{A.14})$$

Using the interface condition in equation A.8, we have

$$\begin{aligned} -E_0 R_1 \cos \theta + \sum_{n=0}^{\infty} \left(\frac{B_n^0}{R_1^{n+1}} \right) P_n(\cos \theta) &= \sum_{n=0}^{\infty} \left(A_n^1 R_1^n + \frac{B_n^1}{R_1^{n+1}} \right) P_n(\cos \theta) \\ -E_0 R_1 \cos \theta + \frac{B_0^0}{R_1} + \frac{B_1^0}{R_1^2} \cos \theta + \sum_{n=2}^{\infty} \left(\frac{B_n^0}{R_1^{n+1}} \right) P_n(\cos \theta) &= A_0^1 + A_1^1 R_1 \cos \theta + \frac{B_0^1}{R_1} + \frac{B_1^1}{R_1^2} \cos \theta + \sum_{n=2}^{\infty} \left(A_n^1 R_1^n + \frac{B_n^1}{R_1^{n+1}} \right) P_n(\cos \theta) \end{aligned}$$

which must hold for all θ . Thus, we can break this up in to a series of smaller equations.

For the $n = 0$ polynomials, we have

$$\begin{aligned} \frac{B_0^0}{R_1} &= A_0^1 + \frac{B_0^1}{R_1} \\ \Rightarrow B_0^0 &= R_1 A_0^1 + B_0^1 \end{aligned} \tag{A.15}$$

For the $n = 1$ polynomials, we have

$$\begin{aligned} -E_0 R_1 + \frac{B_1^0}{R_1^2} &= A_1^1 R_1 + \frac{B_1^1}{R_1^2} \\ \Rightarrow -E_0 R_1^3 + B_1^0 &= A_1^1 R_1^3 + B_1^1 \end{aligned} \tag{A.16}$$

and for $n \geq 2$ (using orthogonality of $P_n(\cos \theta)$)

$$\begin{aligned} \frac{B_n^0}{R_1^{n+1}} &= A_n^1 R_1^n + \frac{B_n^1}{R_1^{n+1}} \\ \Rightarrow B_n^0 &= A_n^1 R_1^{2n+1} + B_n^1 \end{aligned} \tag{A.17}$$

Next, we look to the interface conditions on the derivative of the potential, as described in equation A.6. We first find the derivatives of V_0, V_1 with respect to r :

$$\frac{\partial V_0}{\partial r} = -E_0 \cos \theta + \sum_{n=0}^{\infty} -(n+1) \frac{B_n^0}{r^{n+2}} P_n(\cos \theta) \tag{A.18}$$

$$\frac{\partial V_1}{\partial r} = \sum_{n=1}^{\infty} n A_n^1 r^{n-1} P_n(\cos \theta) + \sum_{n=0}^{\infty} -(n+1) \frac{B_n^1}{r^{n+2}} P_n(\cos \theta) \tag{A.19}$$

Imposing the interface in equation A.6, we have,

$$\begin{aligned} -\sigma_0 E_0 \cos \theta + \sigma_0 \sum_{n=0}^{\infty} -(n+1) \frac{B_n^0}{R_1^{n+2}} P_n(\cos \theta) \\ = \sigma_1 \sum_{n=1}^{\infty} n A_n^1 R_1^{n-1} P_n(\cos \theta) + \sigma_1 \sum_{n=0}^{\infty} -(n+1) \frac{B_n^1}{R_1^{n+2}} P_n(\cos \theta) \end{aligned}$$

Breaking out coefficients up to $n = 2$ gives

$$\begin{aligned} -\sigma_0 E_0 \cos \theta - \sigma_0 \frac{B_0^0}{R_1^2} - 2\sigma_0 \frac{B_1^0}{R_1^3} \cos \theta - \sigma_0 \sum_{n=2}^{\infty} (n+1) \frac{B_n^0}{R_1^{n+2}} P_n(\cos \theta) \\ = \sigma_1 A_1^1 \cos \theta - \sigma_1 \frac{B_0^1}{R_1^2} - 2\sigma_1 \frac{B_1^1}{R_1^3} \cos \theta + \sigma_1 \sum_{n=2}^{\infty} \left(n A_n^1 R_1^{n-1} - (n+1) \frac{B_n^1}{R_1^{n+2}} \right) P_n(\cos \theta) \end{aligned}$$

Again, this must hold for all θ , so we can break this up into a series of smaller equations.

For the $n = 0$ polynomials, we have

$$\begin{aligned} -\sigma_0 \frac{B_0^0}{R_1^2} &= -\sigma_1 \frac{B_0^1}{R_1^2} \\ \Rightarrow \quad \sigma_0 B_0^0 &= \sigma_1 B_0^1 \end{aligned} \tag{A.20}$$

For the $n = 1$ polynomials, we have

$$\begin{aligned} -\sigma_0 E_0 - 2\sigma_0 \frac{B_1^0}{R_1^3} &= \sigma_1 A_1^1 - 2\sigma_1 \frac{B_1^1}{R_1^3} \\ \Rightarrow \quad -\sigma_0 E_0 R_1^3 - 2\sigma_0 B_1^0 &= \sigma_1 A_1^1 R_1^3 - 2\sigma_1 B_1^1 \end{aligned} \tag{A.21}$$

and for the polynomials where $n \geq 2$, we have

$$\begin{aligned} -\sigma_0 (n+1) \frac{B_n^0}{R_1^{n+2}} &= \sigma_1 n A_n^1 R_1^{n-1} - \sigma_1 (n+1) \frac{B_n^1}{R_1^{n+2}} \\ \Rightarrow \quad -\sigma_0 (n+1) B_n^0 &= \sigma_1 n A_n^1 R_1^{2n+1} - \sigma_1 (n+1) B_n^1 \end{aligned} \tag{A.22}$$

Inner sphere

In the inner-most sphere ($r < R_2$), we have that

$$V_2 = \sum_{n=0}^{\infty} \left(A_n^2 r^n + \frac{B_n^2}{r^{n+1}} \right) P_n(\cos \theta)$$

as $r \Rightarrow 0$, $V_2 \Rightarrow 0$ by choice of our ref. point. This implies $B_n^2 = 0 \forall n$, and $A_0^2 = 0$, so we have

$$V_2 = \sum_{n=1}^{\infty} A_n^2 r^n P_n(\cos \theta) \quad (\text{A.23})$$

Now we use the interface conditions at $r = R_2$, given by equations A.7 and A.9. Starting with the continuity of the potential V (equation A.9), we see

$$\sum_{n=0}^{\infty} \left(A_n^1 r^n + \frac{B_n^1}{r^{n+1}} \right) P_n(\cos \theta) = \sum_{n=1}^{\infty} A_n^2 r^n P_n(\cos \theta)$$

which must hold for all θ , giving

$$\begin{aligned} A_0^1 + \frac{B_0^1}{R_2} &= 0 \\ \Rightarrow A_0^1 R_2 + B_0^1 &= 0 \end{aligned} \quad (\text{A.24})$$

and for $n \geq 1$,

$$\begin{aligned} A_n^1 R_2^n + \frac{B_n^1}{R_2^{n+1}} &= A_n^2 R_2^n \\ \Rightarrow A_n^1 R_2^{2n+1} + B_n^1 &= A_n^2 R_2^{2n+1} \end{aligned} \quad (\text{A.25})$$

For the continuity of the current density (equation A.7), we have

$$\sigma_1 \sum_{n=1}^{\infty} nA_n^1 R_2^{n-1} P_n(\cos \theta) - \sigma_1 \sum_{n=0}^{\infty} (n+1) \frac{B_n^1}{R_2^{n+2}} P_n(\cos \theta) = \sigma_2 \sum_{n=1}^{\infty} nA_n^2 R_2^{n-1} P_n(\cos \theta)$$

which must hold for all θ , giving

$$-\sigma_1 \frac{B_0^1}{R_2} = 0$$

and since both σ_1 and R_2 are non-zero,

$$B_0^1 = 0 \quad (\text{A.26})$$

and for $n \geq 1$

$$\begin{aligned} \sigma_1 n A_n^1 R_2^{n-1} - \sigma_1 (n+1) \frac{B_n^1}{R_2^{n+2}} &= \sigma_2 n A_n^2 R_2^{n-1} \\ \Rightarrow \quad \sigma_1 n A_n^1 R_2^{2n+1} - \sigma_1 (n+1) B_n^1 &= \sigma_2 n A_n^2 R_2^{2n+1} \end{aligned} \quad (\text{A.27})$$

Now that we have equations A.15, A.16, A.17, A.20, A.21, A.22, A.24, A.25, A.26 and A.27, we have 10 equations and 10 unknowns. Therefore, we can proceed to solve for each of the coefficients.

By combining A.24 and A.26, we see

$$A_0^1 = 0. \quad (\text{A.28})$$

Combining this with equation A.15, we see

$$B_0^0 = 0 \quad (\text{A.29})$$

From equation A.16, we know $B_1^1 = -E_0 R_1^3 + B_1^0 - A_1^1 R_1^3$, which we put into equation

A.21 to give

$$-\sigma_0 E_0 R_1^3 - 2\sigma_0 B_1^0 = \sigma_1 A_1^1 R_1^3 - 2\sigma_1 (-E_0 R_1^3 + B_1^0 - A_1^1 R_1^3)$$

giving us an equation in A_1^1 and B_1^0 , which we can simplify to

$$-E_0 R_1^3 (\sigma_0 + 2\sigma_1) = 3\sigma_1 A_1^1 R_1^3 + 2(\sigma_0 - \sigma_1) B_1^0 \quad (\text{A.30})$$

From equation A.25, we know $A_n^2 R_2^{2n+1} = A_n^1 R_2^{2n+1} + B_n^1$. Putting this in to eqn A.27, we see

$$\sigma_1 n A_n^1 R_2^{2n+1} - \sigma_1 (n+1) B_n^1 = \sigma_2 n (A_n^1 R_2^{2n+1} + B_n^1) \quad n \geq 1$$

which simplifies to

$$n(\sigma_1 - \sigma_2) A_n^1 R_2^{2n+1} = ((n+1)\sigma_1 + n\sigma_2) B_n^1 R_2^{2n+1} \quad n \geq 1 \quad (\text{A.31})$$

In the case where $n = 1$, we have that

$$\begin{aligned} (\sigma_1 - \sigma_2) A_1^1 R_2^3 &= (2\sigma_1 + \sigma_2) B_1^1 \\ \Rightarrow A_1^1 &= \left(\frac{2\sigma_1 + \sigma_2}{\sigma_1 - \sigma_2} \right) \frac{B_1^1}{R_2^3} \end{aligned} \quad (\text{A.32})$$

which we can put into equation A.30 giving

$$-(\sigma_0 + 2\sigma_1) E_0 R_1^3 = 3\sigma_1 \left(\frac{2\sigma_1 + \sigma_2}{\sigma_1 - \sigma_2} \right) \left(\frac{R_1}{R_2} \right)^3 B_1^1 + 2(\sigma_0 - \sigma_1) B_1^0 \quad (\text{A.33})$$

To get another equation in B_1^0 and B_1^1 , we use equations A.16 and A.32 to get

$$\begin{aligned} B_1^1 &= -E_0 R_1^3 + B_1^0 - \left(\frac{2\sigma_1 + \sigma_2}{\sigma_1 - \sigma_2} \right) \left(\frac{R_1}{R_2} \right)^3 B_1^1 \\ \Rightarrow \quad &\left(1 + \left(\frac{2\sigma_1 + \sigma_2}{\sigma_1 - \sigma_2} \right) \left(\frac{R_1}{R_2} \right)^3 \right) B_1^1 = -E_0 R_1^3 + B_1^0 \end{aligned}$$

to ease notation, define

$$\alpha = \left(\frac{R_1}{R_2} \right)^3 \quad (\text{A.34})$$

which lets us simplify the above to

$$\begin{aligned} B_1^1 &= (-E_0 R_1^3 + B_1^0) \left(1 + \left(\frac{2\sigma_1 + \sigma_2}{\sigma_1 - \sigma_2} \right) \alpha \right)^{-1} \\ &= (-E_0 R_1^3 + B_1^0) \left(\frac{(\sigma_1 - \sigma_2) + (2\sigma_1 + \sigma_2) \alpha}{\sigma_1 - \sigma_2} \right)^{-1} \\ &= (-E_0 R_1^3 + B_1^0) \left(\frac{\sigma_1 - \sigma_2}{(\sigma_1 - \sigma_2) + (2\sigma_1 + \sigma_2) \alpha} \right) \end{aligned} \quad (\text{A.35})$$

With equations A.33 and A.35, we finally have arrived at a set of two equations with two unknowns (B_1^1 and (B_1^0) . Putting equation A.35 into equation A.33 and using the

definition of α as given in equation A.34, we see

$$\begin{aligned}
& -(\sigma_0 + 2\sigma_1)E_0R_1^3 \\
&= 3\sigma_1\alpha \left(\frac{2\sigma_1 + \sigma_2}{\sigma_1 - \sigma_2} \right) \left(\frac{\sigma_1 - \sigma_2}{(\sigma_1 - \sigma_2) + (2\sigma_1 + \sigma_2)\alpha} \right) (-E_0R_1^3 + B_1^0) + 2(\sigma_0 - \sigma_1)B_1^0 \\
\Rightarrow & -(\sigma_0 + 2\sigma_1)E_0R_1^3 \\
&= 3\sigma_1\alpha \left(\frac{2\sigma_1 + \sigma_2}{(\sigma_1 - \sigma_2) + (2\sigma_1 + \sigma_2)\alpha} \right) (-E_0R_1^3 + B_1^0) + 2(\sigma_0 - \sigma_1)B_1^0 \\
\Rightarrow & -(\sigma_0 + 2\sigma_1)E_0R_1^3 \\
&= \left(\frac{3\sigma_1(2\sigma_1 + \sigma_2)\alpha}{(\sigma_1 - \sigma_2) + (2\sigma_1 + \sigma_2)\alpha} \right) (-E_0R_1^3 + B_1^0) + 2(\sigma_0 - \sigma_1)B_1^0 \\
\Rightarrow & - \left((\sigma_0 + 2\sigma_1) - \frac{3\sigma_1(2\sigma_1 + \sigma_2)\alpha}{(\sigma_1 - \sigma_2) + (2\sigma_1 + \sigma_2)\alpha} \right) E_0R_1^3 \\
&= \left(\frac{3\sigma_1(2\sigma_1 + \sigma_2)\alpha}{(\sigma_1 - \sigma_2) + (2\sigma_1 + \sigma_2)\alpha} + 2(\sigma_0 - \sigma_1) \right) B_1^0 \\
\Rightarrow & - \left(\frac{(\sigma_0 + 2\sigma_1)(\sigma_1 - \sigma_2) + (\sigma_0 + 2\sigma_1)(2\sigma_1 + \sigma_2)\alpha - 3\sigma_1(2\sigma_1 + \sigma_2)\alpha}{(\sigma_1 - \sigma_2) + (2\sigma_1 + \sigma_2)\alpha} \right) E_0R_1^3 \\
&= \left(\frac{3\sigma_1(2\sigma_1 + \sigma_2)\alpha + 2(\sigma_0 - \sigma_1)(\sigma_1 - \sigma_2) + 2(\sigma_0 - \sigma_1)(2\sigma_1 + \sigma_2)\alpha}{(\sigma_1 - \sigma_2) + (2\sigma_1 + \sigma_2)\alpha} \right) B_1^0 \\
\Rightarrow & -((\sigma_0 + 2\sigma_1)(\sigma_1 - \sigma_2) + (\sigma_0 - \sigma_1)(2\sigma_1 + \sigma_2)\alpha) E_0R_1^3 \\
&= (2(\sigma_0 - \sigma_1)(\sigma_1 - \sigma_2) + (2\sigma_0 + \sigma_1)(2\sigma_1 + \sigma_2)\alpha) B_1^0
\end{aligned}$$

So the coefficient B_1^0 is given by

$$B_1^0 = -E_0R_1^3 \left(\frac{(\sigma_0 + 2\sigma_1)(\sigma_1 - \sigma_2) + (\sigma_0 - \sigma_1)(2\sigma_1 + \sigma_2)\alpha}{2(\sigma_0 - \sigma_1)(\sigma_1 - \sigma_2) + (2\sigma_0 + \sigma_1)(2\sigma_1 + \sigma_2)\alpha} \right) \quad (\text{A.36})$$

Putting this into equation A.35, we can solve for B_1^1

$$\begin{aligned} B_1^1 &= -E_0 R_1^3 \left(1 + \frac{(\sigma_0 + 2\sigma_1)(\sigma_1 - \sigma_2) + (\sigma_0 - \sigma_1)(2\sigma_1 + \sigma_2)\alpha}{2(\sigma_0 - \sigma_1)(\sigma_1 - \sigma_2) + (2\sigma_0 + \sigma_1)(2\sigma_1 + \sigma_2)\alpha} \right) \\ &\quad \left(\frac{\sigma_1 - \sigma_2}{(\sigma_1 - \sigma_2) + (2\sigma_1 + \sigma_2)\alpha} \right) \\ \Rightarrow B_1^1 &= -E_0 R_1^3 \left(\frac{3\sigma_0(\sigma_1 - \sigma_2) + 3\sigma_0(2\sigma_1 + \sigma_2)\alpha}{2(\sigma_0 - \sigma_1)(\sigma_1 - \sigma_2) + (2\sigma_0 + \sigma_1)(2\sigma_1 + \sigma_2)\alpha} \right) \\ &\quad \left(\frac{\sigma_1 - \sigma_2}{(\sigma_1 - \sigma_2) + (2\sigma_1 + \sigma_2)\alpha} \right) \end{aligned}$$

$$B_1^1 = -E_0 R_1^3 \left(\frac{3\sigma_0(\sigma_1 - \sigma_2)}{2(\sigma_0 - \sigma_1)(\sigma_1 - \sigma_2) + (2\sigma_0 + \sigma_1)(2\sigma_1 + \sigma_2)\alpha} \right) \quad (\text{A.37})$$

Next, we solve for A_1^1 using equation A.32.

$$A_1^1 = \left(\frac{2\sigma_1 + \sigma_2}{\sigma_1 - \sigma_2} \right) \frac{1}{R_2^3} \left(-E_0 R_1^3 \left(\frac{3\sigma_0(\sigma_1 - \sigma_2)}{2(\sigma_0 - \sigma_1)(\sigma_1 - \sigma_2) + (2\sigma_0 + \sigma_1)(2\sigma_1 + \sigma_2)\alpha} \right) \right)$$

which simplifies to

$$A_1^1 = -E_0 \alpha \left(\frac{3\sigma_0(2\sigma_1 + \sigma_2)}{2(\sigma_0 - \sigma_1)(\sigma_1 - \sigma_2) + (2\sigma_0 + \sigma_1)(2\sigma_1 + \sigma_2)\alpha} \right) \quad (\text{A.38})$$

Now, using equation A.27 for $n = 1$, we can solve for A_1^2

$$\begin{aligned} \sigma_2 A_1^2 R_2^3 &= \sigma_1 A_1^1 R_2^3 - 2\sigma_1 B_1^1 \\ A_1^2 &= \frac{\sigma_1}{\sigma_2} \left(A_1^1 - \frac{2}{R_2^3} B_1^1 \right) \\ &= -E_0 \alpha \frac{\sigma_1}{\sigma_2} \left(\frac{3\sigma_0(2\sigma_1 + \sigma_2) - 2(3\sigma_0(\sigma_1 - \sigma_2))}{2(\sigma_0 - \sigma_1)(\sigma_1 - \sigma_2) + (2\sigma_0 + \sigma_1)(2\sigma_1 + \sigma_2)\alpha} \right) \\ &= -E_0 \alpha \frac{\sigma_1}{\sigma_2} \left(\frac{3\sigma_0(3\sigma_2)}{2(\sigma_0 - \sigma_1)(\sigma_1 - \sigma_2) + (2\sigma_0 + \sigma_1)(2\sigma_1 + \sigma_2)\alpha} \right) \end{aligned}$$

$$A_1^2 = -E_0 \alpha \left(\frac{3\sigma_0(3\sigma_1)}{2(\sigma_0 - \sigma_1)(\sigma_1 - \sigma_2) + (2\sigma_0 + \sigma_1)(2\sigma_1 + \sigma_2)\alpha} \right) \quad (\text{A.39})$$

At this point, the remaining coefficients to be found are B_n^0 , A_n^1 and B_n^1 and A_n^2 for $n \geq 2$, and four remaining equations A.17, A.22, A.25 and A.27 for each n . These can be written more concisely as a matrix equation, namely

$$\begin{pmatrix} 0 \\ 0 \\ 0 \\ 0 \end{pmatrix} = \begin{pmatrix} 1 & 0 & -1 & 1 \\ n\sigma_1 & 0 & (n+1)\sigma_0 & -(n+1)\sigma_1 \\ 1 & -1 & 0 & 1 \\ n\sigma_1 & -n\sigma_2 & 0 & -(n+1)\sigma_1 \end{pmatrix} \begin{pmatrix} A_n^1 R_1^{2n+1} \\ B_n^0 \\ A_n^2 R_2^{2n+1} \\ B_n^1 \end{pmatrix} \quad (\text{A.40})$$

The solution to equation A.40 requires the matrix inverse. If the matrix is invertible, than the unique solution is $(0, 0, 0, 0)$. To test if this is invertible, we perform Gaussian elimination to try and reduce it to the identity:

$$\begin{pmatrix} 1 & 0 & -1 & 1 \\ 1 & -1 & 0 & 1 \\ n\sigma_1 & -n\sigma_2 & 0 & -(n+1)\sigma_1 \\ n\sigma_1 & 0 & (n+1)\sigma_0 & -(n+1)\sigma_1 \end{pmatrix} \sim \begin{pmatrix} 1 & 0 & -1 & 1 \\ 0 & -1 & 0 & 1 \\ 0 & 0 & (n+1)\sigma_0 + n\sigma_1 & -(2n+1)\sigma_1 \\ 0 & -n\sigma_2 & n\sigma_1 & -(2n+1)\sigma_1 \end{pmatrix}$$

$$\begin{aligned}
&\sim \begin{pmatrix} 1 & 0 & -1 & 1 \\ 0 & 1 & 0 & -1 \\ 0 & 0 & (n+1)\sigma_0 + n\sigma_1 & -(2n+1)\sigma_1 \\ 0 & 0 & n\sigma_1 & -(2n+1)\sigma_1 - n\sigma_2 \end{pmatrix} \\
&\sim \begin{pmatrix} 1 & 0 & -1 & 1 \\ 0 & 1 & 0 & -1 \\ 0 & 0 & 1 & \frac{-(2n+1)\sigma_1}{(n+1)\sigma_0 + n\sigma_1} \\ 0 & 0 & 0 & -(2n+1)\sigma_1 - n\sigma_2 - n\sigma_1 \frac{-(2n+1)\sigma_1}{(n+1)\sigma_0 + n\sigma_1} \end{pmatrix} \\
&\sim \begin{pmatrix} 1 & 0 & -1 & 1 \\ 0 & 1 & 0 & -1 \\ 0 & 0 & 1 & \frac{-(2n+1)\sigma_1}{(n+1)\sigma_0 + n\sigma_1} \\ 0 & 0 & 0 & 1 \end{pmatrix} \\
&\sim \begin{pmatrix} 1 & 0 & 0 & 0 \\ 0 & 1 & 0 & 0 \\ 0 & 0 & 1 & 0 \\ 0 & 0 & 0 & 1 \end{pmatrix}
\end{aligned}$$

Therefore,

$$A_n^1 = 0 \quad \forall n \geq 2 \quad (\text{A.41})$$

$$B_n^0 = 0 \quad \forall n \geq 2 \quad (\text{A.42})$$

$$A_n^2 = 0 \quad \forall n \geq 2 \quad (\text{A.43})$$

$$B_n^1 = 0 \quad \forall n \geq 2 \quad (\text{A.44})$$

Now we have everything we need to express the potentials in each region. Outside the sphere ($r > R_2$)

$$V_0 = -E_0 r \cos \theta \left(1 + \frac{R_1^3}{r^3} \left(\frac{(\sigma_0 + 2\sigma_1)(\sigma_1 - \sigma_2) + (\sigma_0 - \sigma_1)(2\sigma_1 + \sigma_2)\alpha}{2(\sigma_0 - \sigma_1)(\sigma_1 - \sigma_2) + (2\sigma_0 + \sigma_1)(2\sigma_1 + \sigma_2)\alpha} \right) \right) \quad (\text{A.45})$$

In the outer shell ($R_1 < r < R_2$)

$$V_1 = -E_0 r \cos \theta \frac{3\sigma_0}{2(\sigma_0 - \sigma_1)(\sigma_1 - \sigma_2) + (2\sigma_0 + \sigma_1)(2\sigma_1 + \sigma_2)\alpha} \left((2\sigma_1 + \sigma_2)\alpha + (\sigma_1 - \sigma_2) \frac{R_1^3}{r^3} \right) \quad (\text{A.46})$$

In the inner sphere ($r < R_2$)

$$V_2 = -E_0 r \cos \theta \left(\frac{(3\sigma_0)(3\sigma_1)\alpha}{2(\sigma_0 - \sigma_1)(\sigma_1 - \sigma_2) + (2\sigma_0 + \sigma_1)(2\sigma_1 + \sigma_2)\alpha} \right) \quad (\text{A.47})$$

A.2.2 Sanity Checks

Before moving any further, there are a few end-member cases we can use to validate our solution.

For a number of checks, it is useful to compare to the solution of a single sphere. From Ward and Hohmann (pg. 282-285), we have that the potential exterior to the sphere ($r > R$) is

$$V_e = -E_0 r \cos \theta \left(1 + \frac{R^3}{r^3} \left(\frac{\sigma_e - \sigma_i}{2\sigma_e + \sigma_i} \right) \right) \quad (\text{A.48})$$

where σ_e is the conductivity of the background, σ_i is the conductivity of the sphere, and R is the radius of the sphere. The potential inside the sphere ($r < R$) is given by

$$V_i = -E_0 r \cos \theta \left(\frac{3\sigma_e}{2\sigma_e + \sigma_i} \right) \quad (\text{A.49})$$

Check 1: Equal conductivity of the inner sphere and outer shell

First, if $\sigma_2 = \sigma_1$, then $R = R_1$, and we expect $V_0 = V_e$ and $V_1 = V_2 = V_i$. Starting with V_0 , we see

$$\begin{aligned} V_0 &= -E_0 r \cos \theta \left(1 + \frac{R_1^3}{r^3} \left(\frac{(\sigma_0 + 2\sigma_1)(\sigma_1 - \sigma_0) + (\sigma_0 - \sigma_1)(2\sigma_1 + \sigma_0)\alpha}{2(\sigma_0 - \sigma_1)(\sigma_1 - \sigma_0) + (2\sigma_0 + \sigma_1)(2\sigma_1 + \sigma_0)\alpha} \right) \right) \\ &= -E_0 r \cos \theta \left(1 + \frac{R_1^3}{r^3} \left(\frac{(\sigma_0 - \sigma_1)(3\sigma_1)\alpha}{(2\sigma_0 + \sigma_1)(3\sigma_1)\alpha} \right) \right) \\ &= -E_0 r \cos \theta \left(1 + \frac{R_1^3}{r^3} \left(\frac{\sigma_0 - \sigma_1}{2\sigma_0 + \sigma_1} \right) \right) \\ &= V_e \checkmark \end{aligned}$$

For V_1 , we have

$$\begin{aligned} V_1 &= -E_0 r \cos \theta \frac{3\sigma_0}{2(\sigma_0 - \sigma_1)(\sigma_1 - \sigma_0) + (2\sigma_0 + \sigma_1)(2\sigma_1 + \sigma_0)\alpha} \\ &\quad \left((2\sigma_1 + \sigma_0)\alpha + (\sigma_1 - \sigma_0)\frac{R_1^3}{r^3} \right) \\ &= -E_0 r \cos \theta \frac{3\sigma_0}{(2\sigma_0 + \sigma_1)(3\sigma_1)\alpha} ((3\sigma_1)\alpha) \\ &= -E_0 r \cos \theta \frac{3\sigma_0}{(2\sigma_0 + \sigma_1)} \\ &= V_i \checkmark \end{aligned}$$

For V_2 , we have

$$\begin{aligned}
V_2 &= -E_0 r \cos \theta \left(\frac{(3\sigma_0)(3\sigma_1)\alpha}{2(\sigma_0 - \sigma_1)(\sigma_1 - \sigma_1) + (2\sigma_0 + \sigma_1)(2\sigma_1 + \sigma_1)\alpha} \right) \\
&= -E_0 r \cos \theta \left(\frac{(3\sigma_0)(3\sigma_1)\alpha}{(2\sigma_0 + \sigma_1)(3\sigma_1)\alpha} \right) \\
&= -E_0 r \cos \theta \left(\frac{3\sigma_0}{2\sigma_0 + \sigma_1} \right) \\
&= V_i \checkmark
\end{aligned}$$

Check 2: Conductivity of the outer shell equals that of the background

If $\sigma_1 = \sigma_0$, then $R = R_2$, and we expect $V_0 = V_1 = V_e$ and $V_2 = V_i$. For V_0 , we have

$$\begin{aligned}
V_0 &= -E_0 r \cos \theta \left(1 + \frac{R_1^3}{r^3} \left(\frac{(\sigma_0 + 2\sigma_0)(\sigma_0 - \sigma_2) + (\sigma_0 - \sigma_0)(2\sigma_0 + \sigma_2)\alpha}{2(\sigma_0 - \sigma_0)(\sigma_0 - \sigma_2) + (2\sigma_0 + \sigma_0)(2\sigma_0 + \sigma_2)\alpha} \right) \right) \\
&= -E_0 r \cos \theta \left(1 + \frac{R_1^3}{r^3} \left(\frac{(3\sigma_0)(\sigma_0 - \sigma_2)}{(3\sigma_0)(2\sigma_0 + \sigma_2)\alpha} \right) \right) \\
&= -E_0 r \cos \theta \left(1 + \frac{R_1^3}{r^3} \left(\frac{(\sigma_0 - \sigma_2)}{(2\sigma_0 + \sigma_2)\alpha} \right) \right) \\
&= -E_0 r \cos \theta \left(1 + \frac{R_1^3}{r^3} \left(\frac{\sigma_0 - \sigma_2}{2\sigma_0 + \sigma_2} \right) \frac{R_2^3}{R_1^3} \right) \\
&= -E_0 r \cos \theta \left(1 + \frac{R_2^3}{r^3} \left(\frac{\sigma_0 - \sigma_2}{2\sigma_0 + \sigma_2} \right) \right) \\
&= V_e \checkmark
\end{aligned}$$

For V_1 , we have

$$\begin{aligned}
V_1 &= -E_0 r \cos \theta \frac{3\sigma_0}{2(\sigma_0 - \sigma_0)(\sigma_0 - \sigma_2) + (2\sigma_0 + \sigma_0)(2\sigma_0 + \sigma_2)\alpha} \\
&\quad \left((2\sigma_0 + \sigma_2)\alpha + (\sigma_0 - \sigma_2)\frac{R_1^3}{r^3} \right) \\
&= -E_0 r \cos \theta \frac{3\sigma_0}{(3\sigma_0)(2\sigma_0 + \sigma_2)\alpha} \left((2\sigma_0 + \sigma_2)\alpha + (\sigma_0 - \sigma_2)\frac{R_1^3}{r^3} \right) \\
&= -E_0 r \cos \theta \frac{1}{(2\sigma_0 + \sigma_2)\alpha} \left((2\sigma_0 + \sigma_2)\alpha + (\sigma_0 - \sigma_2)\frac{R_1^3}{r^3} \right) \\
&= -E_0 r \cos \theta \left(1 + \left(\frac{\sigma_0 - \sigma_2}{(2\sigma_0 + \sigma_2)\alpha} \right) \frac{R_1^3}{r^3} \right) \\
&= -E_0 r \cos \theta \left(1 + \left(\frac{\sigma_0 - \sigma_2}{2\sigma_0 + \sigma_2} \right) \frac{R_2^3 R_1^3}{R_1^3 r^3} \right) \\
&= -E_0 r \cos \theta \left(1 + \left(\frac{\sigma_0 - \sigma_2}{2\sigma_0 + \sigma_2} \right) \frac{R_2^3}{r^3} \right) \\
&= V_e \checkmark
\end{aligned}$$

and for V_2 ,

$$\begin{aligned}
V_2 &= -E_0 r \cos \theta \left(\frac{(3\sigma_0)(3\sigma_0)\alpha}{2(\sigma_0 - \sigma_0)(\sigma_0 - \sigma_2) + (2\sigma_0 + \sigma_0)(2\sigma_0 + \sigma_2)\alpha} \right) \\
&= -E_0 r \cos \theta \left(\frac{(3\sigma_0)(3\sigma_0)\alpha}{(3\sigma_0)(2\sigma_0 + \sigma_2)\alpha} \right) \\
&= -E_0 r \cos \theta \left(\frac{3\sigma_0}{2\sigma_0 + \sigma_2} \right) \\
&= V_i \checkmark
\end{aligned}$$

Check 3: Equal radius of the inner sphere and outer shell

If $\alpha = 1$ (i.e. $R_1 = R_2$), we expect $V_0 = V_e$, and $V_2 = V_i$. For V_0 , we have

$$\begin{aligned}
 V_0 &= -E_0 r \cos \theta \left(1 + \frac{R_1^3}{r^3} \left(\frac{(\sigma_0 + 2\sigma_1)(\sigma_1 - \sigma_2) + (\sigma_0 - \sigma_1)(2\sigma_1 + \sigma_2)}{2(\sigma_0 - \sigma_1)(\sigma_1 - \sigma_2) + (2\sigma_0 + \sigma_1)(2\sigma_1 + \sigma_2)} \right) \right) \\
 &= -E_0 r \cos \theta \left(1 + \frac{R_1^3}{r^3} \left(\frac{\sigma_0(\sigma_1 - \sigma_2 + 2\sigma_1 + \sigma_2) + \sigma_1(2\sigma_1 - 2\sigma_2 - 2\sigma_1 - \sigma_2)}{2\sigma_0(\sigma_1 - \sigma_2 + 2\sigma_1 + \sigma_2) + \sigma_1(-2\sigma_1 + 2\sigma_2 + 2\sigma_1 + \sigma_2)} \right) \right) \\
 &= -E_0 r \cos \theta \left(1 + \frac{R_1^3}{r^3} \left(\frac{\sigma_0(3\sigma_1) + \sigma_1(-3\sigma_2)}{2\sigma_0(3\sigma_1) + \sigma_1(3\sigma_2)} \right) \right) \\
 &= -E_0 r \cos \theta \left(1 + \frac{R_1^3}{r^3} \left(\frac{\sigma_0 - \sigma_2}{2\sigma_0 + \sigma_2} \right) \right) \\
 &= V_e \checkmark
 \end{aligned}$$

For V_2 , we have

$$\begin{aligned}
 V_2 &= -E_0 r \cos \theta \left(\frac{(3\sigma_0)(3\sigma_1)}{2(\sigma_0 - \sigma_1)(\sigma_1 - \sigma_2) + (2\sigma_0 + \sigma_1)(2\sigma_1 + \sigma_2)} \right) \\
 &= -E_0 r \cos \theta \left(\frac{(3\sigma_0)(3\sigma_1)}{2\sigma_0(\sigma_1 - \sigma_2 + 2\sigma_1 + \sigma_2) + \sigma_1(-2\sigma_1 + 2\sigma_2 + 2\sigma_1 + \sigma_2)} \right) \\
 &= -E_0 r \cos \theta \left(\frac{(3\sigma_0)(3\sigma_1)}{2\sigma_0(3\sigma_1) + \sigma_1(3\sigma_2)} \right) \\
 &= -E_0 r \cos \theta \left(\frac{3\sigma_0}{2\sigma_0 + \sigma_2} \right) \\
 &= V_i \checkmark
 \end{aligned}$$

Check 4: $\lim R_2 \rightarrow 0$

If we take $R_2 \rightarrow 0$ (i.e. $\alpha^{-1} \rightarrow 0$), we expect $V_0 \rightarrow V_e$ and $V_1 \rightarrow V_i$. For V_0 , we have

$$\begin{aligned}\lim_{\alpha^{-1} \rightarrow 0} V_0 &= \lim_{\alpha^{-1} \rightarrow 0} -E_0 r \cos \theta \left(1 + \frac{R_1^3}{r^3} \left(\frac{(\sigma_0 + 2\sigma_1)(\sigma_1 - \sigma_2) + (\sigma_0 - \sigma_1)(2\sigma_1 + \sigma_2)\alpha}{2(\sigma_0 - \sigma_1)(\sigma_1 - \sigma_2) + (2\sigma_0 + \sigma_1)(2\sigma_1 + \sigma_2)\alpha} \right) \right) \\ &= \lim_{\alpha^{-1} \rightarrow 0} -E_0 r \cos \theta \left(1 + \frac{R_1^3}{r^3} \left(\frac{(\sigma_0 + 2\sigma_1)(\sigma_1 - \sigma_2)\alpha^{-1} + (\sigma_0 - \sigma_1)(2\sigma_1 + \sigma_2)}{2(\sigma_0 - \sigma_1)(\sigma_1 - \sigma_2)\alpha^{-1} + (2\sigma_0 + \sigma_1)(2\sigma_1 + \sigma_2)} \right) \right) \\ &= -E_0 r \cos \theta \left(1 + \frac{R_1^3}{r^3} \left(\frac{(\sigma_0 - \sigma_1)(2\sigma_1 + \sigma_2)}{(2\sigma_0 + \sigma_1)(2\sigma_1 + \sigma_2)} \right) \right) \\ &= -E_0 r \cos \theta \left(1 + \frac{R_1^3}{r^3} \left(\frac{\sigma_0 - \sigma_1}{2\sigma_0 + \sigma_1} \right) \right) \\ &= V_e \checkmark\end{aligned}$$

and for V_1 , we have

$$\begin{aligned}\lim_{\alpha^{-1} \rightarrow 0} V_1 &= \lim_{\alpha^{-1} \rightarrow 0} -E_0 r \cos \theta \frac{3\sigma_0}{2(\sigma_0 - \sigma_1)(\sigma_1 - \sigma_2) + (2\sigma_0 + \sigma_1)(2\sigma_1 + \sigma_2)\alpha} \\ &\quad \left((2\sigma_1 + \sigma_2)\alpha + (\sigma_1 - \sigma_2)\frac{R_1^3}{r^3} \right) \\ &= \lim_{\alpha^{-1} \rightarrow 0} -E_0 r \cos \theta \frac{3\sigma_0}{2(\sigma_0 - \sigma_1)(\sigma_1 - \sigma_2)\alpha^{-1} + (2\sigma_0 + \sigma_1)(2\sigma_1 + \sigma_2)} \\ &\quad \left((2\sigma_1 + \sigma_2) + (\sigma_1 - \sigma_2)\alpha^{-1}\frac{R_1^3}{r^3} \right) \\ &= -E_0 r \cos \theta \frac{3\sigma_0}{(2\sigma_0 + \sigma_1)(2\sigma_1 + \sigma_2)} (2\sigma_1 + \sigma_2) \\ &= -E_0 r \cos \theta \left(\frac{3\sigma_0}{2\sigma_0 + \sigma_1} \right) \\ &= V_i \checkmark\end{aligned}$$

A.3 Effective Conductivity Expression

After all of that, now we want an expression for the effective conductivity of a coated sphere. To clarify, I mean that we want to find a value σ^* such that the potential external to a sphere with radius R_1 and conductivity σ^* is equivalent to the potential due to the concentric spheres with inner radius R_2 and conductivity σ_2 , and outer radius R_1 and conductivity σ_1 .

To proceed, we equate V_0 as defined in equation A.45 with the V_e given by equation A.48 and specify that $\sigma_e = \sigma_0$, $\sigma_i = \sigma^*$ and $R = R_1$, giving

$$V_e = V_0$$

$$\begin{aligned} -E_0 r \cos \theta & \left(1 + \frac{R_1^3}{r^3} \left(\frac{\sigma_0 - \sigma^*}{2\sigma_0 + \sigma^*} \right) \right) \\ &= -E_0 r \cos \theta \left(1 + \frac{R_1^3}{r^3} \left(\frac{(\sigma_0 + 2\sigma_1)(\sigma_1 - \sigma_2) + (\sigma_0 - \sigma_1)(2\sigma_1 + \sigma_2)\alpha}{2(\sigma_0 - \sigma_1)(\sigma_1 - \sigma_2) + (2\sigma_0 + \sigma_1)(2\sigma_1 + \sigma_2)\alpha} \right) \right) \\ \frac{\sigma_0 - \sigma^*}{2\sigma_0 + \sigma^*} &= \frac{(\sigma_0 + 2\sigma_1)(\sigma_1 - \sigma_2) + (\sigma_0 - \sigma_1)(2\sigma_1 + \sigma_2)\alpha}{2(\sigma_0 - \sigma_1)(\sigma_1 - \sigma_2) + (2\sigma_0 + \sigma_1)(2\sigma_1 + \sigma_2)\alpha} \end{aligned}$$

From this, we can solve for σ^*

$$\begin{aligned}
& ((\sigma_0 + 2\sigma_1)(\sigma_1 - \sigma_2) + (\sigma_0 - \sigma_1)(2\sigma_1 + \sigma_2)\alpha)(2\sigma_0 + \sigma^*) \\
& = (2(\sigma_0 - \sigma_1)(\sigma_1 - \sigma_2) + (2\sigma_0 + \sigma_1)(2\sigma_1 + \sigma_2)\alpha)(\sigma_0 - \sigma^*) \\
& \sigma^*((\sigma_0 + 2\sigma_1)(\sigma_1 - \sigma_2) + (\sigma_0 - \sigma_1)(2\sigma_1 + \sigma_2)\alpha \\
& \quad + 2(\sigma_0 - \sigma_1)(\sigma_1 - \sigma_2) + (2\sigma_0 + \sigma_1)(2\sigma_1 + \sigma_2)\alpha) \\
& = \sigma_0(-2(\sigma_0 + 2\sigma_1)(\sigma_1 - \sigma_2) - 2(\sigma_0 - \sigma_1)(2\sigma_1 + \sigma_2)\alpha \\
& \quad + 2(\sigma_0 - \sigma_1)(\sigma_1 - \sigma_2) + (2\sigma_0 + \sigma_1)(2\sigma_1 + \sigma_2)\alpha) \\
& \sigma^*((\sigma_0 + 2\sigma_1 + 2\sigma_0 - 2\sigma_1)(\sigma_1 - \sigma_2) \\
& \quad + (\sigma_0 - \sigma_1 + 2\sigma_0 + \sigma_1)(2\sigma_1 + \sigma_2)\alpha) \\
& = \sigma_0(2(-\sigma_0 - 2\sigma_1 + \sigma_0 - \sigma_1)(\sigma_1 - \sigma_2) \\
& \quad + (-2\sigma_0 + 2\sigma_1 + 2\sigma_0 + \sigma_1)(2\sigma_1 + \sigma_2)\alpha) \\
& \sigma^*((3\sigma_0)(\sigma_1 - \sigma_2) + (3\sigma_0)(2\sigma_1 + \sigma_2)\alpha) \\
& = \sigma_0(2(-3\sigma_1)(\sigma_1 - \sigma_2) + (3\sigma_1)(2\sigma_1 + \sigma_2)\alpha)
\end{aligned}$$

We can cancel a factor of $3\sigma_0$ from each side, giving an expression independent of σ_0

$$\begin{aligned}
& \sigma^*((\sigma_1 - \sigma_2) + (2\sigma_1 + \sigma_2)\alpha) = (-2(\sigma_1)(\sigma_1 - \sigma_2) + (\sigma_1)(2\sigma_1 + \sigma_2)\alpha) \\
& \sigma^*((\sigma_1 - \sigma_2) + (2\sigma_1 + \sigma_2)\alpha) = \sigma_1(-2(\sigma_1 - \sigma_2) + (2\sigma_1 + \sigma_2)\alpha) \\
& \sigma^* = \sigma_1 \frac{-2(\sigma_1 - \sigma_2) + (2\sigma_1 + \sigma_2)\alpha}{(\sigma_1 - \sigma_2) + (2\sigma_1 + \sigma_2)\alpha}
\end{aligned}$$

With a slight re-arrangement and substituting in the definition of α , we see

$$\sigma^* = \sigma_1 \frac{(2\sigma_1 + \sigma_2)R_1^3 - 2(\sigma_1 - \sigma_2)R_2^3}{(2\sigma_1 + \sigma_2)R_1^3 + (\sigma_1 - \sigma_2)R_2^3} \quad (\text{A.50})$$

A few end-members can serve as checks. If $\sigma_1 = \sigma_2$, then $\sigma^* = \sigma_1$, as expected. If

$\alpha \rightarrow \infty$, (ie. $R_2 \rightarrow 0$), then $\sigma^* = \sigma_1$, as expected, and if $\alpha \rightarrow 1$ ($R_1 = R_2$), then $\sigma^* = \sigma_2$, as expected.

Appendix B

Self consistent effective medium theory derivatives

Here, we derive the sensitivity of the effective conductivity calculated via effective medium theory, σ^* with respect to the concentration of the included material ϕ for the inversions discussed in Chapter 6. The effective conductivity is found by solving 6.19, which we restate here:

$$(1 - \varphi)(\sigma^* - \sigma_0)R^{(0,*)} + \varphi(\sigma^* - \sigma_1)R^{(1,*)} = 0 \quad (\text{B.1})$$

where σ_0 is the conductivity of the background, σ_1 is the conductivity of the included phase, and $\mathbf{R}^{(i,*)}$ electric field concentration tensor for the i -th phase. For simplicity, we assume that both phases are randomly oriented and thus the effective conductivity is isotropic. For randomly oriented particles, $\mathbf{R}^{(i,*)}$ is given by (recalling that \mathbf{A} is given in

equation ??),

$$\begin{aligned}
R^{(j,*)} &= \frac{1}{3} \text{trace} \left(\left[\mathbf{I} + \mathbf{A} \boldsymbol{\sigma}^{*-1} (\boldsymbol{\sigma}_j \mathbf{I} - \boldsymbol{\sigma}^*) \right]^{-1} \right) \\
&= \frac{1}{3} \text{trace} \left(\left[\mathbf{I} + \frac{(\boldsymbol{\sigma}_j - \boldsymbol{\sigma}^*)}{\boldsymbol{\sigma}^*} \begin{bmatrix} Q & & \\ & Q & \\ & & 1-2Q \end{bmatrix} \right]^{-1} \right) \\
&= \frac{1}{3} \text{trace} \left(\boldsymbol{\sigma}^* \begin{bmatrix} \boldsymbol{\sigma}^* + Q(\boldsymbol{\sigma}_j - \boldsymbol{\sigma}^*) & & \\ & \boldsymbol{\sigma}^* + Q(\boldsymbol{\sigma}_j - \boldsymbol{\sigma}^*) & \\ & & \boldsymbol{\sigma}_j - 2Q(\boldsymbol{\sigma}_j - \boldsymbol{\sigma}^*) \end{bmatrix}^{-1} \right) \\
&= \frac{\boldsymbol{\sigma}^*}{3} \left(\frac{2}{\boldsymbol{\sigma}^* + Q(\boldsymbol{\sigma}_j - \boldsymbol{\sigma}^*)} + \frac{1}{\boldsymbol{\sigma}_j - 2Q(\boldsymbol{\sigma}_j - \boldsymbol{\sigma}^*)} \right)
\end{aligned} \tag{B.2}$$

where Q is a scalar that depends on the geometry of the particles composing each phase of material. For spherical particles, $Q = 1/3$, for ellipsoidal particles, the expression is given in equations 2.6, 2.5.

For the sensitivity calculation, we require the derivative of $\boldsymbol{\sigma}^*$ with respect to the concentration ϕ . We will solve for it implicitly. Starting from equation B.1, we have

$$\begin{aligned}
&-(\boldsymbol{\sigma}^* - \boldsymbol{\sigma}_0)R^{(0,*)} + (1-\varphi)R^{(0,*)}\frac{\partial \boldsymbol{\sigma}^*}{\partial \varphi} + (1-\varphi)(\boldsymbol{\sigma}^* - \boldsymbol{\sigma}_0)\frac{\partial R^{(0,*)}}{\partial \varphi} \\
&+ (\boldsymbol{\sigma}^* - \boldsymbol{\sigma}_1)R^{(1,*)} + \varphi R^{(1,*)}\frac{\partial \boldsymbol{\sigma}^*}{\partial \varphi} + \varphi(\boldsymbol{\sigma}^* - \boldsymbol{\sigma}_1)\frac{\partial R^{(1,*)}}{\partial \varphi} = 0
\end{aligned}$$

As the only dependence of $R^{(j,*)}$ on φ is through σ^* , we can use the chain rule, giving

$$\begin{aligned} \left[(1 - \varphi) \left(R^{(0,*)} + (\sigma^* - \sigma_0) \frac{\partial R^{(0,*)}}{\partial \sigma^*} \right) + \varphi \left(R^{(1,*)} + (\sigma^* - \sigma_1) \frac{\partial R^{(1,*)}}{\partial \sigma^*} \right) \right] \frac{\partial \sigma^*}{\partial \varphi} \\ = (\sigma^* - \sigma_0) R^{(0,*)} - (\sigma^* - \sigma_1) R^{(1,*)} \end{aligned}$$

Thus, the derivative of the effective conductivity with respect to the concentration of phase-1 material is

$$\frac{\partial \sigma^*}{\partial \varphi} = \left[(1 - \varphi) R^{(0,*)} + \varphi R^{(1,*)} + (1 - \varphi)(\sigma^* - \sigma_0) \frac{\partial R^{(0,*)}}{\partial \sigma^*} + \varphi(\sigma^* - \sigma_1) \frac{\partial R^{(1,*)}}{\partial \sigma^*} \right]^{-1} (\sigma^* - \sigma_0) R^{(0,*)} - (\sigma^* - \sigma_1) R^{(1,*)} \quad (\text{B.3})$$

The derivative of the electric field concentration tensor with respect to the effective conductivity is given by

$$\frac{\partial R^{(j,*)}}{\partial \sigma^*} = \frac{1}{3} (2[\sigma^* + Q(\sigma_j - \sigma^*)]^{-1} + [\sigma_j - 2Q(\sigma_j - \sigma^*)]^{-1}) + \frac{\sigma^*}{3} \left(\frac{-2(1-Q)}{(\sigma^* + Q(\sigma_j - \sigma^*))^2} + \frac{-2Q}{(\sigma_j - 2Q(\sigma_j - \sigma^*))^2} \right) \quad (\text{B.4})$$

Appendix C

A framework for simulation and inversion in electromagnetics

C.1 Introduction

The field of electromagnetic (EM) geophysics encompasses a diverse suite of problems with applications across mineral and resource exploration, environmental studies and geotechnical engineering. EM problems can be formulated in the time or frequency domain. Sources can be grounded electric sources or inductive loops driven by time-harmonic or transient currents, or natural, plane wave sources, as in the case of the magnetotelluric method. The physical properties of relevance include electrical conductivity, magnetic permeability, and electric permittivity. These may be isotropic, anisotropic, and also frequency dependent. Working with electromagnetic data to discern information about subsurface physical properties requires that we have numerical tools for carrying out forward simulations and inversions that are capable of handling each of these permutations.

The goal of the forward simulation is to solve a specific set of Maxwell's equations and obtain a prediction the EM responses. Numerical simulations using a staggered grid discretization (Yee, 1966), have been extensively studied in their application for finite difference, finite volume and finite element approaches (c.f. Newman and Alumbaugh (1999); Haber (2014a)), with many such implementations being optimized for efficient computations for the context in which they are being applied (Haber and Ascher, 2001; Li and Key, 2007; Kelbert et al., 2014; Yang et al., 2014).

Finding a model of the earth that is consistent with the observed data and prior geologic knowledge is the 'inverse problem'. It presupposes that we have a means of solving the forward problem. The inverse problem is generally solved by minimizing an objective function that consists of a data misfit and regularization, with a trade-off parameter controlling their relative contributions. (Tikhonov and Arsenin, 1977; Parker, 1980; Constable et al., 1987). Deterministic, gradient-based approaches to the inverse problem are commonplace in EM inversions. Relevance of the recovered inversion model is increased by incorporating *a priori* geologic information and assumptions. This can be accomplished through, the regularization term (Oldenburg and Li, 2005a; Constable et al., 1987) or parameterizing the inversion model (Pidlisecky et al., 2011; McMillan et al., 2015a; Kang et al., 2015). Multiple data sets may be considered through cooperative or joint inversions (Haber and Oldenburg, 1998; McMillan et al., 2015b).

Each of these advances relies on a workflow and associated software implementation. Unfortunately, each software implementation is typically developed as a stand-alone solution. As a result, these advances are not readily interoperable with regard to concepts, terminology, notations *and* software.

The advancement of EM geophysical techniques and the expansion of their application requires a flexible set of concepts and tools that are organized in a framework so

that researchers can more readily experiment with, and explore, new ideas. For example, if we consider research questions within the growing application of EM for reservoir characterization and monitoring in settings with steel cased wells (cf. Hoversten et al. (2015); Um et al. (2015); Commer et al. (2015); Cuevas (2014b); Hoversten et al. (2014); Pardo and Torres-Verdin (2013)), the numerical tools employed must enable investigation into factors such as the impact of variable magnetic permeability (Wu and Habashy, 1994; Heagy et al., 2015) and casing integrity (Brill et al., 2012) on electromagnetic signals. Various modelling approaches in both time and frequency domain simulations are being explored, these include employing highly-refined meshes (Commer et al., 2015), using cylindrical symmetry (Heagy et al., 2015) or approximating the casing on a coarse-scale (Um et al., 2015), possibly 3D anisotropic approximations (Caudillo-Mata et al., 2014). Beyond forward simulations that predict EM responses, to enable the interpretation of field data with these tools requires that machinery to address the inverse problem and experiment with approaches for constrained and/or time lapse inversions be in place (Devriese and Oldenburg, 2016; Marsala et al., 2015). Typically, addressing each of these complexities would require a custom implementations, particularly for the frequency domain and time domain simulations, although aspects, such as physical properties, are common to both. Inconsistencies between implementations and the need to implement a custom solution for each type of EM method under consideration presents a significant barrier to a researcher's ability to experiment with and extend ideas.

Building from the body of work on EM geophysical simulations and inversions, the aim of our efforts is to identify a common, modular framework suitable across the suite of electromagnetic problems. This conceptual organization has been tested and developed through a numerical implementation. The implementation is modular in design

with the expressed goal of affording researchers the ability to rapidly adjust, interchange, and extend elements. By developing the software in the open, we also aim to promote an open dialog on approaches for solving forward and inverse problems in EM geophysics.

The implementation we describe for EM forward and inverse problems extends a general framework for geophysical simulation and gradient based inverse problems, called SIMPEG (Cockett et al., 2015). The implementation of SIMPEG is open-source, written in Python and has dependencies on the standard numerical computing packages NumPy, SciPy, and Matplotlib (van der Walt et al., 2011; Oliphant, 2007; Hunter, 2007). The contribution described in this paper is the implementation of the physics engine for problems in electromagnetics, including the forward simulation and calculation of the sensitivities. Building within the SIMPEG ecosystem has expedited the development process and allowed developments to be made in tandem with other applications (<http://simpeg.xyz>). SIMPEGEM aspires to follow best practices in terms of documentation, testing, continuous integration using the publically available services Sphinx, Travis CI, and Coveralls (Brandl, 2010; Kalderimis and Meyer, 2011; Merwin et al., 2015). As of the writing of this paper, when any line of code is changed in the open source repository, over 3 hours of testing is completed; documentation and examples are also tested and automatically updated (<http://docs.simpeg.xyz>). We hope these practices encourage the growth of a community and collaborative, reproducible software development in the field of EM geophysics.

The paper is organized as follows. To provide context for the structure and implementation of SIMPEGEM, we begin with a brief overview of the SIMPEG inversion framework as well as the governing equations for electromagnetics in Section C.2. In Section C.3, we discuss the motivating factors for the EM framework, and in Section C.4, we discuss the framework and implementation of the forward simulation and

calculation of sensitivities in SIMPEGEM. We demonstrate the implementation with two synthetic examples and one field example in Section C.5. The first example shows the similarities between the time and frequency implementations for a 1D inversion. In the second example, we invert field data from the Bookpurnong Irrigation district in Australia. The final example demonstrates how the modular implementation is used to compute the sensitivity for a parametric model of a block in a layered space where a transmitter is positioned inside a steel cased well.

C.2 Background

We are focused on geophysical inverse problems in electromagnetics (EM), that is, given EM data, we want to find a model of the earth that explains those data and satisfies prior assumptions about the geologic setting. We follow the SIMPEG framework, shown in Figure C.1, which takes a gradient- based approach to the inverse problem (Cockett et al., 2015). Inputs to the inversion are the data and associated uncertainties, a description of the governing equations, as well as prior knowledge and assumptions about the model. With these defined, the SIMPEG framework accomplishes two main objectives:

1. the ability to forward simulate data and compute sensitivities (Forward Simulation - outlined in green in Figure C.1),
2. the ability to assess and update the model in an inversion (Inversion Elements and Inversion as Optimization - outlined in red in Figure C.1).

The implementation of the framework is organized into the self-contained modules shown in Figure C.1; each module is defined as a base- class within SIMPEG. The `Mesh` provides the discretization and numerical operators. These are leveraged by the `Problem`, which is the numerical physics engine; the `Problem` computes fields

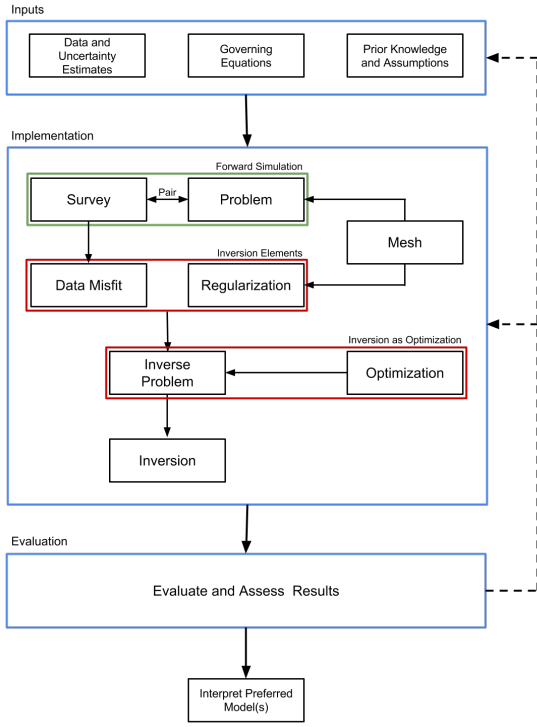


Figure C.1: Inversion approach using the SIMPEG framework. Adapted from Cockett et al. (2015)

and fluxes when provided a model and Sources. The Sources are specified in the Survey, as are the Receivers. The Receivers take the Fields computed by the Problem and evaluate them at the receiver locations to create predicted data. Each action taken to compute data, when provided a model, has an associated derivative with respect to the model; these components are assembled to create the sensitivity. Having the ability to compute both predicted data and sensitivities accomplishes the first objective.

To accomplish the second objective of assessing and updating the model in the context of the data and our assumptions, we consider a gradient-based approach to the inversion. For this, we specify an objective function which generally consists of a DataMisfit and Regularization. The DataMisfit is a metric that evaluates

the agreement between the observed and predicted data, while the `Regularization` is a metric constructed to assess the model’s agreement with assumptions and prior knowledge. These are combined with a trade-off parameter to form a mathematical statement of the `InvProblem`, an optimization problem. The machinery to update the model is provided by the `Optimization`. An `Inversion` brings all of the elements together and dispatches `Directives` for solving the `InvProblem`. These `Directives` are instructions that capture the heuristics for solving the inverse problem; for example, specifying a target misfit that, once reached, terminates the inversion, or using a beta-cooling schedule that updates the value of the trade-off parameter between the `DataMisfit` and `Regularization` (cf. Parker (1994b); Oldenburg and Li (2005a) and references within).

The output of this process is a model that must be assessed and evaluated prior to interpretation; the entire process requires iteration by a human, where underlying assumptions and parameter choices are re-evaluated and challenged. Be it in resource exploration, characterization or development; environmental remediation or monitoring; or geotechnical applications – the goal of this model is to aid and inform a complex decision.

Here we note that the inversion framework described above is agnostic to the type of forward simulation employed, provided the machinery to solve the forward simulation and compute sensitivities is implemented. Specific to the EM problem, we require this machinery for Maxwell’s equations. As such, we focus our attention on the `Forward Simulation` portion of the implementation for the EM problem and refer the reader to Cockett et al. (2015) and Oldenburg and Li (2005a) for a more complete discussion of inversions.

C.2.1 Governing Equations

Maxwell's equations are the governing equations of electromagnetic problems. They are a set of coupled partial differential equations that connect electric and magnetic fields and fluxes. We consider the quasi-static regime, ignoring the contribution of displacement current (Ward and Hohmann, 1988; Telford et al., 1990b; Haber, 2014a)¹

We begin by considering the first order quasi-static EM problem in time,

$$\begin{aligned}\vec{\nabla} \times \vec{e} + \frac{\partial \vec{b}}{\partial t} &= \vec{s}_m \\ \vec{\nabla} \times \vec{h} - \vec{j} &= \vec{s}_e\end{aligned}\tag{C.1}$$

where \vec{e} , \vec{h} are the electric and magnetic fields, \vec{b} is the magnetic flux density, \vec{j} is the current density, and \vec{s}_m , \vec{s}_e are the magnetic and electric source terms. \vec{s}_e is a physical, electric current density, while \vec{s}_m is “magnetic current density”. Although \vec{s}_m is unphysical, as continuity of the magnetic current density would require magnetic monopoles, the definition of a magnetic source term can be a useful construct, as we will later demonstrate in Section C.4 (see also Ward and Hohmann (1988)).

By applying the Fourier Transform (using the $e^{i\omega t}$ convention), we can write Maxwell's equations in the frequency domain:

$$\begin{aligned}\vec{\nabla} \times \vec{E} + i\omega \vec{B} &= \vec{S}_m \\ \vec{\nabla} \times \vec{H} - \vec{J} &= \vec{S}_e\end{aligned}\tag{C.2}$$

where we use capital letters to denote frequency domain variables. The fields and fluxes

¹In most geophysical electromagnetic surveys, low frequencies or late-time measurements are employed. In these scenarios $\sigma \gg \epsilon_0 \omega$ (eg. conductivities are typically less than 1S/m, $\epsilon_0 = 8.85 \times 10^{-12} F/m$ and frequencies considered are generally less than 10^5 Hz), so displacement current can safely be ignored.

are related through the physical properties: electrical conductivity σ , and magnetic permeability μ , as described by the constitutive relations

$$\begin{aligned}\vec{J} &= \sigma \vec{E} \\ \vec{B} &= \mu \vec{H}\end{aligned}\tag{C.3}$$

The physical properties, σ and μ are generally distributed and heterogeneous. For isotropic materials, σ and μ are scalars, while for anisotropic materials they are 3×3 symmetric positive definite tensors. The same constitutive relations can be applied in the time domain provided that the physical properties, σ, μ are not frequency-dependent.

In an EM geophysical survey, the sources provide the input energy to excite responses that depend on the physical property distribution in the earth. These responses, electric and magnetic fields and fluxes, are sampled by receivers to give the observed data. The simulation of Maxwell's equations may be conducted in either the time or frequency domain, depending on the nature of the source; harmonic waveforms are naturally represented in the frequency domain, while transient waveforms are better described in the time domain.

The aim of the inverse problem is to find a model, \mathbf{m} (which may be a voxel-based or a parametric representation) that is consistent with observed data and with prior knowledge and assumptions about the model. Addressing the inverse problem using a gradient-based approach requires two abilities of the forward simulation: (1) the ability to compute predicted data given a model

$$\mathbf{d}_{\text{pred}} = \mathcal{F}[\mathbf{m}]\tag{C.4}$$

and (2) the ability to compute or access the sensitivity, given by

$$\mathbf{J}[\mathbf{m}] = \frac{d\mathcal{F}[\mathbf{m}]}{d\mathbf{m}}. \quad (\text{C.5})$$

To employ second order optimization techniques, we also require the adjoint of the sensitivity, \mathbf{J}^\top . These two elements, when combined into the SIMPEG framework, enable data to be simulated and gradient-based inversions to be run. As such, this work benefits from other peoples' contributions to the underlying inversion machinery, including: discrete operators on a variety of meshes, model parameterizations, regularizations, optimizations, and inversion directives (Cockett et al., 2015).

C.3 Motivation

The motivation for the development of this framework is that it be a resource for researchers in the field of electromagnetic geophysics. To best serve this goal, we require a framework that is modular and extensible in order to enable exploration of ideas. An associated numerical implementation is essential for this work to be tested and acted upon. As such, we provide a tested, documented, fully open-source software implementation of the framework (under the permissive MIT license).

Specific to the EM problem, we require the implementation of Maxwell's equations in both the time domain and frequency domain. The implementation must allow for variable electrical conductivity and magnetic permeability, anisotropic physical properties; various model parameterizations of the physical properties (e.g. voxel log-conductivity or parametric representations); a range of sources including wires, dipoles, natural sources; variable receiver types; variable formulations of Maxwell's equations; solution approaches such as using a primary-secondary formulation; and the flexibil-

ity to work with and move between a variety of meshes such as tensor, cylindrically symmetric, curvilinear, and octree discretizations. Furthermore, the sensitivity computation must be flexible enough to be computed for any sensible combination of these approaches. In the following section, we will outline the framework we have used to organize and implement these ideas.

C.4 Simulation Framework

The aim of the forward simulation is to compute predicted data, \mathbf{d}_{pred} , when provided with an inversion model², \mathbf{m} and `Sources`. SIMPEGEM contains implementations for both time domain (TDEM) and frequency domain (FDEM) simulations, allowing data from commonly used EM methods to be simulated.

The framework we follow to perform the forward simulation is shown in Figure C.2; it consists of two overarching categories:

1. the `Problem`, which is the implementation of the governing equations,
2. the `Survey`, which provides the source(s) to excite the system as well as the receivers to samples the fields and produce predicted data at receiver locations.

Here, we provide a brief overview of each of the components, and discuss them in more detail in the sections that follow.

The ‘engine’ of the forward simulation is the physics; it contains the machinery to solve the system of equations for EM fields and fluxes in the simulation domain when provided with a description of the physical properties and sources. In general, the physics engine may be an analytic or numeric implementation of Maxwell’s equations. Here, we focus our attention on the numerical implementation using a standard

²We use the term *inversion model* to describe a parameterized representation of the earth (e.g. voxel-based or parametric), even if the model is solely used for forward modelling, its form sets the context for the inverse problem and the parameter-space that is to be explored.

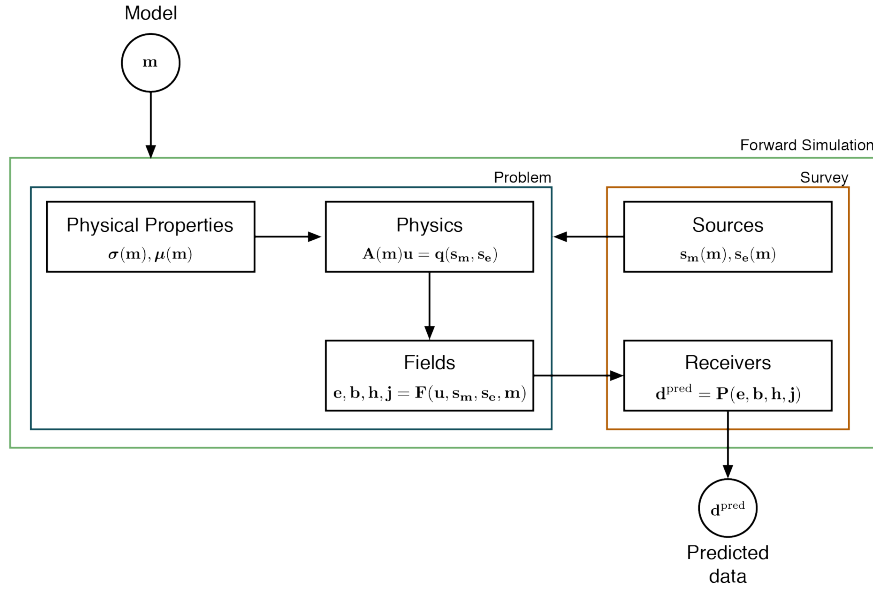


Figure C.2: Forward simulation framework.

staggered-grid finite volume approach, requiring that the physical properties, fields, fluxes and sources be defined on a mesh (cf. Haber (2014a); Hyman et al. (2002); Hyman and Shashkov (1999); Yee (1966)). We discretize fields on edges, fluxes on faces and physical properties in cell centers, as shown in Figure C.3. To construct the necessary differential and averaging operators, we leverage the `Mesh` class within SIMPEG (Cockett et al., 2015, 2016a).

To compute electromagnetic responses, the forward simulation requires the definition of a physical property model describing the electrical conductivity (σ) and magnetic permeability (μ) on the simulation mesh, as well as discrete representations of the sources used to excite EM responses (s_e, s_m). Often in solving an inverse problem, the model which one inverts for (the vector \mathbf{m}), is some discrete representation of the earth that is decoupled from the physical property model. This decoupling requires the definition of a Mapping capable of translating \mathbf{m} to physical properties on the simulation

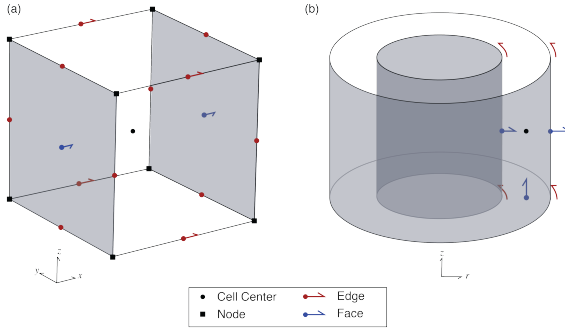


Figure C.3: Location of variables in the finite volume implementation for both a unit cell in (a) cartesian and (b) cylindrical coordinates (after Heagy et al. (2015))

mesh. For instance, if the inversion model is chosen to be log-conductivity, an exponential mapping is required to obtain electrical conductivity (i.e. $\sigma = \mathcal{M}(\mathbf{m})$). To support this abstraction, SIMPEG provides a number of extensible Mapping classes (Cockett et al., 2015; Kang et al., 2015).

With both the physical property model and the source specified, we define and solve the physics, a Maxwell system of the form

$$\mathbf{A}(\mathbf{m})\mathbf{u} = \mathbf{q}(\mathbf{s}_m, \mathbf{s}_e), \quad (\text{C.6})$$

for an electric or magnetic field or flux. Here, \mathbf{A} is the system matrix that may eliminate a field or flux to obtain a system in a single field or flux, \mathbf{u} , the solution vector. Correspondingly, the vector \mathbf{q} is the second order right-hand-side. Note, if there are necessary manipulations to make equation C.6 easier to solve numerically (e.g. symmetry) we can add these here; doing so has no effect on the derivative. The remaining fields and fluxes can be computed from \mathbf{u} anywhere in the simulation domain, through an operation of the form

$$\mathbf{f} = \mathbf{F}(\mathbf{u}(\mathbf{m}), \mathbf{s}_e(\mathbf{m}), \mathbf{s}_m(\mathbf{m}), \mathbf{m}) \quad (\text{C.7})$$

where \mathbf{f} is conceptually a vector of *all* of the fields and fluxes (i.e. \mathbf{e} , \mathbf{b} , \mathbf{h} and \mathbf{j}). This vector is never stored in the implementation, instead the fields are computed on demand through the subset of stored solution vectors (\mathbf{u}). From the computed fields (\mathbf{f}), predicted data are created by the Receivers through an operation of the form

$$\mathbf{d}_{\text{pred}} = \mathbf{P}(\mathbf{f}) \quad (\text{C.8})$$

In the simplest case, the action of \mathbf{P} selects the component of interest and interpolates the fields to the receiver locations, more involved cases could include the computation of ratios of fields, as is the case for impedance or tipper data. Obtaining predicted data from the framework concludes the forward simulation.

The same framework is employed for both time domain (TDEM) and frequency domain (FDEM) implementations within SIMPEGEM. In the case of the FDEM implementation, the matrix $\mathbf{A}(\mathbf{m})$ and the solution vector \mathbf{u} represent all frequencies. As these frequencies are independent (i.e. a block diagonal matrix, \boxplus), each frequency can be solved independently. In the TDEM code, the matrix $\mathbf{A}(\mathbf{m})$ and the solution vector \mathbf{u} represent all timesteps (Oldenburg et al., 2013; Haber, 2014a) and take the form of a lower triangular block matrix (bidiagonal in the case of Backward Euler, \boxminus), meaning the computation of each time-step depends on previous time-steps. The form of these matrices will be discussed further in the Physics section (Section C.4.2)

To perform a gradient-based inversion, we require the sensitivity of the data with respect to the inversion model, thus, each action taken to calculate data from the model must have an associated derivative. The full sensitivity is a dense matrix and is expensive to form and store, but when the optimization problem is solved using an iterative optimization approach, it does not need to be explicitly formed; all that is required are

products and adjoint-products with a vector. We treat this using a modular approach so that individual elements of the framework can be rapidly interchanged or extended. The process we follow to compute matrix-vector products with the sensitivity is shown with red arrows in Figure C.4 (b). The sensitivity-vector product $\mathbf{J}\mathbf{v}$ is built in stages by taking matrix vector products with the relevant derivatives in each module, starting with the derivative of the physical property with respect to the model. The product with the adjoint is similarly shown in Figure C.4 (c) starting with the adjoint of the receiver operation.

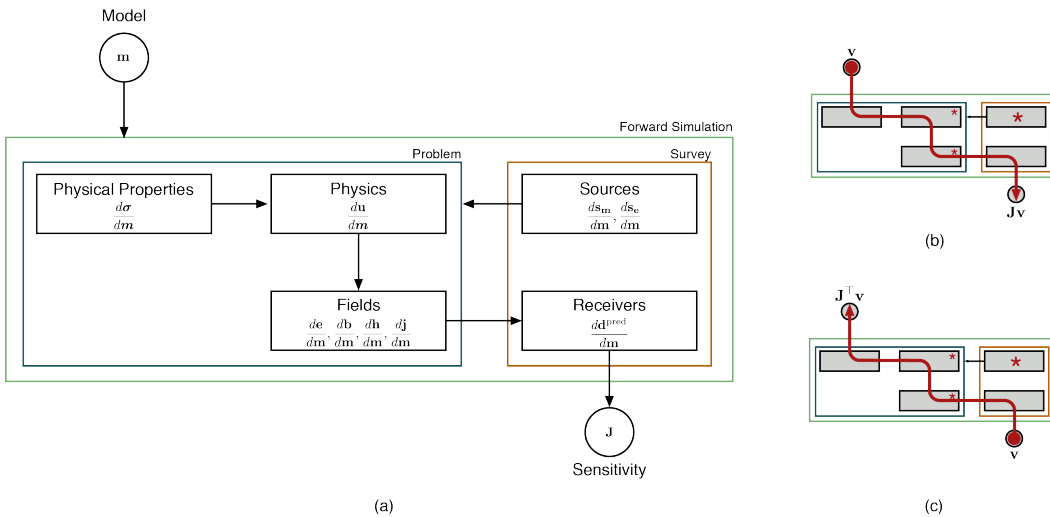


Figure C.4: (a) Contributions of each module to the sensitivity. (b) process for computing $\mathbf{J}\mathbf{v}$ and (c) $\mathbf{J}^\top \mathbf{v}$; stars indicate where the source derivatives are incorporated.

Using electrical conductivity, σ , as the only active property described by the inversion model \mathbf{m} for brevity, the sensitivity takes the form

$$\mathbf{J}[\mathbf{m}] = \frac{d\mathbf{P}(\mathbf{f})}{d\mathbf{f}} \frac{d\mathbf{f}}{d\sigma} \frac{d\sigma}{dm} = \underbrace{\frac{d\mathbf{P}(\mathbf{f})}{d\mathbf{f}}}_{\text{Receivers}} \underbrace{\left(\frac{\partial \mathbf{f}}{\partial \mathbf{u}} \overbrace{\frac{d\mathbf{u}}{d\sigma}}^{\text{Physics}} + \frac{\partial \mathbf{f}}{\partial \mathbf{s}_m} \overbrace{\frac{ds_m}{d\sigma}}^{\text{Sources}} + \frac{\partial \mathbf{f}}{\partial \mathbf{s}_e} \overbrace{\frac{ds_e}{d\sigma}}^{\text{Sources}} + \frac{\partial \mathbf{f}}{\partial \sigma} \right)}_{\text{Fields}} \underbrace{\frac{d\sigma}{dm}}_{\text{Properties}} \quad (\text{C.9})$$

The annotations denote which of the elements shown in Figure C.4 are responsible for computing the respective contribution to the sensitivity. If the model provided is in terms of μ or a source/receiver location, this property replaces the role of σ . The flexibility to invoke distinct properties of interest (e.g. σ , μ , source location, etc.) in the inversion requires quite a bit of ‘wiring’ to keep track of which model parameters are associated with which properties; this is achieved through a property mapping or PropMap (physical properties, location properties, etc.) within SIMPEG.

Although typically the source terms do not have model dependence and thus their derivatives are zero, the derivatives of \mathbf{s}_e and \mathbf{s}_m must be considered in a general implementation. For example, if one wishes to use a primary-secondary approach, where source fields are constructed by solving a simplified problem, the source terms may have dependence on the model meaning their derivatives have a non-zero contribution to the sensitivity (c.f. Coggon (1971); Haber (2014a); Heagy et al. (2015)); this will be demonstrated in the Casing Example in Section C.5.3.

The derivative of the solution vector \mathbf{u} with respect to the model is found by implicitly taking the derivative of equation C.6 with respect to \mathbf{m} , giving

$$\frac{d\mathbf{u}}{d\mathbf{m}} = \mathbf{A}^{-1}(\mathbf{m}) \left(-\underbrace{\frac{\partial \mathbf{A}(\mathbf{m}) \mathbf{u}^{\text{fix}}}{\partial \mathbf{m}}}_{\text{getADeriv}} + \underbrace{\frac{\partial \mathbf{q}}{\partial \mathbf{s}_m} \frac{d\mathbf{s}_m}{d\mathbf{m}} + \frac{\partial \mathbf{q}}{\partial \mathbf{s}_e} \frac{d\mathbf{s}_e}{d\mathbf{m}} + \frac{\partial \mathbf{q}}{\partial \mathbf{m}}}_{\text{getRHSDeriv}} \right) \quad (\text{C.10})$$

The annotations below the equation indicate the methods of the `Problem` class that are responsible for calculating the respective derivatives. Typically the model dependence of the system matrix is through the physical properties (i.e. σ , μ). Thus, to compute derivatives with respect to \mathbf{m} , the derivatives are first taken with respect to σ and the dependence of σ on \mathbf{m} is treated using chain rule. The chain rule dependence is computed and tested automatically in SIMPEG using the composable Mapping classes.

In the following sections, we discuss the implementation of elements shown in Figure C.2 and highlight their contribution to the forward simulation and calculation of the sensitivity. We begin by discussing the inversion model and its relationship to the physical properties (Section C.4.1), move on to the core of the forward simulation, the Physics (Section C.4.2), and to how Sources which excite the system are defined (Section C.4.3). Following these, we then discuss how Fields are calculated everywhere in the domain (Section C.4.4) and how they are evaluated by the Receivers to create predicted data (Section C.4.5). We conclude this section with a Summary and discussion on testing (Section C.4.6).

C.4.1 Model and Physical Properties

For all EM problems, we require an inversion model that can be mapped to meaningful physical properties in the discretized Maxwell system. Typically, we consider the model to be a description of the electrical conductivity distribution in the earth. Often, the model is taken to be log-conductivity, in which case, an exponential mapping is required (`ExpMap`) to convert the model to electrical conductivity. The inversion model may be defined on a subset of a mesh and referred to as an ‘active cell’ model. For instance, air cells may be excluded and only the subsurface considered; in this case an `InjectActiveCells` map is used to inject the active model into the full simulation domain. In the case of a parametric inversion, the inversion model is defined on a domain that is independent of the forward modelling mesh and the mapping takes the parametric representation and defines a physical property on the forward modelling mesh (e.g. a gaussian ellipsoid defined geometrically) (Li et al., 2010; Pidlisecky et al., 2011; McMillan et al., 2015b; Kang et al., 2015). Maps can be composed, for instance, a layered, 1D log conductivity model defined only in the subsurface may be mapped to a 2D cylindrical Mesh, as shown in Figure C.5.

```
import numpy as np
from SimPEG import Mesh, Maps
mesh = Mesh.CylMesh([20, 20])      # SimPEG cylindrically symmetric mesh
m_air = np.log(1e-8)                # value of the model in the air cells
indAct = mesh.vectorCCz < 0.0       # define active cells to be subsurface only
mapping = ( Maps.ExpMap(mesh) *
            Maps.SurjectVertical1D(mesh) *
```

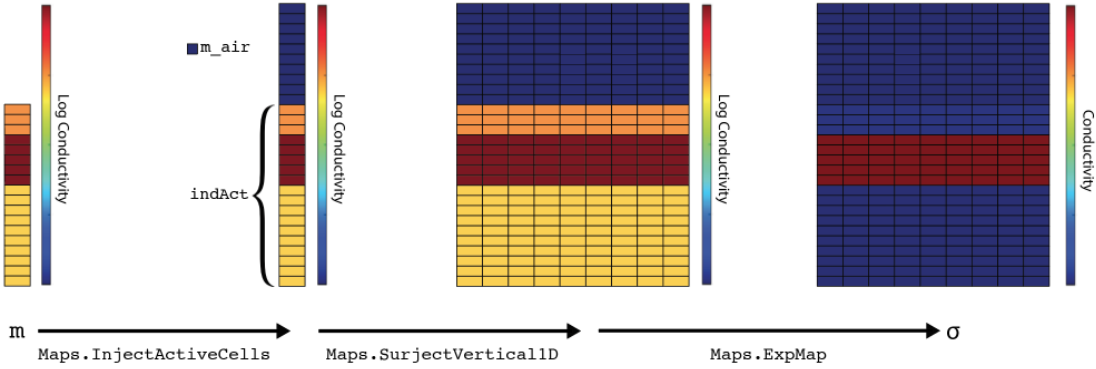


Figure C.5: Mapping an inversion model, a 1D layered, log conductivity model defined below the surface, to electrical conductivity defined in the full simulation domain.

```
Maps.InjectActiveCells(mesh, indAct, m_air, nC=mesh.nCz) )
```

In the code above, the ‘multiplication’ performs the composition of the mappings. For the contribution of this action to the sensitivity, the derivative of the electrical conductivity with respect to the model is computed using the chain rule for the composed maps (cf. Kang et al. (2015); Heagy et al. (2014b)). During an inversion, the electrical conductivity on the simulation mesh associated with the current inversion model and its derivative are accessed through the `BaseEMProblem`, which is inherited by both the TDEM and FDEM problems. In some cases, variable magnetic permeability must be considered; this is accomplished through a property mapping (`PropMap`). The `PropMap` handles the organization and independent mappings of distinct physical properties (i.e. σ, μ).

C.4.2 Physics

To formulate a system of equations from Maxwell’s equations in time (equation C.1) or frequency (equation C.2) that can be solved numerically using a finite volume approach, we require a statement of the problem in terms of two equations with two unknowns,

one of which is a field (discretized on edges), and the other a flux (discretized on faces). Thus, we can consider either the E-B formulation, or the H-J formulation. For the frequency-domain problem, we can discretize the electric field, \vec{e} , on edges, the magnetic flux, \vec{b} , on faces, physical properties σ and μ^{-1} at cell centers, and the source terms \vec{s}_m and \vec{s}_e on faces and edges, respectively (see Figure C.3). Doing so, we obtain the discrete system:

$$\begin{aligned} \mathbf{C}\mathbf{e} + i\omega\mathbf{b} &= \mathbf{s}_m \\ \mathbf{C}^\top \mathbf{M}_{\mu^{-1}}^f \mathbf{b} - \mathbf{M}_\sigma^e \mathbf{e} &= \mathbf{s}_e \end{aligned} \tag{C.11}$$

where \mathbf{C} is the discrete edge curl, $\mathbf{M}_{\mu^{-1}}^f$ is the face inner-product matrix for μ^{-1} , \mathbf{M}_σ^e is the edge inner-product matrix for σ ; these inner product matrices can be computed for isotropic, diagonally anisotropic or fully anisotropic physical properties using operators within SIMPEG's Mesh class (Cockett et al., 2015, 2016a).

Note that the source-term \mathbf{s}_e is an integrated quantity. Alternatively, the H-J formulation discretizes \vec{h} on edges, \vec{j} on faces, ρ and μ at cell centers, and the source terms \vec{s}_m , \vec{s}_e on edges and faces, respectively, giving

$$\begin{aligned} \mathbf{C}^\top \mathbf{M}_\rho^f \mathbf{j} + i\omega \mathbf{M}_\mu^e \mathbf{h} &= \mathbf{s}_m \\ \mathbf{Ch} - \mathbf{j} &= \mathbf{s}_e. \end{aligned} \tag{C.12}$$

Similarly, \mathbf{s}_m is an integrated quantity. In a full 3D simulation, the electric and magnetic contributions for the two formulations are merely staggered from one another. However, if using an assumption of cylindrically symmetry, the appropriate formulation must be used to simulate either rotational electric or magnetic contributions (Heagy et al., 2015). For both the basic FDEM and TDEM implementations, natural boundary

conditions ($\mathbf{b} \times \hat{\mathbf{n}} = 0 \forall \vec{x} \in \partial\Omega$ in E-B formulation or $\mathbf{j} \times \hat{\mathbf{n}} = 0 \forall \vec{x} \in \partial\Omega$ in H-J formulation), in which the fields are assumed to have decayed to a negligible value at the boundary, are employed to construct the differential operators, the framework and implementation are however, extensible to consider other boundary conditions (cf. Haber (2014a); Rivera Rios (2014)).

In order to solve either equation C.11 or equation C.12, we eliminate one variable and solve the second order system. This elimination is performed by the FDEM problem classes. For instance, in FDEM Problem_e, we eliminate \mathbf{b} and obtain a second order system in \mathbf{e}

$$\underbrace{\left(\mathbf{C}^\top \mathbf{M}_{\mu^{-1}}^f \mathbf{C} + i\omega \mathbf{M}_\sigma^e \right)}_{\text{getA}} \underbrace{\mathbf{e}}_{\mathbf{u}} = \underbrace{\mathbf{C}^\top \mathbf{M}_{\mu^{-1}}^f \mathbf{s}_m - i\omega \mathbf{s}_e}_{\text{getRHS}} \quad (\text{C.13})$$

FDEM Problem_e has methods getA and getRHS to construct the system

```
def getA(self, freq):
    MfMui = self.MfMui
    MeSigma = self.MeSigma
    C = self.mesh.edgeCurl
    return C.T*MfMui*C + 1j*omega(freq)*MeSigma

def getRHS(self, freq):
    s_m, s_e = self.getSourceTerm(freq)
    MfMui = self.MfMui
    C = self.mesh.edgeCurl
    return C.T * (MfMui * s_m) - 1j * omega(freq) * s_e
```

and associated methods getADeriv and getRHSDeriv to construct the derivatives of each with respect to the inversion model. These function definitions are methods of the Problem class, where the `self` variable refers to the instance of the class, and is standard Python (cf. Python documentation - <https://docs.python.org/3/tutorial/classes.html>).

For FDEM Problem_e, getRHSDeriv is zero unless one or both of the source terms have model dependence. However, if we eliminate \mathbf{e} and solve for \mathbf{b} (Problem_b), the right hand side contains the matrix \mathbf{M}_σ^e , and therefore will, in general, have a non-zero derivative. To solve this linear system of equations, SIMPEG interfaces to stan-

dard numerical solver packages (e.g. SciPy, Mumps (Oliphant, 2007; Amestoy et al., 2001, 2006), using for example pymatsolver <https://github.com/rowanc1/pymatsolver>). The components used to perform the forward simulation are assembled in the `fields` method of the `BaseFDEMProblem` class; the `fields` method solves the forward simulation for the solution vector \mathbf{u} (from equation C.13) at each frequency and source considered.

Similarly, for the time-domain problem, the semi-discretized E-B formulation is given by

$$\begin{aligned} \mathbf{C}\mathbf{e} + \frac{d\mathbf{b}}{dt} &= \mathbf{s}_m \\ \mathbf{C}^\top \mathbf{M}_{\mu^{-1}}^f \mathbf{b} - \mathbf{M}_\sigma^e \mathbf{e} &= \mathbf{s}_e \end{aligned} \quad (\text{C.14})$$

and the semi-discretized H-J formulation is given by

$$\begin{aligned} \mathbf{C}^\top \mathbf{M}_\rho^f \mathbf{j} + \frac{d\mathbf{M}_\mu^e \mathbf{h}}{dt} &= \mathbf{s}_m \\ \mathbf{C}\mathbf{h} - \mathbf{j} &= \mathbf{s}_e. \end{aligned} \quad (\text{C.15})$$

For the time discretization, we use Backward Euler (cf. Ascher (2008)). To form the TDEM `Problem_b`, we eliminate \mathbf{e} from equation C.14 and apply Backward Euler for the time discretization. A single timestep takes the form

$$\underbrace{\left(\mathbf{C}\mathbf{M}_\sigma^e \mathbf{C}^\top \mathbf{M}_{\mu^{-1}}^f + \frac{1}{\Delta t^k} \right)}_{\mathbf{A}_0^{k+1}(\mathbf{m})} \underbrace{\mathbf{b}^{k+1}}_{\mathbf{u}^{k+1}} + \underbrace{\frac{-1}{\Delta t^k} \mathbf{I}}_{\mathbf{A}_{-1}^{k+1}(\mathbf{m})} \underbrace{\mathbf{b}^k}_{\mathbf{u}^k} = \underbrace{\mathbf{C}\mathbf{M}_\sigma^e \mathbf{s}_e^{k+1} + \mathbf{s}_m^{k+1}}_{\mathbf{q}^{k+1}(\mathbf{s}_m, \mathbf{s}_e)} \quad (\text{C.16})$$

where $\Delta t^k = t^{k+1} - t^k$ is the timestep and the superscripts $k, k+1$ indicate the time index. Each TDEM problem formulation (ie. `Problem_e`, `Problem_b`, `Problem_h`, `Problem_j`) has methods to create the matrices along the block-diagonals, $\mathbf{A}_0^{k+1}(\mathbf{m})$

and $\mathbf{A}_{-1}^{k+1}(\mathbf{m})$, as well as a method to construct the right hand side, $\mathbf{q}^{k+1}(\mathbf{s}_m, \mathbf{s}_e)$, at each timestep. When inverting for a model in electrical conductivity using Problem_b, the subdiagonal matrices are independent of \mathbf{m} , however, in other formulations, such as Problem_e, the subdiagonal matrices do have dependence on electrical conductivity, thus in general, the model dependence must be considered. Depending on the solver chosen, it can be advantageous to make the system symmetric; this is accomplished by multiplying both sides by $\mathbf{M}_{\mu_{-1}}^f{}^\top$. To solve the full time-stepping problem, we assemble all timesteps in a lower block bidiagonal matrix, with on-diagonal matrices $\mathbf{A}_0^k(\mathbf{m})$ and sub-diagonal matrices $\mathbf{A}_{-1}^k(\mathbf{m})$, giving

$$\underbrace{\begin{pmatrix} \mathbf{A}_0^0(\mathbf{m}) & & & \\ \mathbf{A}_{-1}^1(\mathbf{m}) & \mathbf{A}_0^1(\mathbf{m}) & & \\ & & \mathbf{A}_{-1}^2(\mathbf{m}) & \mathbf{A}_0^2(\mathbf{m}) \\ & & \ddots & \ddots & & \\ & & & \mathbf{A}_{-1}^{n-1}(\mathbf{m}) & \mathbf{A}_0^{n-1}(\mathbf{m}) \\ & & & & \mathbf{A}_{-1}^n(\mathbf{m}) & \mathbf{A}_0^n(\mathbf{m}) \end{pmatrix}}_{\mathbf{A}(\mathbf{m})} \underbrace{\begin{pmatrix} \mathbf{u}^0 \\ \mathbf{u}^1 \\ \mathbf{u}^2 \\ \vdots \\ \mathbf{u}^{n-1} \\ \mathbf{u}^n \end{pmatrix}}_{\mathbf{u}} = \underbrace{\begin{pmatrix} \mathbf{q}^0 \\ \mathbf{q}^1 \\ \mathbf{q}^2 \\ \vdots \\ \mathbf{q}^{n-1} \\ \mathbf{q}^n \end{pmatrix}}_{\mathbf{q}(\mathbf{s}_m, \mathbf{s}_e)} \quad (\text{C.17})$$

When solving the forward simulation, the full time-stepping matrix, $\mathbf{A}(\mathbf{m})$, is not formed, instead the block system is solved using forward substitution with each block-row being computed when necessary. The initial condition, \mathbf{u}^0 , depends on the source type and waveform; it is computed numerically or specified using an analytic solution. For example, if using a grounded source and a step-off waveform, \mathbf{u}^0 is found by solving the direct current resistivity or the magnetometric resistivity problem, depending on which field we choose to solve for. When a general current waveform is considered, the initial condition will be $\mathbf{u}^0 = \mathbf{0}$, and either \mathbf{s}_m or \mathbf{s}_e , depending on type of the source used, will

have non-zero values during the on-time.

Derivatives of the matrices along the block-diagonals of $\mathbf{A}(\mathbf{m})$ along with derivatives of the right-hand-side are stitched together in a forward time stepping approach to compute the contribution of $\frac{d\mathbf{u}}{d\mathbf{m}}$ to $\mathbf{J}\mathbf{v}$ and in a backwards time stepping approach for the contribution of $\frac{d\mathbf{u}}{d\mathbf{m}}^\top$ to $\mathbf{J}^\top \mathbf{v}$.

C.4.3 Sources

Sources input EM energy into the system. They can include grounded wires, loops, dipoles and natural sources. Controlled sources are implemented in the FDEM and TDEM modules of SIMPEGEM, and natural sources are implemented in the NSEM module. For simulations, we require that the sources be discretized onto the mesh so that a right-hand-side for the Maxwell system can be constructed (i.e. `getRHS`). This is addressed by the `eval` method of the source which returns both the magnetic and electric sources ($\mathbf{s}_m, \mathbf{s}_e$, shown in Figure C.2) on the simulation mesh.

In some cases, a primary-secondary approach can be advantageous for addressing the forward problem (cf. Coggon (1971); Haber (2014a); Heagy et al. (2015)). We split up the fields and fluxes into primary and secondary components ($\mathbf{e} = \mathbf{e}^{\mathcal{P}} + \mathbf{e}^{\mathcal{S}}$, $\mathbf{b} = \mathbf{b}^{\mathcal{P}} + \mathbf{b}^{\mathcal{S}}$) and define a “Primary Problem”, a simple problem, often with an analytic solution, that is solved in order to construct a source term for a secondary problem. For instance, a point magnetic dipole source may be simulated by defining a zero-frequency primary which satisfies

$$\begin{aligned} \mathbf{e}^{\mathcal{P}} &= 0 \\ \mathbf{C}^\top \mathbf{M}_{\mu^{-1}}^f \mathbf{b}^{\mathcal{P}} &= \mathbf{s}_e^{\mathcal{P}}. \end{aligned} \tag{C.18}$$

If we define $\mu^{-1} \mathcal{P}$ to be a constant, equation C.18 has an analytic solution for $\mathbf{b}^{\mathcal{P}}$ that

may be expressed in terms of a curl of a vector potential (cf. Griffiths (2007)). When using a mimetic discretization, by defining the vector potential and taking a discrete curl, we maintain that the magnetic flux density is divergence free as the divergence operator is in the null space of the edge curl operator ($\nabla \cdot \nabla \times \vec{v} = 0$), so numerically we avoid creating magnetic monopoles (c.f. Haber (2014a)). The secondary problem is then

$$\begin{aligned} \mathbf{C}\mathbf{e}^{\mathcal{S}} + i\omega\mathbf{b}^{\mathcal{S}} &= -i\omega\mathbf{b}^{\mathcal{P}} \\ \mathbf{C}^\top \mathbf{M}_{\mu^{-1}}^f \mathbf{b}^{\mathcal{S}} - \mathbf{M}_\sigma^e \mathbf{e}^{\mathcal{S}} &= -\mathbf{C}^\top \left(\mathbf{M}_{\mu^{-1}}^f - \left(\mathbf{M}_{\mu^{-1}}^f \right)^{\mathcal{P}} \right) \mathbf{b}^{\mathcal{P}} \end{aligned} \quad (\text{C.19})$$

The source terms for the secondary problem are $\mathbf{s}_m = -i\omega\mathbf{b}^{\mathcal{P}}$, and $\mathbf{s}_e = -\mathbf{C}^\top (\mathbf{M}_{\mu^{-1}}^f - \mathbf{M}_{\mu^{-1}}^{f,\mathcal{P}}) \mathbf{b}^{\mathcal{P}}$. In scenarios where magnetic permeability is homogeneous, the electric source contribution is zero.

The left hand side is the same discrete Maxwell system as in equation C.11; the distinction is that we are solving for secondary fields, and a primary problem was solved (analytically or numerically) in order to construct the source terms. To obtain the total fields, which we sample with the receivers, we must add the primary fields back to the solution. To keep track of the primary fields, they are assigned as properties of the source class.

In most cases, source terms do not have a derivative with respect to the model. However, in a primary-secondary problem in electrical conductivity the source term depends on the electrical conductivity and derivatives must be considered (see Section C.5.3). This is similar to inverting for magnetic permeability using a primary-secondary approach described in equation C.19 (Coggon, 1971; Haber, 2014a; Heagy et al., 2015). It is also possible to consider your inversion model to be the location or waveform of the source, in which case the derivative is also non-zero and source derivatives can be

included in the optimization procedure.

C.4.4 Fields

By solving the second-order linear system, as in equation C.13, we obtain a solution vector, \mathbf{u} , of one field or flux everywhere in the domain. In the case of a primary-secondary problem, this solution is a *secondary* field. To examine all of the fields, we require easy access to the total fields and total fluxes everywhere in the domain. This is achieved through the `Fields` object.

For efficient memory usage, only the solution vector is stored, all other fields and fluxes are calculated on demand through matrix vector multiplications. As such, each problem type (`e`, `b`, `h`, `j`) has an associated `Fields` object with methods to take the solution vector and translate it to the desired field or flux. For instance, `Fields_j` stores the solution vector from `Problem_j` and has methods to compute the total magnetic field in the simulation domain by first computing the secondary magnetic field from the solution vector (\mathbf{u} ; in this example, $\mathbf{u} = \mathbf{j}$) and adding back any contribution from the source

$$\mathbf{h} = \frac{1}{i\omega} \mathbf{M}_\mu^{e^{-1}} \left(-\mathbf{C}^\top \mathbf{M}_\rho^f \mathbf{u} + \mathbf{s}_m \right) \quad (\text{C.20})$$

For their contribution to the sensitivity (equation C.9), the fields have methods to compute derivatives when provided the vectors \mathbf{v} and $\frac{d\mathbf{u}}{d\mathbf{m}}\mathbf{v}$ (from the `Physics`). For instance, for \mathbf{h}

$$\frac{d\mathbf{h}}{d\mathbf{m}}\mathbf{v} = \frac{d\mathbf{h}}{d\mathbf{u}} \left(\frac{d\mathbf{u}}{d\mathbf{m}}\mathbf{v} \right) + \left(\frac{d\mathbf{h}}{ds_e} \frac{ds_e}{d\mathbf{m}} + \frac{d\mathbf{h}}{ds_m} \frac{ds_m}{d\mathbf{m}} + \frac{\partial \mathbf{h}}{\partial \mathbf{m}} \right) \mathbf{v} \quad (\text{C.21})$$

The derivatives for **e**, **b**, and **j** take the same form. Conceptually, the product of the full derivative and a vector ($\frac{d\mathbf{f}}{d\mathbf{m}}\mathbf{v}$) can be thought of as a stacked vector of all of the

contributions from all of the fields and fluxes, however, this is never formed in practice.

C.4.5 Receivers

The measured data consist of specific spatial components of the fields or fluxes sampled at the receiver locations at a certain time or frequency. Receivers have the method `eval` that interpolates the necessary components of the fields and fluxes to the receiver locations and evaluates the data required for the problem, such as the frequency domain fields or natural source impedance data. For the frequency domain problem, real and imaginary components are treated as separate data so that when inverting, we are always working with real values. The separation of the data evaluation from fields in receiver objects allows the derivative computation to be performed and tested in a modular fashion; this enables rapid development and implementation of new receiver types.

C.4.6 Summary

Having defined the role of each of the elements in the forward simulation framework outlined in Figure C.2, the necessary machinery to compute predicted data and sensitivities is at hand for both FDEM and TDEM problems. The modular nature of the framework allows us to make several abstractions which make the code more transparent and ensure consistency across implementations. For instance, the definition of the physical properties and associated inner product matrices is common to all formulations in both time and frequency domains. Thus, these are defined as properties of a `BaseEM` class which is inherited by both the TDEM and FDEM modules. Within each of the TDEM and FDEM modules, common methods for the calculation of the fields, sensitivities and adjoint are defined and shared across the approaches that solve for **e**, **b**, **h**, or **j** (see the documentation <http://docs.simpeg.xyz>).

Testing is conducted using comparisons with analytics, cross-comparisons between formulations, order tests on the sensitivity, adjoint tests, examples, tests on the finite volume operators, projections, interpolations, solvers, etc. Tests are run upon each update to the repository through the continuous integration service TravisCI (Kalderimis and Meyer, 2011). This ensures that we can trust the tools that we use and move faster in our research into new methods and implementations. This also supports new developers and researchers in contributing to the code base without fear of breaking assumptions and ideas laid out by previous development.

C.5 Examples

To demonstrate the application and structure of the framework, we explore three examples, one field example and two synthetic examples. The purpose of the first synthetic example is to show simple time and frequency domain electromagnetic inversions, and highlight the common framework. For this, we invert for a 1D layered Earth using a 2D cylindrically symmetric mesh for the forward simulation. In the second example, we show 1D inversions of field data (RESOLVE and SkyTEM) collected over the Bookpurnong Irrigation district in Australia. The final example is a 3D synthetic example that demonstrates a sensitivity analysis using a parametric model of a block in a layered space for a reservoir characterization problem where the transmitter is positioned down-hole in a steel-cased well. We use this example to demonstrate how mappings, multiple physical properties (both electrical conductivity and magnetic permeability), and multiple meshes, a cylindrically symmetric and a 3D tensor mesh, can be composed in a primary-secondary approach for performing the forward simulation and computing the sensitivities. The scripts used to run these examples are available on <http://docs.simpeg.xyz>.

C.5.1 Cylindrically Symmetric Inversions

The purpose of this example is to demonstrate the implementation of the electromagnetic inversion in both time and frequency domains. We have chosen this example as it is computationally light, can be run on any modern laptop without installing complex dependencies, and yet it uses most of the elements and functionality needed to solve a large 3D EM problem. The script used to run this simulation is available at: <https://doi.org/10.6084/m9.figshare.5035175>.

We consider two 1D inversions for log-conductivity from an EM survey, one frequency domain experiment and one time domain experiment. Both surveys use a vertical magnetic dipole (VMD) source located on the surface. For simplicity, we consider a single receiver, measuring the vertical magnetic field, located 50m radially away from the source. The magnetic permeability is taken to be that of free space ($\mu = \mu_0$), and electrical conductivity is assumed to be frequency-independent.

Figure C.6 shows the setup used for: (a) the frequency domain simulation, (b) the time domain simulation, and (c) the common inversion implementation. In both, a cylindrical mesh is employed for the forward simulation and a 1D layered earth, described in terms of log-conductivity. To map the inversion model to electrical conductivity, a composite mapping is used to inject the 1D subsurface model into one including air cells (`InjectActiveCells`), surject the 1D model onto the 2D simulation mesh (`SurjectVertical1D`) and take the exponential to obtain electrical conductivity (`ExpMap`), as described in the Model and Physical Properties section (Section C.4.1).

The distinction between the frequency and time domain inversions comes in the setup of the forward simulations. Each employs the appropriate description of the physics (FDEM or TDEM) in the problem, and the definition of the survey, consisting of both sources and receivers, must be tailored to the physics chosen. For the FDEM

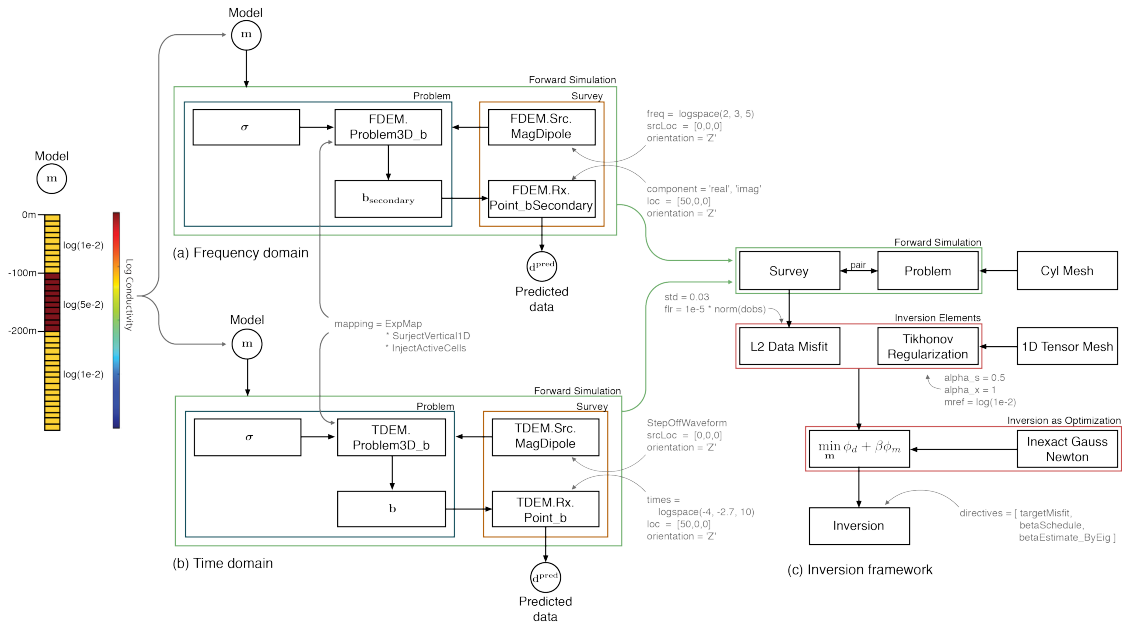


Figure C.6: Diagram showing the entire setup and organization of (a) the frequency domain simulation; (b) the time domain simulation; and (c) the common inversion framework used for each example. The muted text shows the programmatic inputs to each class instance.

survey, a vertical harmonic magnetic dipole located at the origin transmits at five frequencies logarithmically spaced between 100 Hz and 1000 Hz. The receiver is located at (50 m, 0 m, 0 m) and measures the secondary magnetic flux (with the primary being the free-space response of a harmonic magnetic dipole). The observed response is complex-valued, having both real and imaginary components. We consider these as separate data, giving a total of ten data points for this example. For the time domain survey, we again use a vertical magnetic dipole at the origin, however, we now use a step-off waveform. The observed responses are defined through time, and thus are all real-valued. For this example, we sample 10 time channels, logarithmically spaced between 10^{-4} s and 2×10^{-3} s. These time channels were selected to be sensitive to depths similar to the FDEM simulation.

With the forward simulation parameters defined in both the time and frequency do-

main simulations, we can generate synthetic data. The model used consists of a 100m thick conductive layer (0.05 S/m) whose top boundary is 100 m-below from the surface, as shown in Figure C.6. The conductivity of the half-space earth is 0.01 S/m. In both cases, 3% gaussian noise is added to the simulated data, and these are treated as the observed data (\mathbf{d}^{obs}) for the inversion.

For the inversions, we specify the inversion elements: a data misfit and a regularization. We use an L2 data misfit of the form

$$\phi_d = \frac{1}{2} \|\mathbf{W}_d(\mathbf{d}^{\text{pred}} - \mathbf{d}^{\text{obs}})\|_2^2 \quad (\text{C.22})$$

where $\mathbf{W}_{\mathbf{d}_{ii}} = 1/\varepsilon_i$ and we define $\varepsilon_i = 3\%|d_i^{\text{obs}}| + \text{floor}$. For both simulations the floor is set to $10^{-5}\|\mathbf{d}^{\text{obs}}\|$. The regularization is chosen to be a Tikhonov regularization on the 1D model

$$\phi_m = \frac{1}{2} (\alpha_s \|\mathbf{m} - \mathbf{m}_{\text{ref}}\|_2^2 + \alpha_x \|\mathbf{D}_x \mathbf{m}\|_2^2) \quad (\text{C.23})$$

where \mathbf{m}_{ref} is the reference model which is set to be a half-space of $\log(10^{-2})$. The matrix \mathbf{D}_x is a 1D gradient operator. For both examples $\alpha_s = 0.5$ and $\alpha_x = 1$. The data misfit and regularization are combined with a trade-off parameter, β , in the statement of the inverse problem. To optimize, we use the second-order Inexact Gauss Newton scheme. In this inversion, we use a beta-cooling approach, where β is reduced by a factor of 4 every 3 Gauss Newton iterations.

The initial β is chosen to relatively weight the influence of the data misfit and regularization terms. We do this by estimating the largest eigenvalue of $\mathbf{J}^\top \mathbf{J}$ and $\mathbf{W}_m^\top \mathbf{W}_m$ using one iteration of the power method. We then take their ratio and multiply by a scalar to weight their relative contributions. For this example, we used a factor of 10. For a stopping criteria, we use the discrepancy principle, stopping the inversion when

$\phi_d \leq \chi\phi_d^*$, with $\chi = 1$ and $\phi_d^* = 0.5N_{data}$ (with ϕ_d as defined in equation C.22.)

The FDEM inversion reaches the target misfit after 9 iterations, and the TDEM inversion reaches the target misfit after 6 iterations. Figure C.7 shows the recovered models (a), predicted and observed data for the FDEM inversion (b) and predicted and observed data for the TDEM inversion (c). In both the FDEM and TDEM inversions, the data are fit well. The recovered models are smooth, as is expected when employing an L2, Tikhonov regularization and both the location and amplitude of the conductive layer. The structure of both models are comparable, demonstrating that the information content in both the FDEM and TDEM data are similar. The recovered model can be improved by many additional techniques that are not explored here (e.g. using compact norms in the regularization). The SIMPEG package provides a number of additional directives and regularization modules which can be useful for this purpose.

C.5.2 Bookpurnong Field Example

The purpose of this example is to demonstrate the use of the framework for inverting field data and provide an inversion that can be compared with other results in the literature. In particular, we invert frequency and time domain data collected over the Bookpurnong Irrigation District in Southern Australia. The Murray River and adjacent floodplain in the Bookpurnong region have become extensively salinized, resulting in vegetation die-back (Munday et al., 2006; Overton et al., 2004). Multiple electrical and electromagnetic data sets have been collected with the aim of characterizing the near-surface hydrologic model of the area (Munday et al., 2006). For a more complete background on the geology and hydrogeology of the Bookpurnong region, we refer the reader to Munday et al. (2006).

Here, we will focus our attention to the RESOLVE frequency-domain data collected

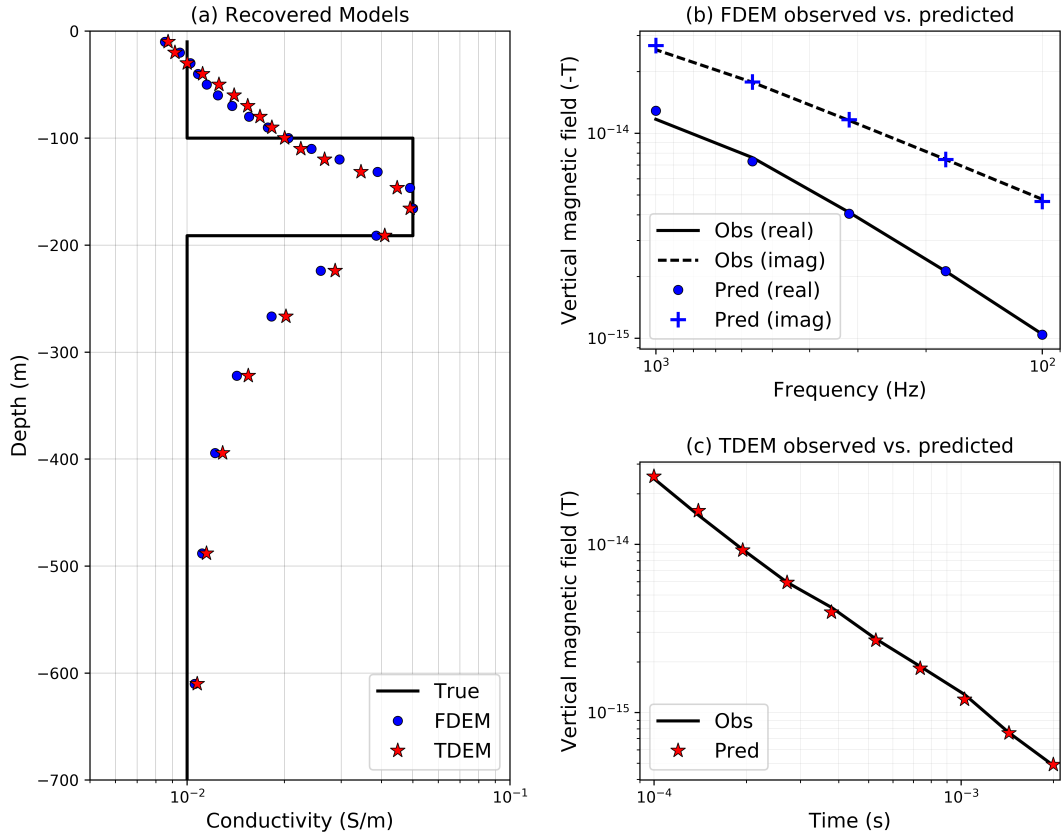


Figure C.7: (a) True and recovered models for the FDEM and TDEM inversions; predicted and observed data for (b) the FDEM example, and (c) the TDEM example. In (b) the magnetic field data are in the negative z-direction.

in 2008 and the SkyTEM time-domain data collected in 2006. These data are shown in Figure C.8. The RESOLVE system consists of 5 pairs of horizontal coplanar coils, with nominal frequencies of 400 Hz, 1800 Hz, 8200 Hz, 40 000 Hz, and 130 000 Hz as well as a vertical coaxial coil pair of coils which operates at 3200Hz. For the Bookpurnong survey, the bird was flown at \sim 50m altitude (Viezzoli et al., 2010). The SkyTEM time-domain system operates in two transmitter modes that can be run sequentially. The high moment mode has high current and operates at a low base frequency (25 Hz and can be lowered to 12.5 Hz), and the low moment operates at a lower current and higher base

frequency (222.5 Hz) (Sørensen and Auken, 2004). The Bookpurnong SkyTEM survey was flown at an altitude of \sim 60m (Viezzoli et al., 2010).

Multiple authors have inverted these data sets; 1D spatially constrained inversions of the SkyTEM and RESOLVE data were performed by (Viezzoli et al., 2009, 2010). Yang (2017) independently inverted these data in 1D and provides a discussion at <http://em.geosci.xyz/content/case>. The SkyTEM data (high moment) were inverted in 3D by (Wilson et al., 2010). In the example that follows, we select a location where both the RESOLVE and SkyTEM datasets have soundings and invert them in 1D, we then proceed to perform a stitched 1D inversion of the RESOLVE data. The data have been made available with the permission of CSIRO and are accessible, along with the script used to run the inversions at <https://doi.org/10.6084/m9.figshare.5107711>.

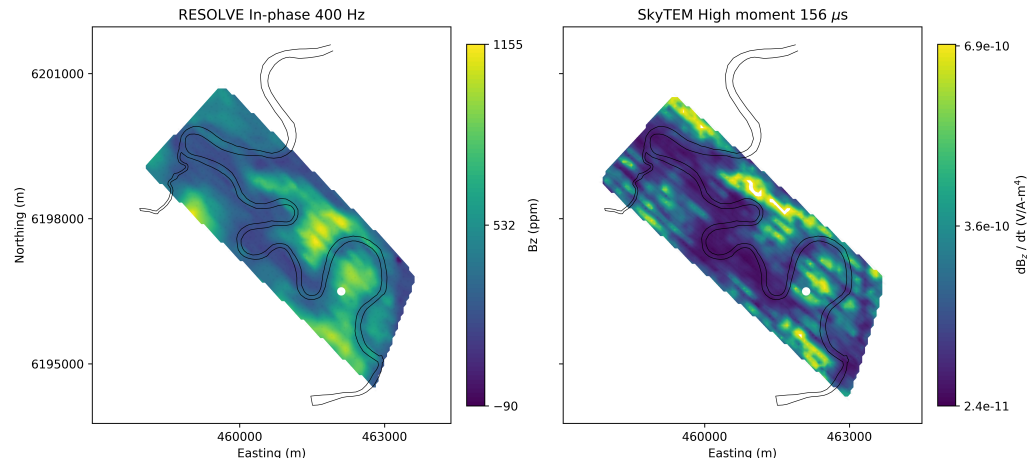


Figure C.8: 400 Hz In-phase RESOLVE data at (left) and High Moment SkyTEM data at $156 \mu s$. The white dot at (462100m, 6196500m) on both images is the location of the stations chosen to demonstrate the 1D inversions in frequency and time.

1D Inversion of RESOLVE and SkyTEM soundings

We have selected a sounding location (462100m, 6196500m) at which to perform 1D inversions of the RESOLVE and SkyTEM (High Moment) data. The observed data at this location are shown in Figure C.9 (b) and (c). For the RESOLVE inversion, we consider the horizontal co-planar data collected at 400 Hz, 1800 Hz, 8200 Hz, 40 000 Hz, and 130 000 Hz. For the noise model, we assign 10% error for the three lowest frequencies and 15% error for the two highest; a noise floor of 20ppm is assigned to all data. The inversion mesh uses cells that expand logarithmically with depth, starting at the surface with a finest cell size of 1m. The forward simulation is carried out on the cylindrically symmetric mesh, similar to the previous example. In the inversion, we employ a Tikhonov regularization in which length scales have been omitted in the regularization function. A fixed trade-off parameter of $\beta = 2$ is used, α_z is set to be 1, and α_s is 10^{-3} . A half-space reference model with conductivity 0.1 S/m is used, this also served as the starting model for the inversion. The inversion reached target misfit after 2 iterations. The resulting model and data fits are shown in Figure C.9. Very close to the surface, we recover a resistor, while below that, we recover a conductive unit (~ 2 S/m). Examining the data (Figure C.9b), we see that the real components are larger in magnitude than the imaginary, and that with increasing frequency, the magnitude of the imaginary component decreases while the real component increases; such behaviour is consistent with an inductive- limit response, and we thus expect to recover conductive structures in the model.

For the time domain inversion, we consider the SkyTEM high moment data. We use the source waveform shown in the inset plot in Figure C.9 (c). For data, we use 21 time channels from 47 μ s to 4.4 ms; the latest three time channels (5.6ms, 7ms and 8.8 ms) are not included. For data errors, we assign a 12% uncertainty and a floor of 2.4×10^{-14}

V/Am^4 . We again use a Tikhonov regularization, here with $\alpha_z = 1$ and $\alpha_s = 10^{-1}$. The trade-off parameter is $\beta = 20$. A half-space starting model of 0.1 S/m is again employed. For the reference model, we use the model recovered from the RESOLVE 1D inversion. As we are using the high-moment data, we do not expect the SkyTEM data to be as sensitive to the near surface structures as the RESOLVE data. By using the model recovered in the RESOLVE inversion as the starting model for the SkyTEM inversion, we can assess agreement between the two and isolate structures that are introduced by the SkyTEM inversion. The inversion reached the target misfit after 3 iteration and the results are shown in Figure C.9. At this location, there is good agreement in the models recovered from the RESOLVE and SkyTEM data, with both supporting a near-surface resistor and showing a deeper conductive structure.

Stitched 1D inversion of RESOLVE data

Next, we perform a stitched 1D inversion of the RESOLVE data set. With this example, we aim to demonstrate a practical inversion workflow that will run on modest computational resources. As such, we have heavily downsampled the data set, taking 1021 stations of the 40 825 collected. A 1D stitched inversion is a relatively straight-forward approach for creating a conductivity model - each sounding is inverted independently and the inversion results are then assembled to create a 3D model. This can be a valuable quality-control step prior to adopting more advanced techniques such as including lateral or 3D regularization across soundings or even performing a 3D inversion. In cases where the geology is relatively simple, a stitched 1D inversion may be sufficient. The inversion parameters are the same as those used in the inversion of the RESOLVE sounding discussed in the previous section. A plan- view of the recovered model 9.9m below the surface is shown in Figure C.10a. A global χ - factor of 0.74 was reached,

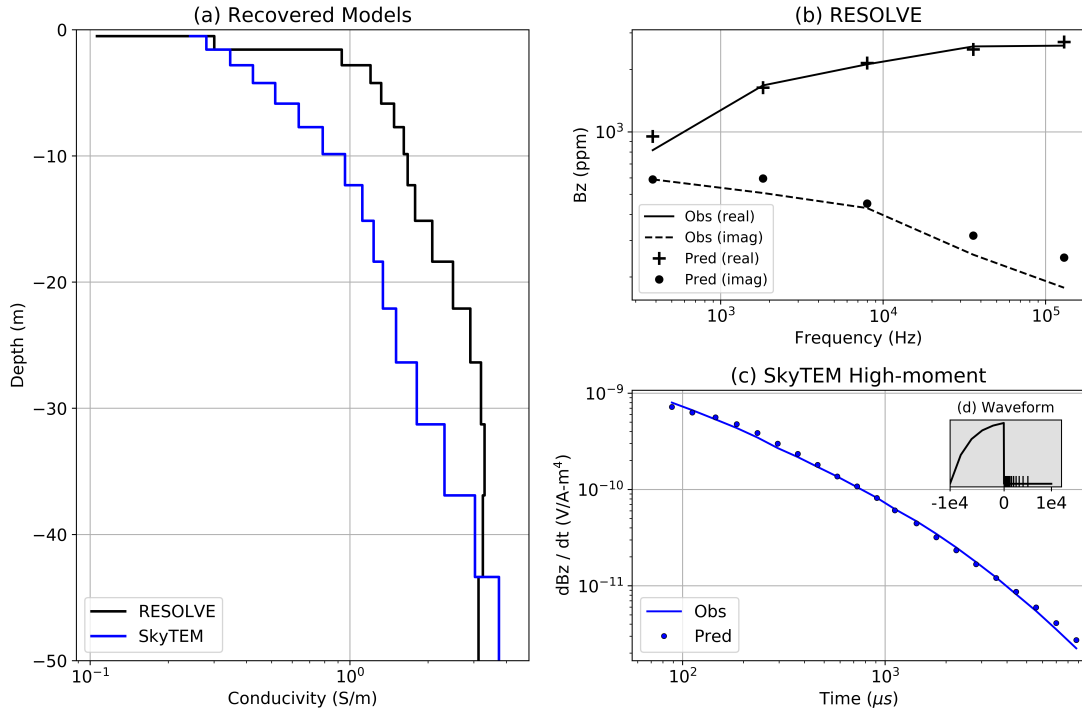


Figure C.9: (a) Models recovered from from the 1D inversion of RESOLVE (back) and SkyTEM (blue) data at the location (462100m, 6196500m). (b) Observed (lines) and predicted (points) frequency domain data. (c) Observed and predicted time domain data. (d) Source waveform used in for the SkyTEM inversion, the x-axis is time (μ s) on a linear scale.

and plots comparing the real component of the observed and predicted data at 400Hz are shown in Figures C.10 (b) & (c).

The recovered model (Figure C.10a), bears similar features to the models found by Viezzoli et al. (2010) (Figure 4 of Viezzoli et al. (2010)) and by Yang (2017). In general, the northwestern portion of the Murray river is more resistive, in particular near (459 000m, 6 200 000m) and (460 000m, 6 198 000m) while the southeastern portion of the river is more conductive. Two mechanisms of river salinization have been discussed in Munday et al. (2006); Viezzoli et al. (2010): the resistive regions are attributed to a “losing” groundwater system, in which freshwater from the Murray River discharges

to adjacent banks, while the conductive regions are attributed to a “gaining” system, in which regional saline groundwater seeps into the river.

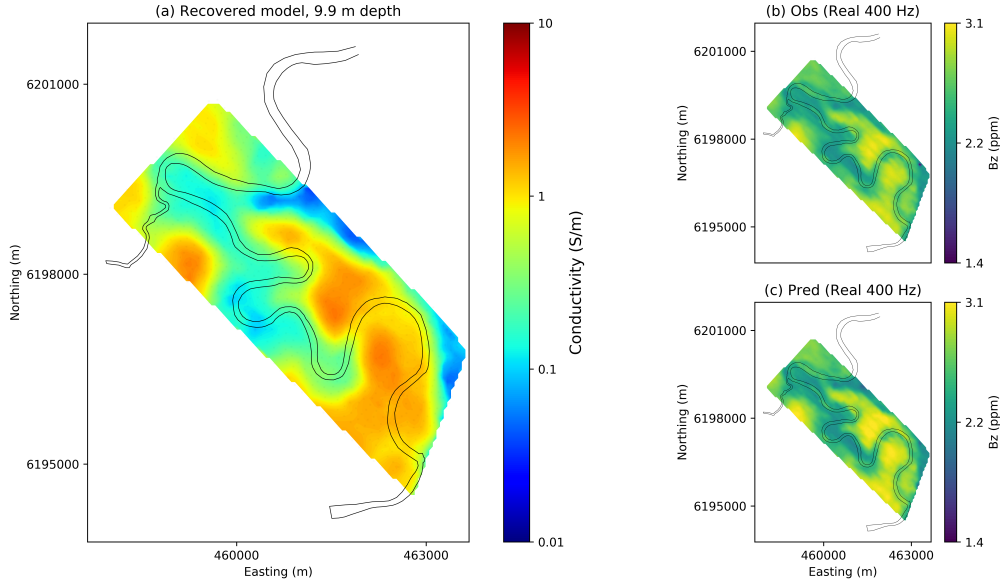


Figure C.10: (a) Conductivity model 9.9m below the surface from a stitched 1D inversion of RESOLVE data. (b) Real component of the observed RESOLVE data at 400Hz. (c) Real component of the predicted data at 400Hz.

C.5.3 Steel-Cased Well: Sensitivity Analysis for a Parametric Model

The purpose of this example is to demonstrate the modular implementation of simpegEM and how it can be used to experiment with simulation and inversion approaches. Conducting electromagnetic surveys in settings where steel casing is present is growing in interest for applications such as monitoring hydraulic fracturing or enhanced oil recovery (Hoversten et al., 2015; Um et al., 2015; Commer et al., 2015; Hoversten et al., 2014; Marsala et al., 2015; Cuevas, 2014a; Weiss et al., 2015; Yang et al., 2016). Steel is highly conductive ($\sim 5.5 \times 10^6 \text{ S/m}$), has a significant magnetic permeability ($\sim 50\mu_0 - 100\mu_0$) (Wu and Habashy, 1994). This is a large contrast to typical geo-

logic settings, with conductivities typically less than 1 S/m and permeabilities similar to that of free space, μ_0 . In addition to the large physical property contrast, the geometry of well casing also presents a significant computational challenge. Well casing is cylindrical in shape and only millimeters thick, while the geologic structures we aim to characterize are on the scale of hundreds of meters to kilometers. Inverting electromagnetic data from such settings requires that we have the ability to accurately simulate and compute sensitivities for models with casing and 3D geologic variations. One strategy that may be considered is using a primary- secondary approach, simulating the casing in a simple background and using these fields to construct a source for the secondary problem which considers the 3 dimensional structures of interest (Heagy et al., 2015). Here, we demonstrate how the framework can be employed to implement this approach and compute the sensitivities. The parametric representation of the model allows us to investigate the expected data sensitivity to specific features of the model such as the location, spatial extent and physical properties of a geologic target. Such an analysis may be used to investigate how well we expect certain features of the model to be resolved in an inversion and it could be employed as a survey design tool. In what follows, we outline the general approach and then discuss a specific implementation. The script used to generate this example is available at: <https://doi.org/10.6084/m9.figshare.5036123>.

Approach

In this example we design a survey to resolve a conductive body in a reservoir layer in the presence of a vertical, steel-cased well as shown in Figure C.11. To calculate the sensitivity of the data with respect to each model parameter requires that we be able to simulate and calculate derivatives of each component used to simulate data.

We use a primary-secondary approach, as described in Heagy et al. (2015). The

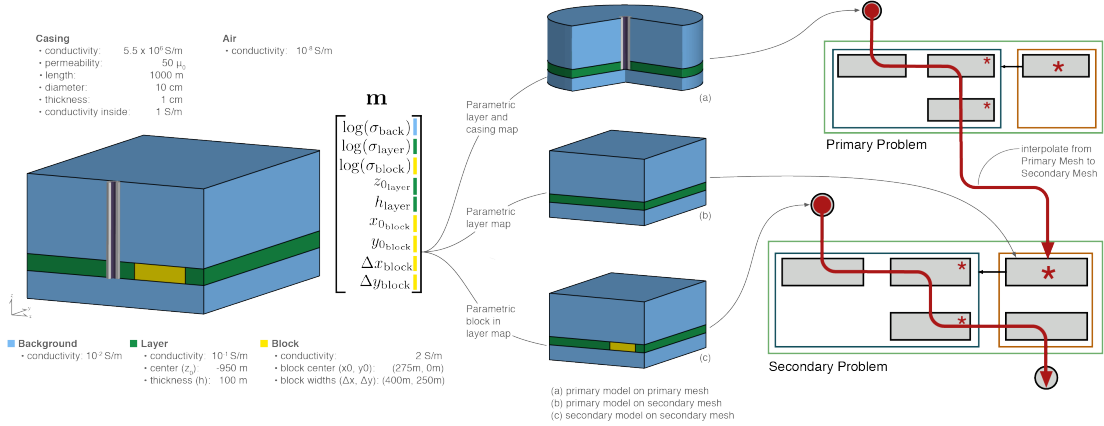


Figure C.11: Setup of parametric models and calculation of the sensitivity for a primary secondary approach of simulating 3D geology and steel casing.

physical properties, fields and fluxes are composed of two parts, a primary and a secondary part. For example in the E-B formulation, $\sigma = \sigma^{\mathcal{P}} + \sigma^{\mathcal{S}}$, $\mu = \mu^{\mathcal{P}} + \mu^{\mathcal{S}}$, $\vec{E} = \vec{E}^{\mathcal{P}} + \vec{E}^{\mathcal{S}}$, $\vec{B} = \vec{B}^{\mathcal{P}} + \vec{B}^{\mathcal{S}}$. A primary problem, which includes the cylindrically symmetric part of the model (casing, source, and layered background) is defined

$$\begin{aligned} \vec{\nabla} \times \vec{E}^{\mathcal{P}} + i\omega \vec{B}^{\mathcal{P}} &= 0 \\ \vec{\nabla} \times \mu^{-1} \vec{B}^{\mathcal{P}} - \sigma^{\mathcal{P}} \vec{E}^{\mathcal{P}} &= \vec{s}_e. \end{aligned} \quad (\text{C.24})$$

This primary problem is solved on a cylindrically symmetric mesh with cells fine enough to capture the width of the casing and its solution yields the primary fields. The primary fields are then interpolated to a 3D tensor mesh, suitable for discretizing 3D reservoir-scale features. The primary fields are used to construct the source current density for the

secondary problem, given by

$$\begin{aligned}\vec{\nabla} \times \vec{E}^{\mathcal{S}} + i\omega \vec{B}^{\mathcal{S}} &= 0 \\ \vec{\nabla} \times \mu^{-1} \vec{B}^{\mathcal{S}} - \sigma \vec{E}^{\mathcal{S}} &= \vec{q} \\ \vec{q} &= (\sigma - \sigma^{\mathcal{P}}) \vec{E}^{\mathcal{P}}.\end{aligned}\tag{C.25}$$

By solving the secondary problem, we then obtain secondary fields and fluxes. These are sampled by the receivers to create predicted data.

In equation C.25, we see that the source term, \vec{q} has model dependence through σ , $\sigma^{\mathcal{P}}$ and $\vec{E}^{\mathcal{P}}$. Typically primary-secondary approaches are used when the background is assumed to be known, as it is captured in the primary. Here, however, we do not wish to assume that the background is known; in practice it may be constrained, but it is not generally well known. The primary solution is used instead to separate the contributions of the casing and the block so that we can avoid a potentially crippling assumption. This approach allows an appropriately tailored mesh to be constructed for each problem. Thus, we require derivatives not only on the 3D secondary mesh, but also derivatives of the primary fields (in this case on a cylindrically symmetric mesh). To implement this type of primary-secondary problem, we construct a Primary-Secondary source which solves the primary problem to provide the primary fields. Since all derivatives are implemented for the primary problem, when computing sensitivities for the secondary problem, the derivatives due to the primary problem are accounted for in the contributions of the source term to the derivative. This is conceptually shown in Figure C.11.

For this example, we wish to investigate how sensitive the specified survey is to aspects of the model which we might want to resolve in a field survey, such as the geometry and location of the anomalous body, as well as the physical properties of the geologic

units. A voxel-based description of the model does not promote investigation of these questions, so we will instead apply a parametric description of the model. The model is parameterized into nine parameters which we consider to be unknowns ($\log(\sigma_{\text{background}})$, $\log(\sigma_{\text{layer}})$, $\log(\sigma_{\text{block}})$, $z_{0_{\text{layer}}}$, h_{layer} , $x_{0_{\text{block}}}$, Δx_{block} , $y_{0_{\text{block}}}$, Δy_{block}). In what follows, we examine the sensitivity of the data with respect to these model parameters.

Implementation

The model we use is shown in Figure C.11. It consists of a 1km long vertical steel cased well (diameter: 10 cm, thickness: 1cm) with conductivity $\sigma = 5.5 \times 10^6$ S/m, and magnetic permeability $\mu = 50\mu_0$. The casing is assumed to be filled with fluid having a conductivity of 1S/m. The background has a resistivity of $100\Omega\text{m}$, and the 100m thick reservoir layer has a resistivity of $10\Omega\text{m}$. The target of this survey is the conductive block (2S/m) with dimensions $400\text{m} \times 250\text{m} \times 100\text{m}$. The source used consists of two grounded electrodes, a positive electrode coupled to the casing at a depth of 950m, and a return electrode 10km from the wellhead on the surface. We consider a frequency-domain experiment at a transmitting frequency of 0.5Hz and 1A current. For data, we consider two horizontal components (x and y) of the real part of the electric field measured at the surface.

To accomplish this simulation and sensitivity calculation, we construct 3 mappings, shown conceptually in Figure C.11, in order to obtain: (1) $\sigma^{\mathcal{P}}$ on the primary (cylindrical) mesh, (2) $\sigma^{\mathcal{P}}$ on the secondary mesh (as is needed in equation C.25) and (3) σ on the secondary mesh. Differentiability of the electrical conductivity models with respect to each of the 9 parameters is achieved by constructing the model using arctangent functions (cf. Aghasi et al. (2011); McMillan et al. (2015b)). Each of these parameterizations can be independently tested for second-order convergence to check the validity

of the computation of the derivatives (cf. Haber (2014a)).

The source term for the secondary fields requires that we simulate the primary fields. For this, we use the mapping of \mathbf{m} to $\sigma^{\mathcal{P}}$ on the primary mesh and employ the H-J formulation of Maxwell's equations in the frequency domain in order to describe a vertically and radially oriented current density and a rotational magnetic field. In this simulation, we also consider the permeability of the casing. The source consists of a wire-path terminating downhole at -950m where it is coupled to the casing. At the surface, the return electrode is 10km radially away from the well³. With these parameters defined, we have sufficient information to solve the primary problem and thereby obtain the primary electric field everywhere in the simulation domain. The real, primary current density for this example is shown in Figure C.12.

This primary field is described on the cylindrical mesh, so in order to use it to construct the source term for the secondary problem, we interpolate it to the 3D tensor mesh. The remaining pieces necessary for the definition of the secondary source on the 3D mesh are defining σ and $\sigma^{\mathcal{P}}$; this is achieved through the mappings defined above. The primary problem and source, along with the mapping required to define $\sigma^{\mathcal{P}}$, are used to define a primary-secondary source, which solves a forward simulation to compute the secondary source-current, \mathbf{s}_e , shown in Figure C.13. Note that the source current density is only present where there are structures in the secondary model that were not captured in the primary, in this case, where the conductive block is present.

With the source term for the secondary problem defined, the secondary problem is then solved resulting in the predicted data at the surface. Here, we focus our attention to the real x, y components of the electric field, as shown in Figure C.14. The top two

³Due to the symmetry employed, the return electrode is a disc. Numerical experiments over a half-space show that the real, radial electric field from the cylindrical simulation exhibits the same character as the 3D simulation but is slightly reduced in magnitude.

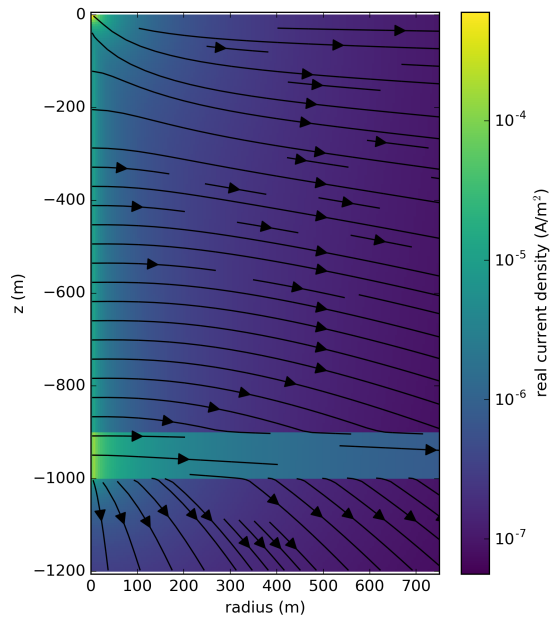


Figure C.12: Cross sectional slice of primary (casing + background) real current density. The colorbar is logarithmically scaled and shows the amplitude of the real current density.

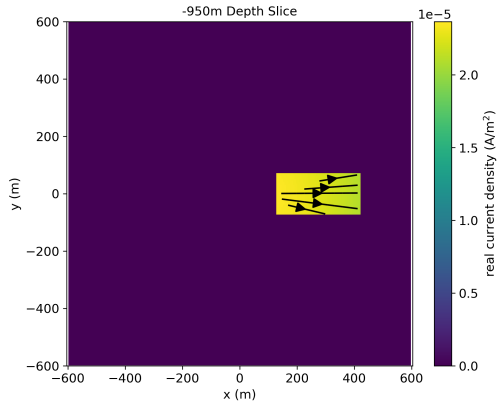


Figure C.13: Depth slice at $z=-950\text{m}$ showing the source current density for the secondary problem.

panels show the total (casing and conductive target) x-component (a) and y-component (b) of the electric field while the bottom two panels show the secondary (due to the conductive target, outlined in white) x-component (c) and y-component (d) of the electric

field. As expected, the total electric field is dominated by the source that is located in the casing. As shown in Figure C.12 the majority of the current is exiting into the layer at depth, but current is still emanating along all depths of the casing. Measured electric fields at the surface are sensitive to the currents that come from the top part of the casing and hence the observed fields are strongest closest to the pipe and they fall off rapidly with distance. The behavior of the secondary electric field is, to first order, like that expected from a dipole at depth oriented in the x-direction. It has a broad smooth signature at the surface.

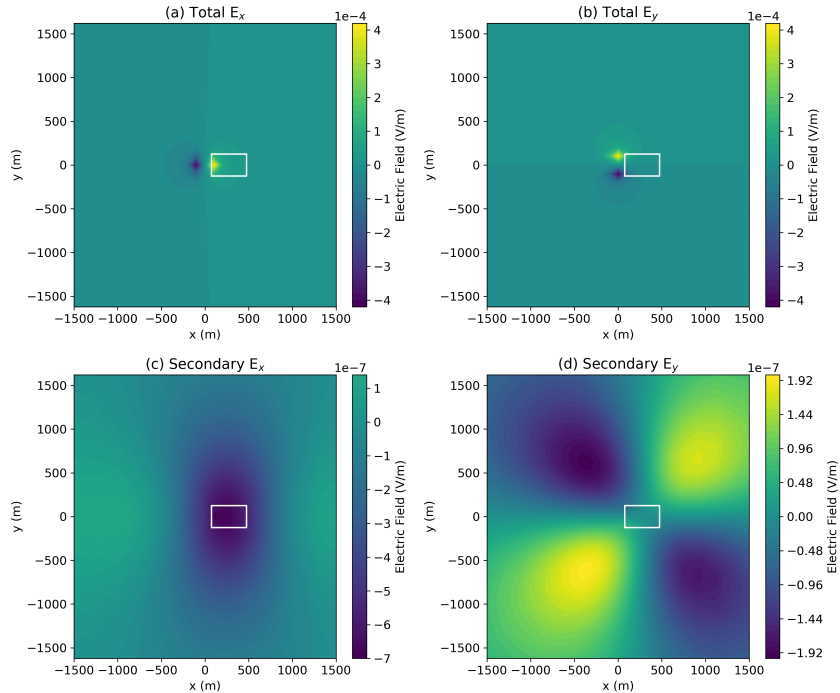


Figure C.14: Simulated real electric field data as measured at the surface using a primary secondary approach for casing and a conductive target (outlined in white). The upper panels show the total E_x (a) and E_y (b); the lower panels show the secondary (due to the conductive block) E_x (c) and E_y (d). Note that the colorbars showing the secondary electric fields are not on the same scale. The limits of the colorbars have been set so that the zero-crossing is always shown in the same color.

Now that the pieces are in place to perform the forward simulation, we want to compute the sensitivity. Generally, we do not form the full sensitivity when performing an inversion as it is a large, dense matrix. Here however, since the inversion model is composed of only nine parameters, the final sensitivity matrix is small (nine by number of data). The steps followed to stitch together and compute the sensitivity are shown in the diagram in Figure C.11. To check the simulation approach for this example, the sensitivity is tested for second-order convergence (cf. Haber (2014a)).

Figures C.15, C.16 and C.17 shows the sensitivity of both the real E_x (left), and real E_y (right) data with respect to each of the 9 model parameters. Note that the colorbars are not identical in each image and the units of the sensitivity are dependent on the parameter under consideration. In each image, the white outline shows the horizontal location of the block.

In Figure C.15, we focus on the physical properties of the background layer and block, all parametrized in terms of $\log(\sigma)$. Clearly, the conductivity of the background has the largest influence on the data, in particular near the well (at the origin), followed by the conductivity of the layer, where the injection electrode is situated. There are 4 orders of magnitude difference between the maximum sensitivity of the data with respect to the conductivity of the block and that of the background. This indicates that in order to resolve such an anomalous body, the background must be well-constrained. When looking at Figure C.15 (f), we see that the areas of largest sensitivity of the E_y data with respect to the physical properties of the block are spatially distant from the body and the well. This indicates that if one is designing a survey, it may be advantageous to collect data in these regions as these are also regions where the influence of the properties of the background are less dominant.

In Figure C.16, we focus on the depth and thickness of the layer. Note that the depth

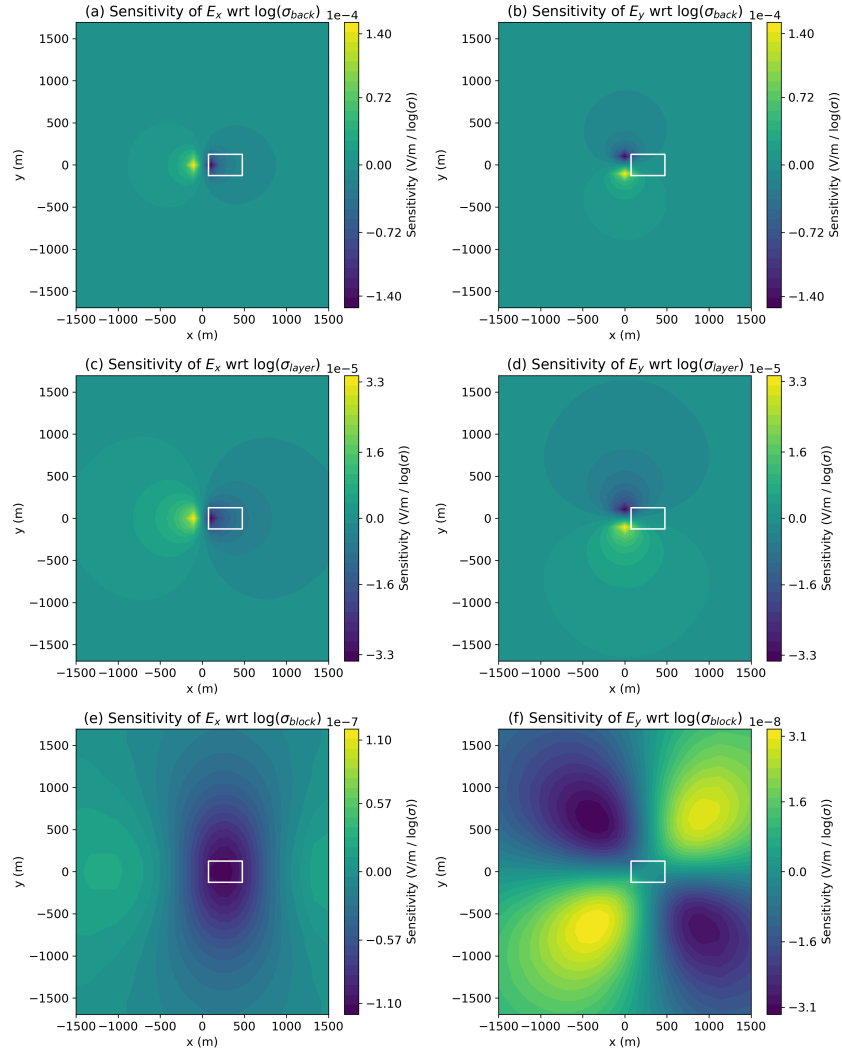


Figure C.15: Sensitivity of surface real E_x (left) and E_y (right) data with respect to the physical properties, $((V/m)/(\log(\sigma)))$

and thickness of the block are constrained to be the same as the layer, so the character of the sensitivity is influenced by the presence of the block. Here, the units of the sensitivity are $(V/m)/m$. Similarly, Figure C.17 shows the sensitivity with respect to the geometric properties of the block.

To compare between the physical properties and geometry of the model, the scales of interest must be taken into consideration. In Table C.1, we show the maximum am-

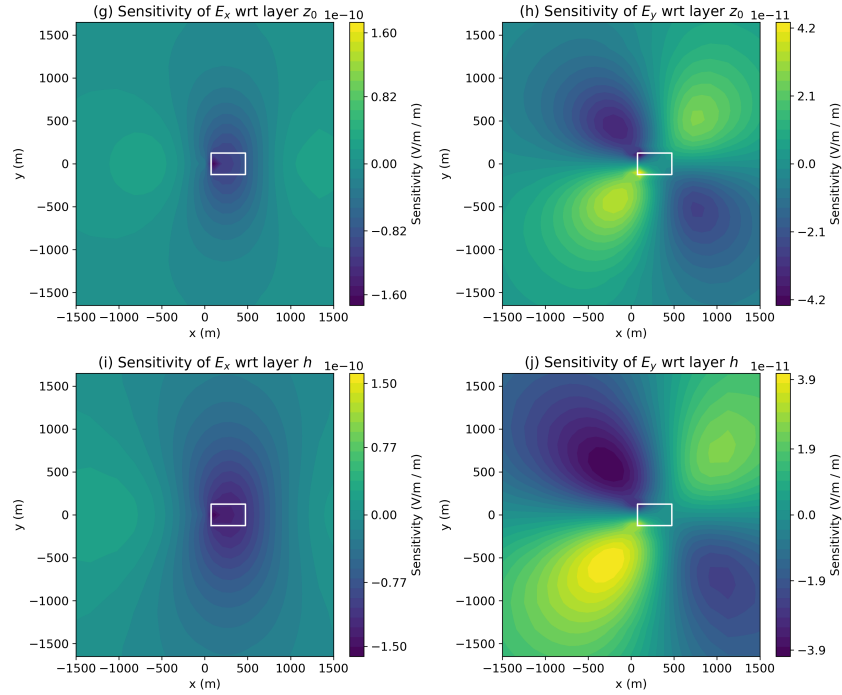


Figure C.16: Sensitivity of surface real E_x (left) and E_y (right) data with respect to the layer geometry, $((V/m)/m)$

plitude of the sensitivity with respect to each individual model parameter. From this, we approximate the sensitivity as linear about the true model and compute the perturbation required to cause a change of 10^{-9} V/m in the data ($\Delta\mathbf{m}_i = 10^{-9}/\max|\mathbf{J}_i|$). For ease of comparison, the perturbations in the log-conductivity of the background, layer, and block were converted to linear conductivity by

$$\Delta\sigma_{\text{unit}} = \frac{\exp[\log(\sigma)_{\text{unit}} + \Delta\log(\sigma)_{\text{unit}}] - \exp[\log(\sigma)_{\text{unit}} - \Delta\log(\sigma)_{\text{unit}}]}{2}. \quad (\text{C.26})$$

In table C.1, we see that to cause a perturbation in the E_x data by $\sim 10^{-9} \text{ V/m}$, requires a 0.007% change in the conductivity of the background, while the conductivity of the block would need to change by 0.8% to have a comparable impact in the E_x data. In comparing between physical properties and geometric features of the model, we see

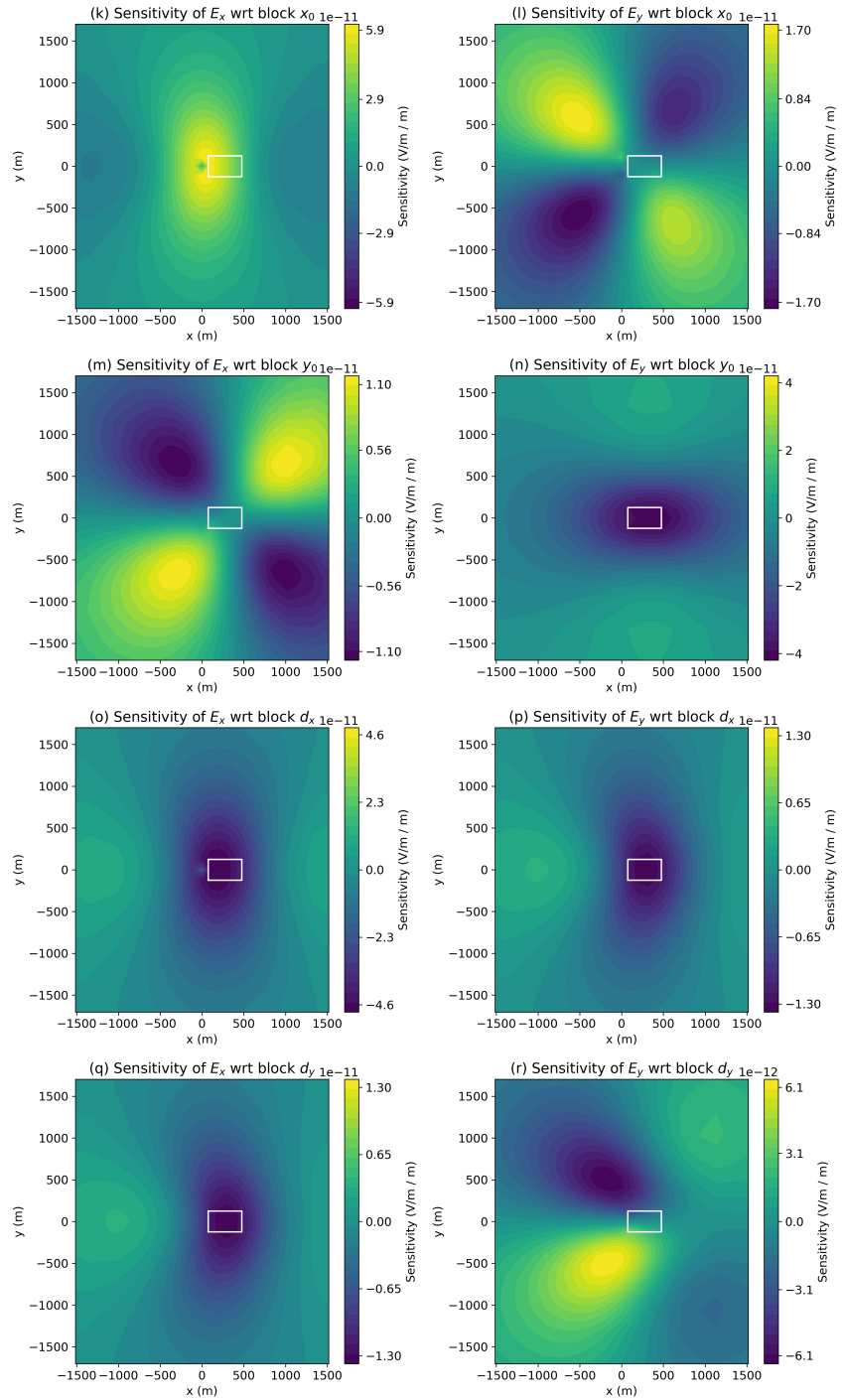


Figure C.17: Sensitivity of surface real E_x (left) and E_y (right) data with respect to the block geometry, $((V/m)/m)$

that a change in the conductivity of the block by 0.8% has a similar impact in the E_x data as moving x_0 of the block by $\sim 16\text{ m}$. For a change in y_0 of the block to have a comparable impact in the E_x data would require that it be perturbed by $\sim 85\text{ m}$. However, the E_y data are more sensitive to y_0 ; a perturbation of $\sim 24\text{ m}$, about 1/3 of that required in the E_x data, would result in a $\sim 10^{-9}\text{ V/m}$ change in the measured responses.

Examining the nature of the sensitivity with respect to parameters describing the target of interest provides insight both into how one might design a survey sensitive to the target, and how well we may be able to resolve various geometric features or physical properties in the model. For the example shown here, we see that it may be advantageous to collect data away from the well and hundreds of meters offset from the block. These are regions where both the E_x and E_y data have high sensitivity to features of the target and are distant from the steel-cased well, where we have the highest sensitivity to the background. Thus, data collected in these regions may improve our ability to resolve the target of interest. The parametric definition of the model provides a mechanism for examining how well we might expect to resolve various aspects of the target, such as its spatial extent. There are clearly further questions that may be investigated here, including exploring survey parameters such as the impact of varying the frequency on our ability to resolve the block, or performing the same analysis for a time-domain survey. A modular framework, with accessible derivatives, is an asset for exploring these types of questions.

C.6 Conclusion

The framework we have laid out has rigorously separated out various contributions to the electromagnetic equations in both time and frequency domain. We have organized these ideas into an object oriented hierarchy that is consistent across formulations and

attends to implementation details and derivatives in a modular way. The organization of the EM framework and numerical implementation are designed to reflect the math. The goal is to create composable pieces such that electromagnetic geophysical inversions and forward simulations can be explored and experimented with by researchers in a combinatorial, testable manner.

We strive to follow best practices in terms of software development including version control, documentation unit testing, and continuous integration. This work and the SIMPEG project are open-source and licensed under the permissive MIT license. We believe these practices promote transparency and reproducibility and we hope that these promote the utility of this work to the wider geophysics community.

parameter	Units of Sensitivity, \mathbf{J}_i	$\max_{\text{wrt } E_x} \mathbf{J}_i $	perturbation required to cause $\pm 10^{-9}V/m$ in E_x	$\max_{\text{wrt } E_y} \mathbf{J}_i $	perturbation required to cause $\pm 10^{-9}V/m$ in E_y
\mathbf{m}_i					
$\log(\sigma_{\text{back}})$	$(V/m)/\log(\sigma)$	1.5e-04	6.6e-08 S/m (6.6e-04%)	1.5e-04	6.6e-08 S/m (6.6e-04%)
$\log(\sigma_{\text{layer}})$	$(V/m)/\log(\sigma)$	3.5e-05	2.9e-06 S/m (2.9e-03%)	3.4e-05	2.9e-06 S/m (2.9e-03%)
$\log(\sigma_{\text{block}})$	$(V/m)/\log(\sigma)$	1.2e-07	1.7e-02 S/m (8.4e-01%)	3.3e-08	6.1e-02 S/m (3.1e+00%)
z_0_{layer}	$(V/m)/m$	1.7e-10	5.8e+00 m	4.4e-11	2.3e+01 m
h_{layer}	$(V/m)/m$	1.6e-10	6.2e+00 m	4.1e-11	2.4e+01 m
x_0_{block}	$(V/m)/m$	6.2e-11	1.6e+01 m	1.8e-11	5.6e+01 m
y_0_{block}	$(V/m)/m$	1.2e-11	8.5e+01 m	4.2e-11	2.4e+01 m
Δx_{block}	$(V/m)/m$	4.8e-11	2.1e+01 m	1.5e-11	6.6e+01 m
Δy_{block}	$(V/m)/m$	1.4e-11	7.3e+01 m	6.5e-12	1.5e+02 m

Table C.1: Comparison of the maximum amplitude of the sensitivity with respect to each model parameter, and the approximate perturbation in that parameter required to produce a $10^{-9} V/m$ change in the measured data. The conversion from a perturbation in log-conductivity to conductivity is given by equation C.26. The perturbation in conductivity is also provided in terms of a percentage of the true model conductivity.